# QUANTUM PHASES OF INTERACTING BOSONS IN OPTICAL LATTICES

Dissertation
zur Erlangung des Grades
des Doktors der Naturwissenschaften
der Naturwissenschaftlich-Technischen Fakultät
der Universität des Saarlandes

von
Rebecca Kraus

Saarbrücken
2021

| | |
|---|---|
| **Tag des Kolloquiums:** | 30.09.2021 |
| **Dekan:** | Prof. Dr. Jörn Walter |
| **Berichterstatter/in:** | Prof. Dr. Giovanna Morigi |
| | Prof. Dr. Michael Fleischhauer |
| | Prof. Dr. George Batrouni |
| **Vorsitz:** | Prof. Dr. Gregor Jung |
| **Akad. Mitarbeiter:** | Dr. Adam Miroslaw Wysocki |

## ABSTRACT

This thesis presents a theoretical analysis of the phase diagram of ultracold bosons in a lattice and interacting with long-range interactions. The theoretical model is an extended Bose-Hubbard model and describes the dynamics of ultracold atoms in optical lattices realised in present experimental platforms. We consider here two situations, where either the long-range forces are global and emerge from the coupling with a high-finesse cavity, or they decay with the interparticle distance and can be due to Rydberg interactions or to the atoms permanent dipoles. We determine the ground state in one and two dimensions using mean-field treatments. In one dimension we complement our studies using numerical programs based on tensor networks. We focus in particular on parameters for which the hopping induced by the kinetic energy competes with the interaction-induced correlated hopping between lattice sites. We analyse the superfluid phases emerging from the competition of these two mechanisms, and identify the parameters, where the two processes destructively interfere. For power-law interactions this quantum interference leads to insulating phases at relatively large kinetic energies, where one would otherwise expect superfluidity. When correlated tunnelling is due to the global potential of a resonator, the ground state is a self-organised topological insulator.



## ZUSAMMENFASSUNG

Diese Arbeit präsentiert eine theoretische Analyse des Phasendiagramms von ultrakalten Bosonen in einem Gitter, die langreichweitige Wechselwirkungen erfahren. Das theoretische Modell ist ein erweitertes Bose-Hubbard Modell und beschreibt die Dynamik von ultrakalten Atomen in einem optischen Gitter, wie sie in heutigen Experimenten realisiert werden kann. Wir betrachten hier zwei Situationen: Zum einen sind die langreichweitigen Kräfte global und entstehen aus der Kopplung mit einem Resonator. Zum anderen zerfällt das Wechselwirkungspotential mit dem Abstand zwischen den Teilchen, wie es zwischen Rydbergatomen oder Atomen mit einem permanenten Dipolmoment auftritt. Wir bestimmen den Grundzustand in einer und zwei Dimensionen durch Mean-Field Analysen. In einer Dimension benutzen wir zudem ein auf Tensornetzwerken basierendes numerisches Programm. Wir betrachten insbesondere Parameter, für die das durch die kinetische Energie induzierte Tunneln mit dem von der

Wechselwirkung induzierten Tunneln konkurriert. Wir analysieren die superfluiden Phasen, die sich aus dieser Kompetition ergeben, und identifizieren die Parameter, bei denen die beiden Prozesse destruktiv interferieren. Für die mit dem Abstand zerfallenden Wechselwirkungen führt diese Quanteninterferenz zu Isolatoren in Parameterbereichen, in denen man sonst Superfluidität erwarten würde. Wenn das Tunneln vom globalen Potential herrührt, ist der Grundzustand ein selbstorganisierter topologischer Isolator.

# CONTENTS

# ACRONYMS

BEC: Bose-Einstein Condensate

BI: Bond Insulator

BSF: Bond Superfluid

BSS: Bond Supersolid

CDW: Charge Density Wave

CGMF: Cluster Gutzwiller Mean-Field

DMRG: Density Matrix Renormalization Group

HI: Haldane Insulator

MI: Mott Insulator

MPS: Matrix Product State

PS: Phase Separation

PSF: Pair Superfluid

PSS: Pair Supersolid

QMC: Quantum Monte Carlo

SF: Superfluid

SGMF: Site-decoupled Gutzwiller Mean-Field

SS: Supersolid

SSF: Staggered Superfluid

SSS: Staggered Supersolid

SVD: Singular Value Decomposition

# INTRODUCTION

The recent years have witnessed a rapid progress in the control of the quantum dynamics of atomic and molecular gases [1–4]. These remarkable advances open the fascinating possibility of shedding new light on the quantum structure of matter and of its interactions with the electromagnetic field [4–6]. One prominent example is the observation of the quantum phase transition between superfluid and Mott insulator in ultracold atomic gases confined by optical lattices [7–9]. This quantum phase transition is predicted by the Bose-Hubbard model [10, 11], that was first theoretically proposed in the condensed matter community for electrons in superconducting systems [12] and then extended to bosons [11]. The experimental observations confirm the capability to simulate these dynamics and control them to the extent to be able of tuning the parameters and explore the equilibrium and the out-of-equilibrium phase diagram [4, 6].

New questions arise from the the experimental realization of novel regimes [5, 13–15]. In the context of optical lattices, the study of the dynamics of dipolar gases [13] or of atoms interacting via long-range optomechanical forces [14, 15] requires one to extend the Bose-Hubbard model by adding the long-range interactions [13–16]. Several theoretical studies included the effect of long-range potentials by means of terms describing interactions between the density at different sites [13, 16–28]. These terms induce density modulations [13, 16–31] and, for power-law interactions and unit density, lead to the onset of topological phases, such as the Haldane insulator [32–35].

A careful derivation of the Bose-Hubbard model, however, shows that the interactions give rise also to additional terms [36–42]. A prominent one is correlated hopping, where the amplitude of the hopping between neighbouring sites depends on the lattice density distribution within the range of the interaction [36–42]. Previous studies including correlated tunneling terms revealed exotic superfluid phases [36, 38, 39, 42]. Nevertheless until now the origin of those exotic phases is not totally clarified and a limited insight on the effect of the interaction-induced tunneling on the phase diagram is gained.

One relevant but unexplored aspect is the interplay between correlated tunneling and the tunneling due to single-particle effects. Since these mechanisms couple the same initial and final state, they can interfere. This quantum interference is one of the central subject of this thesis. We determine the phase diagram in the regime, where the quantum interference between single-particle and correlated tunneling is relevant. By means of mean-field calculations and density matrix renormalization group (DMRG) numerical simulations we iden-

tify and characterize the regime where this mechanism significantly determine the ground state properties.

This thesis consist of three chapters. In the first chapter we summarize the concepts and theoretical models, which set the basis for our studies.

In the second chapter we investigate the phase diagram of the extended Bose-Hubbard model in the presence of dipolar interaction. We set first the focus on the derivation, highlighting the regime where correlated tunneling is relevant. Using a density matrix renormalization group (DMRG) approach we investigate the canonical phase diagram for different densities and in one dimension. We then analyse the ground-state phase diagram of a two-dimensional square lattice by means of two complementary mean-field approaches.

In the third chapter we characterize the phase diagram of the extended Bose-Hubbard model when the interactions are global. This system is realized in experiments with ultracold atoms in a cavity [43, 44]. We determine the phase diagram in the regime of the experiment [43] and then focus our studies to the situation where correlated tunneling due to the global interaction becomes relevant. Our study makes use of mean-field treatments as well as sophisticated density matrix renormalization group (DMRG) simulations. The latter allows us to reveal topological phases that are induced by quantum interference between single-particle tunneling and the global hopping due to the cavity.

# 1

# ULTRACOLD NEUTRAL ATOMS IN AN OPTICAL LATTICE

Ultracold bosonic atoms in an optical lattice undergo a dynamics that is described by the Bose-Hubbard (BH) model. This model possesses a phase transition from an insulating to the superfluid phase, which is controlled by the interplay between contact interactions of the atoms and their kinetic energy. The purpose of this thesis is to determine how these phases are modified by the presence of long-range interactions. This section provides the basic concepts for the rest of this thesis. We will review the superfluid to Mott insulator phase transition of the Bose-Hubbard model and discuss the methods typically applied to determine the phase diagram.

## 1.1 ULTRACOLD ATOMS

The last 50 years witnessed a rapid development in the concepts and techniques of laser cooling and trapping [1–3]. This progress opened the way to realize and tailor quantum states of matter [4, 5, 45] to the point of simulating complex quantum dynamics conjectured for strongly-correlated, condensed matter systems [5]. One important milestone along the progress is the realization of the Bose-Einstein condensation (BEC) of atoms in traps [45–47]. BEC occurs when the ground state of a non-interacting gas is macroscopically occupied at a finite temperature $T$ below a threshold $T_c$. In a gas of atoms with mass $m$ it is observed when the thermal de-Broglie wavelength $\lambda_{\mathrm{dB}}$ becomes comparable with the interparticle distance $n^{-1/3}$[1]. In order to figure out the requirement on the physical parameters, we introduce the thermal de-Broglie wavelength $\lambda_{\mathrm{dB}}$, which is defined as

$$\lambda_{\mathrm{dB}} = \sqrt{\frac{2\pi\hbar^2}{m k_{\mathrm{B}} T}} \ , \tag{1.1}$$

where $\hbar$ ist the Planck constant and $k_B$ the Boltzmann constant. Thus condensation of the bosons can be reached for $\lambda_{\mathrm{dB}} n^{1/3} \gtrsim 1$ by either decreasing the temperature $T$ or increasing the density $n$. The parameters necessary to observe BEC in an experiment are for instance given

1 Here one considers a homogeneous 3D system with a density of $n$.

by $T = 170$ nK and $n = 2.5 \times 10^{12}$ cm$^{-3}$ [45]. The first observation of BEC in an atomic gas was reported by Anderson et al. [45]. Under certain conditions the quantum gas forming a condensate can possess a frictionless flow [48]. In this case the quantum gas is in the so-called superfluid [48].

This section provides a short introduction on BEC and superfluidity: In Subsection 1.1.1 we will discuss a BEC of an ideal Bose gas. The influence of weak contact interactions will be reported at the end of Subsection 1.1.1. In the following Subsection 1.1.2 we will shortly discuss the connection between BEC and superfluidity. This section is based on the literature in Refs. [4, 6, 48–51].

### 1.1.1 *Bose-Einstein condensation in an atomic gas*

We consider $N$ non-interacting particles with mass $m$ in a box of volume $V = L^d$ in $d$-dimensional space. Their Hamiltonian takes the form

$$\hat{H} = \sum_{j=1}^{N} \hat{H}_j \ , \tag{1.2}$$

where $\hat{H}_j = \frac{\hat{\mathbf{p}}_j}{2m}$ is the Hamiltonian of the particle $j$ with $j = 1, ..., N$. Here $\hat{\mathbf{p}}_j$ is the particle's momentum operator in $d$-dimensional space and is canonically-conjugated to the position operator $\hat{\mathbf{r}}_j$ fulfilling the commutation relations

$$\left[\hat{x}_{l,j}, \hat{p}_{k,j'}\right] = i\hbar\delta_{l,k}\delta_{j,j'} \quad \text{with } l,k = \{1,..,d\} \quad \text{and} \quad j,j' \in \{1,..,N\} \ ,$$

where $\hat{x}_{l,j}$ and $\hat{p}_{k,j'}$ are the entries of the $d$-dimensional vectors $\hat{\mathbf{r}}_j$ and $\hat{\mathbf{p}}_{j'}$, respectively. Since $\left[\hat{p}_{l,j}, \hat{H}_j\right] = 0$ for all $l \leq d$ and $j \in \{1,..,N\}$ we can choose the basis of common eigenstates of both operators: Thus we consider the eigenstates of the momentum operator in position space

$$\psi_{\mathbf{p}}(\mathbf{r}) = \frac{1}{\sqrt{V}} e^{i\mathbf{p}\cdot\mathbf{r}/\hbar} \tag{1.3}$$

at eigenvalue $\mathbf{p}$. By imposing periodic boundary conditions[2] the momentum takes values $\mathbf{p} = 2\pi\hbar\mathbf{n}/L$, where $\mathbf{n}$ is a $d$-dimensional vector with integer entries.

The many-body eigenstates $\Psi_k$ of the $N$-particle Hamiltonian in Eq. (1.2) are given by superpositions of the product over all particles in a certain single-particle state, Eq. (1.3), and is here labeled by $k$. Its form depends on the spin degree of freedom of the particles. The many-body eigenstate of particles exhibiting a half integer spin has to be anti-symmetric under permutation of the particles. In this

2 Here one requires on the eigenstates $\psi(x,y,z)$ in 3D system the relation $\psi(x,y,z) = \psi(x+L,y,z)$ for the $y$-, $x$- and $z$-direction.

case the particles are called fermions. Particles with integer spin are called bosons. Their many-body wavefunction is symmetric under permutation of the bosons. We will consider here particles with zero spin and thus bosons.

The corresponding eigenenergies of the Hamiltonian, Eq. (1.2), take the values

$$E_k = \sum_{\mathbf{p}} \epsilon_{\mathbf{p}} n_{\mathbf{p}} \tag{1.4}$$

with

$$\epsilon_{\mathbf{p}} = \frac{\mathbf{p}^2}{2m} \tag{1.5}$$

and $n_{\mathbf{p}} \in \{0, .., N\}$ the occupation number of the single-particle state with momentum $\mathbf{p}$. The ground state of the Hamiltonian in Eq. (1.2) is given by

$$\Psi_{k=0}(\mathbf{r}_1, \mathbf{r}_2, ..., \mathbf{r}_N) = \prod_{j=1}^{N} \psi_0(\mathbf{r}_j) \ , \tag{1.6}$$

where the single-particle state $\psi_0(\mathbf{r}_j)$ is the one in Eq. (1.3) with $\mathbf{p} = (0, .., 0)$ for all particles.

We now consider a grand-canonical ensemble and denote by $T$ the temperature and by $\mu$ the chemical potential. Since we consider particles with zero spin they fulfill the Bose-Einstein statistics. Within the grand-canonical ensemble the average occupation numbers of each single-particle state at energy $\epsilon_{\mathbf{p}}$ follows the Bose-Einstein statistics [48]

$$\bar{n}(\epsilon_{\mathbf{p}}) = \frac{z e^{-\beta \epsilon_{\mathbf{p}}}}{1 - z e^{-\beta \epsilon_{\mathbf{p}}}} \ . \tag{1.7}$$

Here $z = ^{\beta\mu}$ is the fugacity and $\beta = 1/k_B T$. We single out the average occupation of the ground state

$$\bar{n}(\epsilon_0) = \frac{1}{e^{-\beta\mu} - 1} \ , \tag{1.8}$$

which we denote by $N_0$. We note that the chemical potential shall fulfill $\mu < 0$ in order to ensure that $\bar{n}(\epsilon_{\mathbf{p}}) \geq 0$ for all $\mathbf{p}$. The number of particles in the excited states constitutes the thermal component and it is the sum over the mean number of particles with energy $\epsilon_{\mathbf{p}} > \epsilon_0$:

$$N_{\text{ex}} = \sum_{\mathbf{p}}{}' \bar{n}(\epsilon_{\mathbf{p}}) \ , \tag{1.9}$$

where the sum runs over all different vectors $\mathbf{p}$ except for the one of the ground state. The total number of bosons $N$ is conveniently

written as the sum of the number of bosons in the condensate and in the thermal fraction:

$$N = N_0 + N_{\text{ex}} \ . \tag{1.10}$$

Bose-Einstein condensation occurs when $N_0$ is macroscopically occupied [51]. We therefore analyze $N_0 = N - N_{\text{ex}}$. For a large volume $V$ we can take the continuum limit of Eq. (1.9)[3] and write the thermal fraction as an integral over the energies

$$N_{ex} = \int_0^\infty \rho(\epsilon)\bar{n}(\epsilon)d\epsilon \ , \tag{1.11}$$

where $\bar{n}(\epsilon)$ is the continuum limit of Eq. (1.7) and $\rho(\epsilon)$ denotes the density of states [6]

$$\rho(\epsilon) = \left(\frac{2\pi}{\hbar}\right)^d 2mL^d S_d (2m\epsilon)^{(d-2)/2} \ , \tag{1.12}$$

where $S_d$ is the surface of the $d$-dimensional sphere[4] .

An inspection of the properties of the integral in Eq. (1.11) as a function of the temperature shows that for $d = 3$ and for $T \leq T_c$ [48]

$$N_{\text{ex}}(T) = N\left(\frac{T}{T_c}\right)^{\frac{3}{2}} \ , \tag{1.13}$$

when $T_c$ is given by the expression [48]

$$T_c = \frac{2\pi\hbar^2}{mk_B}\left(\frac{N}{Vg_{3/2}(1)}\right)^{2/3} \tag{1.14}$$

with $g_{3/2}(1) = 2.612$. In this case the condensate fraction is given by [48]

$$\frac{N_0}{N} = 1 - \left(\frac{T}{T_c}\right)^{\frac{3}{2}} \tag{1.15}$$

and thus the ground state is macroscopically occupied for $T < T_c$. Its behaviour as a function of $T$ in units of $T_c$ is shown in Fig. 1.1. For $d \leq 2$, instead, $N_{ex}(T)$ is not bounded for any $T \neq 0$ [6].

3 The continuum limit is justified when the spacing between two neighboring energies is much smaller then the thermal energy.

4 Note for $d = 2$ the zero has to be excluded in the integral (1.11)

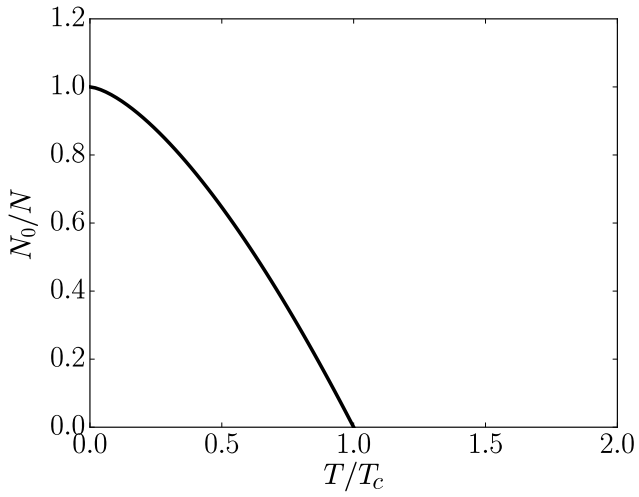


Figure 1.1: The condensate fraction $N_0/N$ as function of the temperature $T$ for a uniform ideal Bose gas in three dimension. Below a critical temperature $T_c$, Eq. (1.14), the condensate occupation is macroscopic.

*Properties*

In an ideal case, the state where the bosons condensate is the eigenstate at $\mathbf{p} = (0, .., 0)$. In the following we inspect the properties of the BEC in the limit $T = 0$, where $N = N_0$ and the thermal fraction vanishes. We now introduce some useful concepts by inspecting the properties of the condensate. Since the condensate is an eigenstate of the momentum, it has spatial coherence over the whole box. This becomes visible by inspecting the one-body density matrix. In position space the corresponding one-body density matrix reads [48]

$$\rho_1(\mathbf{r}, \mathbf{r}') = N_0 \int d\mathbf{r}_2 ... d\mathbf{r}_{N_0} \Psi^*_{k=0}(\mathbf{r}, \mathbf{r}_2, ..., \mathbf{r}_{N_0}) \Psi_{k=0}(\mathbf{r}', \mathbf{r}_2, ..., \mathbf{r}_{N_0}) \tag{1.16}$$

$$= N_0 |\psi_0(\mathbf{r}')|^2 = \frac{N_0}{V} , \tag{1.17}$$

where we insert the many-body ground state (1.6). $\rho_1(\mathbf{r}, \mathbf{r}')$ is thus constant and independent from the distance $s = |\mathbf{s}| = |\mathbf{r} - \mathbf{r}'|$. In particular in the thermodynamic limit

$$\lim_{s \to \infty} \rho_1(s) \to \frac{N_0}{V} = \text{const.} \tag{1.18}$$

and the condensate thus exhibits off-diagonal long-range order [48]. We can extract the momentum distribution of Bose gas by taking the Fourier transform of the one-body density matrix [48]

$$n(\mathbf{p}) = \int d\mathbf{s} \; e^{i\mathbf{p}\cdot\mathbf{s}/\hbar} \rho_1(s) \quad . \tag{1.19}$$

Inserting the expression in Eq. (1.17) reveals a singular behaviour at zero momentum [48] :

$$n(\mathbf{p}) = N_0 \delta(\mathbf{p}) \tag{1.20}$$

This behaviour is revealed in an experiment by means of a time of flight measurement [45–47], and was the smoking gun of BEC in [45]. These properties survive for $T < T_c$ with corrections due to the thermal fraction.

*Adding weak contact interactions*

Naturally interactions occur between the particles. Atoms typically interact via Van-der-Waals interactions. Their potential range is typically much smaller than the de Broglie wavelength in Eq. (1.1) [48]. Therefore one can typically replaces the interaction potential by a contact interaction potential [6, 48]

$$U_{int}(\mathbf{r}) = g\delta\left(\mathbf{r} - \mathbf{r}'\right) \ , \tag{1.21}$$

where the prefactor reads [6, 48]

$$g = \frac{4\pi\hbar^2 a_s}{m} \tag{1.22}$$

and $a_s$ is the so-called s-wave scattering length [6, 48].

A 3D and 2D homogeneous bose gas at low temperature possesses off-diagonal long-range order even in the presence of weak contact interactions[5] [48]. The situation is different in 1D, where quantum fluctuations become particularly important [50] and lead to the disappearance of off-diagonal long-range order even at $T = 0$ [50]. In this case at large distance the off-diagonal correlations fall off as a power law and one denotes the state of matter a quasi-condensate [50].

In this thesis we will consider temperatures very close to $T = 0$, for which the gas is either a BEC or a quasi-condensate.

### 1.1.2 *Superfluidity*

Fluids who exhibit a frictionless flow are dubbed by superfluids. Superfluidity (SF) is exquisitely quantum mechanical and is characteristic of bosons. In the literature BEC and SF are often used interchangeably, yet they do not necessarily coincide. In order to define SF, we will use Landau's criterion [48].

*Landau's criterion*

We consider a uniform fluid flowing at zero temperature along a capillary at a constant velocity $v$. Here we account for dissipative processes only through the creation of elementary excitations. We first consider a reference frame $K$ moving with the fluid. Let $E_0$ be the energy of the fluid in the reference frame $K$. The appearance of a single excitation with momentum $\mathbf{p}$ and energy $\epsilon(\mathbf{p})$ leads to the total energy

$$E = E_0 + \epsilon(\mathbf{p}) \ . \tag{1.23}$$

Let us now consider the reference frame $K'$ moving with velocity $-\mathbf{v}$ relative to $K$. Here the capillary is at rest. In this reference frame the

5 Meaning the interaction energy is a perturbation to the kinetic energy.

energy $E'$ and the momentum $\mathbf{P}'$ of the fluid are determined according to the Galilean transform

$$E' = E + \mathbf{p}\cdot\mathbf{v} + \frac{1}{2}M|\mathbf{v}|^2 \quad , \quad \mathbf{P}' = \mathbf{p} + M\mathbf{v} \, , \tag{1.24}$$

where $M$ is the total mass of the fluid. In Eq. (1.24) one can identify $\epsilon(\mathbf{p}) + \mathbf{p}\cdot\mathbf{v}$ as the change of the energy due to the appearance of the excitation with momentum $\mathbf{p}$. Therefore $\epsilon(\mathbf{p}) + \mathbf{p}\cdot\mathbf{v}$ is the energy of the elementary excitation when the capillary is at rest. An elementary excitation will spontaneously appear, if the energy in $K'$ is decreased. This leads to the condition

$$\epsilon(\mathbf{p}) + \mathbf{p}\cdot\mathbf{v} < 0 \, , \tag{1.25}$$

which requires velocities fulfilling $|\mathbf{v}| > \epsilon(\mathbf{p})/|\mathbf{p}|$. For such velocities the flow of the fluid is unstable and the kinetic energy will be converted into heat. These considerations lead to the identification of the critical velocity $v_c$, below which the superfluid is stable [48]:

$$v_c = \min_{\mathbf{p}} \frac{\epsilon(\mathbf{p})}{|\mathbf{p}|} \, . \tag{1.26}$$

Here the minimum is taken over all values of $\mathbf{p}$. Thus, for an absolute value $v$ of the velocity between the fluid and the capillary smaller then a critical velocity $v_c$ there will be a persistent flow without friction.

For the ideal Bose gas without interaction the condition (1.25) is never fulfilled, since $\epsilon(\mathbf{p}) = \mathbf{p}^2/2m$ and $v_c = 0$. Thus an ideal Bose gas is never a superfluid. Weakly interacting bosons instead exhibit a low energy spectrum with phonon like dispersion relation [48]. The critical velocity is finite and is given by the sound velocity.

## 1.2 ULTRACOLD ATOM IN AN OPTICAL LATTICE

Neutral atoms can be confined in external potentials by means of the mechanical effects of light [1–3]. One prominent example is the optical lattice, which is realized by means of lasers creating a periodic potential such as a standing wave [4, 52]. The resulting dynamics simulate quantum solid state systems and allow one to shed light on quantum phases of strongly correlated matter [5]. In this section we review the description of a quantum particle in an optical lattice [52–55], which is at the basis of the Bose-Hubbard model.

### 1.2.1 *Realization of an optical lattice*

An optical lattice is a periodic potential for neutral atoms. It is created by spatially modulated electric field, which couples to an atomic transition. Confinement results from the mechanical force due to the spatial gradient of the potential in the electric dipole approximation.

Thus in the following we will consider a system consisting of a single atom coupling to a spatially modulated electric field. In one dimension the electric field is a classical standing wave [52]

$$\mathbf{E}(\mathbf{r}) = E_0 \vec{\epsilon} \sin(k_L x) \left( e^{-i\omega_L t} + c.c \right) , \tag{1.27}$$

where $E_0$ is the amplitude and $\vec{\epsilon}$ the normalized polarization vector of the electric field. The frequency $\omega_L$ of the electric field is connected with its wave number $k_L = |\mathbf{k}_L|$ via the dispersion relation $\omega_L = ck_L$, where $c$ is the speed of light in vacuum.

The energy of the system consist of the energy of the free moving particle $\hat{H}_{\text{at}}$ and the interaction energy between atom and field $\hat{H}_{int}$:

$$\hat{H} = \hat{H}_{\text{at}} + \hat{H}_{int} \tag{1.28}$$

with [56, 57]

$$\hat{H}_{\text{int}} = -\hat{\mathbf{d}} \cdot \mathbf{E}(\hat{\mathbf{r}}) \tag{1.29}$$

and $\hat{\mathbf{d}}$ is the electric dipole operator. We consider here the field to be sufficiently weak, such that the internal degrees of freedom can be reduced to the ground state $|g\rangle$ and the excited state $|e\rangle$ of the optical dipole transition at frequency $\omega_{\text{L}}$. In this limit the Hamiltonian describing the internal and external degrees of freedom of the atom is given by

$$\hat{H}_{\text{at}} = \hbar\omega_a \hat{\sigma}^\dagger \hat{\sigma} + \frac{\hat{\mathbf{p}}^2}{2m} , \tag{1.30}$$

where $m$ is the mass of the atom and $\hat{\mathbf{p}}$ is the momentum of the center of mass motion, canonical-conjugated to $\hat{\mathbf{r}}$. Here we introduced the lowering operator $\hat{\sigma} = |g\rangle \langle e|$ in the internal degrees of freedom and its hermitian conjugate $\hat{\sigma}^\dagger = |e\rangle \langle g|$. In the basis of the internal states $\{|e\rangle , |g\rangle\}$ the electric dipole operator exhibits the form[6]

$$\hat{\mathbf{d}} = \mathbf{d}_{eg} \hat{\sigma}^\dagger + \mathbf{d}_{ge} \hat{\sigma} , \tag{1.31}$$

where $\mathbf{d}_{eg} = \mathbf{d}^*_{ge} = \left\langle g|\hat{\mathbf{d}}|e \right\rangle$.

Inserting the expression of the dipolar operator, Eq. (1.31), and of the electric field, Eq. (1.27), into the interaction Hamiltonian in Eq. (1.29) leads within the rotating-wave approximation[7] [56, 57] to the form [56]

$$\hat{H}_{\text{int}} = \hbar\Omega \left(\hat{x}, t\right) \hat{\sigma}^\dagger + h.c. \tag{1.32}$$

with $\Omega(\hat{x}, t) = \Omega \sin(k_L \hat{x}) e^{-i\omega_L t}$. The parameter $\Omega = \frac{E_0 |\mathbf{d}_{eg} \cdot \vec{\epsilon}_1|}{\hbar}$ has the dimension of a frequency and is denoted by Rabi frequency [57][8].

6 Note that due to parity the diagonal elements of the electric dipole matrix are zero.

7 Here one neglects the fast rotating terms in the interaction Hamiltonian, which is valid for sufficiently small coupling frequency $\Omega$ with respect to $\omega_L + \omega_a$.

8 The complex phase of the scalar product between dipole vector and polarisation is picked to $\pi$.

Trapping of atoms is typically realized in the regime where the time scale on which the internal degrees of freedom evolve is much larger then the time scale on which the external degrees of freedom evolve. In perturbation theory the interaction induces an effective shift of the internal ground state energy of the atom, which reads

$$\delta E_g = \frac{\hbar\Omega^2}{\Delta}\sin^2(k_L\hat{x}) \,, \tag{1.33}$$

where the frequency $\Delta = \omega_L - \omega_a$ is the detuning between the laser frequency $\omega_L$ and the atomic resonance frequency $\omega_a$. By assuming that $\langle \hat{\mathbf{p}}^2/2m \rangle \ll |\Delta|$ Eq. (1.33) gives rise to a position dependent potential, which rewrites as [52]

$$V_{\text{lat}} = V_0 \sin^2(k_L\hat{x}) \text{ with } V_0 = \frac{\hbar\Omega^2}{\Delta} \,. \tag{1.34}$$

This is the potential of the optical lattice. Its depth can be controlled by the detuning $\Delta$ and the Rabi frequency $\Omega$ within the limits of the validity of the description. The sign of the potential is determined by the sign of the detuning $\Delta$. Therefore the minima of the potential will be at the nodes of the laser standing wave, if $\Delta > 0$. For $\Delta < 0$ the atoms are confined by the regions where the intensity is maximal. The periodicity of the lattice $a = \pi/k_L$ is controlled by the effective wavenumber $k_L$, which can be controlled by means of the geometry of the setup. In the rest of the thesis the unit of the energy will be the so-called recoil energy [52]

$$E_R = \frac{(\hbar k_L)^2}{2m} \,. \tag{1.35}$$

### 1.2.2 *Eigenstates of a single atom in an optical lattice*

In this section we analyze the eigenstate of a particle in the one-dimensional optical lattice potential of Eq. (1.34). We assume a full length of $L$ with $N_L = L/a$ minima and periodic boundary conditions, namely $V_{\text{lat}}(x + L) = V_{\text{lat}}(x)$. The eigenstates $\psi(x)$ solve the Schrödinger equation[9]

$$\left(-\frac{\hbar^2}{2m}\frac{d^2}{dx^2} + V_{\text{lat}}(x)\right)\psi(x) = E\psi(x) \,, \tag{1.36}$$

where $E$ is the eigenenergy and

$$V_{\text{lat}}(x) = V_{\text{lat}}(x + a) \,. \tag{1.37}$$

Due to the periodicity of the Hamiltonian the eigenfunctions are *Bloch states*

9 We consider here the eigenstates only in one-dimension, since the eigenstates in the remaining directions are given by plane waves. The total wave function is then given by product of the plane waves in $y$ and $z$ and the eigenstates studied here.

Bloch functions [53, 54]:

$$\psi_q^n(x) = e^{iqx} u_{n,q}(x) \,, \tag{1.38}$$

where $n$ denotes the band, $q$ is the quasi-momentum, and the function $u_{n,q}(x)$ is periodic with periodicity $a$. We choose the Brillouin zone $q \in (-\pi/a, \pi/a]$. Fig. 1.2 displays the eigenenergies $E_n(q)$ of the Bloch waves for different lattice depth as a function of $q$ in the first Brillouin zone. For $V_0 = 0$ we have the solution of a free particle, which results in folded parabolas to the first Brillouin zone. For $V_0 > 0$ a gap opens at the borders of the Brillouin zone (see Fig. 1.2 (b) and (c)). The Bloch functions form a complete set of orthonormal functions of the single particle Hilbert space. Furthermore they are delocalized over the whole lattice, i.e.

$$|\psi_q^n(x)|^2 = |\psi_q^n(x + ja)|^2 \tag{1.39}$$

for any integer value $j = 1, ..., N_L$.

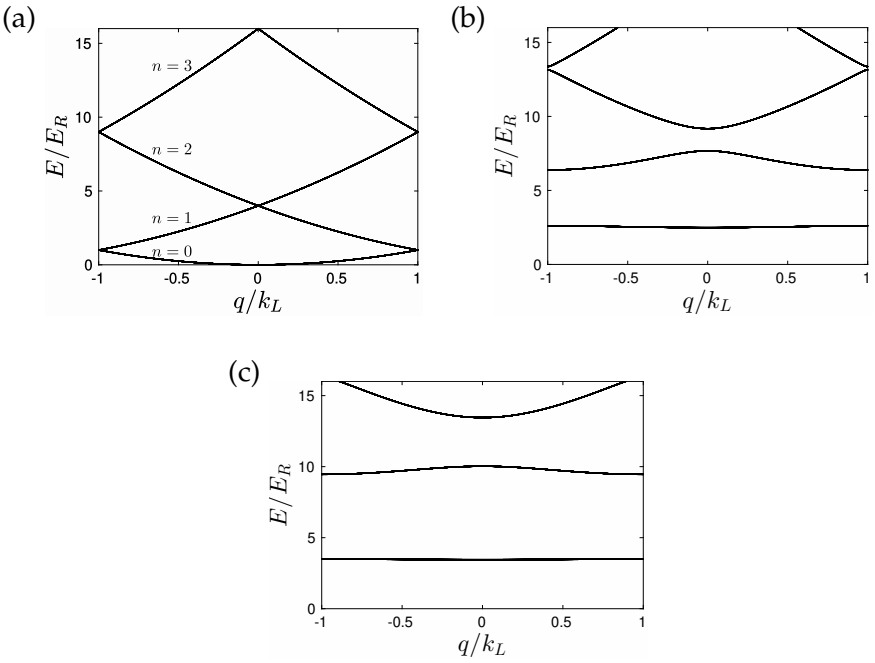


Figure 1.2: Eigenenergies in units of the recoil energy $E_R$ as a function of the quasi momentum $q$ for the different potential depth (a) $V_0 = 0$, (b) $V_0 = 8E_R$ and (c) $V_0 = 14E_R$. The integer number $n$ labels the band index. The number of lattice site is fixed to $N_L = 13$. $q$ is in units of $\pi/a$.

*Wannier states*

In order to analyze the site occupancy, it is convenient to use Wannier functions. These are the Fourier transform of the Bloch functions in Eq. (1.38) and are defined as [53–55]

$$w_n(x - x_j) = \frac{1}{\sqrt{N_L}} \sum_{q \in \left(-\frac{\pi}{a}, \frac{\pi}{a}\right]} e^{-iqx_j} \psi_q^n(x) \,, \tag{1.40}$$

where $x_j = ja$ label the minimas of the optical lattice potential and are here enumerated by $j \in \{0, ...., N_L - 1\}$. The Wannier functions form an orthonormal basis in the Hilbert space of a single particle, fulfilling the completeness relation [55]:

$$\sum_{n=1}^{\infty} \sum_{j=0}^{N_L-1} w_n^*(x - x_j) w_n(x' - x_j) = \delta(x - x') \tag{1.41}$$

and the orthonormal relation [55]

$$\int_0^{N_L a} dx \; w_n^*(x - x_j) w_{n'}(x - x_{j'}) = \delta_{n,n'} \delta_{j,j'} \; . \tag{1.42}$$

In this thesis we will consider solely the Wannier functions of the lowest band. In this case one can choose the Wannier functions to be real and symmetric about $x_j$ [53]. Furthermore they fall of exponentially with the distance from $x_j$ [53]. The last two properties are visible in the two examples of the absolute value squared of the Wannier function in the lowest band plotted in Fig. 1.3 for two different lattice depths of $V_0$ and for $x_j = 0$.

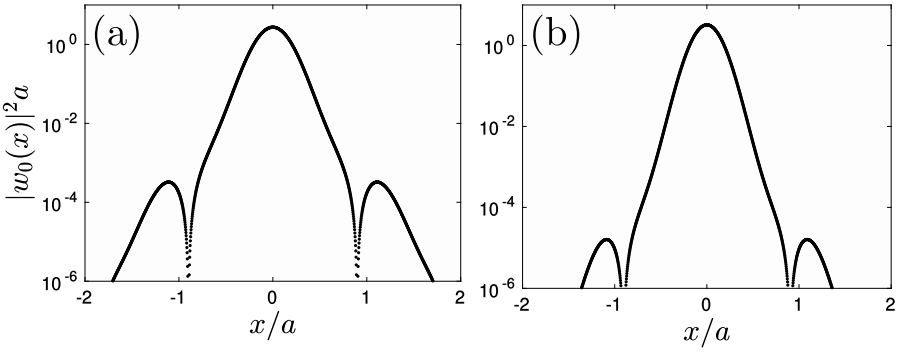


Figure 1.3: $|w_0(x)|^2$ as a function of $x$ over five lattice sites for two different potential depths (a) $V_0 = 8E_R$ and (b) $V_0 = 14E_R$ with $x_j = 0$. The absolute value squared of the Wannier function is in units of $1/a$ and the position in units of $a$.

## 1.3 SUPERFLUID TO MOTT INSULATOR PHASE TRANSITION

We now review the many-body dynamics of a quantum gas of bosons in an optical lattice. When the atoms are in the tight-binding regime, their dynamics can be mapped to the Bose-Hubbard model [10]. This model has a quantum phase transition from a so-called Mott insulating phase to a superfluid [11]. Experimentally the phase transition was first measured by Greiner et al. [7] in 3D and later also by Stöferle et al. [8] and Spielman et al. [9] in lower dimensions. In this section we first report the mapping of the ultracold bose gas in the optical lattice to the standard Bose-Hubbard model for a one-dimensional geometry. We then discuss the resulting phases and phase transition. We finally

report the methods used in this thesis to study the ground-state phase diagram. The section serves as an introduction to the studies presented in this thesis.

### 1.3.1 *Mapping on the Bose-Hubbard model*

We consider $N$ ultracold bosons of mass $m$ in an optical lattice of periodicity $a$ along $x$ with $N_L = L/a$ lattice sites. Moreover, we consider a tight harmonic potential in the $y-z$ plane. The total trap potential is then given by

$$V_{\text{trap}} = \frac{m\omega^2}{2}\left(y^2+z^2\right) + V_0 \sin^2(\pi x/a) \,, \tag{1.43}$$

where we denote the harmonic trap frequency by $\omega$ and the optical lattice depth by $V_0$. We inspect the regime in which the interaction potential $U_{\text{int}}$ can be modeled as a contact interaction potential given by the expression in Eq. (1.21) [6, 48]. The dynamics of the bosons are determined by the second-quantized Hamiltonian:

$$\begin{aligned}\hat{H} = &\int d^3\mathbf{r}\hat{\Psi}(\mathbf{r})\left[-\frac{\hbar^2}{2m}\nabla^2 + V_{\text{trap}}(\mathbf{r})\right]\hat{\Psi}(\mathbf{r}) \\ &+ \frac{1}{2}\int d^3\mathbf{r}\int d^3\mathbf{r}'\hat{\Psi}^\dagger(\mathbf{r})\hat{\Psi}^\dagger(\mathbf{r}')U_{\text{int}}\,\hat{\Psi}(\mathbf{r}')\hat{\Psi}(\mathbf{r}) \,,\end{aligned} \tag{1.44}$$

where $\hat{\Psi}(\mathbf{r})$ and $\hat{\Psi}^\dagger(\mathbf{r})$ are the bosonic field operators. They fulfill the bosonic commutation relation

$$\left[\hat{\Psi}(\mathbf{r}), \hat{\Psi}^\dagger(\mathbf{r}')\right] = \delta(\mathbf{r}-\mathbf{r}') \,. \tag{1.45}$$

When the mean interaction energies at a single site are much smaller than the separation to the first excited band the model is effectively one-dimensional. In this regime the bosons are in the ground state of the transversal potential, which we denote here by the scalar function $\phi_0(y,z)$, and the field operator $\hat{\Psi}(\mathbf{r})$ takes the form [10]:

$$\hat{\Psi}(\mathbf{r}) = \sum_{j=1}^{N_L} \phi_0(y,z)\omega_j(x)\,\hat{a}_j \tag{1.46}$$

Here the bosonic operator $\hat{a}_j$ annihilates a particle at the $j$-th lattice site in the lowest band and the scalar function $w_0(x-x_j) = w_j(x)$ is the real-valued Wannier function for the lowest lattice band. The bosonic operators $\hat{a}_j$, $\hat{a}_j^\dagger$ obey the bosonic commutation relation

$$\left[\hat{a}_j, \hat{a}_l^\dagger\right] = \delta_{j,l} \text{ and } \left[\hat{a}_j^\dagger, \hat{a}_l^\dagger\right] = \left[\hat{a}_j, \hat{a}_l\right] = 0 \,, \tag{1.47}$$

which follows from Eq. (1.45) and the completeness of the Wannier function. Inserting Eq. (1.46) into Eq. (1.44) leads to the Hamiltonian

$$\hat{H} = -\sum_{i,j} t_{i,j}\hat{a}_i^\dagger\hat{a}_j + \sum_{i,j,k,l} V_{i,j,k,l}\hat{a}_i^\dagger\hat{a}_j^\dagger\hat{a}_k\hat{a}_l \,, \tag{1.48}$$

where the coefficients $t_{i,j}$ read

$$t_{i,j} = \int_{-L/2}^{+L/2} dx\; w_i(x) \left( \frac{\hbar^2}{2m} \frac{\partial^2}{\partial x^2} - V_0 \sin(\pi x/a) \right) w_j(x)\,, \qquad (1.49)$$

the coefficients $V_{i,j,k,l}$ are due to the interaction term and are defined by the expressions

$$\begin{aligned} V_{i,j,k,l} =& \frac{1}{2} \int\int d\mathbf{r}_1 d\mathbf{r}_2 w_i(x_1) w_j(x_2) \times \\ & \times U_{\text{int}}(\mathbf{r}_1 - \mathbf{r}_2) w_k(x_2) w_l(x_1) \Phi_0(y_1, z_1; y_2, z_2)\,, \end{aligned} \qquad (1.50)$$

and $\Phi_0(y_1, z_1; y_2, z_2) \equiv |\phi_0(y_1, z_1)|^2 |\phi_0(y_2, z_2)|^2$. For sufficiently deep depths $V_0$ one observes $t_{i,i} \gg t_{i,i+1}$. In the following we neglect all the coupling terms beyond nearest neighbor and the nearest neighbor interaction term. The Hamilton operator then reduces to the expression [11]:

$$\hat{H}^{(0)}_{\text{BH}} = -t \sum_{j=1}^{N_L - 1} \left( \hat{a}_j^\dagger \hat{a}_{j+1} + \text{H.c.} \right) + \epsilon \sum_{j=1}^{N_L} \hat{n}_j + \frac{U}{2} \sum_{j=1}^{N_L} \hat{n}_j \left( \hat{n}_j - 1 \right) \qquad (1.51)$$

where $\hat{n}_j = \hat{a}_j^\dagger \hat{a}_j$ is the occupation operator acting on site $j$. Its expectation value counts the number of particles at site $j$. Hamiltonian (1.51) is the Bose-Hubbard Hamiltonian [11]. The coefficients $t = t_{i,i+1}$, $\epsilon = t_{i,i}$ and $U = V_{i,i,i,i}$ are the tunnelling amplitude, single-particle energy and the onsite interaction strength, respectively. The coefficient $t$ and $\epsilon$ is determined by the overlap integral including solely the single-particle Hamiltonian. The coefficient $U$ results from the expectation value of the interaction (see Eq. 1.50). In the following we will shift the energy zero-point such that we can set the onsite energy to zero.

In this thesis we study the system in the canonical and in the grand-canonical ensemble. In the canonical ensemble we determine the ground state of Hamiltonian in Eq. (1.51) at fixed density $\rho = N/N_L$. In the grand-canonical ensemble we determine the ground state of

$$\hat{H}^{GC}_{\text{BH}} = \hat{H}^{(0)}_{BH} - \mu \sum_{j=1}^{N_L} \hat{n}_j\,, \qquad (1.52)$$

where the density is given by

$$\rho = \frac{1}{N_L} \sum_{j=1}^{N_L} \langle \hat{n}_j \rangle \qquad (1.53)$$

and is controlled by $\mu$.

### 1.3.2 *Ground state of the Bose-Hubbard model*

#### 1.3.2.1 *Mott-Insulator phase*

We consider the limit $t/U \to 0$ of the Bose-Hubbard Hamiltonian in Eq. (1.52). In this limit and for a chemical potential in the region

$$n - 1 < \frac{\mu}{U} < n \tag{1.54}$$

the ground state of the Hamiltonian in Eq. (1.52) can be approximated as

$$|\Psi\rangle = \bigotimes_{j=1}^{N_L} \frac{\left(\hat{a}_j^\dagger\right)^n}{\sqrt{n!}} |0\rangle \tag{1.55}$$

with $|0\rangle$ the vacuum state and $n \in \mathbb{N}$, which is the occupation per site and coincides in this case with the density $\rho$. Here the first two excited states are an extra particle or a hole in one site of the lattice. These states are described by

$$|\Psi\rangle^{\mathrm{p}} = \frac{1}{\sqrt{n+1}} \sum_{j=1}^{N_L} \hat{a}_j^\dagger |\Psi\rangle \tag{1.56}$$

for the extra particle and

$$|\Psi\rangle^{\mathrm{h}} = \frac{1}{\sqrt{n}} \sum_{j=1}^{N_L} \hat{a}_j |\Psi\rangle \tag{1.57}$$

for the hole. The energy needed to create a particle on a single site in the lattice is given by

$$\Delta_+(n) \equiv \langle\Psi|^p \hat{H}_{BH}^{GC} |\Psi\rangle^p - \langle\Psi| \hat{H}_{BH}^{GC} |\Psi\rangle \tag{1.58}$$

and the energy to create a hole on a single site in the lattice by

$$\Delta_-(n) \equiv \langle\Psi|^h \hat{H}_{BH}^{GC} |\Psi\rangle^h - \langle\Psi| \hat{H}_{BH}^{GC} |\Psi\rangle \quad . \tag{1.59}$$

When the chemical potential fulfills (1.54) those energies are positive and finite, i.e. $\Delta_-, \Delta_+ > 0$. Thus the ground state is insulating and incompressible. These are the defining properties of the Mott insulator (MI) phase [50].

In the following we will identify further characteristics of the MI phase by evaluating several observables with respect to the state in Eq. (1.55), which is the state corresponding to the MI phase in the limit $t/U \to 0$. For this purpose we introduce the charge gap [32, 58]

$$\Delta_c(n) = \Delta_+(n) + \Delta_-(n) \,, \tag{1.60}$$

which gives the energy required to create a particle-hole pair. A further useful quantity is the neutral gap [58]

$$\Delta_n(n) = E_{\text{ext}}(n) - E(n) \,, \tag{1.61}$$

which is the energy difference between the first excited state, $E_{ext}(n)$, and the ground state, $E(n)$. Both charge and neutral gaps are finite for values of $\mu/U$ in the interval $]n-1, n[$ for any density $n$. The compressibility is defined here as [59]

$$\kappa = \frac{\partial \rho}{\partial \mu} \tag{1.62}$$

with the average density $\rho$ in Eq. (1.53). Thus for $\mu/U$ values fulfilling the inequality (1.54) the ground state is incompressible with $\kappa = 0$. Moreover, the state in Eq. (1.55) exhibits a zero variance of the occupation on a site $j$

$$\Delta n_j = \left\langle \hat{n}_j^2 \right\rangle - \left\langle \hat{n}_j \right\rangle^2 \tag{1.63}$$

over the whole lattice. The off-diagonal correlations in discrete space are determined by the quantity

$$\mathcal{C}(r) = \left\langle \hat{a}_j^\dagger \hat{a}_{j+r} \right\rangle \,. \tag{1.64}$$

When the expectation value is taken over the state in Eq. (1.55), then one can observe $\mathcal{C}(r) = 0$ for $r \neq 0$ and thus the state in Eq. (1.55) has no off-diagonal long range order. It is useful to directly study the Fourier transform of (1.64), since this quantity can by revealed by a time of flight measurement in an experiment [7]. This is given by

$$M_1(q) = \frac{1}{N_L^2} \sum_{i,j=1}^{N_L - 1} e^{-iq(i-j)} \left\langle \hat{a}_i^\dagger \hat{a}_j \right\rangle \,. \tag{1.65}$$

In the considered limit this quantity vanishes for all values of $q$ in the thermodynamic limit signaling the lack of off-diagonal long-range order. Note that away from the limit $t/U \to 0$ but still within the MI phase the correlation function in Eq. (1.64) decays exponentially for large distances $r$ [50].

#### 1.3.2.2 *Superfluid*

Let us now study the limit $t \gg U$. For this purpose we first consider the canonical ensemble. For $t/U \to \infty$ the ground state of the Bose-Hubbard Hamiltonian, Eq. (1.51), is given by

$$|\Psi_N\rangle = \frac{1}{\sqrt{N!}} \left( \frac{1}{\sqrt{N_L}} \sum_{j=1}^{N_L} \hat{a}_j^\dagger \right)^N |0\rangle \,. \tag{1.66}$$

The many-body state (1.66) is the one of an ideal BEC, where all $N$ atoms are in the $q = 0$ Bloch state of the lowest band [4]. In the thermodynamic limit where the particle number $N$ and the number of lattice sites $N_L$ go to infinity, while the density is kept constant, the ground state is described by the coherent state [4]

$$e^{\left(\sqrt{N}\hat{a}^\dagger_{q=0}\right)}|0\rangle = \bigotimes_{i=1}^{N_L}\left[e^{\sqrt{\frac{N}{N_L}}\hat{a}^\dagger_i}|0\rangle_i\right] . \tag{1.67}$$

In this state the probability distribution for the number of atoms at site $i$ is given by a Poissonian distribution [4] and thus the variance of the occupation on a site $\Delta n_i$, Eq. (1.63), is finite. In this limit the momentum distribution shows the behaviour $M_1(q) \propto N\delta(q)$ similar to Eq. (1.20), thus signaling off-diagonal long-range order (see Subsec. 1.1.1).

For finite but small values of $U/t$ the low energy excitations are collective modes with linear dispersion [50, 51] and thus according to Landau's criterion the gas is superfluid. Here the charge gap and the neutral gap vanish [51, 58], resulting in a finite compressibility within the grand-canonical ensemble.

In one dimension the asymptotic behaviour of the off-diagonal correlations, Eq. (1.64), show a power-law decay [50, 60]:

$$C(r) \propto r^{-K/2} \tag{1.68}$$

with the Luttinger parameter $K < 1/2$ [50, 60]. This behaviour of the off-diagonal correlations leads to a finite value of the distribution in Eq. (1.65) at $q = 0$ for finite systems and approaches zero in the thermodynamic limit.

#### 1.3.2.3 *Grand-canonical Phase diagram*

Fig. 1.4, taken from Ref. [60], shows the ground-state phase diagram of the one-dimensional Bose-Hubbard Hamiltonian, Eq. (1.52), in the grand-canonical ensemble. The phase diagram is presented in the $(\mu$-$t)$-plane, where the coefficients are in units of the on-site interaction $U$. The black lines were calculated by means of a perturbation theory approach [60, 61]. The upper line indicates the line with particle energy $\Delta_+ = 0$ and the lower line corresponds to the line where the energy to create a hole goes to zero. Thus the lines correspond to the transition line from MI to SF. The region enclosed by these lines is the MI phase with the commensurate density $\rho = 1$. The difference in energy between the lower line and the upper line corresponds to the charge gap, i.e. Eq. (1.60), which shrinks for increasing ratio between the tunnelling rate and the on-site energy. It approaches zero for a commensurate density $\rho = 1$ at the tip of the insulating lobe, where the ground state goes from MI to SF [60]. This transition is driven by phase fluctuations and belongs to the $(d+1)$-dimensional XY universality

class [50]. For incommensurate densities $\rho$ the ground state is always SF. Changing the density from commensurate to incommensurate the MI-SF transition is driven by density fluctuations [60]. Note that in the one-dimensional case the transition discussed before is properly a crossover.

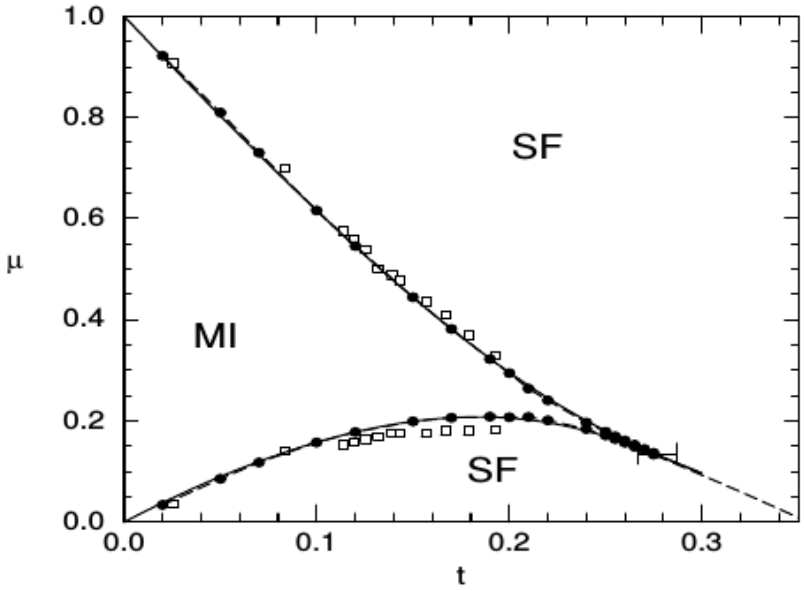


Figure 1.4: The phase diagram of the one-dimensional Bose-Hubbard model at zero temperature in the grand-canonical ensemble. The transition lines between the Mott insulating phase and the superfluid are here shown as a function of the chemical potential $\mu$ and the tunnelling rate $t$ in units of the onsite energy. The solid lines show the result of a 12th order strong coupling expansions, the boxes show Quantum Monte Carlo data and the circles show the Density Matrix Renormalization Group (DMRG) results. The phase diagram is taken from Ref. [60] with the permission of the American Physical Society and of their authors.

The dots and squares in the phase diagram in Fig. 1.4 were calculated numerically. Among others the authors in Ref. [60] used a Density Matrix Renormalization Group (DMRG) [62, 63] approach (dots) and a Quantum Monte Carlo approach [64, 65] (squares) to calculated the off diagonal correlations given by Eq. (1.64). Here they identified the critical tunnelling by means of an extrapolated value of the decay exponent $K$ in Eq. (1.68) from its finite size values. Thus the authors were able to identify the region of $K < 1/2$, i.e. the superfluid region, in the thermodynamic limit.

### 1.3.3 *Numerical methods*

In this subsection we shortly discuss the numerical methods used in this thesis to calculate the ground-state phase diagram. This subsection is based on the literature in Refs. [6, 63, 66].

#### 1.3.3.1 *Density Matrix Renormalization Group method*

One numerical method employed in this thesis is the Density Matrix Renormalization Group (DMRG) ground state algorithm. The underlying idea of the Density Matrix Renormalization Group (DMRG) methods is to truncate the Hilbert space in a reliably and controllable way, such that we can describe the system almost exactly in the truncated Hilbert space [6, 63]. For an one-dimensional system of bosons in an optical lattice the Hamiltonian is given by the Bose-Hubbard Hamiltonian $\hat{H}_{BH}^{(0)}$ in Eq. (1.51). An eigenstate $|\Psi\rangle$ of $\hat{H}_{BH}^{(0)}$ can be decomposed into the Basis $\left\{|n_1, ..., n_{N_L}\rangle \,|n_j \in \mathbb{N} \text{ with } j = 1, ..., N_L\right\}$ and reads

$$|\Psi\rangle = \sum_{n_1=0}^{\infty} ... \sum_{n_{N_L}=0}^{\infty} C_{n_1,n_2,...,n_{N_L}} |n_1, ..., n_{N_L}\rangle \ . \tag{1.69}$$

The normalization of the state requires $\sum_{n_1=0}^{\infty} ... \sum_{n_{N_L}=0}^{\infty} |C_{n_1,n_2,...,n_{N_L}}|^2 = 1$. It was shown that the coefficients in (1.69) can by written in terms of a product of matrices $\Gamma^{n_1}, ..., \Gamma^{n_{N_L}}$ [6, 63], meaning

$$C_{n_1,n_2,...,n_{N_L}} = \sum_{\alpha_1=1}^{\beta_1} ... \sum_{\alpha_{N_L-1}=1}^{\beta_{N_L-1}} \Gamma^{n_1}_{\alpha_1} s_{\alpha_1} \Gamma^{n_2}_{\alpha_1,\alpha_2} s_{\alpha_2} \Gamma^{n_3}_{\alpha_2,\alpha_3} ... s_{\alpha_{N_L-1}} \Gamma^{n_{N_L}}_{\alpha_{N_L-1}} \ . \tag{1.70}$$

Here a singular value decomposition (SVD) [63] for every partition of the lattice was performed. In Eq. (1.70) the $s_{\alpha_k}$ are the singular values belonging to those singular value decompositions, in which the system was partitioned between the site $k$ and $k+1$ of the lattice. The singular values are connected to the eigenvalues $s^2_{\alpha_k}$ of the reduced density matrices $\rho_k = Tr_k |\Psi\rangle \langle\Psi|$, where the trace over the subsystem is taken from site 1 to site $k$. Note that this decomposition requires an upper bound $n_{max}$ for the number of particles per site, i.e. $n_{max} \geq n_j$ for all $j \in \{1, ..., N_L\}$. The upper bounds in Eq. (1.70) $\beta_1$,... $\beta_{N_L-1}$ are following directly from the singular value decomposition. Those bounds are called bond dimensions. A state $|\Psi\rangle$ in Eq. (1.69) with its coefficients in the form of (1.70) is called a Matrix Product State (MPS) [6, 63].

The idea of the DMRG approach is to reduce the Hilbert space by reducing the dimension of the matrices $\Gamma^{n_1}, ..., \Gamma^{n_{N_L}}$ in the MPS state (see Eq. (1.70)). This can be done by setting a certain number of the smallest singular values to zero. Fortunately for translational invariant

one-dimensional systems with short-range interactions the singular values fall off exponentially fast, namely $s_\alpha \sim e^{-\alpha}$ [6]. Thus one can discard large numbers of singular values in the decomposition (1.70) and the overlap between the exact and truncated state remains close to one.

In this thesis we are interested in finding the ground state of the Bose-Hubbard Hamiltonian $\hat{H}_{BH}^{(0)}$ in Eq. (1.51). For this purpose we search for the MPS $|\Psi\rangle$ that minimizes the energy

$$E = \frac{\langle\Psi|\, \hat{H}_{BH}^{(0)} \,|\Psi\rangle}{\langle\Psi|\Psi\rangle} \,. \tag{1.71}$$

Thereby one minimizes $E$ with respect to a single matrix in the MPS (1.70) and keeps the rest of them fixed. After this, one minimizes the energy with respect to the matrix elements on the next lattice site and so on. One performs those steps several times across the lattice until the energy is converged, where $\left\langle \hat{H}_{BH}^{(0)2} \right\rangle - \left( \left\langle \hat{H}_{BH}^{(0)} \right\rangle \right)^2$ is smaller then $\epsilon_{\text{goal}}$[10]. In each step the minimization problem can be reduced to an eigenvalue problem. In order to restore the MPS form of the state after each diagonalization step, one needs to perform a singular value decomposition. In this singular value decomposition step the bond dimension of the MPS can be adjusted. Here one sets a upper limit $\epsilon$ for the singular value discarded. In general the maximal bond dimension $\beta_{\text{max}}$ possible is fixed in the MPS during the algorithm.

As mentioned earlier the success of the approach depends on the behaviour of the singular values of the system. It was shown that in two-dimensional systems the singular values decay slowly, such that the DMRG approach is inefficient [63]. In this thesis we will apply DMRG to analyze one-dimensional ground-state phase diagrams.

For further details on the DMRG method and MPS, we refer the interested reader to Refs. [63] and [67].

#### 1.3.3.2 *Mean-field approaches*

The mean-field ansatz discards correlations between sites of the lattice. Since those correlations are particularly important in one-dimensional systems, it turns out that mean-field fails in 1D [50]. Nevertheless the approach becomes more reliable for increasing dimensionality [6]. In this thesis we will use mean-field to analyze the lattice dynamics in 2D. We consider here a 2D lattice with $K = N_L \times N_L$ sites, where we label the lattice sites by the vector $i = (i_1, i_2)$ with integer entries. The 2D Bose-Hubbard Hamiltonian in the grand-canonical ensemble is given by

$$\hat{H}_{BH}^{2D,G} = \hat{H}_{BH}^{2D} - \mu \sum_i \hat{n}_i \tag{1.72}$$

10 One performs several sweeps across the lattice starting from site one going to site $N_L$ and then going backwards again. Starting for $N_L$ to site 1.

with

$$\hat{H}_{BH}^{2D} = -t \sum_{\langle j,i \rangle} \hat{a}_i^\dagger \hat{a}_j + \frac{U}{2} \sum_i \hat{n}_i \left( \hat{n}_i - 1 \right) \ , \tag{1.73}$$

where $\langle j, i \rangle$ stands for the sum over nearest neighbors.

The underlying approximation of the local mean-field (LMF) approach is given by the decoupling of the hopping term by neglecting second-order fluctuations of bosonic annihilation and creation operator: $\left( \hat{a}_i^\dagger - \langle \hat{a}_i^\dagger \rangle \right) \left( \hat{a}_j - \langle \hat{a}_j \rangle \right) \simeq 0$. We define here the expectation value of the field operator at site $i$ as

$$\phi_i = \langle \hat{a}_i \rangle \ . \tag{1.74}$$

The 2D extension of Hamiltonian (1.51) reduces then to the local mean-field Hamiltonian

$$\hat{H}_{BH}^{MF} = \sum_i \hat{h}_i^{MF} \ , \tag{1.75}$$

where the single-site Hamiltonian is written as

$$\hat{h}_i^{MF} = \frac{U}{2} \hat{n}_i \left( \hat{n}_i - 1 \right) - \mu \hat{n}_i - t \eta_i \left( \hat{a}_i^\dagger - \frac{\phi_i^*}{2} \right) + h.c. \tag{1.76}$$

and $\eta_i = \sum_{\langle i,j \rangle} \phi_j$ is the mean-field on site $i$.

With Eq. (1.76) we reduced the problem to a single site problem. Correspondingly the many-body wavefunction is now approximated by the product state

$$|\Psi\rangle = \bigotimes_i^{N_L \times N_L} |\psi\rangle_i \ . \tag{1.77}$$

Rewriting it in the truncated local Fock basis $\{ |n\rangle \, , n_{\leq} n_{max} \}$ leads to

$$|\Psi\rangle = \bigotimes_i^{N_L \times N_L} \sum_{n=0}^{n_{max}} c_n^i \, |n\rangle_i \ . \tag{1.78}$$

One requires for the coefficients $c_n^i$ to fulfill $\sum_{n=0}^{n_{max}} |c_n^i|^2 = 1$. For a homogeneous system we can consider the expectation value in Eq. (1.74) to be site independent, $\phi_i \equiv \phi$. The expectation value $\phi$, Eq. (1.74), is the mean-field superfluid order parameter [6, 68]. Indeed writing the off-diagonal correlations (1.64) in terms of the expectation value $\phi$, one can identify the proportionality

$$\mathcal{C}(r) \sim |\phi|^2 \ . \tag{1.79}$$

For $\phi \neq 0$ the quantum state posses off-diagonal long range order. The value $\phi = 0$ is characteristic of the MI phase.

In order to find the ground state within the mean-field ansatz one initializes the SF order parameter $\phi$. By diagonalizing the single

particle Hamiltonian Eq. (1.76) one gets the ground state of the form (1.78). With this updated state one can then calculated the SF order parameter $\phi$, Eq. (1.74), and gets an updated local Hamiltonian (see Eq. (1.76)), which is the starting point of the next loop. The loop is repeated until the order parameter converges.

An equivalent approach to the local mean-field is the so-called Gutzwiller mean-field approach [69–71]. Here one considers also the ansatz in Eq. (1.78) for the many-body wavefunction. The ground state is then determined by finding the state that minimizes the expectation value $\left\langle \Psi | \hat{H}_{BH}^{2D,G} | \Psi \right\rangle$. In detail one searches for the coefficient $c_n^i$ minimizing the mean-field energy. The SF order parameter is here given by[11]

$$\phi_i = \sum_{n=0}^{n_{max}} \sqrt{n+1} c_n^{i*} c_{n+1}^i \ . \tag{1.80}$$

*Cluster Gutzwiller mean-field theory (CGMF)*

The Cluster Gutzwiller mean-field theory (CGMF) [72] is an extension to the Gutzwiller mean-field theory introduced before. Within this approach the system of $K = N_L \times N_L$ lattice sites is partitioned into $W$ clusters of sizes $M \times N$. Here one takes care that $W = (N_L \times N_L)/(M \times N)$ is an element of the natural numbers $\mathbb{N}$. The local mean-field approximation is now only applied at the terms connecting two clusters. Therefore the CGMF Bose-Hubbard Hamiltonian is written as a sum of the cluster Hamiltonians [66]:

$$\hat{H}_{BH}^{CGMF} = \sum_{C=1}^{W} \hat{H}_C \tag{1.81}$$

with

$$\hat{H}_C = \sum_{i \in \delta C} \hat{h}_i^{\mathrm{MF}} + \hat{H}_{BH,C}^{2D,G} \ , \tag{1.82}$$

where $C$ is the cluster index and $\delta C$ is the set of the lattice sites at the boundary of the cluster $C$. The cluster Hamiltonian $\hat{H}_C$ is partitioned into $\hat{H}_{BH,C}^{2D,G}$, which is the Bose-Hubbard Hamiltonian in Eq. (1.72) defined solely within the cluster $C$, and into the mean-field Hamiltonian in Eq. (1.75), which describes the mean-field coupling between the clusters. The ground state of the CGMF Bose-Hubbard Hamiltonian, Eq. (1.81), is given by the product of the cluster ground states [66]

$$|\Psi_{\mathrm{CGMF}}\rangle = \bigotimes_{C=1}^{W} |\Phi\rangle_C \ . \tag{1.83}$$

To calculate the ground state $|\Phi\rangle_C$ of the cluster Hamiltonian, Eq.(1.82), one initializes the order parameters $\phi_i$ at the cluster boundaries. The

11 Similar to before the order parameter can here be site independent for a homogeneous system.

cluster Hamiltonian $\hat{H}_C$, Eq. (1.82), is then diagonalized. Using the resulting ground state the values of the order parameters are then updated. This procedure is repeated until the order parameters converge.

With the Cluster Gutzwiller mean-field one accounts for a certain correlations between the lattice sites, but it can not capture long-range correlations across the whole lattice.

# 2

# CORRELATED TUNNELLING INDUCED BY THE DIPOLAR INTERACTIONS

We theoretically study the effect of power-law interactions on the phases of the extended Bose-Hubbard model. We particularly focus on the interference between correlated tunnelling, due to the power-law interactions, with the single-particle hopping. This model describes the experimental setup [73]. In the second section we introduce the extended Bose-Hubbard model in 1D, including the correlated tunnelling. In the follow up section we discuss the corresponding ground-state phase diagrams. The effect of the dimensionality will be considered in the third section by studying the corresponding two-dimensional system.

This chapter contains results, text and figures taken from:

- "Superfluid phases induced by dipolar interactions",
  Rebecca Kraus, Krzysztof Biedroń, Jakub Zakrzewski, and Giovanna Morigi,
  *Physical Review B* **101**, 174505 (2020)

- "Staggered superfluid phases of dipolar bosons in two-dimensional square lattices",
  Kuldeep Suthar, Rebecca Kraus, Hrushikesh Sable, Dilip Angom, Giovanna Morigi, and Jakub Zakrzewski,
  *Physical Review B* **102**, 214503 (2020)

## 2.1 INTRODUCTION

Recent experimental observations of quantum phases of ultracold dipolar gases [74–76] and their confinement in optical lattices [13, 73, 77–81] pave the way towards the characterization of strongly correlated quantum matter. These systems are theoretically described by the so-called extended Bose-Hubbard model [13, 16–22]. Here the effect of power-law interactions is usually included by means of a density-density interaction between neighboring sites [13, 16–22]. The density-density interaction leads to a density modulation within the lattice [13, 16–22]. In one dimension, moreover, it is responsible for the appearance of a topological non-trivial phase the so-called Haldane insulator [32, 33, 35, 58, 82, 83]. Due to the anisotropy of the dipolar potential

its contribution to the onsite interaction can lead to instabilities [21, 40, 84, 85]. Ab initio derivations of the Bose-Hubbard model show that interactions are also responsible for the appearance of correlated hopping terms [86].

Until now there is a limited knowledge on the effect of this interaction-induced tunnelling on the ground state properties of a dipolar gas in an optical lattice. Results obtained from exact diagonalization of a chain of few bosons indicated the appearance of exotic superfluid and charge-density wave phases [38]. Density matrix renormalization group (DMRG) studies of the extended grand-canonical Bose-Hubbard model predicted superfluid order with spatially modulated phase whose periodicity can be either commensurate or incommensurate with the lattice periodicity, depending on the lattice depth [39]. These studies point out that the interplay between the various quantities is by no means trivial. They call for a systematic study.

In this chapter we study the effect of the correlated tunnelling on the ground state of the extended Bose-Hubbard model. In Section 2.2 we first introduce the extended Bose-Hubbard model including the density dependent tunnelling and make preliminary considerations. In Section 2.3 we report the corresponding ground-state phase diagram for a one-dimensional lattice using DMRG. The two-dimensional extended Bose-Hubbard model and its corresponding mean-field phase diagrams at zero temperature are presented in Section 2.4 .

## 2.2 EXTENDED BOSE-HUBBARD MODEL INCLUDING THE DIPOLAR INTERACTIONS

We consider ultracold dipolar bosons of mass $m$ in an anisotropic trap which is elongated along the $x$ axis. The dipolar bosons are polarized by an external field perpendicular to the trap axis and interact via the dipolar and the van-der Waals ($s$-wave) interactions. The dynamics is governed by the second-quantized Hamiltonian for the bosonic field $\hat{\Psi}(\mathbf{r})$ [40]:

$$\begin{aligned}\hat{H} = &\int d^3\mathbf{r}\hat{\Psi}^\dagger(\mathbf{r})\left[-\frac{\hbar^2}{2m}\nabla^2 + V_{\text{trap}}(\mathbf{r})\right]\hat{\Psi}(\mathbf{r}) \\ &+ \frac{1}{2}\int d^3\mathbf{r}\int d^3\mathbf{r}'\hat{\Psi}^\dagger(\mathbf{r})\hat{\Psi}^\dagger(\mathbf{r}')U_{\text{int}}(\mathbf{r}-\mathbf{r}')\hat{\Psi}(\mathbf{r}')\hat{\Psi}(\mathbf{r}) \ , \end{aligned} \tag{2.1}$$

where the field operators $\hat{\Psi}(\mathbf{r})$ and $\hat{\Psi}^\dagger(\mathbf{r})$ obey the commutation relation

$$\left[\hat{\Psi}(\mathbf{r}), \hat{\Psi}(\mathbf{r}')^\dagger\right] = \delta^{(3)}\left(\mathbf{r}-\mathbf{r}'\right) \ . \tag{2.2}$$

The function $V_{\text{trap}}$ denotes the trap potential, which is the sum of a tight harmonic potential in the $y$-$z$ plane, and an optical lattice of periodicity $a$ along the $x$ axis,

$$V_{\text{trap}} = \frac{m\omega^2}{2}\left(y^2 + z^2\right) + V_0 \sin^2(\pi x/a)\,. \tag{2.3}$$

Here, $\omega$ is a harmonic trap frequency and $V_0$ denotes the amplitude of the optical lattice. The interaction potential is the sum of the contact and of the power-law interactions,

$$U_{\text{int}}(\mathbf{r}) = U_g(\mathbf{r}) + U_\alpha(\mathbf{r})\,. \tag{2.4}$$

Specifically, $U_g(\mathbf{r}) = g\delta^{(3)}(\mathbf{r})$ is the contact potential with $g = 4\pi\hbar^2 a_s/m$ and $a_s$ the $s$-wave scattering length. The power-law interactions, $U_\alpha(\mathbf{r})$, scale with the inter particle distance $r$ as $U_\alpha(\mathbf{r}) \propto 1/r^\alpha$. In this work we consider dipoles polarized by an external field along the $z$ axis. In this case $U_\alpha(\mathbf{r}) \equiv U_d(\mathbf{r})$, where

$$U_d(\mathbf{r}) = \frac{C_{dd}}{4\pi}\frac{1 - 3\cos^2(\theta)}{r^3}\,, \tag{2.5}$$

and $\theta$ is the angle between the dipole and $\mathbf{r}$. The dipole-dipole interaction is anisotropic in space since the force depends on the dipoles orientation. The coefficient $C_{dd}$ scales the strength of the dipole-dipole interactions: for magnetic dipoles with moment $\mu_m$, the coefficient is $C_{dd} = \mu_0\mu_m^2$; for electric dipoles with moment $\mu_e$ it reads as $C_{dd} = \mu_e^2\epsilon_0$, where $\mu_0$ and $\epsilon_0$ are the magnetic and the electric permeability, respectively. In the rest of this chapter, in place of $C_{dd}$ we will use the rescaled, dimensionless quantity $d$, that is defined as [39, 87]

$$d = \frac{mC_{dd}}{2\pi^3\hbar^2 a}\,. \tag{2.6}$$

Following the approach shown in Subsec. 1.3.1 we can map the system onto an extended Bose Hubbard model.

The resulting extended Bose Hubbard Hamiltonian is then given by

$$\hat{H}_{\text{EBH}} = \hat{H}^{(0)}_{\text{BH}} + \hat{H}_\alpha\,. \tag{2.7}$$

Here we decompose the extended Bose-Hubbard Hamiltonian into the sum of the Hamiltonian $\hat{H}^{(0)}_{\text{BH}}$, describing the onsite interactions and tunnelling term, and of the Hamiltonian $\hat{H}_\alpha$, which includes the other terms such as next nearest neighbor and beyond.

The Hamiltonian $\hat{H}^{(0)}_{\text{BH}}$ has the same form as the one in Eq. (1.51). Here in contrast to Subsec. 1.3.1 the onsite interaction coefficient $U$ includes also the local contribution of the power-law interactions (for details see Appendix 2.6). Depending on the trap geometry, this contribution can lead to vanishing or negative values of the onsite interactions, which may cause a collapse of the system [38, 40, 84, 85,

88]. In this work we will restrict ourselves to geometries for which the coefficient $U$ is positive, thus the onsite interactions are repulsive and the gas is stable.

The Bose-Hubbard Hamiltonian $\hat{H}_{\mathrm{BH}}^{(0)}$ is obtained (i) by truncating the hopping processes to the nearest neighbors and (ii) by solely taking the local contribution of the interactions. Deep in the tight-binding regime the first approximation is justified. On the contrary, for large values of the onsite potentials and/or in the presence of power-law interactions one shall consistently include the coupling between $\ell$-th next neighbors. These terms are contained in the Hamiltonian $\hat{H}_\alpha$, which we write as the sum of the terms coupling $\ell$-th nearest neighbor:

$$\hat{H}_\alpha = \sum_{\ell=1}^{N_L} \hat{H}_\alpha^{(\ell)} ,$$

and whose detailed form is given below for $\ell = 1, 2$.

In this work we truncate the sum over $\ell$ and analyze the phase diagrams of the Hamiltonian for two cases. First we consider the ground state of the Bose-Hubbard Hamiltonian, where we truncate the power-law interactions to the nearest-neighbors:

$$\hat{H}_{\mathrm{BH}}^{(1)} = \hat{H}_{\mathrm{BH}}^{(0)} + \hat{H}_\alpha^{(1)} . \tag{2.8}$$

We then compare the corresponding phase diagrams with the ones obtained by keeping also the coupling to the next-nearest neighbors:

$$\hat{H}_{\mathrm{BH}}^{(2)} = \hat{H}_{\mathrm{BH}}^{(1)} + \hat{H}_{\mathrm{NNN}} + \hat{H}_\alpha^{(2)} . \tag{2.9}$$

Here, $\hat{H}_{\mathrm{NNN}}$ describes the next-nearest neighbor hopping terms due to the kinetic energy and to the trapping potential, which we include for consistency (see Appendix 2.6).

In the rest of this subsection we discuss the detailed form of $\hat{H}_\alpha^{(1)}$ and of $\hat{H}_\alpha^{(2)}$. The Hamiltonian $\hat{H}_\alpha^{(1)}$ reads [38, 41, 42, 89]

$$\begin{aligned}\hat{H}_\alpha^{(1)} =& V \sum_{j=1}^{N_L-1} \hat{n}_j \hat{n}_{j+1} - T \sum_{j=1}^{N_L-1} \left[ \hat{a}_j^\dagger \left( \hat{n}_j + \hat{n}_{j+1} \right) \hat{a}_{j+1} + \mathrm{H.c.} \right] \\ &+ \frac{P}{2} \sum_{j=1}^{N_L-1} \left( \hat{a}_{j+1}^\dagger \hat{a}_{j+1}^\dagger \hat{a}_j \hat{a}_j + \mathrm{H.c.} \right) ,\end{aligned} \tag{2.10}$$

where $\hat{n}_j = \hat{a}_j^\dagger \hat{a}_j$ counts the number of particles at site $j$ and the annihilation operator $\hat{a}_j$ (creation operator $\hat{a}_j^\dagger$) fulfill the commutation relations given in Eq. (1.47). The term scaled by the positive amplitude $V$ describes a repulsive density-density interaction. This term tends to inhibit the occupation of neighboring sites and promotes density modulations. In the following we denote $V$ by blockade coefficient. The other two terms describe tunnelling effects induced by the interactions. In detail, coefficient $T$ scales a hopping term which nonlinearly

depends on the occupation number of neighboring sites. We will denote this term by "density-assisted tunnelling". The term scaled by $P$ describes pair hopping between nearest-neighbors and we will refer to it as "pair-hopping term".

The form of the higher-order coupling terms is similar to the one of $\hat{H}_\alpha^{(1)}$. We report here the coupling to next-nearest neighbors:

$$\hat{H}_\alpha^{(2)} = V_{\mathrm{NNN}} \sum_{j=1}^{L-2} \hat{n}_j \hat{n}_{j+2} + \sum_{j=1}^{L-2} \left( \hat{T}_j^{(2)} + \hat{P}_j^{(2)} \right) . \tag{2.11}$$

Here $V_{\mathrm{NNN}}$ scales the term describing the repulsive next-nearest neighbor density-density interaction and is positive. The corresponding interaction-induced tunnelling and pair hopping terms are now collected in operators $\hat{T}_j^{(2)}$ and $\hat{P}_j^{(2)}$, respectively, and take the form:

$$\begin{aligned} \hat{T}_j^{(2)} &= -T_{\mathrm{NNN}} \hat{a}_j^\dagger \left( \hat{n}_j + \hat{n}_{j+2} \right) \hat{a}_{j+2} - T_{\mathrm{NNN}}^1 \hat{a}_{j+1}^\dagger \hat{n}_j \hat{a}_{j+2} \\ &\quad - T_{\mathrm{NNN}}^2 \hat{a}_j^\dagger \hat{n}_{j+2} \hat{a}_{j+1} - T_{\mathrm{NNN}}^3 \hat{a}_j^\dagger \hat{n}_{j+1} \hat{a}_{j+2} + \mathrm{H.c.}\,, \end{aligned} \tag{2.12}$$

$$\begin{aligned} \hat{P}_j^{(2)} &= \frac{P_{\mathrm{NNN}}^1}{2} \hat{a}_{j+1}^\dagger \hat{a}_{j+2}^\dagger \hat{a}_j \hat{a}_j + \frac{P_{\mathrm{NNN}}^2}{2} \hat{a}_{j+2}^\dagger \hat{a}_j^\dagger \hat{a}_{j+1} \hat{a}_{j+1} \\ &\quad + \frac{P_{\mathrm{NNN}}^3}{2} \hat{a}_{j+2}^\dagger \hat{a}_{j+2}^\dagger \hat{a}_{j+1} \hat{a}_j + \mathrm{H.c.}\,. \end{aligned} \tag{2.13}$$

The specific form of the coefficients $V_{\mathrm{NNN}}$, $T_{\mathrm{NNN}}^\ell$, $P_{\mathrm{NNN}}^\ell$ is given in the Appendix 2.6.

We remark that correlated hopping terms have been also discussed for atoms solely interacting via $s$-wave scattering but in the limit of large ratios $U/t$ [89, 90]. In this case, for repulsive interactions the coefficients are all positive and the density-dependent tunnelling leads to a reduction of the incompressible region [90]. In the next subsection we identify a parameter regime where there is a sign change of the interaction-induced hopping coefficients as a function of $d$.

### 2.2.1 *Interaction-induced tunnelling*

By changing the quantum species, and thus changing $d$, one modifies the relative weight between $s$-wave and dipolar interactions. The first one typically dominates at short-range distances, while the dipolar interactions are expected to determine the non-local terms. We now consider a trap geometry where $s$-wave scattering is negative and the onsite contribution of the dipolar interactions stabilizes the gas, making the onsite interactions repulsive, $U > 0$. In this regime, we identify the parameter regime where the correlated tunnelling coefficients become negative.

Figure 2.1 (a) and (b) display the contour plots of the density-assisted tunnelling coefficient $T$ and of the pair tunnelling coefficient $P$ as a function of $U$ and $V$, keeping $t$ fixed. For later convenience we label

the axis by $V/U$ and $t/U$. In Fig. 2.1(a), moreover, we explicitly show lines at constant dipolar interaction $d$. We observe that the value of $T$ becomes comparable with $V$ at large dipolar interaction strengths and for small ratios $t/U$. Therefore, when $t/U \to 0$, one still has significant hopping due to the interactions. We note, moreover, that the pair tunnelling coefficients remain very small across the phase diagram. We will keep these terms in our simulations, and anticipate that they play a negligible role in determining the phases of the ground state for deep lattices.

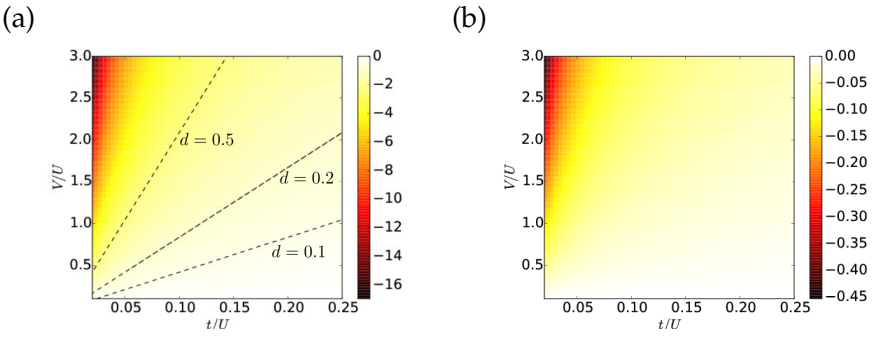


Figure 2.1: Contour plot in the $V/U - t/U$-plane of the (a) density-assisted tunnelling coefficient $T$ and (b) the pair tunnelling coefficient $P$ for the nearest-neighbor coupling and in units of the tunnelling rate $t$. The black dashed lines show the values of $V$ and $U$ at some constant dipolar interaction strengths $d$. The other parameters are discussed in the text.

Let us here specify the parameters we used for evaluating these coefficients and which we will use in the rest of this section and the following section, unless otherwise stated. The depth of the optical lattice in the axial direction is kept fixed to the value $V_0 = 8E_R$, where $E_R$ is the recoil energy. The transverse trap frequency is $\omega = \sqrt{2V_{\text{har}}\pi^2/a^2 m}$, where we choose $V_{\text{har}} = 50E_R$. The tunnelling rate $t$ between nearest-neighbor and the tunnelling rate between next-nearest neighbor $t_{\text{NNN}}$ are constant, and for the given lattice depth $t_{\text{NNN}} = 0.0123\,t$.

### 2.2.2 *Interaction-induced atomic limit: Quantum Interference*

We now analyze the behaviour of the interaction-induced tunnelling coefficients as a function of $t/U$ and at a given ratio $V/U$. Figure 2.2 (a) displays the density-assisted tunnelling coefficient $T$ and the pair hopping coefficient $P$ in units of $t$. The coefficients $T$ and $P$ are negative over the considered parameter range. In particular, $P$ is one order of magnitude smaller than the density dependent tunnelling coefficient $T$, while $T$ is of the same order of magnitude as the tunnelling rate. Therefore, single-particle tunnelling and correlated tunnelling have opposite sign and can mutually cancel. Correlated (density-assisted)

tunnelling, in particular, is dominant for $t/U \to 0$, while single-particle hopping is dominant at large ratios $t/U$. There is a parameter range at finite ratios $t/U$, thus, where this destructive interference leads to an effective atomic limit. Fig. 2.2(b) displays the values of the scattering length and of the dipolar interaction strength corresponding to the curves in Fig. 2.2(a). The ratio $t/U$ for which one finds the interaction-induced atomic limit is indicated by the vertical black line in Fig. 2.2(a) for density $\rho = 2$. Here, $T = t/3$.

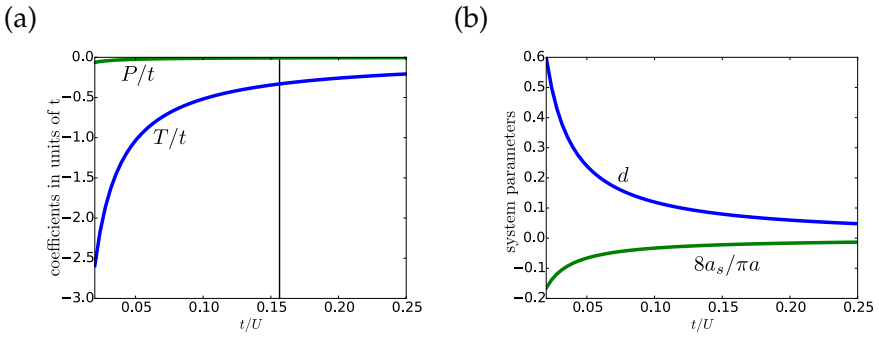


Figure 2.2: (a) Density-assisted tunnelling coefficient $T$ (blue) and pair-hopping coefficient $P$ (green) as a function of $t/U$ for $V/U = 0.5$. Panel (b) displays the corresponding values of the dimensionless dipolar interaction strength $d$ (blue) and of the $s$-wave scattering length $a_s$ in units of $a$ (green). The ratio $V/U$ is increased by changing both $d$ and the scattering length $a_s$. Note that here we choose negative scattering lengths, so that the $s$-wave potential partially cancels out with the local repulsive component of the dipolar interactions. The other parameters are given in the text. The vertical black line in panel (a) indicates the value of $t/U$ for which linear tunnelling and density-assisted tunnelling between nearest-neighbor sites mutually cancel for $\rho = 2$.

In order to find a systematic way to identify the regime of the interaction-induced atomic limit, we consider the one-particle hopping terms of Hamiltonian $H_{\mathrm{BH}}^{(1)}$ in Eq. (2.10) and collect them in the operator $\hat{\mathcal{T}}_{\mathrm{eff}}$, which reads as [90]:

$$\hat{\mathcal{T}}_{\mathrm{eff}} = \sum_{j=1}^{L-1} \hat{a}_j^\dagger \left[-t - T(\hat{n}_j + \hat{n}_{j+1})\right] \hat{a}_{j+1} + \mathrm{H.c.}\,. \tag{2.14}$$

The expectation value of this term on a homogeneous distribution at average density $\langle \hat{n}_i \rangle = \rho$ scales as

$$\langle \hat{\mathcal{T}}_{\mathrm{eff}} \rangle \simeq L \mathrm{Re}\{\langle \hat{a}_j^\dagger \hat{a}_{j+1} \rangle\} [-t - T(2\rho - 1)]\,. \tag{2.15}$$

This expression shows that, for non-vanishing off-diagonal correlations, then $\langle \hat{\mathcal{T}}_{\mathrm{eff}} \rangle$ can vanish when

$$-t - T(2\rho - 1) = 0\,.$$

Solutions with $t \neq 0$ exist for densities $\rho \neq 1/2$. In particular, for $0 < \rho < 1/2$, destructive interference occurs for $T > t > 0$. In this

case, $\langle \hat{\mathcal{T}}_{\text{eff}} \rangle = 0$ for $T/t = 1/(1-2\rho)$. In the other regime, for $\rho > 1/2$, the interaction-induced atomic limit requires $T < 0$ and is found for

$$\frac{|T|}{t} = \frac{1}{2\rho - 1}\,. \tag{2.16}$$

Relation (2.16) can be fulfilled at relatively small dipolar strength when the density is sufficiently high. In order to explore the effects of this interference on the ground state properties, in our numerical studies we focus on the phases of a dipolar gas with the commensurate densities $\rho = 1$ and $\rho = 2$.

### 2.2.3 *Mean-field considerations*

In this subsection we use a mean-field ansatz and an approximated model in order to infer some features of the following phase diagrams.

#### 2.2.3.1 *Atomic limit*

We analyze the ground state in the limit in which all hopping terms are set to zero. For convenience we consider the simplified Hamiltonian

$$H_{\text{at}} = \frac{U}{2}\sum_j \hat{n}_j(\hat{n}_j - 1) + V\sum_j \sum_{r>0} \frac{1}{r^\alpha}\hat{n}_j\hat{n}_{j+r}\,, \tag{2.17}$$

where $\alpha$ is the power law exponent, $\alpha > 1$, and $V$ scales the interaction in the limit in which the Wannier functions are approximated by Dirac-delta function.

For $\alpha \to \infty$ the interaction reduces to nearest-neighbors and the ground state results from the interplay between the onsite interaction, which tends to minimize the onsite occupation, and the repulsive interaction between neighoring sites, which favours the onset of density waves with double lattice periodicity. In the following we will discuss the atomic limit for a specific density of $\rho = 2$. We denote by MI[2] the Mott-insulator state with two particle per site and by CDW$[n_1, n_2]$ the charge-density wave state where neighboring sites are occupied by a repeating sequence of $n_1$ and $n_2$ particles per site. For $\rho = 2$ these are CDW$[3,1]$ and CDW$[4,0]$. The MI[2] is stable when $V \leq V_c^{(1)}$, where:

$$V_c^{(1)} = \frac{U}{2}\frac{1}{\zeta(\alpha)\left(1 - \frac{1}{2^{\alpha-1}}\right)}\,, \tag{2.18}$$

and $\zeta(\alpha)$ is the Riemann's zeta function. For $\alpha \to \infty$ we recover the value $V_c^{(1)} = U/2$. For $\alpha$ finite the boundary is shifted to larger values of $V$: the power-law tails tend to stabilize the MI[2] state.

For $\alpha > 1$ the three phases, MI[2], CDW$[3,1]$ and CDW$[4,0]$, are degenerate at $V = V_c^{(1)}$. In the interval $V_c^{(1)} < V < V_c^{(2)}$ the ground

state is the CDW[4,0]. The upper bound $V_c^{(2)}$ is given by the expression

$$V_c^{(2)} = \frac{2U}{\zeta(\alpha)} \frac{2^\alpha/8}{\left(1-(2/3)^\alpha/6\right)}, \tag{2.19}$$

which separates the phase CDW[4,0] from the CDW$[6,0,0]$ with triatomic Wigner-Seitz cell. For repulsive dipolar interactions, when $\alpha = 3$, then this bound takes the value $V_c^{(2)} \simeq 2U$. In general, $V_c^{(2)}$ monotonously increases with $\alpha$ and reaches $V_c^{(2)} \to \infty$ for $\alpha \to \infty$. For finite $\alpha$ one finds for $V > V_c^{(2)}$ further transition points to structures with increasing Wigner-Seitz cells, until all particles are localized at one lattice site in the limit $V/U \to \infty$.

#### 2.2.3.2 *Staggered superfluidity: mean-field analysis*

For nearest-neighour interactions and $\rho > 1/2$, correlated tunnelling dominates the hopping events for $T < 0$ and $t < |T|(2\rho - 1)$. In this regime, in the absence of interactions the state with minimum energy has momentum $q = \pi$ (here in units of $1/a$). Following these considerations, we now assume a site-dependent superfluid order parameter, which we define as [91]

$$\langle \hat{a}_j \rangle = \phi e^{i\theta_j}, \tag{2.20}$$

and use it to calculate the mean-field energy of the nearest-neighbor hopping term:

$$\begin{aligned} H_{\text{hop}} =& 2[-t + |T|(2\rho - 1)] \sum_{j=1}^{L-1} \phi^2 \cos(\theta_j - \theta_{j+1}) \\ &+ \frac{P}{2} \sum_{j=1}^{L-1} \phi^4 \cos(2(\theta_j - \theta_{j+1})), \end{aligned} \tag{2.21}$$

where $P < 0$ for the parameters of this chapter. Discrete translational invariance gives $\theta_j = -j\theta$, such that $\theta_j - \theta_{j+1} = \theta$ is a constant phase increment from site to site [91]. This ansatz shows that the energy is minimal for $\theta = \pi$ in the regime where density-assisted tunnelling dominates. The SF order parameter has thus a Fourier component at $q = \pi$. The alternating sign of the local superfluid parameter leads to the denomination "staggered superfluidity" (SSF) [91].

We now consider the power-law behaviour of the interactions, and thus the coupling to the other neighbors. For this purpose we write the single-particle hopping terms due to the single-particle tunnelling and to the density-assisted tunnelling in the compact form

$$\hat{H}'_{\text{hop}} = \sum_j \sum_{r>0} \left(-t_r - T'_r[\hat{n}_1, \ldots, \hat{n}_L]\right) \hat{a}_j^\dagger \hat{a}_{j+r} + \text{H.c.}, \tag{2.22}$$

where $T'_r[n_1, \ldots, n_L]$ is a generic function of the density distribution and scales with $1/r^\alpha$, and $t_r$ is the hopping term due to the single-particle energy, such that $t_1 = t$ and $t_2 = t_{\mathrm{NNN}}$. For the uniform density distribution $\rho$ we make the simplifying assumptions $\langle T'_r \rangle \sim -T'[\rho]/r^\alpha$. Using Eq. (2.20) we obtain the expression:

$$H'_{\mathrm{hop}} \sim 2\phi^2 \sum_{j=1}^{L-1} \sum_{r>0} \left( -t_r + \frac{T'[\rho]}{r^\alpha} \right) \cos(\theta_j - \theta_{j+r}) \,. \tag{2.23}$$

This is the relation that the site-dependent phase $\theta_j$ shall fulfill in order to achieve the interaction-induced atomic limit. For a shallow lattice and in the regime where interactions are dominant superfluid phases can have Fourier components that are incommensurate with the lattice periodicity [39]. For sufficiently deep lattices, which is the case we consider in this chapter, the sum can be truncated at the next-nearest neighbors. Then an approximated root of the equation $H'_{\mathrm{hop}} = 0$ is found by imposing $-t + T'[\rho] = 0$, where now

$$T'[\rho] = |T|(2\rho - 1) - |T^2_{\mathrm{NNN}}|\rho \,. \tag{2.24}$$

One consequence is that the coupling beyond nearest-neighbors shifts the interaction-induced atomic limit to smaller values of the ratio $t/U$. The interval where $-t + T'[\rho] > 0$ is now expected to be smaller than for nearest-neighbor coupling. Here, the superfluid phase is to good approximation the staggered superfluid with $\theta_j = -j\pi$.

## 2.3 1D GROUND-STATE PHASE DIAGRAM

In this section we numerically determine the properties of the ground state of the extended Bose-Hubbard Hamiltonian as a function of the strength of the dipolar interactions. We choose the commensurate densities $\rho = 1$ and $\rho = 2$. We calculate the ground state when the coupling is first truncated to the nearest-neighbor. For $\rho = 2$ also the next-nearest neighbors are included.

Our results are obtained by means of a DMRG numerical program [63], which is based on the ITensor C++ library for implementing tensor network calculations [67]. The simulations are run for $N$ particles in a lattice with $N_L$ sites with open boundary conditions, for different lattice sites and for different initial states. The interested readers are referred to Appendix 2.6 for details on the implementation. Unless mentioned otherwise, the system parameters are given in Subsec. 2.2.1.

We first review the observables, by means of which we characterize the phases. We then report the phase diagram of the extended Bose-Hubbard Hamiltonian with nearest-neighbor coupling, Eq. (2.8), for the density $\rho = 1$. In Subsec. 2.3.3 we discuss the ground-state phase diagram for a density of two. Here we first take into account solely nearest-neighbor coupling, Eq. (2.8), and later include next-nearest-neighbor couplings, Eq. (2.9).

### 2.3.1 *Order parameter*

In this work we consider a system of atoms with a finite particle numbers at vanishing temperature. We determine the phases by means of the following observables, whose expectation values are taken over the ground state.

We analyze the behaviour of local density fluctuations by means of the local variance $\Delta n_j$ [40]:

$$\Delta n_j = \langle \hat{n}_j^2 \rangle - \langle \hat{n}_j \rangle^2 . \tag{2.25}$$

This quantity is connected to the local compressibility [92]. A sufficient condition for a phase to be incompressible is that $\Delta n_j$ vanishes at all sites $j$.

The superfluid phase is signalled by the non-vanishing value of single particle correlations $\langle \hat{a}_i^\dagger \hat{a}_j \rangle$ across the lattice. In particular, we analyze the Fourier transform of the off-diagonal single particle correlations

$$M_1(q) = \frac{1}{N_L^2} \sum_{i,j=1}^{N_L-1} e^{iq(i-j)} Re \left\langle \hat{a}_i^\dagger \hat{a}_j \right\rangle . \tag{2.26}$$

The phase is a superfluid when $M_1(q) \neq 0$ and the maximum Fourier component is $q = q_{\max}$ with $q_{\max} = 0$. When the maximum of $M_1(q)$ is at $q_{\max} = \pi$ the phase is a staggered superfluid (SSF) [42]. Furthermore we calculate the charge gap $\Delta_c$, Eq. (1.60), and the neutral gap $\Delta_n$, Eq. (1.61). The gaps vanish in the thermodynamic limit in the superfluid phases and are finite in the insulating phases [32, 33, 35, 58] .

Diagonal long-range order is revealed by a peak of the static structure form factor $S(q)$ at the corresponding Fourier component, where

$$S(q) = \frac{1}{N_L^2} \sum_{i,j=1}^{N_L-1} \langle \hat{n}_i \hat{n}_j \rangle \, e^{-iq(j-i)} . \tag{2.27}$$

A single peak of $S(q)$ at $q = 2\pi/j$ signals a periodic structure with periodicity $ja$. We denote this phase by charge-density wave $\mathrm{CDW}_j$ if it is insulating. If instead the phase is superfluid, it is denoted by lattice supersolid phase $\mathrm{SS}_j$. We distinguish between two kinds of lattice supersolid phases, depending on the Fourier spectrum of the single-particle off-diagonal correlations. The phase is $\mathrm{SS}_j$ when $q_{\max} = 0$. If the peak is instead at $q_{\max} = \pi$, then the phase is a staggered supersolid $\mathrm{SSS}_j$ [42].

Additionally, pair tunnelling terms are expected to favour the onset of what has been denoted by pair superfluidity (PSF)[38, 39, 42, 91, 93, 94]. For the parameter regime of our study we do not find PSF, but for completeness we report the observables we use in order to come to our conclusions. PSF is signalled by a non-vanishing expectation value

of the pair-correlation function. In this work we analyze the Fourier transform of the pair correlations $\langle \hat{a}_i^\dagger \hat{a}_i^\dagger \hat{a}_j \hat{a}_j \rangle$, which we define as [95]:

$$M_2(q) = \frac{1}{N_L^2} \sum_{i,j=1}^{N_L-1} e^{iq(i-j)} Re \left\langle \hat{a}_i^\dagger \hat{a}_i^\dagger \hat{a}_j \hat{a}_j \right\rangle \ . \tag{2.28}$$

In the pair superfluid (PSF) and in the pair supersolid (PSS) phases the Fourier components of $M_2(q)$, Eq. (2.28), are larger than the corresponding Fourier components of $M_1(q)$, Eq. (1.65) [95].

The MI phase is characterized by vanishing off-diagonal correlations, finite gaps and $S(q \neq 0) = 0$. We verify the existence of the Haldane insulator by calculating the expectation value of the modified string-order parameter [58, 96]

$$\mathcal{O}_S = \lim_{r\to\infty} \langle \delta\hat{n}_i e^{\left(i\theta \sum_{k=i}^{i+r} \delta\hat{n}_k\right)} \delta\hat{n}_{i+r} \rangle \tag{2.29}$$

with $\delta\hat{n}_i = \hat{n}_i - \rho$. For unit density we take $\theta = \pi$ and for density $\rho = 2$ we choose $\theta = \pi/2$ [96]. The HI is then characterized by a finite value of the string-order parameter, a vanishing static structure form factor at $q \neq 0$, Eq. (2.27), and finite gaps. In our analysis we will evaluate the string order parameter at $r = N_L/2$, where we neglect the outer $N_L/4$ sites to account for boundary effects similar to Ref. [32, 58].

Finally, we analyze the entanglement entropy for a partition of the chain into two equally long subsystems A and B:

$$S_{\text{vN}} = -\text{Tr}\{\hat{\rho}_B \ln \hat{\rho}_B\} \,, \tag{2.30}$$

where $\hat{\rho}_B = \text{Tr}_A\{|\phi_0\rangle\langle\phi_0|\}$ and $|\phi_0\rangle$ is the ground state. We refer the readers to Appendix 2.6 for further details on the numerical implementations (including how we treat the boundary effects). Table 2.1 summarizes the expectation values that characterize the phases here discussed.

### 2.3.2 *Density* $\rho = 1$

We first analyze the ground-state phase diagrams for unit density. Fig. 2.3 shows the contour plot of the relevant observables for (a) SF phase, (b) the SSF phase, (c) incompressible phases and (d) the phases with diagonal long-range orders in the $V - t$ plane.

In Fig. 2.3 we identify a superfluid region for sufficiently large single particle tunnelling $t$ and $V/U \lesssim 1$. Moreover, a MI-CDW transition occurs around $V/U = 0.5$ for small tunnelling rates $t$. In Fig. 2.3(b) the Fourier component of the single particle off-diagonal correlations at $q = \pi$ is zero over the whole phase diagram. Therefore no SSF phases are present for the here considered parameters. This behaviour is expected, since the destructive quantum interference region, i.e. white dashed line, lies close to the atomic limit.

| Phase | $M_1(q)$ Eq. (2.26) | $M_2(q)$ Eq. (2.28) | $S(q)$ Eq. (2.27) | $O_S$ Eq. (2.32) | $\Delta_c$ Eq. (1.60) | $\Delta_n$ Eq. (1.61) |
|---|---|---|---|---|---|---|
| Mott-Insulator MI | 0 | 0 | $q_{\max} = 0$ | 0 | $\neq 0$ | $\neq 0$ |
| Density Wave $\text{CDW}_j$ | 0 | 0 | $q_{\max} = 2\pi/j$ | $\neq 0$ | $\neq 0$ | $\neq 0$ |
| Haldane-In. HI | 0 | 0 | $q_{\max} = 0$ | $\neq 0$ | $\neq 0$ | $\neq 0$ |
| Superfluid SF | $q_{\max} = 0$ | $M_2(q) < M_1(q)$ | $q_{\max} = 0$ | 0 | 0 | 0 |
| Staggered Superfluid SSF | $q_{\max} = \pi$ | $M_2(q) < M_1(q)$ | $q_{\max} = 0$ | 0 | 0 | 0 |
| Supersolid $\text{SS}_j$ | $q_{\max} = 0$ | $M_2(q) < M_1(q)$ | $q_{\max} = 2\pi/j$ | 0 | 0 | 0 |
| Staggered Supersolid $\text{SSS}_j$ | $q_{\max} = \pi$ | $M_2(q) < M_1(q)$ | $q_{\max} = 2\pi/j$ | 0 | 0 | 0 |
| Pair Superfluid PSF | $M_1(q) < M_2(q)$ | $q_{\max} = 0$ | $q_{\max} = 0$ | 0 | 0 | 0 |
| Pair Supersolid $\text{PSS}_j$ | $M_1(q) < M_2(q)$ | $q_{\max} = 0$ | $q_{\max} = 2\pi/j$ | 0 | 0 | 0 |

Table 2.1: Table of the phases, of their acronyms, and of the corresponding values of the observables. The subscript $j$ of the Density Wave and of the Supersolid phases refer to the component $q = 2\pi/j$ of the structure form factor which is different from zero, correspondingly the density modulation has periodicity $ja$. $q_{\max}$ indicates the Fourier component at which the spectra of $M_1$, $M_2$, $S(q)$ may have a maximum.

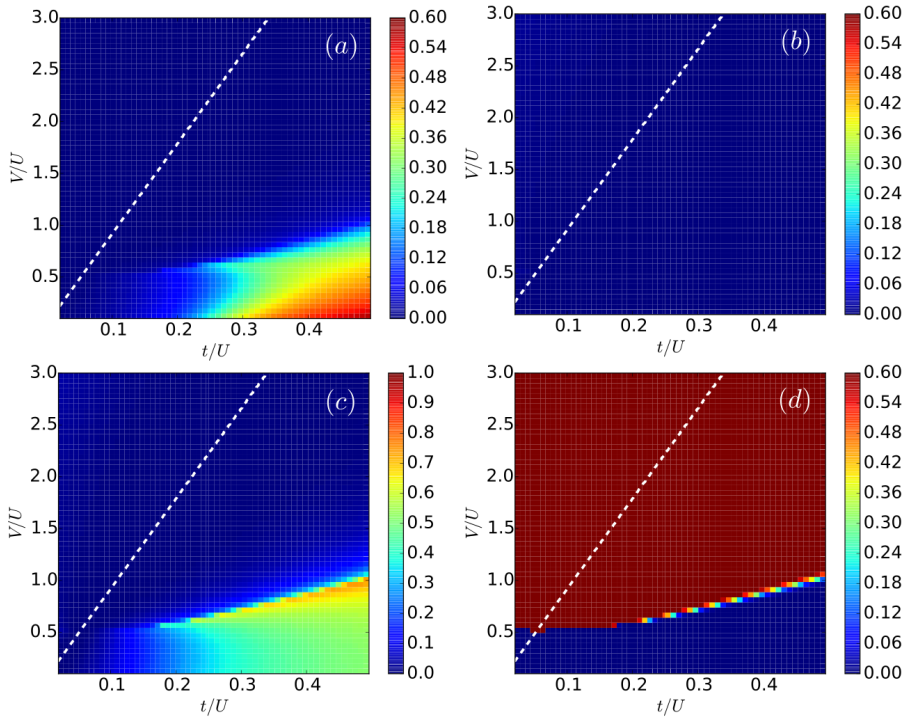


Figure 2.3: Contour plot of the relevant observables in the $V/U$-$t/U$ plane for the Bose-Hubbard model of Eq. (2.10) and density $\rho = 1$. Panel (a) and (b) signal SSF and SF through the Fourier components $q = 0$ and $q = \pi$, respectively, of the single particle off-diagonal correlations $M_1(q)$. Panel (c) reports the maximum value of the local variance $\Delta n_j$ across the lattice, Eq. (2.25), and panel (d) the structure form factor $S(q = \pi)$ (2.27), signaling the onset of a density modulation. The number of lattice sites is fixed to $N_L = 60$ and the number of particles is given by $N = 60$. The white dashed line indicates the interaction-induced atomic limit.

For $\rho = 1$ it was shown that a topological non-trivial phase, the Haldane insulator, is present for zero correlated tunnelling [32–35, 58]. In the following subsubsection we study how the topological phase is affected by the correlated tunnelling.

#### 2.3.2.1 *Haldane Insulator*

The transition between the MI and CDW phase can be captured by the local order parameter, so called density wave order parameter [32, 34]

$$\mathcal{O}_{\mathrm{DW}} = \lim_{r\to\infty} (-1)^r \langle \delta\hat{n}_i \delta\hat{n}_{i+r} \rangle \tag{2.31}$$

with $\delta\hat{n}_i = \hat{n}_i - \rho$. Here local refers to the fact that $\mathcal{O}_{\mathrm{DW}}$ is the expectation value of two single-site operators. It is zero in the MI, whereas it is finite in the CDW. Previous studies of the extended Bose-Hubbard at unit density revealed the appearance of a peculiar insulating phase in between the MI and CDW insulator in the $U - V$ plane [32–35]. It

turns out that this phase can not be revealed by any local order parameter and falls into the category of the so called topological non-trivial insulators [97, 98]. Topological non-trivial insulators can possess edge states, which are robust against a certain class of perturbations [97, 98]. The topological-nontrivial insulator of the extended one-dimensional Bose-Hubbard model is called the Haldane insulator (HI) [32–35, 58] and is characterized by a non-local order in its particle-hole defects. This becomes clear by analyzing the lattice occupations in the HI state. One example is illustrated in Fig. 2.4(a). Here the plus refers to an extra particle on the site and the minus to a hole while the zeros are the sites with unit occupation. The HI exhibit particle-hole pairs, which can be extended over several sites $r$ with $r < N_L$. Thus one calls those pairs unbounded. Moreover those particle-hole pairs show an order. This can be seen by neglecting in a given configuration all sites with an occupation $\rho$ (zeros). As a result, the order of the particle hole defects is the one characteristic of a CDW state. In contrast to the CDW state the order in the HI is hidden, i.e. the HI phase can only be revealed by neglecting the sites with average occupancy. Therefore the HI phase can not be signaled by the order parameter in Eq. (2.31). Nevertheless it can be captured by the non-local string order parameter [32–35, 58]

$$\mathcal{O}_S = \lim_{r\to\infty} \langle \delta\hat{n}_i e^{\left(i\pi \sum_{k=i}^{i+r} \delta\hat{n}_k\right)} \delta\hat{n}_{i+r} \rangle \ , \tag{2.32}$$

where non-local here refers to the operator measuring the site occupations in between any pair of sites $i$ and $i+r$ (see Eq. (2.29)). The string order parameter is different from zero when $\mathcal{O}_{\mathrm{DW}} \neq 0$. In the parameter region where $\mathcal{O}_{\mathrm{DW}} = 0$ but $\mathcal{O}_S \neq 0$ the phase is HI. In the MI instead, where the defects are local, extended over a few sites, and not ordered (see Fig. 2.4(b)), $\mathcal{O}_{\mathrm{DW}} = \mathcal{O}_S = 0$.

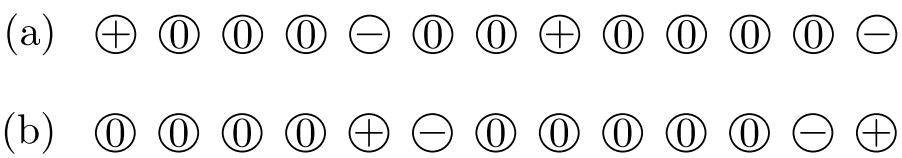


Figure 2.4: Illustration of configurations of the defects in (a) the Haldane Insulator and (b) in the Mott insulator ground states. The plus denotes an extra particle and the minus to a hole. The zeros stands for an occupations given by the average density $\rho = 1$.

The Haldane insulator was extensively characterized in numerical studies of the one-dimensional extended Bose-Hubbard model with repulsive density-density interaction [32–35, 58, 82, 83]. This is a limit of our model in Eq. (2.8) obtained after setting $T = P = 0$. The resulting phase diagram is depicted in Fig. 2.5 and taken from Ref. [33]. For small $U$ and $V$ the ground state is in the SF phase. By increasing the on-site interaction $U$ the system enters the insulating phases. For small $V$ the nearest neighbor interaction can be neglected and the

insulating phase is MI: Here the string order parameter (2.32) and the structure form factor (2.27) at $q = \pi$ vanish. Increasing the ratio between the nearest-neighbor interaction and single particle tunnelling $V/t$ leads to a finite string order parameter signaling the transition to the HI phase. For large $V/t$ the system ends up in the CDW phase, which is signaled by a finite value of the structure form factor at $q = \pi$. The black squares are calculated by means of DMRG [32].

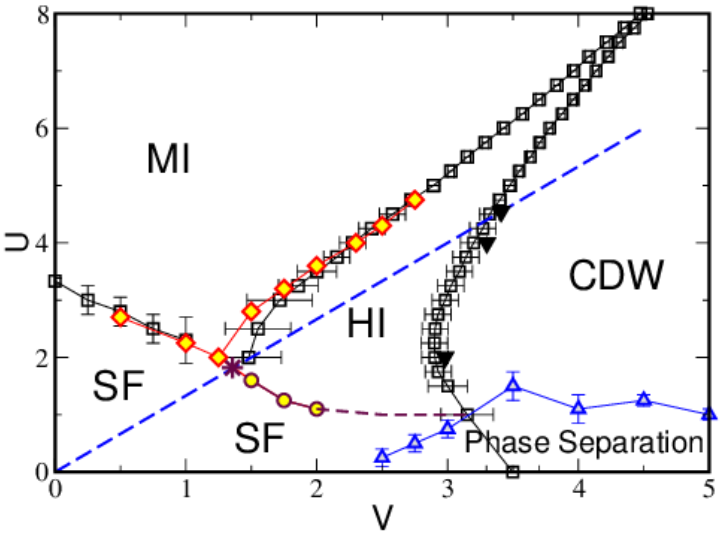


Figure 2.5: Phase diagram of Hamiltonian $\hat{H}^{(1)}_{\mathrm{BH}}$, Eq. (2.8), for $T = P = 0$ in the $(U, V)$-plane for a density of $\rho = 1$. The open squares are the results of Ref. [32] using DMRG. All other symbols are the results obtained by means of a QMC calculations in Ref. [33]. The QMC confirms the DMRG results in Ref. [32] within the error bars. The QMC simulations also identified a phase separation region for small $U$ and large $V$ that was not reported in [32]. The dashed line indicates the function $U = 4V/3$. This figure is taken from Ref. [33] with the permission of the American Physical Society and of their authors.

For large $V/t$ but small $U/t$ the ground state of the canonical ensemble consists of a mixture of two or more phases [33]. This feature is characteristic of a phase separation [33] and can be revealed by looking for instance at the behaviour of the occupation and its variance across the lattice. In the grand-canonical ensemble it can be identified by analyzing the density as a function of the chemical potential: If the density shows a jump, such that the phase at unit density is unstable, the ground state will possess a phase separation [33]. The phase diagram in Fig. 2.5 was calculated in the canonical ensemble by means of the DMRG ground state algorithm and in the grand-canonical ensemble[1] by a QMC simulation [33]. The phase

1 Here one chooses the right chemical potential to achieve a density of one across the phase diagram.

boundaries identified with both approaches are in good agreement with each other (see Fig. 2.5) .

*Effect of correlated tunnelling on the Haldane insulator*

We now analyze the effect of the correlated tunnelling on the phase transition MI-HI and HI-CDW. This question is also of experimental relevance, since correlated tunnelling is naturally present in experiments of ultracold dipolar gases like in Ref. [73]. For this purpose we determine the phase diagram for unit density in the $U - V$ plane for finite correlated tunnelling $T$. The values of the density dependent tunnelling $T$ are calculated as discussed in Subsec. 2.2.1 and its behaviour across the phase diagram is depicted in Fig. 2.6.

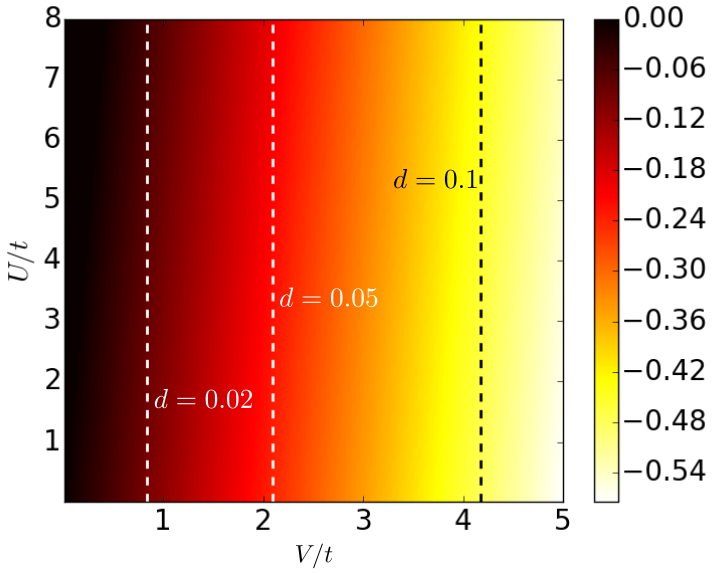


Figure 2.6: Contour plot in the $V/t - U/t$-plane of the density-assisted tunnelling coefficient $T$ in Eq. (2.10) for the nearest-neighbor coupling and in units of the tunnelling rate $t$. The black (white) dashed lines show the values of $V$ and $U$ at some constant dipolar interaction strengths $d$. The other parameters are discussed in Subsec. 2.2.1.

Here, one observes an increase in the absolute value of the correlated tunnelling with $V/t$. Since the pair tunnelling coefficient is several orders of magnitude smaller then the density assisted tunnelling $P \ll T$, we discard the pair tunnelling contribution in the following.

Like in Refs. [33, 39] we identify the phase transitions by means of the extrapolated behaviour for $N_L \to \infty$ of the charge gap (1.60), the neutral gap (1.61), the string order parameter (2.32) and the density wave order parameter (2.31). Therefore we proceed as in Ref. [33] and first calculate the order parameters for lattices of size $N_L = 32, 48, 64, 100$. The extrapolation of the order parameters for an infinite system is then done according to

$$\mathcal{O}(N_L) = \mathcal{O}(N_L \to \infty) + \text{const.}/N_L \,, \tag{2.33}$$

where $\mathcal{O}(N_L)$ stands for a given observable as a function of $N_L$. By means of the values of $\mathcal{O}(N_L \to \infty)$ we identify the phase boundaries according to Table 2.1. In this procedure we neglect the outer $N_L/4$ sites at both sides of the lattice in order to get rid of boundary effects and evaluate the string, Eq. (2.32), and density wave order parameter, Eq. (2.31), for $r = N_L/2$ [32, 33]. The resulting phase diagram for $\rho = 1$ in the $U - V$ plane is drawn in Fig. 2.7.

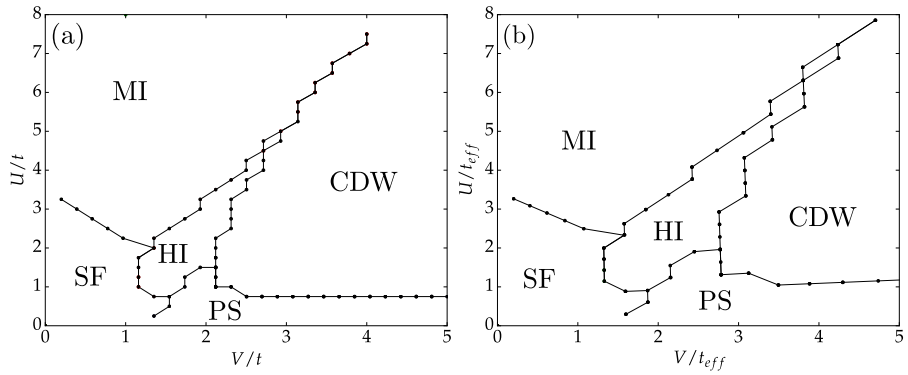


Figure 2.7: Phase diagram of Hamiltonian $\hat{H}^{(1)}_{\mathrm{BH}}$, Eq. (2.8), for $\rho = 1$ in the $U - V$ plane (a) in units of the single-particle tunneling rate $t$ including the correlated tunnelling $T$ and (b) in units of the effective mean-field tunnelling rate $t_{\mathrm{eff}} = t - |T|$ (see Eq. (2.15)). The boundaries were identified by extrapolating the order parameter for $N_L \to \infty$, where we use $N_L = 32, 48, 64, 100$. The ground state is calculated by means of a DMRG method. Note that the error in the transition lines is given by the grid steps chosen for the parameters $U/t$ and $V/t$.

The Phase diagram in Fig. 2.7(a) is qualitatively similar to the phase diagram in Fig. 2.5. We observe, however, two main differences: First the size of the HI region in between the MI and CDW is reduced. Second the size of the phase separation region is increased. The reduction of the HI region can be explained by a decrease of the effective mean-field tunnelling rate $t_{\mathrm{eff}} = t - |T|$ (see Eq. (2.15)). This is visible in Fig. 2.7(b), where the phase diagram is plotted as a function of $U$ and $V$ both in units of the effective mean-field tunnelling rate $t_{\mathrm{eff}}$. Within the error bars, the rescaled phase diagram agrees well with the phase boundaries depicted in Fig. 2.5 for $P = T = 0$, apart for the PS region.

In order to determine the PS region in the canonical ensemble, we analyze here the occupation $n_i = \langle \hat{n}_i \rangle$ as a function of the site index $i$ and its variance $\Delta n_i$ across the lattice, Eq. (2.25), for $N_L = 100$ (see Fig. 2.8). Comparing Fig. 2.7(b) with Fig. 2.5 we observe that the size of the PS region seems to increase. We therefore compare the occupation distribution and its variance over the lattice for $T = 0$ and $T \neq 0$. The results are shown in Fig . 2.8 (a)-(d). Here we started the algorithm with the same initial state and parameters within the PS region. In Fig. 2.8(a) and (c) we observe that the PS region consist of

alternating SF and SS clusters (see also Ref. [33]). Interestingly for a finite $T$ in Fig. 2.8(b) the cluster at constant density has significantly smaller size and the occupation is around $1/2$ over several lattice sites. We note that at $\rho = 1/2$ the mean-field correlated tunnelling term vanishes. We observe in this region a reduced local variance of the occupation, see Fig. 2.8(d), in comparison to the SF region for $T = 0$, see Fig. 2.8(c). In the rest of the lattice sites the occupation and its variance show the properties of a CDW and SS phase. In order to determine whether the occupation in Fig. 2.8(b) is the one of the actual ground state, we intend to run the DMRG simulations for different initial states, like we did for determining the phase diagram of Fig. 2.7. This analysis is going to be performed in the near future and is not reported in this thesis.

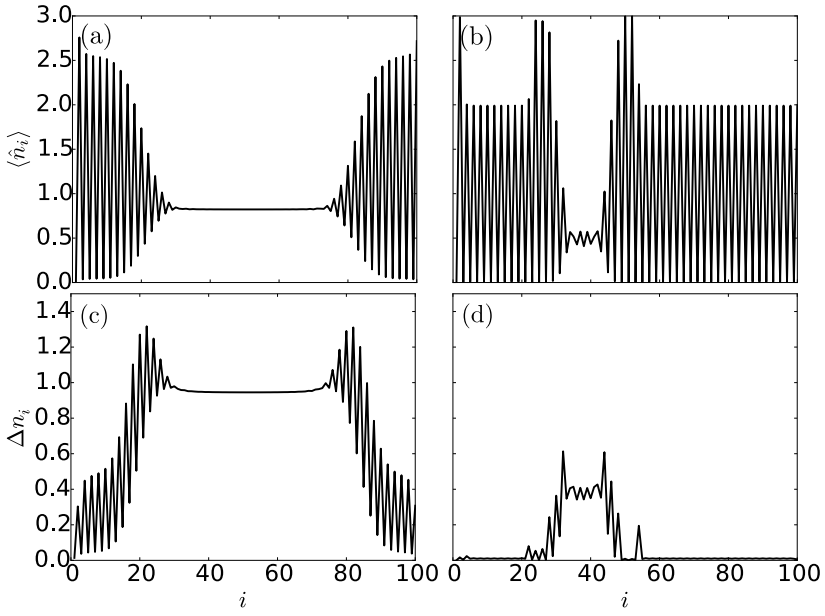


Figure 2.8: Occupation (a),(b) and its variance (c),(d), Eq. (2.25), as a function of the lattice site index $i$ for $U = 0.5t$ and $V = 4t$. In panel (a) and (c) the correlated tunnelling is set to zero, i.e. $T = 0$, and in panel (b) and (d) the value of $T$ is finite. We initialized the DMRG algorithm with a MI state. The density is given by $\rho = 1$ and the number of lattice sites are fixed to $N_L = 100$.

Fig. 2.9(a) displays the difference between the string order parameter and the density wave order parameter $\Delta = \mathcal{O}_s - \mathcal{O}_{DW}$ as a function of $V/U$ and $t/U$ for a finite correlated tunnelling $T$. By inspecting Fig. 2.9(a) one can identify a small region, where the density wave order parameter is zero, yet the string order parameter is finite signaling the HI. Fig. 2.9(b) displays the entanglement entropy. While for the insulating phases, MI and CDW, the entanglement entropy is zero, it is finite in the SF and in the HI phase. The latter behaviour is due to non-local correlations between defects.

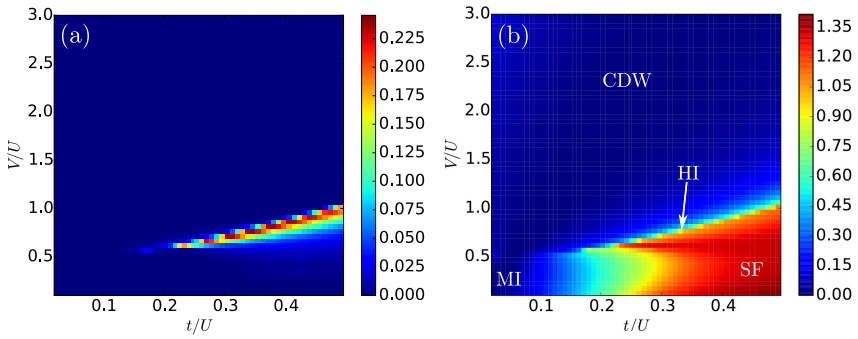


Figure 2.9: Contour plot of (a) the difference between the string order parameter and the density wave order parameter $\Delta = \mathcal{O}_s - \mathcal{O}_{DW}$ and of (b) the von Neumann entropy for the ground state of Eq. (2.8) as a function of the ratio $V/U$ and of the ratio $t/U$ for $N_L = 60$ with $T \neq 0$. The string order parameter, Eq. (2.32), and density wave order parameter, Eq. (2.31), are evaluated for $r = N_L/2$, where we discard the outer $N_L/4$ lattice sites at both boundaries. The phases are labeled according to the classification of Table 2.1. in order to calculate the von Neumann entropy we choose the size of the subsystem to be $L_B = 30$ sites. The rest of the parameters are the same as in Fig. 2.3.

The influence of the next-nearest neighbor terms together with the correlated tunnelling on the HI phase was studied before for a fixed ratio $V/U$ and $U/t$ in Ref. [39]. The results for a fixed $U/t$ reveals a shrinking of the HI region for sufficiently large dipole-dipole interaction strength, which is consistent with our observation in Fig. 2.7(a). Moreover, the authors of Ref. [39] observe a shift of the SF-HI transition to smaller values of $U/t$ for a fixed ratio $V/U$, which can be also identified in Fig. 2.7.

### 2.3.3 *Density $\rho = 2$*

Our considerations in Subsec. 2.2.3 predict a shift of the destructive interference region to larger values of $t/U$ for larger densities. Thus we expect a larger impact of the correlated tunnelling on the ground state properties for larger densities. Therefore we study in this Subsection the ground-state phase diagrams for $\rho = 2$.

#### 2.3.3.1 *Nearest-Neighbor interactions*

In this subsubsection the properties of the ground state of the extended Bose-Hubbard Hamiltonian $H^{(1)}_{\mathrm{BH}}$, Eq. (2.8), are studied for a finite chain at a fixed density $\rho = 2$. We report the phase diagrams as a function of the blockade coefficient between nearest-neighbor, $V/U$, and of the tunnelling rate $t/U$. For computational reasons we will identify the insulating phases, i.e. CDW, MI and HI, in the following by means of

the Fourier transform of the off-diagonal correlations $M_1(q)$, Eq. (2.26), and not by the charge and neutral gap. Figures 2.10(a)-(d) display the contour plots of the relevant observables for (a) the SF phase, (b) the SSF phase, (c) the incompressible phase and (d) the phases with diagonal long range orders.

We first identify the MI-SF phase transition at $V \to 0$: the transition point $(t/U)_c$ is in qualitative agreement with the literature [99], the discrepancy is attributed to the finite size of the chain. At finite and nonvanishing ratios $V/U$ the insulating phase moves to larger values of $t/U$. It is localized about the white dashed line, which indicates the atomic limit due to quantum interference (see Sec. 2.2.3). By inspecting Figs. 2.10 (a) and (b) it is evident that this phase divides the diagram into two disconnected SF phases: According to our classification, on the left the phase is a staggered SF (SSF), on the right it is a SF. It is remarkable that also at $t/U \to 0$ the phase is superfluid. According to our preliminary considerations, this superfluid phase is due to the correlated hopping of the dipolar interactions.

Inspecting the single-particle off-diagonal correlations, panel (a), and the structure form factor, panel (d), we further observe a transition about the line $V = U/2$. The properties at this transition depend on $t/U$. We recall that at this value and in the atomic limit we expect a first-order transition from a MI to a CDW[4,0] [29]. This is consistent with our numerical results along the values of the interaction-induced atomic limit. When hopping is dominated by the kinetic energy (on the right of the interaction-induced atomic limit) the phase is expected to undergo a continuous transition from SF to SS (not included in our phase diagram). When instead hopping is due to interactions we observe a continuous transition from SSF to staggered SS (SSS).

In the following we discuss some of those behaviours in detail.

*Superfluidity*

In one dimension there is no long-range off-diagonal order, and superfluidity is signalled by the power-law decay of the single-particle correlation function with the distance [49]. In the SSF phase this behaviour is modulated by an oscillation with (dimensionless) wave number $q = \pi$, so that the correlation function changes sign every time the distance is increased by one lattice site. This oscillation is visible in Fig. 2.11(a), which reports the off-diagonal correlation in the parameter regime of the SSF phase. Fig. 2.11(b) provides evidence of the power-law decay of the envelope. We note that this behaviour was also reported in Refs. [38, 39], and was there denoted by "pair superfluidity". We consider here more appropriate to denote this phase by "staggered SF", since it is due to the dominant contribution of the density-assisted tunnelling term in establishing off-diagonal correlations. Interestingly, the oscillation is already captured by a mean-field model, cf. Sec. 2.2.3. In general, the analysis of the Fourier transform of $M_1(q)$ across the diagram shows that in the superfluid phase the Fourier components different from zero are solely at $q = 0$

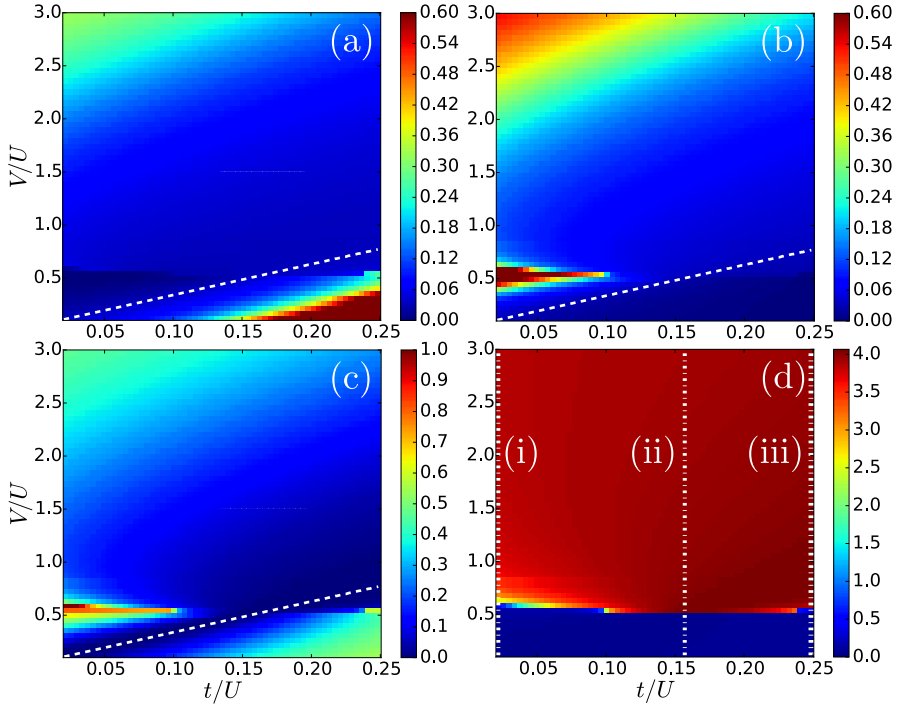


Figure 2.10: Contour plot of the relevant observables in the $V/U - t/U$ plane for the ground state of the Bose-Hubbard model of Eq. (2.8) for $\rho = 2$. (a) and (b) signal SF and SSF through the Fourier components $q = 0$ and $q = \pi$, respectively, of the single particle off-diagonal correlations $M_1(q)$. (c) reports the maximum value of the local variance $\Delta n_j$ across the lattice, Eq. (2.25), and (d) the component at momentum $\pi$ of the structure form factor, signaling the onset of a density modulation. The number of lattice sites is fixed to $N_L = 60$ and the number of particles is given by $N = 120$. The white dashed line in (a)-(c) indicates the interaction-induced atomic limit. The vertical dotted lines in (d) indicate the parameters of the sweeps in Fig. 2.13. See Appendix 2.6 for further details.

and $q = \pi$. This is visible, for instance, in Figs. 2.12 (a) and (d). We now analyze the onset and the features of the SF phase along two specific transition lines: along the axis $V/U$ for $t/U = 0.02$ and along the axis $t/U$ for $V = U/2$.

We first consider $V = U/2$. Fig. 2.12(a) displays the Fourier spectrum of the single particle correlation function, $M_1(q)$, as a function of $t/U$: The non-vanishing Fourier components are at $q = 0$ (at large $t/U$) and at $q = \pi$ (at small $t/U$). These two Fourier components are reported in panel (b): they are different from zero on the right and on the left, respectively, of the interaction-induced atomic limit. When moving towards the atomic limit they decrease until they vanish. The entanglement entropy (c) vanishes for an interval of values centered about the transition point.

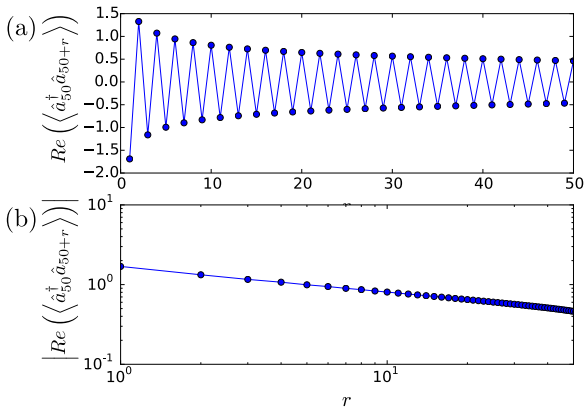


Figure 2.11: (a) Single particle off-diagonal correlation $\langle \hat{a}^\dagger_\ell \hat{a}_{\ell+r}\rangle$ for a particle at the center of the chain and as a function of the distance $r$ (in units of the lattice constant $a$). Here, $V/U = 0.529$ and $t/U = 0.042$, corresponding to a point in the SSF phase. The chain has $N_L = 120$ sites and $N = 240$ particles, the site close to the center is $\ell = 50$. (b) Same as (a) but in logarithmic scale. Here the absolute value of the correlation function is reported and the power-law decay is evident.

The behaviour of superfluidity for small ratios $t/U$ is determined by the correlated hopping. Fig. 2.12(d) displays $M_1(q)$ as a function of $V/U$ and small ratio $t/U$. In panel (e) we report the Fourier components at $q = 0$ and $q = \pi$. The phase is insulating for a small interval about $V = 0$, after which the Fourier component at $q = \pi$ rapidly grows and reaches a maximum about $V = U/2$. At the same value the entanglement entropy, (f) displays a maximum. After this maximum, the Fourier component at $q = \pi$ drops to smaller values, while the $q = 0$ component starts to grow from zero to a small but finite value (the numerics converge very slowly at these points and we cannot provide more detailed sampling). The Fourier component at $q = \pi$ is always larger than $M_1(0)$, therefore according to our definition the SF phase is staggered. We have analyzed the scaling of the peak at $V = U/2$ with the system size: by means of a fit we extract that the peak height at the asymptotics is finite and tends to the finite value $M_1(\pi) \to 0.47$ (see Appendix 2.6 for further details).

We note that across the phase diagram we do not observe pair superfluidity: In fact, the expectation value of observable $M_2$ is always smaller than the one of $M_1$ at the corresponding $q$ value (see Appendix 2.6 for details). Moreover, we do not find spatial modulation in the pair correlations. We believe that this is because the pair tunnelling coefficient $P$ is negative over the considered parameter range.

*Diagonal long-range order*

Let us now discuss the onset of diagonal long-range order. This is here signalled by the non-vanishing component at $q = \pi$ of the structure form factor. Fig. 2.13(a) displays its behaviour as a function of $V/U$ for three different values of $t/U$. The parameters of these

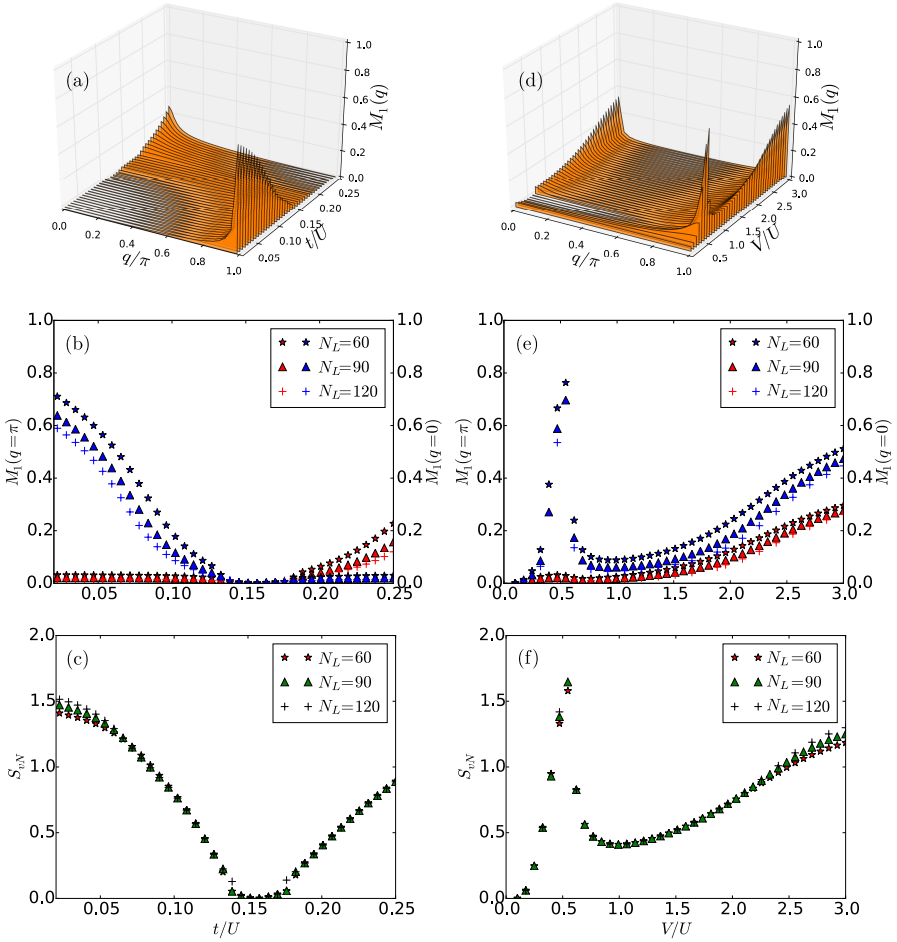


Figure 2.12: Fourier transform of the single particle off-diagonal correlations $M_1(q)$ (2.26) as a function of $q$ and in (a) of $t/U$ for $V/U = 0.5$ and in (b) of $V/U$ for $t/U = 0.02$ with $\rho = 2$. (b) and (e) show the behaviour of the Fourier components at $q = 0$ (red) and $q = \pi$ (blue) as a function of $q$, where in (b) $V/U = 0.5$ and in (e) $t/U = 0.02$. Here, we discard the onsite contribution of the sum in Eq. (2.26). (c) and (f) display the corresponding values of the entanglement entropy. Different symbols correspond to different system sizes $N_L$ ($N_L = 60, 90, 120$, see legenda), keeping $N = 2N_L$. (a) and (d) are reported for $N_L = 60$. The peak of the entanglement entropy in (f) for a fixed $t/U = 0.02$ is located in the SSF region visible in Fig. 2.11(c) at $V/U = 0.5$. The behaviour of the entanglement entropy suggests a continuous phase transition at this point.

sweeps are indicated by the vertical lines in Fig. 2.10(d). The data of (i) correspond to the sweep across the transition from SSF to SSS and show a continuous, even though rapid, growth of the structure form factor. This rapid growth occurs in the same parameter interval where the superfluid Fourier component at $q = 0$ increases from zero to a finite value.

Sweep (ii) is taken across the transition MI-CDW[4,0]. It shows a discontinuity at $V/U = 0.5$, indicating a first-order phase transition. This agrees with prediction in Subsec. 2.2.3. Sweep (iii) moves across the SF to the CDW[4,0] phase. The behaviour suggests a discontinuous, first-order transition. We also expect a continuous transition SF to SS at $V = U/2$ but for slightly larger ratios $t/U$, that are not included in this phase diagram.

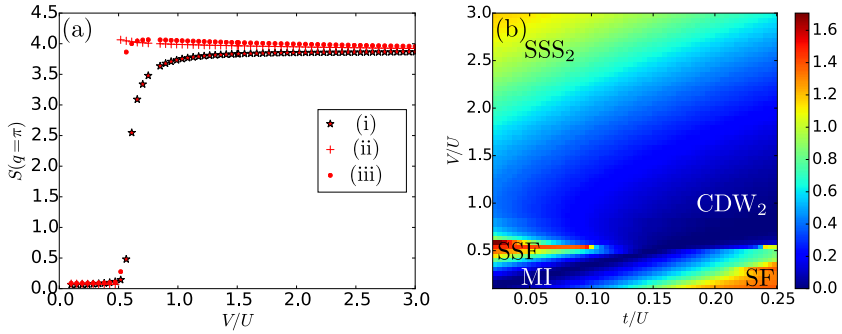


Figure 2.13: Panel (a) shows the component at $q = \pi$ of the structure form factor, Eq. (2.27), signaling the onset of density modulations. The data are taken at the sweeps (i), (ii), (iii) of Fig. 2.10(d). Here, $t/U = 0.02$ at (i), $t/U = 0.157$ at (ii), and $t/U = 0.25$ at (iii). Panel (b) shows the contour plot of the von Neumann entropy for the ground state of Eq. (2.8) as a function of the ratio $V/U$ and of the ratio $t/U$. The phases are labeled according to the classification of Table 2.1. The parameters are the same as in Fig. 2.10, the size of the subsystem is $L_B = 30$ sites. The density is fixed to two, i.e. $\rho = 2$.

Fig. 2.13(b) displays the contour plot of the entanglement entropy. The region with non-vanishing values are the ones we identified before as superfluid phases. We observe in particular the maximum at the transition from SSF to SSS at $t/U \simeq 0$ and $V \simeq U/2$. We label the phases in the diagram according to our classification in Table 2.1.

#### 2.3.3.2 *Next-nearest-neighbor interactions*

We now analyze the ground state of the extended Bose-Hubbard Hamiltonian by including the next-nearest-neighbors interactions. The Hamiltonian is given in Eq. (2.9). The properties of the relevant observables are shown in Fig. 2.14. They share some similarities with the nearest-neighbor model, (compare with Fig. 2.10). For instance, also in this case we observe an insulating phase at the interaction-induced atomic limit, which separates staggered superfluidity from "normal" superfluidity. However, now the SF phases occur in larger parameter regions and the insulating phase shrinks. Moreover, the transition to the diagonal long-range order is located about $V \sim 0.5U$, even though it is shifted to a slightly larger value than for the nearest-neighbor case.

A striking difference is the appearance of a third phase at $V \sim 2U$, which is signalled by a peak of the structure form factor at $q = 2\pi/3$ .

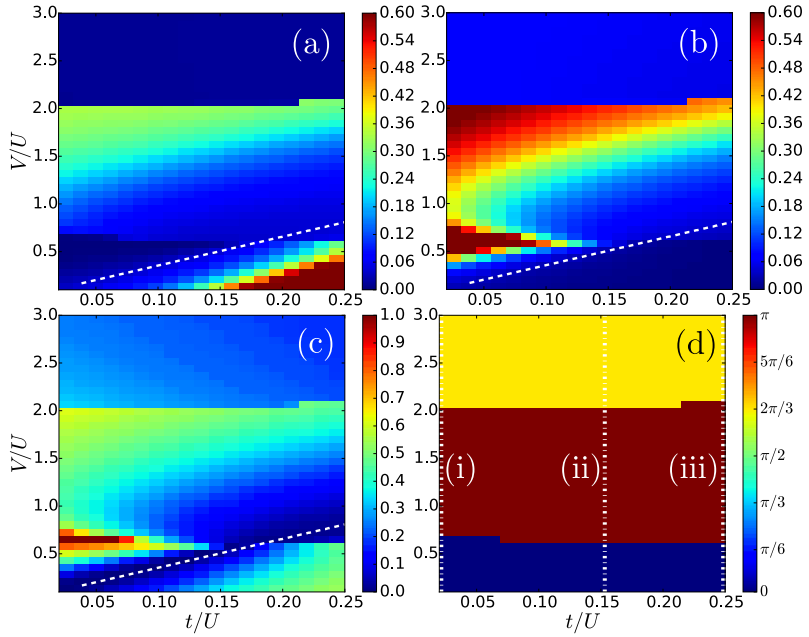


Figure 2.14: Contour plot of relevant observables in the $V/U - t/U$ plane for the ground state of the Bose-Hubbard model of Eq. (2.9), which includes next-nearest neighbor interactions. (a) and (b) signal SF and SSF through the Fourier components $q = 0$ and $q = \pi$, respectively, of the single particle off-diagonal correlations $M_1(q)$. (c) reports the maximum value of the local variance $\Delta n_j$ across the lattice, Eq. (2.25), and panel (d) the component at momentum $\pi$(red) and $2\pi/3$ (yellow) of the structure form factor, signalling the onset of a density modulation with the corresponding periodicity. The number of lattice sites is fixed to $N_L = 60$ and the number of particles is given by $N = 120$. The white dashed line in (a)-(c) indicates the interaction-induced atomic limit. The vertical dotted lines in (d) indicate the parameters of the sweeps in Fig. 2.16. We fixed the density to $\rho = 2$. See Appendix 2.6 for further details.

In the superfluid phase the spectrum of the single-particle off-diagonal correlations have non-vanishing Fourier component at $q = 0$ and at $q = \pi$. Figure 2.15(a) displays these Fourier components as a function of $t/U$ for $V = U/2$. The behaviour is similar to the nearest-neighbor case, Fig. 2.12(a). Now, however, the insulating phase occurs on a substantially smaller interval of $t/U$ values. We attribute this effect to the next-nearest-neighbor terms of the interaction-induced tunnelling. In fact, from Eq. (2.24) we can see that these terms tend to increase the effective hopping coefficient.

The behaviour of the Fourier components for $t \ll U$ is shown in Fig. 2.15(b) as a function of $V/U$. For $V/U \lesssim 2$ it is similar to the nearest-neighbor model. Also in this case it exhibits the features of a continuous transition. The maximum of the $\pi$ component, however, is shifted to larger values (compare to Fig. 2.12), which is consistent with our preliminary considerations. Moreover, for $V/U$ to the right of the maximum, the slope with which both Fourier components at $q = 0$ and $q = \pi$ increase is larger than for the nearest-neighbor interaction. At $V \sim 2U$ both components undergo an abrupt transition to a very small, non-vanishing value. At this point, the structure acquires a periodic density modulation at wave number $q = 2\pi/3$, as visible from Fig. 2.16. The transition is thus discontinuous. The new phases exhibits a finite value of the maximum value of the local variance $\Delta n_j$, Eq. (2.25), across the lattice. However, in the corresponding region the entanglement entropy, Fig. 2.16, takes small values. Its nature shall be clarified by a future analysis for larger system sizes.

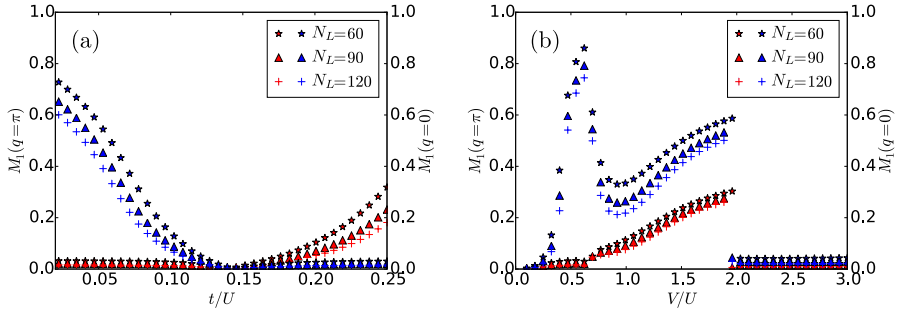


Figure 2.15: Fourier components of the single particle off-diagonal correlations $M_1(q)$ (2.26) discarding the onsite contribution at $q = 0$ (red) and $q = \pi$ (blue) as a function of (a) $t/U$ for $V/U = 0.5$ and of (b) $V/U$ for $t/U = 0.02$. Different symbols correspond to different system sizes $N_L$ ($N_L = 60, 90, 120$, see legenda), keeping $N = 2N_L$ and $\rho = 2$. The discontinuity at $V/U \simeq 2$ is associated with the appearance of density modulations with quasi-momentum $q = 2\pi/3$, see also Fig. 2.16.

The entanglement entropy (2.70) in Fig. 2.16(b) in the $V - t$ plane is finite in the superfluid phases and close to zero in the insulating phases.

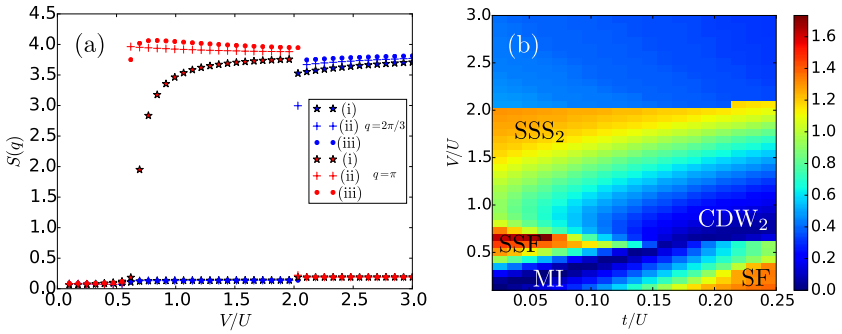


Figure 2.16: Panel (a) shows the component at $q = \pi$ (red) and $q = 2\pi/3$ (blue) of the structure form factor, Eq. (2.27), signalling the onset of density modulations for $\rho = 2$. The data are taken at the sweeps (i), (ii), (iii) of Fig. 2.10(d). Here, $t/U = 0.02$ at (i), $t/U = 0.157$ at (ii), and $t/U = 0.25$ at (iii). Panel (b) shows the contour plot of the von Neumann entropy as a function of the ratio $V/U$ and of the ratio $t/U$ for the ground state of Eq. (2.9). The phases are labeled according to the classification of Table 2.1. The parameters are the same as in Fig. 2.10, the size of the subsystem is $L_B = 30$ sites.

## 2.4 EFFECT OF CORRELATED HOPPING IN A QUADRATIC, TWO-DIMENSIONAL LATTICE

Previous studies on ultracold dipolar bosons in a two-dimensional lattices included density-density interaction terms to the 2D Bose-Hubbard Hamiltonian (1.72) in order to account for the dipole-dipole interaction [20, 100–102]. Those density-density interaction terms stabilize different order phases in the 2D plane [20, 30, 100–105]. The aim of this section is to study the influence of the density assisted tunnelling on the ground state of a gas of ultracold dipolar atoms loaded in a two-dimensional square lattice. We will focus on the regime where the correlated and single particle tunnelling can destructively interfere.

### 2.4.1 *2D extended Bose-Hubbard model*

We consider a gas of ultracold bosons which are confined in two dimensions in a square optical lattice in the $x - y$ plane with $L = L_x \times L_y$ sites and periodic boundary conditions.. The motion in the direction orthogonal to the plane is assumed to be frozen out. The bosons interact via the contact potential and the dipolar interactions. The dipoles are polarized perpendicularly with respect to the plane of the lattice, thus they interact repulsively and isotropically in the plane.

We denote by $\hat{a}_{p,q}$ and $\hat{a}^\dagger_{p,q}$ the operators annihilating and creating a particle at site $\mathbf{i} = \{p, q\}$ with commutation relations $[\hat{a}_{p,q}, \hat{a}^\dagger_{p',q'}] = \delta_{p,p'}\delta_{q,q'}$. Here $p$ $(q)$ is the lattice site index along the $x$ $(y)$ direction. Let $\hat{n}_{p,q} = \hat{a}^\dagger_{p,q}\hat{a}_{p,q}$ denote the corresponding number operator.

We consider here a grand-canonical ensemble. Following the procedure as for the one-dimensional case (see Sec. 2.2) the resulting two-dimensional extended Bose-Hubbard model (eBHM) is described by the Hamiltonian $\hat{H}^{2D}_{EBH}$ which we separate into the contribution of onsite, nearest-neighbour and next-nearest neighbour interactions:

$$\hat{H}^{2D}_{EBH} = \hat{H}^{2D}_{BH} + \hat{H}^{(1)} + \hat{H}^{(2)}. \tag{2.34}$$

Here, $\hat{H}^{2D}_{BH}$ is the standard Bose Hubbard model of Eq. (1.73).

The nearest neighbor (NN) contributions to the Hamiltonian are given by

$$\begin{aligned}\hat{H}^{(1)} &= V\sum_{p,q}\hat{n}_{p,q}\left(\hat{n}_{p+1,q}+\hat{n}_{p,q+1}\right)\\ &\quad -T\sum_{p,q}\Big[\hat{a}^{\dagger}_{p+1,q}\left(\hat{n}_{p,q}+\hat{n}_{p+1,q}\right)\hat{a}_{p,q}\\ &\quad +\hat{a}^{\dagger}_{p,q+1}\left(\hat{n}_{p,q}+\hat{n}_{p,q+1}\right)\hat{a}_{p,q}+\text{H.c.}\Big]\\ &\quad +\frac{P}{2}\sum_{p,q}\left(\hat{a}^{\dagger 2}_{p+1,q}+\hat{a}^{\dagger 2}_{p,q+1}\right)\hat{a}^{2}_{p,q}+\text{H.c.}\,.\end{aligned} \tag{2.35}$$

Here we label the coefficients using the same convention as in the one-dimensional case: $V$ is the density-density interaction between neighbouring sites, $T$ is the amplitude scaling density-dependent tunnelling, and $P$ is the pair tunnelling coefficient. The Hamiltonian of Eq. (2.35) is the two-dimensional extension of Eq. (2.10).

The Hamiltonian corresponding to the NNN coupling is specific to a 2D square lattice and couples sites along the diagonals of the lattice. Explicitly:

$$\begin{aligned}\hat{H}^{(2)} =& V_{\text{diag}}\sum_{p,q}\hat{n}_{p,q}\big(\hat{n}_{p+1,q+1}+\hat{n}_{p-1,q+1}\\ &+\hat{n}_{p+1,q-1}+\hat{n}_{p-1,q-1}\big)\\ &-T_{\text{diag}}\sum_{p,q}\Big[\hat{a}^{\dagger}_{p+1,q+1}\left(\hat{n}_{p,q}+\hat{n}_{p+1,q+1}\right)\hat{a}_{p,q}\\ &+\hat{a}^{\dagger}_{p-1,q+1}\left(\hat{n}_{p,q}+\hat{n}_{p-1,q+1}\right)\hat{a}_{p,q}+\text{H.c.}\Big]\,.\end{aligned} \tag{2.36}$$

The coefficients scale the corresponding terms as in Eq. (2.35). The subscript “diag" indicates that we accounted for the lattice geometry in evaluating the interactions between NNN.

Similar to the one-dimensional case the coefficient are calculated by taking into account the algebraic scaling of the dipolar interactions and the lattice geometry. In determining the phase diagram we tune the strength of the contact interaction and of the dipole interactions, see Subsubsec. 2.2.1, keeping in mind that now the functions in the overlap integrals are two-dimensional Wannier functions in the $x-y$

plane. The details on the calculation of the coefficients are reported in Appendix 2.6.

We note that the strength of the coefficients of Hamiltonian (2.35) and (2.36) follow $|V| > |T| \gg |P|$ and $|V_{\text{diag}}| > |T_{\text{diag}}|$. In our isotropic lattice geometry the overlap integral giving $P$ is orders of magnitude smaller than $V$ or $T$ and is much smaller than the coefficients appearing in $\hat{H}^{(2)}$. We have checked explicitly that taking the term scaling with $P$ into account does not modify our results. For that reason, from now on we omit the term proportional to $P$ in (2.35) - this justifies also that the corresponding term is also missing in (2.36) from the very beginning. For completeness, we remark that the pair tunnelling coefficient can be enhanced by modifying the confinement in the $z$ direction [38].

The parameters used in our calculations are varied by changing the dipole interaction strength and the s-wave scattering length (see Subsubsec. 2.2.1). In particular we will focus on the parameter regime where $T < 0$, namely, where we expect to observe destructive interference between correlated tunnelling and the single-particle hopping.

### 2.4.2 *Extended mean-field approach*

In order to determine the ground-state phase diagram of the 2D extended Bose-Hubbard model we consider a grand-canonical ensemble and apply the site-decoupled Gutzwiller mean-field (SGMF) and the cluster Gutzwiller mean-field (CGMF) introduced in 1.3.3.2. Due to the density dependent tunnelling these approaches have to be modified as we discuss in the following.

#### 2.4.2.1 *Site-decoupled Gutzwiller mean-field approach (SGMF)*

The SGMF allows one to reduce the model to a single site by neglecting second order fluctuations of the bosonic annihilation and creation operators. Within this treatment the expectation value of the annihilation operator is the order parameter of the superfluid phase (see Subsubsec. 1.3.3.2). In the presence of correlated tunnelling the SGMF has to be modified by including additional order parameters connected with the correlated hopping [42]. In this treatment the correlated tunnelling is decoupled as follows

$$\begin{aligned}\hat{a}^{\dagger}_{p,q}\left(\hat{n}_{p,q}+\hat{n}_{p',q'}\right)\hat{a}_{p',q'} \approx{}& \left\langle \hat{a}^{\dagger}_{p,q}\hat{n}_{p,q}\right\rangle \hat{a}_{p',q'} + \left\langle \hat{a}_{p',q'}\right\rangle \hat{a}^{\dagger}_{p,q}\hat{n}_{p,q} \\ &+ \left\langle \hat{n}_{p',q'}\hat{a}_{p',q'}\right\rangle \hat{a}^{\dagger}_{p,q} + \left\langle \hat{a}^{\dagger}_{p,q}\right\rangle \hat{n}_{p',q'}\hat{a}_{p',q'}\ ,\end{aligned} \tag{2.37}$$

where the expectation value is taken over the 2D Gutzwiller mean-field wave function of Eq. (1.78). One introduces here the "density-assisted correlation order parameter", which reads

$$\eta_{p,q} = \langle\Psi|\hat{n}_{p,q}\hat{a}_{p,q}|\Psi\rangle = \sum_n \sqrt{n}(n-1)\; c_{n-1}^{(p,q)^*} c_n^{(p,q)} \;, \tag{2.38}$$

where the state $|\Psi\rangle$ is given in Eq. (1.78). Moreover, one writes the density-density interactions as

$$\hat{n}_{p.q}\hat{n}_{p',q'} = n_{p,q}\hat{n}_{p',q'} + n_{p',q'}\hat{n}_{p,q} - n_{p',q'}n_{p,q} \;. \tag{2.39}$$

Here $n_{p,q}$ is the expectation value of the occupation operator at the $(p,q)$th site:

$$n_{p,q} = \langle\Psi|\hat{n}_{p,q}|\Psi\rangle = \sum_n n|c_n^{(p,q)}|^2 \tag{2.40}$$

and is connected with the average density $\rho$ by the relation

$$\rho = \sum_{p,q} n_{p,q}/L$$

where $L = L_x \times L_y$ is the system size. According to this procedure, the mean-field Hamiltonian of the system may be written as a sum of single-site Hamiltonians $\hat{H}_{\mathrm{EBH}}^{\mathrm{MF}} = \sum_{p,q}\hat{h}_{p,q}$. For NN interactions the individual summands $\hat{h}_{p,q}$ read

$$\begin{aligned}\hat{h}_{p,q} =& \hat{h}_{p,q}^{\mathrm{MF}} + V\bar{n}_{p,q}\left(\hat{n}_{p,q} - \frac{n_{p,q}}{2}\right) \\ &+ T\left(\hat{a}_{p,q}^\dagger\hat{n}_{p,q}\bar{\phi}_{p,q} + \hat{n}_{p,q}\hat{a}_{p,q}\bar{\phi}_{p,q}^* + \hat{a}_{p,q}^\dagger\bar{\eta}_{p,q} + \hat{a}_{p,q}\bar{\eta}_{p,q}^*\right) \\ &- T\left(\bar{\eta}_{p,q}\phi_{p,q}^* + \bar{\phi}_{p,q}\eta_{p,q}^*\right) \;,\end{aligned} \tag{2.41}$$

where $\hat{h}_{p,q}^{\mathrm{MF}}$ is the single-site Hamiltonian in Eq. (1.76) and the rest is due to the dipolar interaction. Here we have introduced the average mean-field [42]

$$\bar{x}_{p,q} = x_{p,q+1} + x_{p,q-1} + x_{p+1,q} + x_{p-1,q} \;, \tag{2.42}$$

where $x$ can be $\phi$, $\eta$ or $n$ in Eq. (2.41).

The mean-field Hamiltonian corresponding to higher order (NNN) terms is found by applying the same procedure.

We solve the single-site model by using the standard mean-field algorithm explained in Subsubsec. (1.3.3.2) . Here we initialize the Gutzwiller coefficients by $1/\sqrt{n_{\max}}$ on each-site and evaluate the corresponding initial order parameters. Then, we diagonalize the local Hamiltonians sequentially and redefine the order parameters using the ground states found from these diagonalizations. After each diagonalization the order parameters $\phi$, and $\eta$ are updated. This procedure is repeated until the convergence criteria of the order parameter is satisfied. For the present work, we consider the iteration converged when the value of $\phi$ changes less then $10^{-12}$ for two consecutive steps.

#### 2.4.2.2 *Cluster Gutzwiller mean-field (CGMF)*

The disadvantage of the SGMF theory is that the inter-site coupling is incorporated solely through the mean-fields $\bar{x}_{p,q}$. This accounts for the poor resolution of inter-site correlations. This problem can be partially overcome by the application of the so-called Cluster Gutzwiller mean-field (CGMF) method, see Subsubsec. 1.3.3.2. The CGMF-Hamiltonian consists of the Hamiltonian of the cluster, while the coupling between clusters is treated in mean-field:

$$\hat{H}_{\mathrm{EBH}}^{\mathrm{CGMF}} = \sum_{C=1}^{W} \left[ \sum_{\mathbf{i}\in\delta C} \hat{h}_{\mathbf{i}} + \hat{H}_{\mathrm{EBH},C}^{2D,G} \right] \tag{2.43}$$

with $W$ the number of clusters in the lattice. The terms $\hat{h}_{\mathbf{i}}$ are the local mean-field Hamiltonians of (2.41) accounting for the mean-field coupling with the other clusters. The sum goes over $\delta C$, which is the set of all lattice sites at the boundary of the cluster. The Hamiltonian within the cluster is given by

$$\hat{H}_{\mathrm{EBH},C}^{2D,G} = \hat{H}_{\mathrm{EBH},C}^{2D} - \mu \sum_{\mathbf{i}} \hat{n}_{\mathbf{i}} \,, \tag{2.44}$$

where the first part is the Hamiltonian given in Eq. (2.34) restricted to the cluster $C$ and $\mu$ is the chemical potential. Here the sum is restricted to the sites in the cluster $C$.

We initialize the CGMF state, Eq. (1.83), similar to the GW state in the SGMF. We then diagonalize the cluster Hamiltonians, and update the values of the order parameters based on the ground states obtained during the diagonalization. The convergence criteria are the one discussed for the SGMF.

#### 2.4.2.3 *Mean field order parameter*

The classification of various quantum phases in 2D can be obtained by inspecting the behaviour of the two-dimensional extension of the Fourier transform of the off-diagonal correlations

$$M_1(\mathbf{k}) = \frac{1}{L^2} \sum_{\mathbf{j},\mathbf{j}'} e^{i\mathbf{k}\cdot(\mathbf{j}-\mathbf{j}')} \left\langle \hat{a}_{\mathbf{j}}^{\dagger} \hat{a}_{\mathbf{j}'} \right\rangle \tag{2.45}$$

and of the structure form factor

$$S(\mathbf{k}) = \frac{1}{L^2} \sum_{\mathbf{j},\mathbf{j}'} e^{i\mathbf{k}\cdot(\mathbf{j}-\mathbf{j}')} \left\langle \hat{n}_{\mathbf{j}} \hat{n}_{\mathbf{j}'} \right\rangle \tag{2.46}$$

as a function of the dimensionless quasi-momentum $\mathbf{k} = (k_x, k_y)$ and with $\mathbf{j} = (j_x, j_y)$. The expectation values in Eq. (2.45) and (2.46) are taken over $|\Psi\rangle$, Eq. (1.78), in the SGMF approach and over $|\Psi_{CGMF}\rangle$, Eq. (1.82), in the CGMF. In SGMF the observables, Eq. (2.45) and Eq. (2.46), can be cast in terms of the mean-field superfluid order parameter, Eq.

(1.74), and the density on a specific site by just replacing the operators with their expectation values:

$$M_1(\mathbf{k}) = \frac{1}{L^2}\sum_{j,j'} e^{i\mathbf{k}\cdot(\mathbf{j}-\mathbf{j'})}\phi_{\mathbf{j}}\phi_{\mathbf{j}'} \quad , \tag{2.47}$$

$$S(\mathbf{k}) = \frac{1}{L^2}\sum_{j,j'} e^{i\mathbf{k}\cdot(\mathbf{j}-\mathbf{j}')} n_{\mathbf{j}} n_{\mathbf{j}'} \, . \tag{2.48}$$

In the CGMF theory, the correlated wave function $|\Psi_{CGMF}\rangle$, Eq. (1.82), prevents the replacement of the operators by their expectation value. The classification of various quantum phases can be obtained using the behaviour of $M_1$, Eq. (2.45), and structure form factor, Eq. (2.46), at zero and finite $\mathbf{k}$.

In contrast to the one-dimensional case the NN Hamiltonian give rise to spatially periodic structures with $2 \times 2$ cells [20, 100]. Those checkerboard density modulations can be characterized by their sublattice distributions $\mathbf{n} = (n_{\mathbf{e}}, n_{\mathbf{o}})$, where $\mathbf{e} = (p, q)$ labels an even site with $p + q = even$ and $\mathbf{o} = (p', q')$ an odd site with $p' + q' = odd$. Similarly, correlated tunnelling gives rise to a periodic modulation of the off-diagonal correlations, Eq. (1.64), (see Sec. 2.3). Within mean-field one can identify those modulations in the SF mean-field order parameter $\boldsymbol{\phi} = (\phi_{\mathbf{e}}, \phi_{\mathbf{o}})$ [42]. The onset of these structures is also signaled by the finite values of $S$ and $M_1$, respectively, at the wave vector $\mathbf{k} = (\pi, \pi)$. Depending on the ratio between $M_1(0,0)$ and $M_1(\pi,\pi)$ the phase is either a staggered or a normal superfluid.

The inclusion of NNN terms break this symmetry. In general, it is known that the NNN repulsion tends to stabilize striped order of the supersolid phase [30, 101, 103–105]. The coexistence of NN and NNN stabilizes various solid orders, for $V \geqslant 2V_{\text{diag}} (V < 2V_{\text{diag}})$, checkerboard (striped) solid ordered state is formed [30, 102, 105]. Here, in order to distinguish between various orders of solid, supersolid and staggered phases, we determine the Fourier transform of the single-particle correlations $M_1(\mathbf{k})$ and structure factor $S(\mathbf{k})$ at $\mathbf{k} = (\pi,\pi), (0,\pi)$ and $(\pi, 0)$. A finite value of those observables at $(\pi,\pi)$ reflects checkerboard order whereas a finite value at $(0,\pi)$ or $(\pi, 0)$ shows striped order. Thus a finite value of $M_1(\mathbf{k})$ and $S(\mathbf{k})$ at $\mathbf{k} = (\pi,\pi), (0,\pi)$ and $(\pi, 0)$ is the characteristic property of a quarter-filled ordered superfluid phase [103, 104]. Depending on the ratio between $M_1(0,0)$ and $M_1(\pi,\pi)$ the quarter-filled order superfluid phase is either a staggered or a normal superfluid. In this thesis we will find quarter-filled ordered staggered SS phases, which we will label by the acronym QF-SSS.

In the SGMF approach it is also convenient to look at the density-assisted correlation order parameter, which comes naturally out of the

| Phase | $\boldsymbol{n} = (n_{\mathbf{e}}, n_{\mathbf{o}})$ | $M_1(\mathbf{k})$ (2.45) | $S(\mathbf{k})$ (2.27) | $\boldsymbol{\phi} = (\phi_{\mathbf{e}}, \phi_{\mathbf{o}})$ | $\phi_{\text{avg}}$ (2.49) | $\eta_{\text{avg}}$ (2.50) |
|---|---|---|---|---|---|---|
| Mott-Insulator MI | $(n, n)$ | 0 | $\mathbf{k}_{\max} = (0,0)$ | $(0,0)$ | 0 | 0 |
| Density Wave CDW | $(n, n')$ | 0 | $\mathbf{k}_{\max} = (\pi,\pi)$ | $(0,0)$ | 0 | 0 |
| Superfluid SF | $(n, n)$ | $\mathbf{k}_{\max} = (0,0)$ | $\mathbf{k}_{\max} = (0,0)$ | $(\phi, \phi)$ | $> \eta_{\text{avg}}$ | $\leq \phi_{\text{avg}}$ |
| Staggered Superfluid SSF | $(n, n)$ | $\mathbf{k}_{\max} = (\pi,\pi)$ | $\mathbf{k}_{\max} = (0,0)$ | $(\phi, -\phi)$ | $< \eta_{\text{avg}}$ | $\geq \phi_{\text{avg}}$ |
| Supersolid SS | $(n, n')$ | $\mathbf{k}_{\max} = (0,0)$ | $\mathbf{k}_{\max} = (\pi,\pi)$ | $(\phi, \phi')$ | $> \eta_{\text{avg}}$ | $\leq \phi_{\text{avg}}$ |
| Staggered Supersolid SSS | $(n, n')$ | $\mathbf{k}_{\max} = (\pi,\pi)$ | $\mathbf{k}_{\max} = (\pi,\pi)$ | $(\phi, -\phi')$ | $< \eta_{\text{avg}}$ | $\geq \phi_{\text{avg}}$ |

Table 2.2: Classification of phases: Sublattice values of the occupation $\boldsymbol{n} = (n_{\mathbf{e}}, n_{\mathbf{o}})$, FT of the off-diagonal correlations, structure form factor, mean-field SF order parameter, its average and the average density-correlated order parameter. When single-particle correlations and structure form factor do not vanish, we report the value $\mathbf{k} = \mathbf{k}_{\max}$ at which their absolute value is maximum. Here $\mathbf{e}$ refers to an even site and $\mathbf{o}$ labels an odd site. The entries of the orderparameter $\boldsymbol{\phi}$ and $\boldsymbol{n}$ are given by Eq. (1.74) and Eq. (2.40) respectively. The occupation $n$ and $n'$ are different. The same holds for the expectation values $\phi$ and $\phi'$.

algorithm. The staggered superfluid phase can here be captured by the average density-correlated order parameter [42]

$$\eta_{\text{avg}} = \sum_{p,q} |\eta_{p,q}| / L \,. \tag{2.49}$$

For convenience we also use in the following the average SF order parameter

$$\phi_{\text{avg}} = \sum_{p,q} |\phi_{p,q}| / L \,. \tag{2.50}$$

Here, we consider the absolute values of $\phi$'s and $\eta$'s since for staggered phases their distributions over the lattice sites alternate in sign and thus their average without absolute value would become zero. The properties of the quantum phases in terms of the correlation and order parameters is summarized in Table 2.2.

### 2.4.3 *Phase transitions at fixed density*

We numerically determine the ground states of the system in the grand-canonical ensemble and at fixed density. For this purpose we first obtain the distributions of the chemical potential $\mu$ corresponding to a

constant average density. The model parameters are obtained using Wannier function formalism as described in Appendix 2.6, where changes of $T$ and $V$ are induced by changing the interaction strength. Below we choose to plot $V$ instead of the interaction strength. We remind the reader that finite values of $V$ implies also finite values of $T$.

The phases are identified by analyzing the behaviour of correlations and order parameters introduced in the previous Subsubsec. 2.4.2.3. We first discuss the role of NN interaction and density-dependent tunnelling. We then investigate the role of NNN terms in determining the ground state properties. Note that below we label the coordination number by the parameter $z$. In our lattice geometry $z = 4$.

#### 2.4.3.1 *Phase diagram for nearest-neighbor interactions*

*Density $\rho = 1$*

We now discuss the phase diagram at density $\rho = 1$. We first recall that the properties of the ground state are very well studied in the absence of density-dependent tunnelling (for $T = 0$). In this limit the inclusion of NN density-density interaction to BHM leads to additional quantum phases which we shortly review in the following [13, 18, 32, 106]. For large $V$ bosons occupy every alternate lattice site forming CDW phase, an insulating phase which spontaneously breaks sublattice symmetry. When the NN interaction $V$ is comparable to the on-site repulsion, the system breaks both $U(1)$ gauge symmetry and translational invariance to form a SS phase. The SS phase of eBHM is found to be stable in wide range of interaction strengths [20, 85, 107, 108]. For unit filling the stability of SS of soft-core bosons has been demonstrated in Refs. [109, 110]. When $4V \ll U$, the system exhibits MI-SF phase transition as $t$ increases. At stronger NN interactions $4V \approx U$, the MI phase becomes unstable and CDW phase replaces the MI phase [22, 107, 110, 111]. The dependence of the hopping parameter $t$ on various phase transitions for fixed densities has been discussed [112]. We report the corresponding phase diagram with $T = 0$ in the Appendix 2.6.

The effect of correlated hopping in determining the phases is now visible in Fig. 2.17, which displays the correlation $M_1$ at $(0,0)$ and $(\pi,\pi)$, the average SF order parameter, and the structure form factor $S(\pi,\pi)$. These quantities are reported in the $t - V$ plane and have been obtained using the SGMF approach. The properties of $M_1$ and $S(\pi,\pi)$ allow us to identify the phases. At $V/U \leqslant 0.25$, as $t$ increases, $M_1(0,0)$ remains nonzero whereas it vanishes at $(\pi,\pi)$. In addition, $S(\pi,\pi)$ is zero in this region. The region where both $M_1(0,0)$ and $S(\pi,\pi)$ vanishes is MI, whereas the region with finite $M_1(0,0)$ is SF. At lower $V$ we recover the MI-SF transition of BHM [10, 11]. The critical hopping strength of MI-SF transition $t_c$ increases for $0 \leqslant 4V \leqslant U$ with finite $T$. This shift is due to the finite value of correlated hopping, which interferes destructively with single-particle tunnelling.

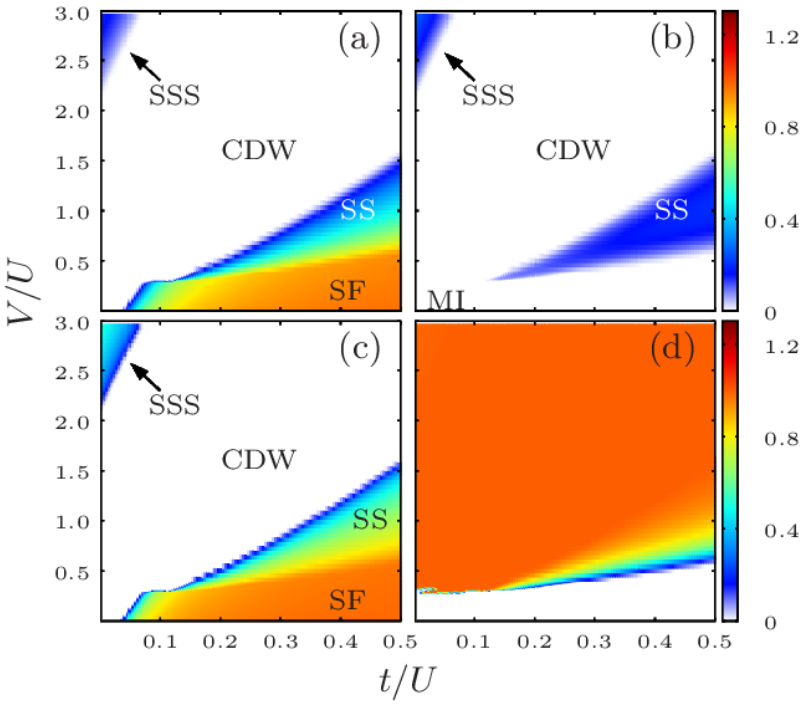


Figure 2.17: Observables for the ground-state of the 2D eBHM at $\rho = 1$ for the mean-field Hamiltonian, Eq. (2.41), truncated at NN. Here the ground state was calculated by means of the SGMF approach. (a) and (b) show the Fourier transform of the off-diagonal single-particle correlation $M_1$ at $(k_x, k_y) = (0, 0)$ and $(k_x, k_y) = (\pi, \pi)$, respectively. (c) displays the average SF order parameter, Eq. (2.50). The structure factor $S$ at $(k_x, k_y) = (\pi, \pi)$ is shown in (d). We consider $12 \times 12$ system with periodic boundary conditions and $n_{\max} = 8$.

At $V/U \simeq 0.25$ we observe the onset of periodic density modulations, which are signalled by the finite value of $S(\pi,\pi)$. The CDW phase corresponds to the large region with vanishing off-diagonal order, $M_1(\mathbf{k}) = 0$. This region is centered about the line of perfect interference $|T| = t$, Eq. (2.16). There is a direct MI-CDW transition for a finite range of values $t/U$ at $V/U \simeq 0.25$, which is characterized by a fast increase of $S(\pi,\pi)$ from zero to the maximum value. In the presence of SF this increase is gradual and characterised by the appearance of a finite value of $M_1(\pi,\pi)$. We identify this region with the SS phase since $|M_1(\pi,\pi)| < |M_1(0,0)|$, see Table 2.2. The boundary $t_c/U$ of the transition CDW-SS increases with $V$. We have checked that $t_c/U$ is shifted to larger values with respect to the phase boundary one obtains by setting $T = 0$, see Appendix 2.6. The resulting domain of the CDW phase is larger. We attribute this effect to the destructive interference between single-particle and correlated hopping.

At larger values $V \approx 2U$ and for vanishing $t/U$ we observe the appearance of finite off-diagonal long-range order with $|M_1(\pi,\pi)| > |M_1(0,0)|$, which we identify with a staggered supersolid (SSS). This phase is due to correlated hopping, which becomes dominant at large ratios $V/U$.

These behaviours can be understood on the basis of mean-field considerations: correlated hopping favours staggered SF for $t/U \to 0$. The size of this region increases as $V$ (and thus the strength of the dipolar interactions) increases. At large ratios $t/U$, instead, the kinetic energy dominates and the phase is SF. The two contributions interfere destructively in an intermediate region, where the phase is insulating. Diagonal long-range order is found for $V/U \geqslant 0.25$. We observe that the size of the SSS region at $V/U \geqslant 0.25$ is now significantly smaller. Comparing the two-dimensional mean-field results in Fig. 2.17 with the one-dimensional DMRG results in Fig. 2.3, we observe a stabilization of the SSF phase in the two-dimensional study.

*Density $\rho = 2$*

Figure 2.18 displays the phase diagrams of the relevant quantities in $t - V$ plane for the average density $\rho = 2$. Similarly to the unit filling case, for $V/U < 0.25$ the phase is either MI or SF. The phase boundary $t_c$ separating the two phases depends on the strength of the dipolar interactions due to the interference between correlated hopping and single-particle hopping. For $V/U \gtrsim 0.25$ the structure form factor $S(\pi,\pi)$ is different from zero and signals the onset of density modulations. As compared to quantum phases at unit filling [Fig. 2.17], the size of the region of insulating CDW phase is reduced whereas the size of the SSS parameter region is significantly larger. A striking difference with respect to the phase diagram at unit filling is the appearance of SSF at $V/U \sim 0.25$ and $t/U \to 0$.

The behaviour reported in Fig. 2.18 qualitatively agrees with the phase diagram in one dimension and using DMRG, shown in Fig. 2.10. However, it is worth noting that the parameter regime of SSF is shifted

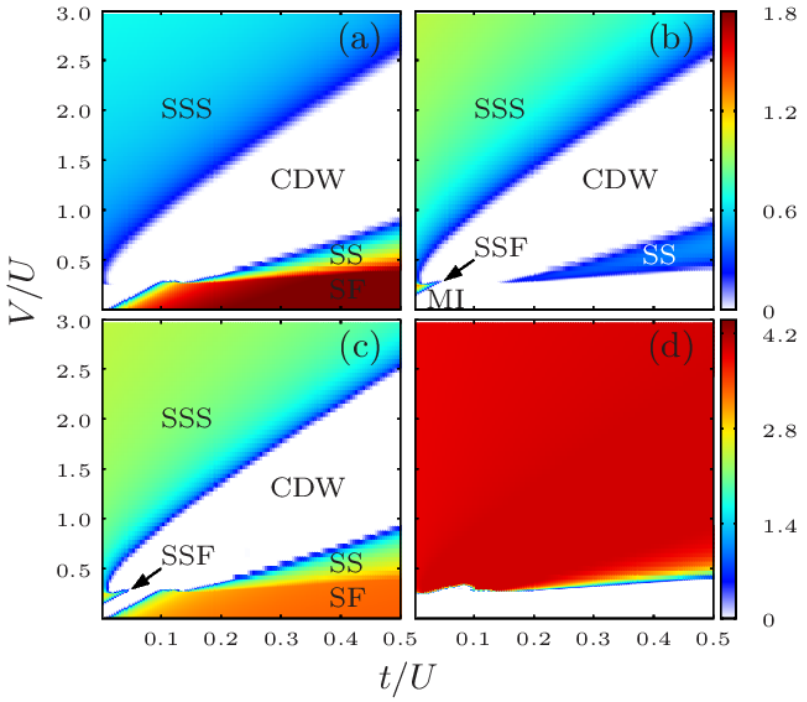


Figure 2.18: Observables for the ground-state of the 2D eBHM at $\rho = 2$ for the mean-field Hamiltonian, Eq. (2.41), truncated at NN. Here the ground state was calculated by means of the SGMF approach. (a) and (b) show the Fourier transform of the off-diagonal single-particle correlation $M_1$ at $(k_x, k_y) = (0, 0)$ and $(k_x, k_y) = (\pi, \pi)$, respectively. (c) displays the average SF order parameter, Eq. (2.50). The structure factor $S$ at $(k_x, k_y) = (\pi, \pi)$ is shown in (d). As for $\rho = 1$, we consider $12 \times 12$ system with periodic boundary conditions and $n_{\max} = 8$.

to lower $V$ values as compared to 1D. This is due to the larger coordination number of square lattices and for $d$-dimensional lattices the staggered superfluidity exist at and around $2dV \approx U$, where $2d = z$ is the lattice coordination number. As in the one-dimensional case, Fig. 2.10, the finite value of $T$ is responsible for the appearance of SSF at $V/U \sim 1/z$ and $t/U \to 0$. The size of the SSF phase is now significantly smaller. In order to perform a systematic comparison with the one-dimensional case, we now consider a small, fixed value $t/U$ and analyse the phases as a function of $V/U$. Figure 2.19 displays the behaviour of $M_1(\pi, \pi)$ as a function of $V/U$ for (a) $t/U = 0.002$, (b) $t/U = 0.02$, (c) $t/U = 0.23$, and (d) $t/U = 0.35$. For $t/U = 0.002$ the phase is first MI. In the atomic limit, at $V/U = 0.25$ MI and several CDW phases are degenerate. Here, the phase becomes SSF due to the prevailing role of correlated hopping and is signalled by the peak of $M_1(\pi, \pi)$ at $V/U \sim 0.25$. This peak was also observed in one dimension around $V/U \sim 0.5$ (see Fig. 2.12). At higher $V$ the value of $M_1(\pi, \pi)$ increases again with $V$, together with the finite value of the structure form factor we identify this phase as SSS. At $t/U = 0.02$, the phases SSF and SSS are separated by a CDW phase. At higher $t$ in (c), the single-particle hopping dominates over the correlated tunnelling. Here, the system is driven first from SF to SS and then to SSS with an intermediate insulating CDW phase. The width of CDW phase in between the SS and SSS phases increases and the region of SSS phase reduces with $t$. This is evident from the behaviour of $M_1(\pi, \pi)$ at $t/U = 0.35$ shown in Fig. 2.19(d).

In order to examine the effects of quantum fluctuations within our mean-field ansatz, we use the CGMF method and compute the $M_1(\pi, \pi)$ with a $2 \times 2$ cluster. The resulting behaviour is reported by the dashed red line in Fig. 2.19. At $t/U = 0.002$ the domain of the SSF phase, signalled by the peak in the $M_1(\pi, \pi)$, is the same as in the SGMF method, while the SSF-SSS transition becomes sharper. For $t/U = 0.02$, Fig. 2.19(b), the critical value of $V/U$ for the CDW-SSS transition shows a small increase as compared to SGMF transition. When $t/U$ is increased to $t/U = 0.23$, Fig. 2.19(c), we observe a shift in the peak of $M_1(\pi, \pi)$, signalling the SS phase, to higher values of $V/U$. In detail, the peak occurs at $V/U = 0.3$ with SGMF, this shifts to $V/U = 0.36$ with the $2 \times 2$ cluster. We note that the shift between the boundary SF-SS predicted by CGMF and the one predicted by SGMF is consistent with the findings reported in [110, 113] for the SF-SS transition.

#### 2.4.3.2 *Phase diagram for next nearest-neighbor*

We now include the NNN terms in our mean-field treatment. We first recall that the quantum phases of eBHM due to competition between NN and NNN repulsion at various fillings have been studied before in the absence of the density-dependent tunnelling [104, 114, 115]. We

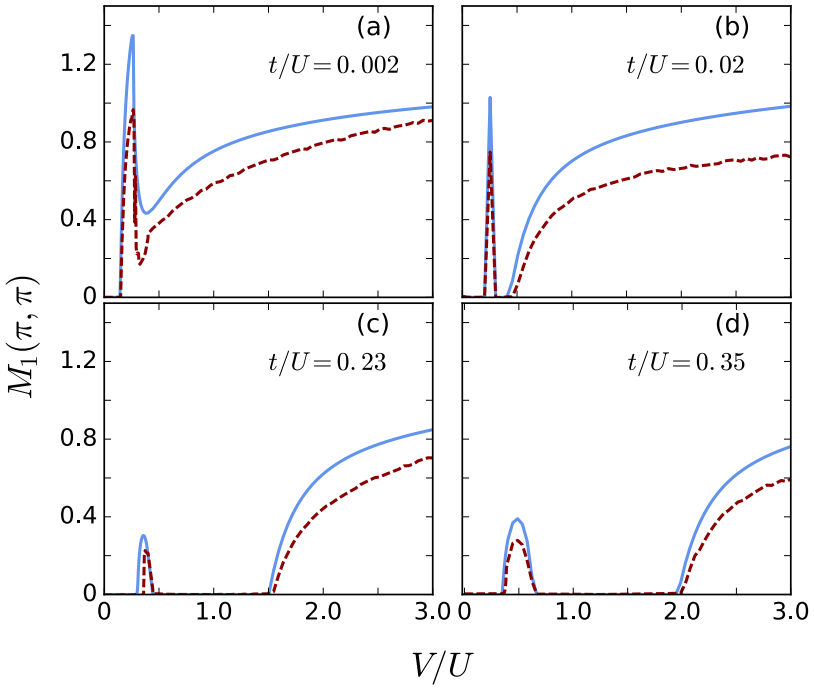


Figure 2.19: Off-diagonal single-particle correlation $M_1(\pi, \pi)$ as a function of $V/U$. The blue lines report the behaviour corresponding to Fig. 2.18(b) for hopping strengths $t/U = 0.002, 0.02, 0.23, 0.35$. The values of $t/U$ is reported in the figures. The dashed red line is obtained using $2 \times 2$ cluster in CGMF theory. Here, we consider the maximum occupancy per lattice site $n_{\max} = 8$: this choice of $n_{\max}$ is sufficient to obtain converging results for densities considered. The density is fixed to $\rho = 2$.

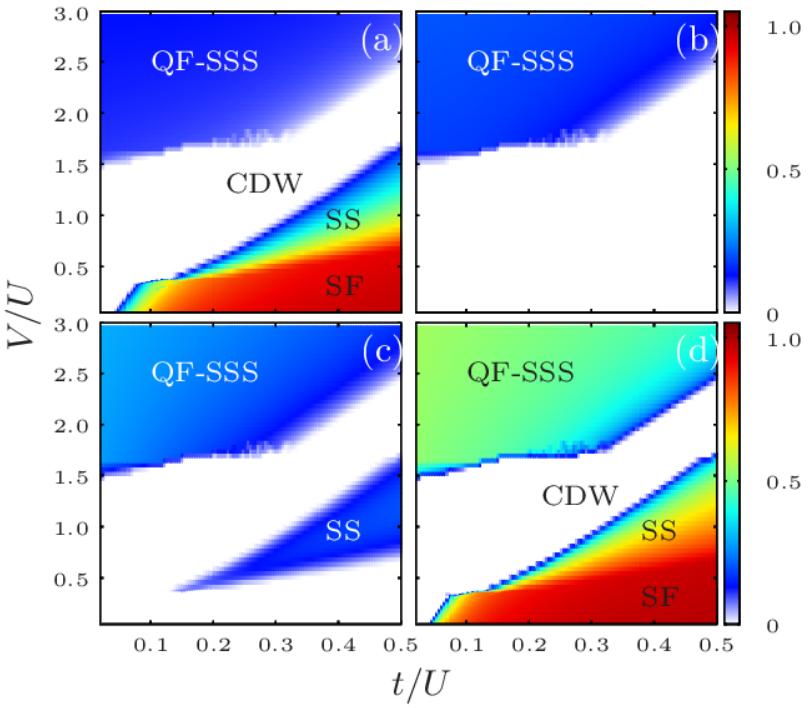


Figure 2.20: Observables for the ground-state of the 2D eBHM at $\rho = 1$ for the mean-field Hamiltonian, Eq. (2.41), truncated at NNN, and calculated by means of the SGMF approach. (a), (b) and (c) show the Fourier transform of the off-diagonal single-particle correlation $M_1$ at $(k_x, k_y) = (0,0)$, $(0,\pi)$, and $(k_x, k_y) = (\pi,\pi)$, respectively. At $V/U \gtrsim 1.5$, the finite values of $M_1$ both at $(0,\pi)$ and $(\pi,\pi)$ signals the quarter-filled ordered phase. The phase is QF-SSS because $|M_1(0,0)| < |M_1(0,\pi)|, |M_1(\pi,\pi)|$. (d) displays the average SF order parameter.

now include density-dependent tunnelling and analyse the ground state of the model Hamiltonian in Eq. (2.41) when the NNN terms of density-density repulsion and of correlated tunnelling are included.

We first discuss the phase diagram at density $\rho = 1$. Figure 2.20 displays the Fourier transform of the single-particle correlations for different values of $\mathbf{k}$ and the average SF order parameter. Some qualitative features are similar to the NN case, compare with Fig. 2.17. A striking difference from the NN case is the decrease of the size of the insulating CDW phase. Moreover, correlated hopping here gives rise to a QF-SSS phase.

These features become more enhanced as the density is increased. Figure 2.21 shows $M_1$ for different values of $\mathbf{k}$ and the average SF order parameter for density $\rho = 2$. With respect to the NN case (cif. Fig. 2.18) we observe that the SSS phase now disappears above a critical value $V/U \sim 1.5$ and becomes QF-SSS. The size of the QF-SSS phase is significantly larger than for unit filling. In particular, the phase boundary of CDW to QF-SSS transition weakly depends on $t/U$.

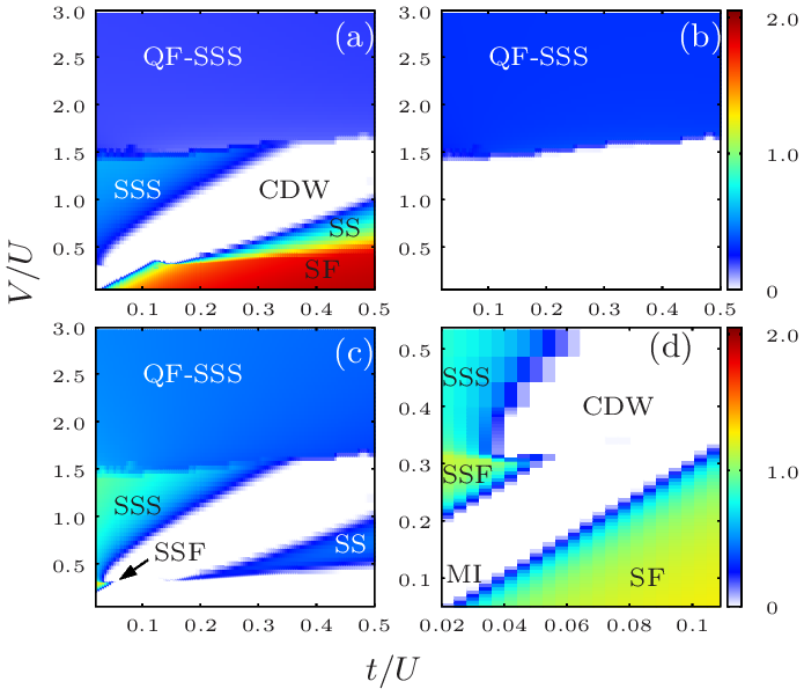


Figure 2.21: The Fourier transform of the single-particle correlations $M_1$ for $\rho = 2$ with NNN at (a) $(k_x, k_y) = (0,0)$, (b) $(k_x, k_y) = (0,\pi)$ and (c) $(k_x, k_y) = (\pi,\pi)$. Unlike at unit filling, here for lower values of NN interaction a CDW-SSS transition occurs and at $V/U \gtrsim 1.5$, the system enters into QF-SSS phase. The QF-SSS phase region is characterized by a finite value of $M_1(0,\pi)$ (see (b)) and of $M_1(\pi,\pi) > M_1(0,0)$ (see (c)). The presence of the SSF phase at around $V/U \sim 0.25$ exhibits the robustness of this phase in presence of NNN density-density interaction. (d) shows the average SF order parameter in the vicinity of the SSF phase.

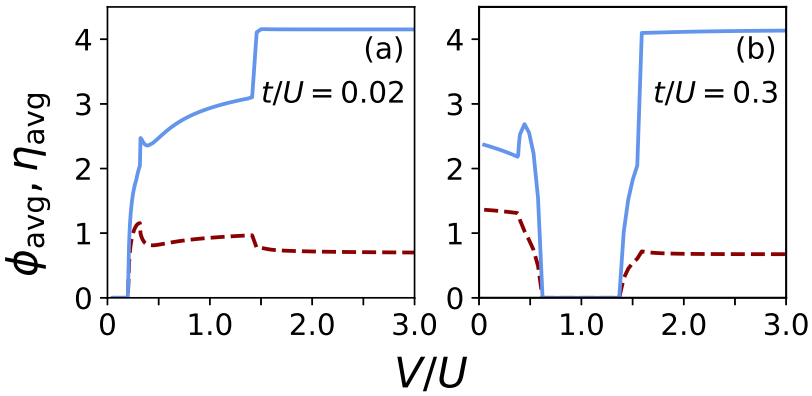


Figure 2.22: The average SF, Eq. (2.50), and density-correlated order parameter, Eq. (2.49), as a function of $V/U$ for $\rho = 2$ with NNN terms of the eBHM, Eq. (2.36). (a) has been calculated for $t/U = 0.02$ and (b) for $t/U = 0.3$. Here, the solid blue (dashed red) line is $\eta_{\text{avg}}$ ($\phi_{\text{avg}}$).

These behaviours qualitatively agree with the one-dimensional phase diagram in Fig. 2.14. Important differences are that the SSF phase results to be smaller. Moreover, in the one-dimensional case we could not uniquely identify the nature of the phase, which is here QF-SSS.

Figure 2.22 displays the average SF order parameter, $\phi_{\text{avg}}$, and the average density-correlated order parameter $\eta_{\text{avg}}$, Eq. (2.49), as a function of $V/U$ and fixed values of $t/U$. We first consider the value $t/U = 0.02$, panel (a). Here, at $V = 0$ the phase is MI. As $V$ is increased, the transitions MI-SSF-SSS take place at $V/U \sim 0.25$ and is here signalled by a sharp increase and a local maximum of both parameters. Finally, at the transition SSS to QF-SSS $\eta_{\text{avg}}$ increases whereas $\phi_{\text{avg}}$ decreases. At $t/U = 0.3$, the system shows SF-SS-CDW-SSS transition as $V/U$ is increased. The corresponding trends of $\eta_{\text{avg}}$ and $\phi_{\text{avg}}$ are visible in Fig. 2.22(b).

### 2.4.4 *Phase transitions at fixed $V/U$*

We now discuss the ground-state phase diagrams in $t - \mu$ plane and for fixed values of $V/U$. For these values the NN repulsion energy becomes comparable to the on-site interaction energy and the insulating phases are CDW [111]. At $4V = U$, in particular, the MI phase with $n_0$ boson per site becomes degenerate with the CDW with occupancies $(2n_0, 0)$. Moreover, the CDW phases with $(n_0 + 1, n_0)$ and with $(2n_0 + 1, 0)$ are degenerate [111]. We vary $\mu$ from 0 up to $4U$ in order to include the density $\rho = 2$. In the $t - \mu$ plane the line of destructive interference, Eq. (2.16), moves to higher $t$ values as $\mu$ is increased, since the density $\rho = \rho(\mu)$ increases monotonically with $\mu$.

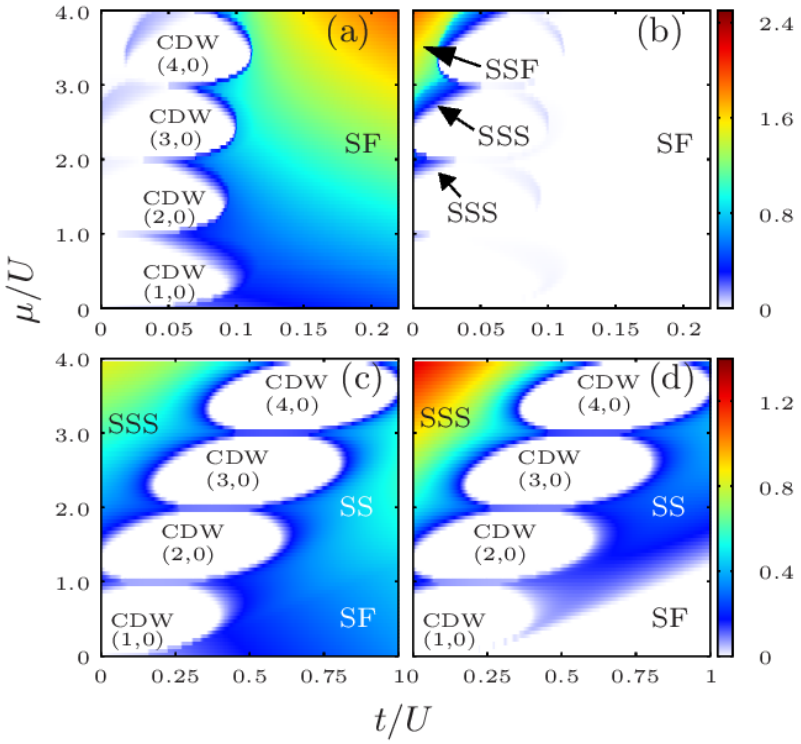


Figure 2.23: The off-diagonal single-particle correlations $M_1(0,0)$ and $M_1(\pi,\pi)$ as a function of $\mu/U$ and $t/U$ for $V/U = 0.25$ (upper panels) and $V/U = 2$ (lower panels). The left panels show the contour plot of $M_1(0,0)$, the right panels of $M_1(\pi,\pi)$. The diagram has been calculated using the SGMF method and truncating the interactions to the NN terms.

### 2.4.4.1 *Results using SGMF*

Figure 2.23 displays the phase correlation functions $M_1(0,0)$ and $M_1(\pi,\pi)$ for $V/U = 0.25$ (upper panels) and $V/U = 2$ (lower panels) calculated with SGMF. The phase diagram is separated into two regions by the sequence of insulating CDW lobes, which are localized along the values of $\rho$ and $t$ fulfilling Eq. (2.16). On the left side, where correlated hopping dominates, the phase is SSS. The size of this region increases with $V$, and thus with the value of $|T|$. The SSF phase is observed only for $V/U = 0.25$ and at sufficiently high values of $\mu$, here at $\mu \geqslant 3$, where $\rho \approx 2$. Here, a direct SSF-CDW transition is observed in a small parameter region at $\mu \approx 3.2$. On the right side single-particle hopping is responsible for the emergence of the SS phases. At higher $t$, the system enters into the SF phase. At $V/U = 2$ we observe the SS-SF phase boundary, which varies linearly as a function of $t$. This feature is consistent with the findings of quantum Monte Carlo studies of 2D eBHM [110].

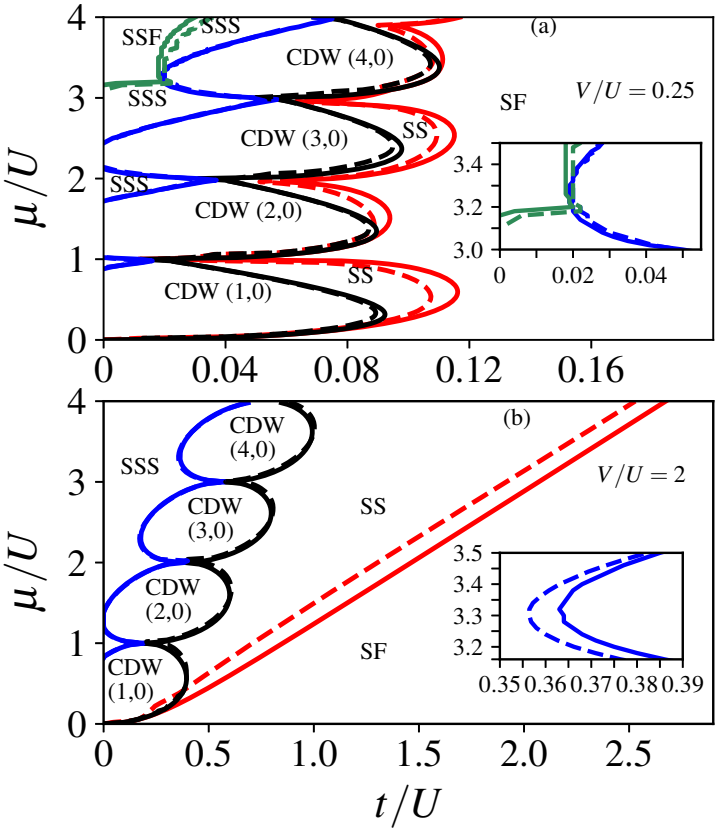


Figure 2.24: Ground state phase diagram of Eq. (2.34) with NN interactions and density-dependent tunnelling. The solid and dashed lines are phase boundaries obtained using the SGMF and CGMF methods, respectively, for simulating Eq. (2.34). The CGMF method uses $2 \times 2$ clusters. The CDW phases are indicated by their sublattice occupancies $(n_a, n_b)$. The insets zoom into regions of the phase diagram where CGMF predicts an increase of the size of the SSF phase (a) and a decrease of the size of the SSS phase (b) with respect to the SGMF predictions.

#### 2.4.4.2 *Comparison between SGMF and CGMF*

We explore the effects of quantum fluctuations and the intersite correlations on the quantum phase transitions by means of the CGMF method using $2 \times 2$ cluster. We restrict here to the NN case. Figure 2.24 shows the ground-state phase diagram of our model in the $t - \mu$ plane for $V/U = 0.25$ and $V/U = 2$. To illustrate the differences, the boundaries between various phase transitions computed with the SGMF and CGMF methods are shown. For $V/U = 0.25$, Fig. 2.24(a), the CGMF method predicts smaller domains of the $(n_0, 0)$ CDW lobes. For instance, the phase boundary separating the CDW $(1,0)$ from the SS phase is at $t_c/U \approx 0.093$ for SGMF, and it is decreased to $t_c/U \approx 0.089$ with the CGMF. A similar trend of the phase boundary $t_c/U$ for the CDW-SS transition was reported in [113] for $V/U = 0.2$. It is to be noted that the size of the SSF phase increases with the CGMF

method. This is visible in the inset of Fig. 2.24(a). At $\mu/U = 3.8$, the SSF phase persists upto $t/U \approx 0.023$ using SGMF, and with CGMF this is modified to $t/U \approx 0.03$. Our computations show that CGMF predicts an increase of the size of the SSF phase while the SSS-CDW phase boundary remains unaffected. This results in a reduction of the SSS phase domain. Thus, the quantum fluctuations captured by the CGMF tend to correct the SGMF predictions by increasing the size of the uniform density phases like the SSF and the SF, while the domains of the structured density phases like the CDW, SSS and SS are tendentially decreased. As with the $V/U = 0.25$ case, the CGMF results show a decrease in the domain of the SS phase in the phase diagram with $V/U = 2$, from the inset in Fig. 2.24(b). On the contrary, the domain of the CDW phase remains unaffected.

## 2.5 CONCLUSIONS

In this work we have characterized the extended Bose-Hubbard model of dipolar bosons in an one-dimensional and two-dimensional square lattice. The one-dimensional model was studied by means of DMRG program in the canonical ensemble. For the two-dimensional case we studied the ground state in the grand-canonical ensemble using two kind of mean-field approaches. For all cases we considered a parameter regime, where tunnelling induced by interactions can interfere with the hopping due to the kinetic energy. We have found that significant effects of interaction-induced hopping are particularly important for sufficiently large densities.

Quantum interference between correlated and single-particle tunnelling qualitatively modifies the phase diagram. One important result is that it gives rise to an effective "interaction-induced atomic limit". This interaction-induced atomic limit is responsible for the appearance of an insulating phase for finite values of the kinetic energy, where one otherwise expects superfluidity. Another important consequence of correlated tunnelling is that at vanishing kinetic energy the dipolar interaction establishes superfluidity with a site-oscillating phase called staggered superfluidity.

While the staggered superfluid is present for $\rho = 1$ in the two-dimensional case for large dipolar interaction strength, it was not observed in the one-dimensional system. We note that we expect these behaviours become visible at larger values of the dipolar interactions, for which one shall consider the contribution of higher bands, as done for instance in Ref. [116–118]. Moreover, in the one-dimensional case with $\rho = 1$ we could identify the HI phase between the MI and CDW phase. A comparison with previous studies without correlated tunnelling [32, 33] reveals a shrinking of the HI region, which confirms the observations in Ref. [39]. On the other hand we observe an increase of a PS region.

For $\rho = 2$ the staggered superfluidity is separated from a staggered supersolidity by a continuous transition at $V \simeq U/z$, where $z$ is the coordination number. We also have compared the phase diagrams when the terms of the power-law interactions of the Bose-Hubbard model are truncated to (i) the first nearest neighbors and then to (ii) the next-nearest neighbors both. Qualitative differences with respect to the nearest neighbor study are visible at sufficiently large interaction strengths, where the next-nearest neighbor terms start to compete with the other terms. In particular, for next-nearest neighbor interactions, at larger dipolar strengths we have found discontinuous transitions to structures with larger Wigner-Seitz cells. Those properties remain the same in a two-dimensional square lattice with $\rho = 2$.

The interference between single-particle and correlated hopping is a consequence of the behaviour of the Bose-Hubbard coefficients as a function of the dipole moment. This interference cuts the phase diagram into two topologically different superfluid phases for sufficiently high densities. In an experiment with given atomic species one would sweep along the line at fixed dipole moment. Then our results indicate that, by tuning the ratio $t/U$ one would observe either transitions from insulating to SSF phases or to "normal" SF. Therefore, species with different dipole moments are characterized by either SSF or "normal" SF phases. Moreover, our results indicate that special values of the dipole moment $d$ can exist, for which the gas remains always in the interaction induced atomic limit, independently of $t$.

Future studies will analyze the effect of correlated tunnelling on the phases at incommensurate densities [119] as well as at fractional densities, where it might significantly affect the physics of Fibonacci anyon excitations [120].

## 2.6 APPENDICES

*Coefficients of the extended Bose-Hubbard Hamiltonian*

In this appendix we shortly review the calculation of the Bose-Hubbard coefficients for the one-dimensional and two-dimensional case.

*One-dimensional case*

The extended Bose-Hubbard model we consider is obtained by inserting Eq. (1.46) into the Hamiltonian of Eq. (2.1):

$$\hat{H} = -\sum_{i,j} t_{i,j}\hat{a}_i^\dagger \hat{a}_j + \sum_{i,j,k,l} V_{i,j,k,l}\hat{a}_i^\dagger \hat{a}_j^\dagger \hat{a}_k \hat{a}_l \,. \tag{2.51}$$

The tunneling coefficients are given by the integrals

$$t_{i,j} = \int_{-L/2}^{L/2} dx\; w_i(x)\left(\frac{\hbar^2}{2m}\frac{\partial^2}{\partial x^2} - V_0\sin(\pi x/a)\right) w_j(x)\,, \tag{2.52}$$

where $w_j(x)$ is the real-valued Wannier function. We define $t = t_{i,i+1}$ and $t_{\mathrm{NNN}} = t_{i,i+2}$ and discard higher order terms. The interaction coefficients are defined by the expressions

$$\begin{aligned} V_{i,j,k,l} =& \frac{1}{2}\int_{-L/2}^{L/2}\int_{-L/2}^{L/2} d\mathbf{r}_1 d\mathbf{r}_2 w_i(x_1)w_j(x_2)\times \\ &\times U_{\mathrm{int}}(\mathbf{r}_1-\mathbf{r}_2)w_k(x_2)w_l(x_1)\Phi_0(y_1,z_1;y_2,z_2)\,, \end{aligned} \tag{2.53}$$

where $U_{\mathrm{int}}(\mathbf{r}) = U_g(\mathbf{r}) + U_\alpha(\mathbf{r})$ and $\Phi_0 \equiv |\phi_0(y_1,z_1)|^2|\phi_0(y_2,z_2)|^2$, see Subsubsec. 3.3.3. The coefficients we use in Subsubsec. 3.3.3 are connected to the integral expression in Eq. (2.53) as follows:
The onsite interaction present is given by $U = 2V_{i,i,i,i}$. The coefficients of the extended nearest neighbor Bose-Hubbard Hamiltonian, Eq. (2.8), have the form

$$V = 2\left(V_{i,i+1,i+1,i} + V_{i,i+1,i,i+1}\right)\,, \tag{2.54}$$
$$T = -\left(V_{i,i,i+1,i} + V_{i,i,i,i+1}\right)\,, \tag{2.55}$$
$$P = 2V_{i,i,i+1,i+1}\,. \tag{2.56}$$

These coefficients include the overlap integrals of Wannier functions of nearest neighboring sites. The expression of the next-nearest neighbor interaction coefficients in Eq. (2.9) are:

$$V_{\mathrm{NNN}} = 2\left(V_{i,i+2,i,i+2} + V_{i,i+2,i+2,i}\right)\,, \tag{2.57}$$
$$T^1_{\mathrm{NNN}} = -2\cdot\left(V_{i+2,i,i+1,i} + V_{i+2,i,i,i+1}\right)\,, \tag{2.58}$$
$$T^2_{\mathrm{NNN}} = -2\cdot\left(V_{i+2,i,i+2,i+1} + V_{i+2,i+1,i,i+2}\right)\,, \tag{2.59}$$
$$T^3_{\mathrm{NNN}} = -2\cdot\left(V_{i+2,i+1,i+1,i} + V_{i+2,i+1,i,i+1}\right)\,, \tag{2.60}$$
$$T_{\mathrm{NNN}} = -\left(V_{i,i,i+2,i} + V_{i,i,i,i+2}\right)\,, \tag{2.61}$$
$$P^1_{\mathrm{NNN}} = 2\left(V_{j+2,j+1,j,j} + V_{j+1,j+2,j,j}\right)\,, \tag{2.62}$$
$$P^2_{\mathrm{NNN}} = 2\left(V_{j+2,j,j+1,j+1} + V_{j,j+2,j+1,j+1}\right)\,, \tag{2.63}$$
$$P^3_{\mathrm{NNN}} = 2\left(V_{j+2,j+2,j+1,j} + V_{j+2,j+2,j,j+1}\right)\,. \tag{2.64}$$

We determine the Hamiltonian parameters as follows. We first decompose the coefficient $V_{i,j,k,l}$ as

$$V_{i,j,k,l} = V^{\alpha}_{i,j,k,l} + V^{g}_{i,j,k,l} \, ,$$

where the contribution of the contact interaction to the overall coefficient is given by

$$V^{g}_{i,j,k,l} = \frac{g}{2} \int_{-L/2}^{L/2} dx w_i(x) w_l(x) w_j(x) w_k(x) \, . \tag{2.65}$$

The coefficients due to the power law interactions are then calculated by means of the convolution method [121]:

$$\begin{aligned} V^{\alpha}_{i,j,k,l} = & \frac{1}{2} \int_{-L/2}^{L/2} \int_{-L/2}^{L/2} dx dy w_i(x) w_l(x) \Phi(y) \\ & \times \mathcal{F}^{-1}_{\mathbf{k}} \left[ \tilde{V}^{\alpha}_{2D}(\mathbf{k}) \mathcal{F}_{\mathbf{k}} \left[ w_j(x') w_k(x') \Phi(y') \right] \right] \, , \end{aligned} \tag{2.66}$$

where $\mathcal{F}_{\mathbf{k}}$ is the Fourier transform from position to momentum space. Here $\Phi(y) = \frac{1}{\sqrt{\pi}\sigma} e^{-y^2/\sigma^2}$ is the probability density of the ground state of the harmonic trap along the $y$-direction, the width is $\sigma = \sqrt{\hbar/m\omega}$ and it is the same for the $y$- and the $z$-direction. In Eq. (2.66) the expression $\tilde{V}^{\alpha}_{2D}(\mathbf{k})$ is the effective interaction in momentum space and reads as [40]

$$\tilde{V}_{2D}(k_y, k_x) = \frac{C_{dd}}{2\sigma} \left[ \frac{2}{3} \sqrt{\frac{2}{\pi}} - q\sigma \, \mathrm{erfc} \left( \frac{\sigma q}{\sqrt{2}} \right) \right] \, , \tag{2.67}$$

where $q^2 = k_x^2 + k_y^2$. The expression in Eq. (2.67) is the effective 2D interaction in momentum space, where we integrate out the $z$-coordinate. For further details see Ref. [40]. We calculate numerically the integral in Eq. (2.65) and (2.66) as a function of $d$ and $a_s$. In our calculations the lattice and trap parameters are kept constant and take the values $V_0 = 8E_R$ and $\sigma/a = 1/\pi\sqrt[4]{50}$.

*Two-dimensional case*

We present here the integral expression of the coefficients in the two-dimensional Bose-Hubbard Hamiltonian in Eq. (2.35) and Eq. (2.36). In contrast to the one-dimensional case the coefficients here consist of the overlap integral of the Wannier function in $y$- and $x$- direction. Along the $z$ direction we expand the field operator in a gaussian function $\phi_0(z)$. The two-dimensional extension of the single-particle tunnelling coefficient is given by the overlap integral [10]

$$t_{ij} = -\int d\mathbf{r} \, w_i(\mathbf{r}) \left[ -\frac{\hbar^2}{2m} \left( \frac{\partial^2}{\partial x^2} + \frac{\partial^2}{\partial y^2} \right) + V_{\mathrm{latt}}(\mathbf{r}) \right] w_j(\mathbf{r}), \tag{2.68}$$

where $w_i(\mathbf{r})$ is a product of standard (real) Wannier functions at $i \equiv \{p, q\}$ and $V_{\mathrm{latt}}$ is the two-dimensional lattice potential. Note that

due to separability of $V_{\text{latt}}$ the coefficients $t_{ij}$ are non-zero only along $x$ or along the $y$ directions. Therefore, "diagonal" tunnellings such as e.g. $i \equiv \{p, q\}$ and $j \equiv \{p+1, q \pm 1\}$ are strictly vanishing. We define $t = t_{i,i+1}$ with $i+1 = \{p, q \pm 1\}$ and $t = t_{i,i+2}$ with $j+2 = \{p \pm 1, q \pm 1\}$.

The situation is different for the interaction terms. In contrast to the one-dimensional case, the integration goes over the two-dimensional plane. We denote the interactions by the potential $U_{\text{int}}(\mathbf{r}) = U_g(\mathbf{r}) + U_{\text{dip}}(\mathbf{r})$. The corresponding interaction coefficients in the site basis read

$$V_{ijst} = \frac{1}{2} \int d\mathbf{r}\, d\mathbf{r}' w_i(\mathbf{r}) w_j(\mathbf{r}') U_{\text{int}}(\mathbf{r} - \mathbf{r}') w_s(\mathbf{r}') w_t(\mathbf{r}) \Phi_0(z_1; z_2), \quad (2.69)$$

with $\Phi_0(z_1; z_2) \equiv |\phi_0(z_1)|^2 |\phi_0(z_2)|^2$. We define here the coefficients as $V^{(j)} = 2(V_{i,i+j,i+j,i} + V_{i,i+j,i,i+j})$, $T^{(j)} = -(V_{i,i,i+j,i} + V_{i,i,i,i+j})$ and $P = 2V_{i,i,i+1,i+1}$. For the nearest neighbor contribution $j = 1$ the lattice sites connected are $i = \{p, q\}$ and $i+1 = \{p, q \pm 1\}$. Thus the nearest neighbor coefficients read $V = V^{(1)}$ and $T = T^{(1)}$. The diagonal sites with respect to site $i$ are labeled as $i+2 = \{p \pm 1, q \pm 1\}$ and the diagonal coefficients are given by $V_{\text{diag}} = V^{(2)}$ and $T_{\text{diag}} = T^{(2)}$.

*Supplementary details on the ground-state phase diagram*

In this appendix we provide supplementary details on the ground-state phase diagram of the one-dimensional and the two-dimensional Bose-Hubbard model.

*One-dimensional case*

Here we provide additional details on the results of Subsubsec. 2.3.3.1. We checked the presence of a pair superfluid phase over the whole parameter range by looking at the Fourier transform of the pair correlations $M_2(q)$ given by Eq. (2.28). We found non-vanishing Fourier components of $M_2(q)$ only at $q = 0, \pi$. Moreover, when $M_2(q)$ has non-vanishing components, then we always find that $M_2(q = 0) > M_2(q = \pi)$. Figure 2.25 displays the contour plot of the Fourier transform at $q = 0$ in the $V/U - t/U$ parameter plane for (a) the nearest-neighbor and (b) the next-nearest neighbor case. We note that the contour plot of the Fourier transform at $q = \pi$ is finite if $M_2(q = 0)$ and $S(q = \pi)$ are both finite.

The behaviour of observable $M_2(q = 0)$ across the phase diagram follows the behaviour of the Fourier transform of the single particle correlations, see Fig. 2.10 and 2.14. Nevertheless, where they are finite, the Fourier components $M_2(q)$ are always smaller than the corresponding Fourier components of the single particle correlations. We conclude that there is no PSF in the parameter regime we considered.

In Subsubsec. 2.3.3.1 we observe the presence of a staggered superfluid phase around $V/U \sim 0.5$ and for small $t/U$. Here we check the

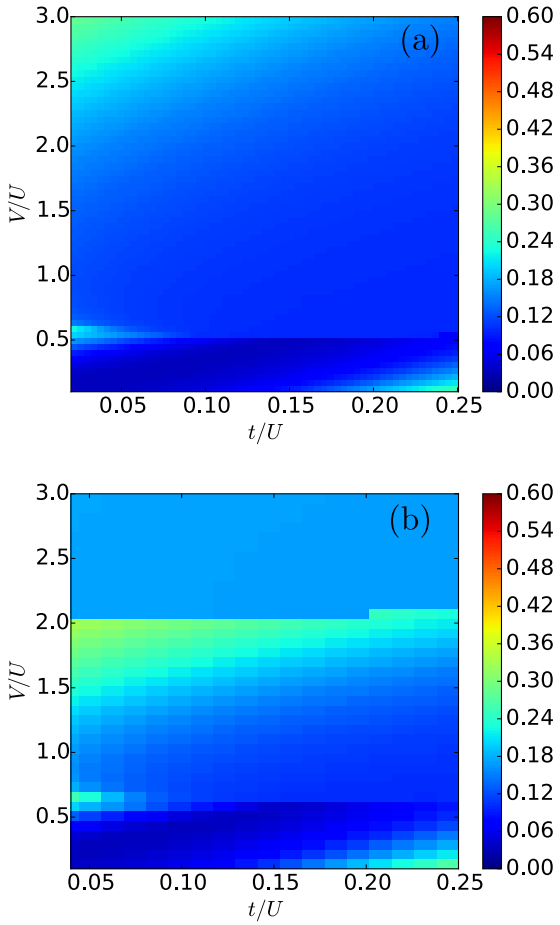


Figure 2.25: Contour plot of the pair condensate density $M_2(q = 0)$ (2.28) as a function of the nearest neighbor interaction strength $V$ and the tunnelling rate $t$ both in units of the on-site interaction strength $U$ for the (a) nearest-neighbor and (b) next-nearest-neighbor model. The number of particles is fixed to $N = 120$ and the number of lattice sites is given by $N_L = 60$.

presence of this phase in the thermodynamic limit. Therefore Fig. 2.26 shows in panel (a) the von Neuman entropy (2.70) and in panel (b) the Fourier transform of the single particle correlations $M_1(q)$, see Eq. (2.26), at $q = \pi$ as a function of one over the number of lattice sites $1/N_L$ for a fixed $t/U = 0.04$ and $V/U = 0.5$. By inspecting Fig. 2.26 we can identify a convergence of the observables with increasing system size. By fitting the curve in Fig. 2.26(b) with an exponential function and taking the limit for $N_L$ going to infinity we get a limit of $M_1(\pi)(N_L \to \infty) = 0.47$ . We conclude that the staggered superfluid phase around $V/U \approx 0.5$ and for small $t/U$ is present in the thermodynamic limit.

We verify the existence of the Haldane insulator for density of $\rho = 2$ by calculating the expectation value of the modified string-order parameter in Eq. (2.29). Fig. 2.27 displays the contour plot of the string

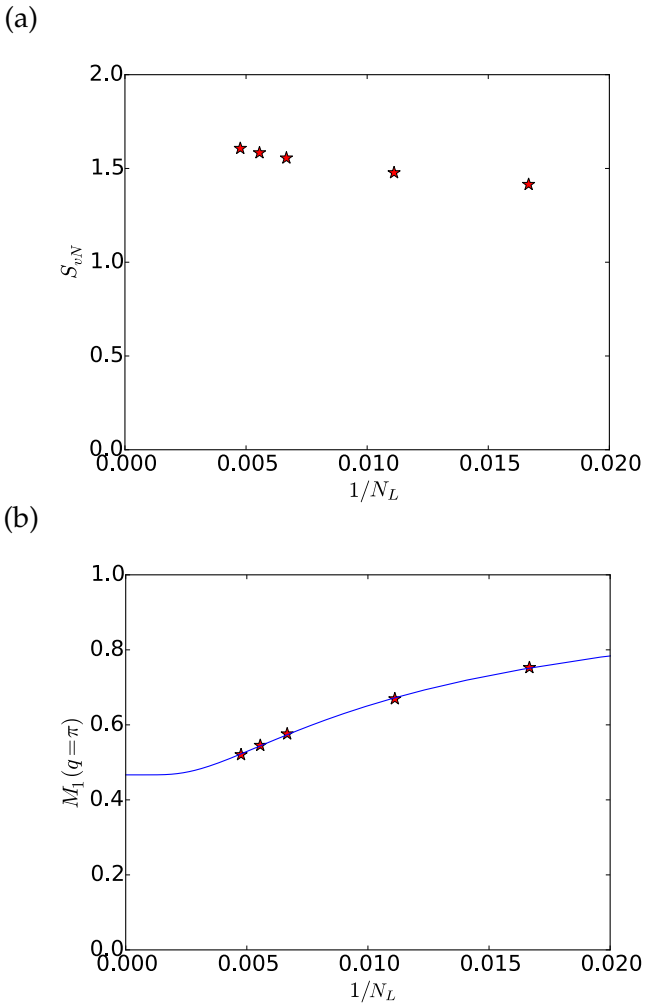


Figure 2.26: (a) The von Neuman entropy (2.70) and (b) the Fourier transform of the single particle correlations $M_1(q)$ (2.26) at $q = \pi$ at a tunnelling rate of $t/U = 0.04$ and a nearest neighbor interaction strength of $V/U = 0.5$ as a function of one over the number of lattice sites $N_L$. The blue curve in (b) shows the exponential function $F(N_L) = 0.45\exp(-0.01(N_L + 18.64)) + 0.47$.

order parameter given by Eq. (2.29) with $\theta = \pi/2$. By comparing the string order parameter in Fig. 2.27 with the structure form factor in Fig. 2.10(d) we cannot identify any region, where the string order parameter is finite and the structure form factor vanishes. Thus we do not find any Haldane insulator for a a density $\rho = 2$ and the here considered parameters.

*Two-dimensional case*

We discuss here the ground-state phase diagram of the model considered in the absence of the density dependent tunnellings ($T$ is put to zero by force). In Fig. 2.28, the single-particle correlations at $(0, 0)$ and $(\pi, \pi)$ are shown for the average densities $\rho = 1$ and $\rho = 2$. We first

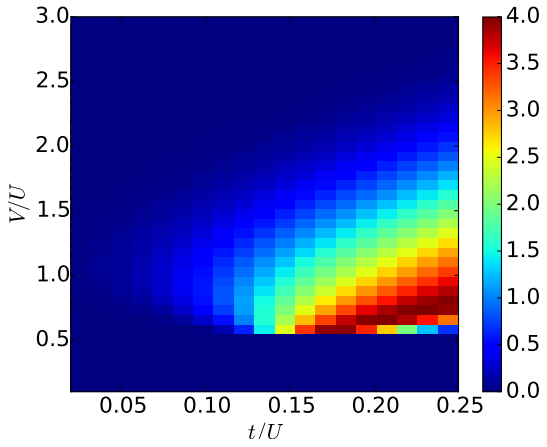


Figure 2.27: Contour plot of the string order parameter, Eq. (2.32), for the ground state of Eq. (2.8), as a function of the ratio $V/U$ and $t/U$. The parameters are the same as in Fig. 2.10.

discuss the quantum phase transitions at $\rho = 1$. The $M_1(0,0)$ which is a measure of ODLRO has a finite value for compressible SF and SS phases whereas it remains zero for insulating MI and CDW phases. At low NN interaction $zV/U \ll 1$, there is MI-SF transition where the critical hopping $t_c$ is independent on $V$. When NN interaction is comparable or overcomes to the onsite interaction $zV/U \geqslant 1$, the transition between density modulated quantum phases CDW-SS occurs. The $t_c$ of CDW-SS transition increases as a function of $V$ [112]. The finite value of $M_1(\pi,\pi)$ for SS phase clearly demarcates it from SF and CDW phases, as evident from Fig. 2.28(b). At $t/U = 0.05$, the MI-CDW transition of $\rho = 1$ as a function of $V$ is consistent to the previous quantum Monte Carlo study [109]. At $\rho = 2$, the qualitative features of various phase transitions remain similar to $\rho = 1$ case, however quantitatively the critical hopping varies.

*Details on the numerical implementation*

*One-dimensional case*

Our results are obtained with a DMRG numerical program, where we make use of the ITensor C++ library for implementing tensor network calculations [67]. In our simulations we use a maximum bond dimension of $\beta = 600$. The cutoff $\epsilon$ is set to $\epsilon = 10^{-12}$, which determines the number of singular values discarded after each singular value decomposition (SVD) step. The energy error goal is set to $\epsilon_{\text{goal}} = 10^{-16}$ and the maximum number of particles per site is fixed to $n_{\max} = 10$. We also add a boundary term $\hat{H}_{ad} = [2\rho]\,(Vn_1 + V_{\text{NNN}}n_2)$ in order to lift the degeneracy in the CDW$_j$ phases and the Haldane phase. To improve the convergence we run the simulation for four different

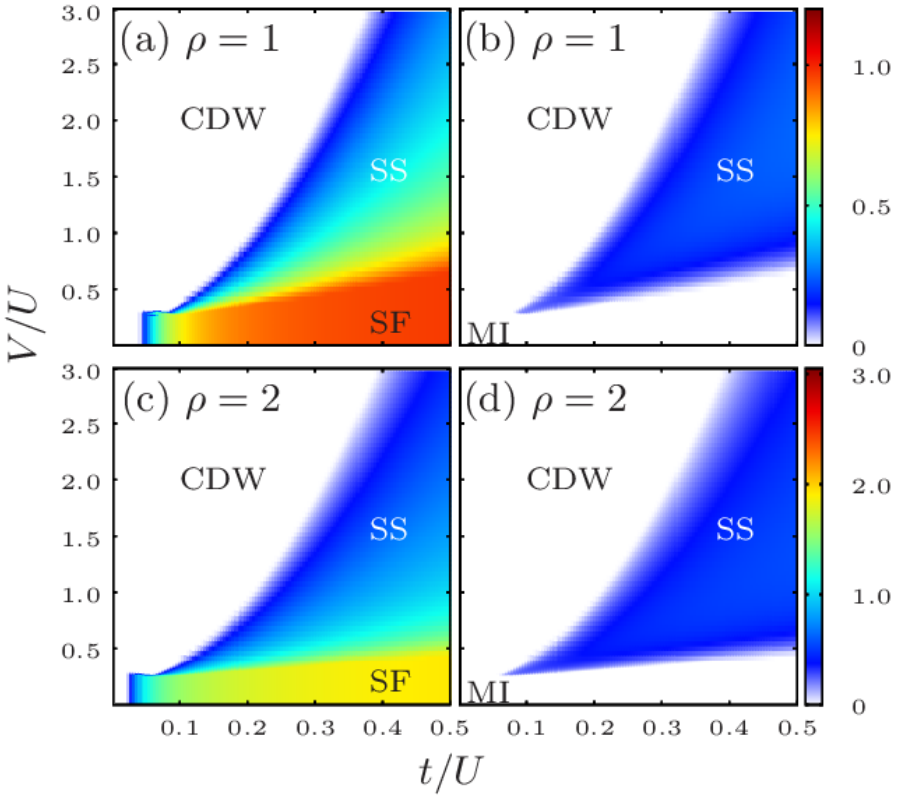


Figure 2.28: Single-particle correlation with NNN interaction and density-dependent tunnelling of dipolar bosons. The correlation for $\rho = 1$ are shown at (a) $(k_x, k_y) = (0, 0)$ and (b) $(k_x, k_y) = (\pi, \pi)$, and for $\rho = 2$ these are shown at (c) $(k_x, k_y) = (0, 0)$ and (d) $(k_x, k_y) = (\pi, \pi)$

initial states: the CDW$_j$ states $|\Phi\rangle_{\text{init}} = \otimes_k |j \cdot \rho\rangle_k \otimes_l |0\rangle_l$ with $k \in \{\mathbb{A} = j \cdot m | m \in \mathbb{N}\}$ and $l \in \mathbb{N} \backslash \mathbb{A}$, the MI state $|\Phi\rangle_{\text{init}} = \otimes_{k=1}^{L} |\rho\rangle_k$ and a random initial state. The random state is a superposition of Fock states $|\Phi\rangle_{\text{init}} = \frac{1}{\sqrt{n_{\text{iter}}}} \sum_k^{n_{\text{iter}}} (\otimes_i |n_i\rangle)_k$, where $n_i \in \mathbb{N}$ is chosen randomly out of the interval $[0, n_{\max}]$ with the constrain $\sum_{i=1}^{L} n_i = \rho$. We choose the number of superimposed Fock state to be $n_{\text{iter}} = 100$. At the end of the simulation we identify the ground state with the state at lowest energy. In order to eliminate the boundary effects we determine the expectation values over the ground state by reducing the chain length by $n_{\text{sit}}$ on each edge in order to eliminate boundary effects. We choose $n_{\text{sit}} = 10$.

In order to calculate the von Neuman entropy introduced in Subsec. 2.3.1 we split the system into subsystem A and B. We then perform at the bond of these two subsystems A and B a singular value decomposition (SVD) of the final ground state coefficients. We determine the von Neuman entropy using the singular values $s_\alpha$ given by the eigenvalues of the diagonal $S$-matrix of the SVD [63, 67]

$$S_{\text{vN}} = -\sum_\alpha s_\alpha^2 \ln\left(s_\alpha^2\right) \ . \tag{2.70}$$

Here we choose the length of the subsystem A to be half of the length of the system.

# 3

# CORRELATED TUNNELLING INDUCED BY ATOM-PHOTON INTERACTIONS

In this chapter we theoretically investigate the influence of a global interaction on the phase diagram of the Bose-Hubbard model. We theoretically analyze the emergence of long-range order and of topological phases for different geometries and dimensions. These dynamics can be realized with ultracold bosonic atoms in optical lattices and coupled to a single-mode cavity.

The following sections of this chapter contain results, text and figures from:

- "Mean-field phase diagram of the extended Bose-Hubbard model of many-body cavity quantum electrodynamics",
  Lukas Himbert, Cecilia Cormick, Rebecca Kraus, Shraddha Sharma, and Giovanna Morigi
  *Physical Review A* **99**, 043633 (2019)

- "Self-organized topological insulator due to cavity-mediated correlated tunneling",
  Titas Chanda, Rebecca Kraus, Giovanna Morigi, and Jakub Zakrzewski
  arXiv:2011.01687 (2020)

## 3.1 INTRODUCTION

The experimental realization of the coupling between ultracold atomic gases and the electromagnetic field of a high finesse cavity has opened the possibility of studying novel dynamics of strongly-correlated ultracold matter [14, 15]. A particularly interesting regime is realized when the atom-cavity coupling is dispersive [14, 15]. In this case photon scattering is associated with conservative optomechanical long-range forces [31, 37, 122]. In a single-mode cavity these forces are global [31, 37, 122]. The combination of optical lattices and optomechanical forces permits one to study the extended Bose-Hubbard model with global interactions [23, 26, 28, 31, 36]. This dynamics has been experimentally realized in Ref. [43, 44]. The purpose of this chapter is to provide a theoretical characterization of the extended Bose-Hubbard model with global interactions. Our analysis uses the parameters of the experiment

at ETH [43, 44] and considers one-dimensional and two-dimensional geometries.

This chapter is organized as follows. In Sec. 3.2 we introduce the two-dimensional long-range Bose-Hubbard Hamiltonian. In Sec. 3.3 we present the local mean-field study for a special geometry, where the global potential takes the form of a modulated density-density interaction. In Sec. 3.4 we then analyze the general situation, where the global potential gives rise to both density-density and correlated tunneling effects and study their interplay in determining the phase diagram. Sec. 3.5 is devoted to the special case, where the global potential gives solely rise to global correlated tunneling. In one dimension we report the appearance of a topological non-trivial phase, which is reminiscent of the Su-Schrieffer-Heeger model [123]. The conclusions are drawn in Sec. 3.6.

## 3.2 EXTENDED BOSE-HUBBARD MODEL WITH CAVITY-MEDIATED INTERACTIONS

We consider $N$ ultracold bosonic atoms with mass $m$ in a two dimensional optical lattice in the $x-y$ plane given by

$$V_{\text{lat}}(x,y) = V_0 \left(\sin^2(k_L x) + \sin^2(k_L y)\right).$$

We will refer in the following to this potential as the static optical lattice. The optical lattice has $K = N_L \times N_L$ sites and we label each site by the index $i = (i_1, i_2)$, where $i_1$ ($i_2$) labels the site index along the $x$ ($y$) direction. In the $x$-$y$ plane the bosons are confined by a harmonic trap. Thus in total the bosons experience the potential $V_{\text{trap}}(\mathbf{r}) = V_{\text{lat}}(x,y) + \frac{m\omega^2}{2}z^2$, where $\omega$ is the frequency of the trap along the $z$ direction.

The bosons interact via $s$-wave scattering and thus feel the contact interaction potential given in Eq. (1.21). Furthermore they are strongly coupled to a cavity standing-wave mode. The mode has the spatial function $h(x) = \cos(kx + \phi)$ and wave vector $\mathbf{k} = k\mathbf{e}_x$. The atoms are transversally driven by a laser and scatter photons into the cavity mode. The spatial mode function of the laser mode transversally pumping the atoms is here given by $f(y) = \cos(ky)$. The system dissipates photons through the cavity mirrors, and we denote by $\kappa$ the linewidth of the cavity [43]. A sketch of the setup is depicted in Fig. 3.1.

In this thesis the dynamics is studied in the parameter regime in which one can eliminate the atoms' internal degrees of freedom and scattering processes can be considered elastic [31, 37, 122]. This leads to a shift of the resonance frequency of the cavity mode and to a coherent pump whose strength depends on the atomic positions within the mode [31, 37]. We will analyze the quantum phases of the atoms in the limit in which the cavity field follows adiabatically the atomic motion and the cavity field can be eliminated from the equations of

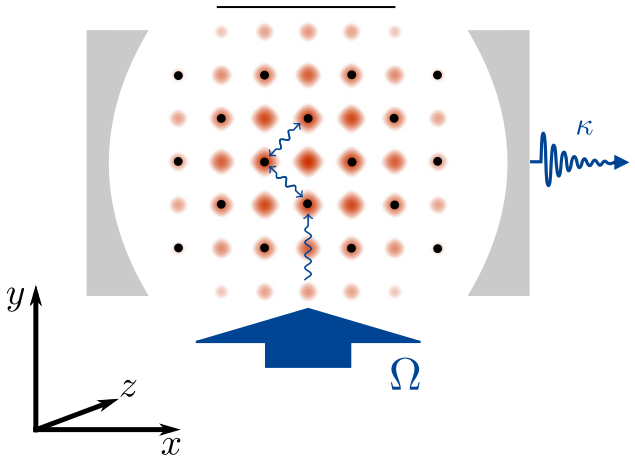


Figure 3.1: The atoms (black dots) are confined by a two-dimensional optical lattice (the intensity is given by red spots) and dispersively interact with a standing-wave mode of the cavity (blue). The atoms are pumped transversally with a laser field with a Rabi-frequency $\Omega$. The field at the cavity output is emitted with rate $\kappa$.

the bosonic variables [31, 37, 122]. This can be achieved by a time scale separation of the atomic and cavity degrees of freedom [31, 37, 122], for which the dynamics of the external degrees of freedom of the atoms are determined by the effective Hamiltonian [31, 37, 122]

$$\hat{H}_{\text{Cavity}} = \hat{H} + \hat{H}_{\text{L}} + \hat{H}_{\text{LR}} \ . \tag{3.1}$$

Here $\hat{H}$ consists of the kinetic energy, the potential of the optical lattice and contact interaction between the atoms, see Eq. (1.44). The Hamiltonian $\hat{H}_{\text{L}}$ describes the potential associated with the laser field and is given by [31]

$$\hat{H}_{\text{L}} = V_{\text{L}} \int d^3\mathbf{r} \hat{\Psi}^\dagger(\mathbf{r}) f(y)^2 \hat{\Psi}(\mathbf{r}) \ , \tag{3.2}$$

where $V_{\text{L}}$ can be tuned by varying the pumping laser parameters. The field operators obey the bosonic commutation relation of Eq. (2.2). The effect of the atom-cavity coupling is described by the effective long-range (LR) Hamiltonian [31, 37]

$$\hat{H}_{\text{LR}} = \frac{U_1}{K} \left( \int d^3\mathbf{r} \hat{\Psi}^\dagger(\mathbf{r}) h(x) f(y) \hat{\Psi}(\mathbf{r}) \right)^2 \ , \tag{3.3}$$

where the dispersive shift is neglected. The coefficient $U_1$ gives the strength of the long-range interactions. It can be either positive of negative, its sign is experimentally controlled by the sign of the detuning between the cavity and laser frequency $\Delta_c$.

We take the effective cavity potential to be a small perturbation with respect to the static optical lattice potential and expand the field operator in the Wannier basis of the lowest band of the static optical lattice. Within the single band approximation we discard the overlap

integral contributions beyond nearest neighbor. One then gets the extended Bose-Hubbard Hamiltonian with global interactions [31, 36, 37]

$$\hat{H}^{\mathrm{BH}}_{\mathrm{Cavity}} = \hat{H}^{2D}_{\mathrm{BH}} + \hat{H}^{\mathrm{BH}}_{\mathrm{L}} + \hat{H}^{\mathrm{BH}}_{\mathrm{LR}} \ . \tag{3.4}$$

Here the first term is the standard Bose-Hubbard Hamiltonian of Eq. (1.73). The second term is due to the pumping laser along the $y$ direction and is given by [31]

$$\hat{H}^{\mathrm{BH}}_{\mathrm{L}} = V_{\mathrm{L}} \sum_j \epsilon^{(j)}_L \hat{n}_j \ , \tag{3.5}$$

with

$$\epsilon^{(j)}_L = \int_0^{aN_L} dy \ w_{j_2}(y)^2 \cos(ky)^2 \ . \tag{3.6}$$

Here the nearest neighbor contribution can be neglected [31] and the operator $\hat{n}_j = \hat{a}^\dagger_j \hat{a}_j$ counts the number of atoms per site $j$. The operator $\hat{a}_j$ ($\hat{a}^\dagger_j$) annihilates (creates) a boson at site $j$ in the lowest lattice band fulfilling the commutation relations $\left[\hat{a}_i, \hat{a}^\dagger_j\right] = \delta_{i_1,j_1}\delta_{i_2,j_2}$.

The third part is the extension due to the atom-cavity coupling and takes the form [36, 37]

$$\hat{H}^{\mathrm{BH}}_{\mathrm{LR}} = \frac{U_1}{K}\left(\hat{\mathcal{D}}^2 + \left(\hat{\mathcal{D}}\hat{\mathcal{B}} + \hat{\mathcal{B}}\hat{\mathcal{D}}\right) + \hat{\mathcal{B}}^2\right) \ , \tag{3.7}$$

where

$$\hat{\mathcal{B}} = \sum_{\langle j,i\rangle} y^\alpha_{j,i} \hat{a}^\dagger_j \hat{a}_i \tag{3.8}$$

is a tunneling term with site dependent amplitude and

$$\hat{\mathcal{D}} = \sum_j z^\alpha_j \hat{n}_j \tag{3.9}$$

is an average density with site-dependent amplitude. Here $\sum_{\langle i,j\rangle}$ is restricted to the pairs of nearest neighbor sites $i$ and $j$. The coefficients $y^\alpha_{j,i}$ and $z^\alpha_j$ in Eq. (3.8) and (3.9) are the overlap integrals over the spatial mode function $h(x)$, $f(y)$ and the Wannier function $W_j(x,y) = w_{j_1}(x)w_{j_2}(y)$ in the lowest band of the static optical lattice [31, 36, 37]:

$$\begin{aligned} z^\alpha_j &= \int_0^{aN_L} dx \int_0^{aN_L} dy \ W_j(x,y)^2 \cos(\alpha k_L x + \phi)\cos(\alpha k_L y) \\ y^\alpha_{j,j+1} &= \int_0^{aN_L} dx \int_0^{aN_L} dy \ W_j(x,y) W_{j+1}(x,y) \times \\ &\qquad \times \cos(\alpha k_L x + \phi)\cos(\alpha k_L y) \ , \end{aligned} \tag{3.10}$$

where we used that $h(x) = \cos(kx + \phi)$, $f(y) = \cos(ky)$ and $j+1 \in \{(j_1, j_2 \pm 1), (j_1 \pm 1, j_2)\}$. The parameter $\phi$ is here the phase shift between the static optical lattice potential and the cavity mode standing

wave and determines the value of the overlap integrals. The periodicity of the mode function $h(x)$ and $f(y)$ depends on the absolute value of the wavevector of the cavity mode $k = |\mathbf{k}|$, whereas the underlying periodicity of the static optical lattice is given by $a = \pi/k_L$ with $k_L = |\mathbf{k}_L|$. The ratio $\alpha = k/k_L$ between these two wavenumbers determines the value of the overlap integrals in Eq. (3.10). Details on the calculation of the two-dimensional extension can be taken from Ref. [31].

In this thesis we focus on the ratio $\alpha = 1$, which is also the situation experimentally realized in [43]. In this case the integrals can be written as $z_j^{\alpha=1} = (-1)^j z_{2D}$ and $y_{j,j+1}^{\alpha=1} = (-1)^j y_{2D}$ with

$$\begin{aligned} z_{2D} &= \int_0^{aN_L} dx \int_0^{aN_L} dy\; w_1(x)^2 w_1(y)^2 \cos(k_L x + \phi)\cos(k_L y) \\ y_{2D} &= \int_0^{aN_L} dx \int_0^{aN_L} dy\; w_1(x) w_2(x) w_1(y)^2 \cos(k_L x + \phi)\cos(k_L y) \end{aligned} \tag{3.11}$$

and $(-1)^j \equiv (-1)^{j_1+j_2}$. In the rest of this chapter we denote a site $(j_1, j_2)$ by even (odd) when $j_1 + j_2$ is an even (odd) number. In this case the long-range part of the Bose-Hubbard Hamiltonian in Eq. (3.4) takes the form

$$\hat{H}_{\mathrm{LR}}^{\mathrm{BH},2D} = \frac{U_1}{K}\left(z_{2D}^2 \hat{D}_{2D}^2 + z_{2D} y_{2D}\left(\hat{D}_{2D}\hat{B}_{2D} + \hat{B}_{2D}\hat{D}_{2D}\right) + y_{2D}^2 \hat{B}_{2D}^2\right) . \tag{3.12}$$

We here extracted the overlap integrals in Eq. (3.11) out of the operators (3.9) and (3.8), which leads to

$$\hat{D}_{2D} = \sum_j (-1)^j \hat{n}_j \tag{3.13}$$

and

$$\hat{B}_{2D} = \sum_{\langle j,i\rangle} (-1)^j \hat{a}_j^\dagger \hat{a}_i \ . \tag{3.14}$$

Note that the expectation value of the operator (3.13) can signal an imbalance of the occupation on the even and odd sites in the state, while the expectation value of (3.14) can signal a staggered behaviour of the off-diagonal correlations.

Note that for $\alpha = 1$ the Hamiltonian in Eq. (3.5) leads solely to a shift of the onsite energy in the standard Bose-Hubbard Hamiltonian in Eq. (1.73) and thus we can include it into the standard Bose-Hubbard Hamiltonian.

In this thesis we will analyze the interplay between $\hat{D}_{2D}$ and $\hat{B}_{2D}$ in determining the phase diagram. We will tune their relative weight, which here corresponds to vary the parameter $\phi$.

## 3.3 MEAN-FIELD PHASE DIAGRAM OF THE EXTENDED BOSE-HUBBARD MODEL

Setting the phase shift $\phi$ between static lattice potential and cavity mode equal to zero, the long-range interaction term (3.12) in the extended Bose-Hubbard Hamiltonian in Eq. (3.4) reduces to a modulated density-density interaction. In this regime the experimentally measured phase diagram [43, 44] reports the existence of MI, SF, CDW and SS.

Several theoretical works reproduced the salient features of the phase diagram using the extended Bose-Hubbard Hamiltonian in this limit. Most works use different implementations of the mean-field treatment [23–27], nevertheless their predictions do not agree across the whole phase diagram. Moreover, some predictions [23–27] exhibit several discrepancies with state-of-the-art two-dimensional quantum Monte Carlo (QMC) study [28]. It has been further argued that the mean-field predictions for this kind of Bose-Hubbard model shall be the same as the one of Bose-Hubbard with nearest-neighbour (and thus also repulsive dipolar) coupling [23, 26].

In this section we provide an extensive mean-field analysis of the two-dimensional extended Bose-Hubbard model with global density-density interactions. For this analysis we consider a grand-canonical ensemble. We determine the ground-state phase diagram using a mean-field approach. We take particular care of the convergence criterion of the numerical results and compare them with analytical results. We then discuss our results comparing them in detail with the analytical predictions and with previous theoretical studies for the cavity Bose-Hubbard model and for repulsively interacting dipolar gases in two dimensions.

We here first review the two-dimensional extended Bose-Hubbard Hamiltonian for the geometry we are considering. We then discuss the exact result for the eigenstates and eigenspectrum in the so-called atomic limit, where the kinetic energy is set to zero. This limit is relevant for the followed mean-field study, where we determine the ground state for finite values of the hopping term.

### 3.3.1 *Grand-canonical Hamiltonian*

We consider the system introduced in the previous Sec. 3.2 depicted in Fig. 3.1 with $\alpha = 1$ and $\phi = 0$. The resulting two-dimensional extended Bose-Hubbard Hamiltonian $\hat{H}^{\mathrm{BH}}_{\mathrm{Cavity}}$ consist of the standard Bose-Hubbard Hamiltonian (1.73) and the long-range Bose-Hubbard Hamiltonian in Eq. (3.12) setting $y_{2D} = 0$. For later convenience we

decompose the Hamiltonian $\hat{H}^{\mathrm{BH}}_{\mathrm{Cavity}} = \hat{H}_t + \hat{V}_0$ into the kinetic energy $\hat{H}_t$ and interaction energy $\hat{V}_0$. They individually read [23, 26, 31]

$$\hat{H}_t = -t \sum_{\langle ij \rangle} \hat{a}_i^\dagger \hat{a}_j, \tag{3.15}$$

$$\hat{V}_0 = \frac{U_0}{2} \sum_i \hat{n}_i(\hat{n}_i - 1) + \frac{U_1}{K} z_{2D}^2 \hat{D}_{2D}^2 \,, \tag{3.16}$$

where the operator $\hat{D}_{2D}$ is the one in Eq. (3.13) and $z_{2D}$ is the two-dimensional overlap integral given in Eq. (3.11). The kinetic energy in Eq. (3.15) is scaled by the hopping coefficient $t$, which is positive and uniform across the lattice, and $\sum_{\langle ij \rangle}$ is restricted to the pairs of nearest neighbor sites $i$ and $j$. The potential energy in Eq. (3.16) is diagonal on the eigenstates of operator $\hat{n}_i = \hat{a}_i^\dagger \hat{a}_i$ and consists of the onsite repulsion, which is scaled by the strength $U_0 > 0$, and of the infinite-range interactions with strength $U_1$. For later convenience we here introduce the operator

$$\hat{\Phi} = \hat{D}_{2D}/K \tag{3.17}$$

and redefine the infinite-range interaction strength as

$$U_\infty = -z_{2D}^2 U_1 \,. \tag{3.18}$$

The expectation value of $\hat{\Phi}$ is maximum when the atoms form a checkerboard pattern.

In the rest of this section we will study the phase diagram of a grand-canonical ensemble at zero temperature. For this purpose we analyze the ground state of the grand-canonical Hamiltonian, defined as

$$\hat{H}_{GC} = \hat{H}_t + \hat{V}_0 - \mu \sum_j \hat{n}_j \,. \tag{3.19}$$

Here, $\mu$ is the chemical potential which controls the mean occupation number $\rho$,

$$\rho = \frac{1}{K} \sum_j \langle \hat{n}_j \rangle \,, \tag{3.20}$$

and the expectation value is taken over the grand-canonical ensemble. In the following we also use the parameter $\theta$, which is proportional to the expectation value of operator $\hat{\Phi}$ according to the relation:

$$\theta = 2 \left| \langle \hat{\Phi} \rangle \right| , \tag{3.21}$$

where the proportionality factor 2 is introduced for later convenience. The value of $\theta$ measures the population imbalance between even and odd sites, thus when it is non-vanishing the atomic density is spatially modulated. In particular, it is proportional to the value of the structure form factor at the wave number of the cavity field [26].

### 3.3.2 *Atomic limit*

We now consider the limit $t = 0$. In this case the energy eigenstates are the Fock states $|n_{(1,1)}, \ldots, n_{(L,L)}\rangle$, with $|n_i\rangle$ Fock state at site $i$. It is convenient to decompose the Fock number $n_j$ of each site $j$ as the sum

$$n_j = \rho + (-1)^j \frac{\theta}{2} + \delta_j \,, \tag{3.22}$$

where $\delta_j$ ensures that $n_j$ is a natural number. This condition, together with Eqs. (3.20) and (3.21), lead to the relations

$$\sum_j \delta_j = 0 \,, \tag{3.23}$$

$$\sum_j (-1)^j \delta_j = 0 \,. \tag{3.24}$$

Using these relations and Eq. (3.22) one can verify that, whenever $\rho \pm \theta/2$ is an integer number, the configuration with minimal energy has $\delta_j = 0$. In fact, using Eq. (3.22) one can cast the energy of the state $|n_{(1,1)}, \ldots, n_{(L,L)}\rangle$ into the form

$$E(\rho, \theta, \{\delta_j\}) = E_0(\rho, \theta) + \frac{U_0}{2} \sum_j \delta_j^2 \,, \tag{3.25}$$

where $E_0(\rho, \theta)$ is the energy of the configuration when $\delta_j$ vanishes at all sites,

$$E_0(\rho, \theta) = K \left[ \frac{U_0}{2} \rho(\rho - 1) + \left( \frac{U_0}{2} - U_\infty \right) \frac{\theta^2}{4} - \mu\rho \right] \,, \tag{3.26}$$

and is visibly extensive. This expression is correct when $|\theta| \leq 2\rho$. The ground state is found by the configuration which minimizes the energy $E_0(\rho, \theta)$. Therefore the ground-state properties are determined by two independent parameters, which we choose here to be $U_\infty$ and $\mu$ in units of $U_0$. More generally, the states at energy $E_0$ are characterised by two-site translational symmetry along both directions of the lattice, such that the sites with the same parity are equally populated. Hence, we can denote the ground state by the ket $\{n, m\}$ where $n$ ($m$) is the Fock number for the even (odd) sites, or vice versa.

In the following we review the ground-state properties in the thermodynamic limit $K \to \infty$ by analysing Eq. (3.26). They can be displayed by means of a phase diagram in the $U_\infty - \mu$ space shown in Fig. 3.2, see also Ref. [23–25]. We first notice that in the limit $U_\infty = 0$ the phase is MI with commensurate density $\rho = n$ in the interval $\mu \in [U_0(n-1), U_0 n]$, while for $\mu < 0$ the density is $\rho = 0$. At $\mu = U_0 n$ there is an infinite degeneracy of SF phases with density continuously varying from $n$ to $n + 1$. For increasing value of $U_\infty$, but $U_\infty < U_0/2$,

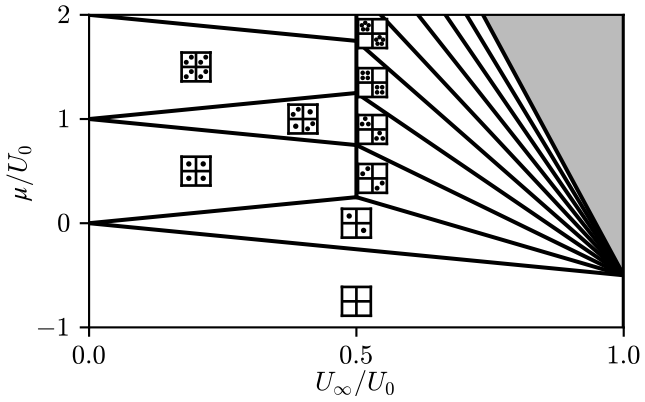


Figure 3.2: Ground-state phase diagram of the extended Bose-Hubbard model with repulsive cavity-mediated long-range interaction and repulsive onsite interaction $U_0 > 0$ in the atomic limit ($t = 0$), as a function of the chemical potential $\mu$ and the long-range interaction coefficient $U_\infty$ (both in units of $U_0$). The lines denote the boundaries between the incompressible phases, which are found assuming an elementary $2 \times 2$ cell (indicated by the inset squares) for the CDW phase. The grey region contains CDW phases with increasingly large density. The boundaries are given by Eq. (3.27) for $0 < U_\infty < U_0/2$. For $U_0/2 < U_\infty < U_0$ the lines correspond to Eq. (3.28). For $U_\infty > U_0$, the model based on the grand-canonical ensemble becomes invalid.

the MI phase with commensurate density $n$ is the ground state for values of the chemical potential such that

$$U_0(n-1) + \frac{U_\infty}{2} < \mu < U_0 n - \frac{U_\infty}{2}. \tag{3.27}$$

At the upper (lower) boundary there is an abrupt jump from the MI to a CDW phase with fractional density $n + 1/2$ ($n - 1/2$) and population imbalance $|\theta| = 1$. In this CDW the occupation of two adjacent sites is $\{n, n+1\}$ ($\{n, n-1\}$), or vice versa, the CDW ground state being doubly degenerate. These boundaries are the lines depicted in Fig. 3.2. At $U_\infty = U_0/2$ there is a discontinuity: For $U_\infty > U_0/2$ the ground state at density $\rho$ is a CDW with the largest population imbalance $|\theta| = 2\rho$ (where $2\rho$ is an integer) in the interval

$$(U_0 - U_\infty)(\theta - 1) - \frac{U_\infty}{2} < \mu < (U_0 - U_\infty)\theta - \frac{U_\infty}{2}, \tag{3.28}$$

while at $\mu = 2(U_0 - U_\infty)\rho - \frac{U_\infty}{2}$ there is an infinite manifold of SF states with density varying from $\rho$ to $\rho + 1/2$. The corresponding phases and boundaries are shown in Fig. 3.2, they all converge to the same point at $U_\infty = U_0$. For $U_\infty \geq U_0$ the onsite energy is attractive, the energy is not bound from below and the grand-canonical ensemble becomes unstable.

This analysis reproduces the results of Ref. [23–25] for $t = 0$. In what follows we will study the phase diagram for finite tunneling rates by means of the mean-field analysis.

### 3.3.3 *Mean-field analysis*

In this subsection we review the mean-field model which is at the basis of our numerical calculations and the definition of the observables that identify the phases. We then use the path-integral formalism to analytically determine the transition from incompressible to SF phase.

#### 3.3.3.1 *Mean-field treatment*

We here apply the local mean-field approach introduced in Subsubsec. 1.3.3.2, where the expectation value of the annihilation operator $\hat{a}_i$ at site $i$

$$\varphi_i = \langle \hat{a}_i \rangle \tag{3.29}$$

is used as a "local superfluid order parameter". To remind the reader the mean-field approximation consists of neglecting terms in second-order in the fluctuations $\delta\hat{a}_i$ of the annihilation operator about $\varphi_i$, with $\delta\hat{a}_i = \hat{a}_i - \varphi_i$. With this approximation the Hamiltonian term (3.15) can be cast into the sum of local Hamiltonians $\hat{H}_t^{\mathrm{mf}} = \sum_i \hat{H}_t^{(i)}$ with

$$\hat{H}_t^{(i)} = -t\left(\hat{a}_i^\dagger \eta_i + \hat{a}_i \eta_i^* - \mathrm{Re}\{\varphi_i^* \eta_i\}\right), \tag{3.30}$$

and where $\eta_i = \sum_{\langle j \rangle_i} \varphi_j$ is the sum of local SF order parameters of the neighbors of site $i$. Without loss of generality in the numerical calculations we assume that these parameters are real.

In order to write the total Hamiltonian in terms of local operators, we perform a second approximation by writing the cavity potential in the mean-field form: $\hat{\Phi}^2 \approx \theta\hat{\Phi} - \theta^2/4$, thus we discard fluctuations of $\hat{\Phi}$ to second order. With this approximation we can now write the grand-canonical Hamiltonian, Eq. (3.19), in its mean-field form $H_{\mathrm{GC:mf}} = \sum_i \hat{H}_{\mathrm{mf}}^{(i)}$, namely, as the sum of local-site Hamiltonians $\hat{H}_{\mathrm{mf}}^{(i)}$ that read

$$\hat{H}_{\mathrm{mf}}^{(i)} = \hat{H}_t^{(i)} + \frac{U_0}{2} n_i(n_i - 1) - (-1)^i U_\infty \theta n_i + U_\infty \frac{\theta^2}{4} - \mu n_i \,. \tag{3.31}$$

In the following we assume two-site symmetry, as in Ref. [23]. Using this assumption all even and all odd sites possess the energy $\hat{H}_{\mathrm{mf}}^{(e)}$ and $\hat{H}_{\mathrm{mf}}^{(o)}$, respectively, such that $\hat{H}_{\mathrm{GC:mf}} = K(\hat{H}_{\mathrm{mf}}^{(e)} + \hat{H}_{\mathrm{mf}}^{(o)})/2$. It is now convenient to introduce the annihilation and creation operators $\hat{a}_e$ and $\hat{a}_e^\dagger$ ($\hat{a}_o$ and $\hat{a}_o^\dagger$) for a particle in an even (odd) site, and the corresponding number operator $\hat{n}_e = \hat{a}_e^\dagger \hat{a}_e$ ($\hat{n}_o = \hat{a}_o^\dagger \hat{a}_o$). The even (odd) sites have SF order parameter $\varphi_e$ ($\varphi_o$) and the population imbalance operator reads $\hat{\Phi} = (\hat{n}_e - \hat{n}_o)/2$. With these definitions we write

$$\begin{aligned} H_{s\in\{\mathrm{e,o}\}} = &- zt\varphi_{\bar{s}}(\hat{a}_s + \hat{a}_s^\dagger - \varphi_s) + \frac{U_0}{2}\hat{n}_s(\hat{n}_s - 1) \\ &- \mu\hat{n}_s - \sigma_s U_\infty \theta \hat{n}_s + U_\infty \theta^2/4 \,, \end{aligned} \tag{3.32}$$

where we have used that $\bar{\varphi}_s = z\varphi_{\bar{s}}$, with $z$ the coordination number (here equal to 4) and $\varphi_{\bar{e}} = \varphi_o$ ($\varphi_{\bar{o}} = \varphi_e$). Moreover, we have introduced the symbol $\sigma_e = +1$, $\sigma_o = -1$. Hamiltonian (3.32) is at the basis of the numerical results presented in the next section.

### 3.3.3.2 *Transition from incompressible to compressible phases*

We now determine the critical tunneling rate which separates compressible from incompressible phases. For this purpose we start from Hamiltonian (3.19) and consider an elaborate form of mean-field treatment following Refs. [11, 68, 124]. We consider the partition function [11, 125]:

$$Z = \mathrm{Tr}\left\{ e^{-\beta \hat{H}_0} T_\tau e^{-\int_0^\beta d\tau \hat{H}_I(\tau)} \right\} \tag{3.33}$$

where $\beta$ is the inverse temperature, $\tau$ is the imaginary time, $T_\tau$ is the imaginary-time ordering operator, $\hat{H}_0 = \hat{V}_0 - \mu \sum_i \hat{n}_i$ is the grand-canonical Hamiltonian without the kinetic energy, and we take $\hbar = 1$ to simplify the notation. Moreover,

$$\hat{H}_I(\tau) = e^{\tau \hat{H}_0} \hat{H}_t e^{-\tau \hat{H}_0}\,, \tag{3.34}$$

where $\hat{H}_t$ is the tunneling Hamiltonian, Eq. (3.15). We can also write Equation (3.33) as $Z = Z_0 \left\langle T_\tau e^{-\int_0^\beta d\tau \hat{H}_1(\tau)} \right\rangle_0$ [11], where $Z_0$ the partition function for the model corresponding to $\hat{H}_0$ and the expectation value evaluated for the thermal state of the same model at inverse temperature $\beta$. Equivalently, one can cast the expression in terms of coherent-state path integrals [68, 124, 126]:

$$Z = \int \mathcal{D}\alpha_j \mathcal{D}\alpha_j^* e^{-\int_0^\beta d\tau \mathcal{L}(\tau)} \tag{3.35}$$

where

$$\mathcal{L} = \sum_j \alpha_j^* \frac{d\alpha_j}{d\tau} + H(\{\alpha_j^*, \alpha_j\})\,. \tag{3.36}$$

where $H$ is assumed to be written in normal form and the path integral is over variables satisfying periodic boundary conditions. The two formalisms can be related by noting that for an operator $A[\{\hat{a}_j^\dagger(\tau_j), \hat{a}_{j'}(\tau_{j'})\}]$ [126]:

$$\langle T_\tau A[\{\hat{a}_j^\dagger(\tau_j), \hat{a}_{j'}(\tau_{j'})\}]\rangle_0 = \tag{3.37}$$

$$\frac{1}{Z_0} \int \mathcal{D}\alpha_j \mathcal{D}\alpha_j^* e^{-\int_0^\beta d\tau \mathcal{L}(\tau)} A[\{\alpha_{j'}^*(\tau_{j'}), \alpha_j(\tau_j)\}]\,, \tag{3.38}$$

where the imaginary time dependence of the operators is defined in the same way as in Eq. (3.34).

We define a new basis of Fourier-transformed variables $\alpha_q, \alpha_q^*$, with $q = (q_1, q_2)$:

$$\alpha_q = \frac{1}{\sqrt{K}} \sum_j \alpha_j \exp[2\pi i (j_1 q_1 + j_2 q_2)/\sqrt{K}] \tag{3.39}$$

with $L = \sqrt{K}$. We then write

$$\mathcal{L} = \mathcal{L}_0 - t \sum_q w_q \alpha_q^* \alpha_q \,, \tag{3.40}$$

where $w_q = 2(\cos(2\pi q_1/\sqrt{K}) + \cos(2\pi q_2/\sqrt{K}))$ are the eigenvalues of the vicinity matrix, and where $\mathcal{L}_0$ is the Lagrangian without the tunneling terms. By means of the Hubbard-Stratonovich transformation we obtain

$$e^{t\int d\tau \sum_q w_q \alpha_q^* \alpha_q} = \int \mathcal{D}\psi_q \mathcal{D}\psi_q^* e^{-\int d\tau \mathcal{L}_2 + \mathcal{L}_c} \,, \tag{3.41}$$

where all normalization factors are now included in the definition of the functional integral, and

$$\mathcal{L}_2 = t \sum_q \psi_q^* \psi_q \,, \tag{3.42}$$

$$\mathcal{L}_c = -t \sum_q \sqrt{w_q} (\alpha_q^* \psi_q + \psi_q^* \alpha_q) \,. \tag{3.43}$$

The prefactors here are chosen so that $\psi_q$ are dimensionless. In particular, the auxiliary variables $\psi_q, \psi_q^*$ are related to the Fourier transform of the expectation values $\varphi_i$ by the equation $\langle \psi_q \rangle = \sqrt{w_q} \varphi_q$.

We now integrate Eq. (3.35) over the variables $\alpha_j, \alpha_j^*$ and obtain

$$Z = Z_0 \int \mathcal{D}\psi_q \mathcal{D}\psi_q^* e^{-S_{\text{eff}}} \,, \tag{3.44}$$

where we have introduced the effective action $S_{\text{eff}}$. The effective action is non-local in time and is given by the expression

$$\begin{aligned} S_{\text{eff}} &= -\ln\left(\frac{1}{Z_0} \int \mathcal{D}\alpha_j \mathcal{D}\alpha_j^* e^{-\int_0^\beta d\tau \mathcal{L}_0 + \mathcal{L}_c}\right) + \int_0^\beta d\tau \mathcal{L}_2 \\ &= -\ln\left(\langle e^{-\int_0^\beta d\tau \mathcal{L}_c} \rangle_0\right) + \int_0^\beta d\tau \mathcal{L}_2 \,. \end{aligned} \tag{3.45}$$

In order to find the transition points, it is sufficient to consider $S_{\text{eff}}$ up to second order in the auxiliary fields. One recovers the expression [124]:

$$S_{\text{eff}}^{(2)} = -\frac{1}{2} \left\langle \left( \int_0^\beta d\tau \mathcal{L}_c \right)^2 \right\rangle_0 + \int_0^\beta d\tau \mathcal{L}_2 \,, \tag{3.46}$$

Owing to the phase invariance of the model, Eq. (3.46) reduces to the form:

$$\begin{aligned} S_{\text{eff}}^{(2)} = \int_0^\beta d\tau \mathcal{L}_2 - t^2 \sum_{q,q'} \sqrt{w_q w_{q'}} \int_0^\beta d\tau \int_0^\tau d\tau' \\ \left[ \psi_q^*(\tau) \psi_{q'}(\tau') \langle \hat{a}_q(\tau) \hat{a}_{q'}^\dagger(\tau') \rangle_0 + \psi_q(\tau) \psi_{q'}^*(\tau') \langle \hat{a}_q^\dagger(\tau) \hat{a}_{q'}(\tau') \rangle_0 \right] , \end{aligned} \tag{3.47}$$

where the Fourier-transformed operators $\hat{a}_q$ of the site operators $\hat{a}_j$ are defined in analogous form as Eq. (3.39).

The time correlators of the model with no hopping can be calculated easily in the site basis. For the case $T \to 0$ (*i.e.* $\beta \to \infty$) they are found to be:

$$\langle \hat{a}_j^\dagger(\tau)\hat{a}_{j'}(\tau-\tau_0)\rangle_0 = \delta_{jj'} n_j e^{-tE_j^-}, \tag{3.48}$$

$$\langle \hat{a}_j(\tau)\hat{a}_{j'}^\dagger(\tau-\tau_0)\rangle_0 = \delta_{jj'}(n_j+1)e^{-tE_j^+}, \tag{3.49}$$

where the values of $n_j$ and $\langle\Phi\rangle$ are the ones that correspond to the ground state for $t = 0$, see Subsec. 3.3.2. The energy $E_j^\pm$ is the energy variation resulting from the addition or subtraction of a particle at site $j$,

$$E_j^- = \mu - U_0(n_j - 1) + 2U_\infty\langle\Phi\rangle(-1)^j, \tag{3.50}$$

$$E_j^+ = -\mu + U_0 n_j - 2U_\infty\langle\Phi\rangle(-1)^j, \tag{3.51}$$

where we neglected a term of order $1/K$ (note that $E_j^-$ is defined for $n_j > 0$).

In the ground state, $n_j$ and $E_j^\pm$ only depend on the parity of the site, so one can cast the correlators of Eqs. (3.48) and (3.49) in the form:

$$\langle \hat{a}_j^\dagger(\tau)\hat{a}_j(\tau-\tau_0)\rangle_0 = C^-_{s\in\{e,o\}}(\tau_0), \tag{3.52}$$

$$\langle \hat{a}_j(\tau)\hat{a}_j^\dagger(\tau-\tau_0)\rangle_0 = C^+_{s\in\{e,o\}}(\tau_0), \tag{3.53}$$

where the subindices correspond to $j$ being even or odd. This can be used to calculate the Fourier-transformed correlators:

$$\langle \hat{a}_q^\dagger(\tau)\hat{a}_{q'}(\tau-\tau_0)\rangle_0 = C_e^-(\tau_0)\frac{\delta_{qq'}+\delta_{q\bar{q}'}}{2} + C_o^-(\tau_0)\frac{\delta_{qq'}-\delta_{q\bar{q}'}}{2}, \tag{3.54}$$

$$\langle \hat{a}_q(\tau)\hat{a}_{q'}^\dagger(\tau-\tau_0)\rangle_0 = C_e^+(\tau_0)\frac{\delta_{qq'}+\delta_{q\bar{q}'}}{2} + C_o^+(\tau_0)\frac{\delta_{qq'}-\delta_{q\bar{q}'}}{2}. \tag{3.55}$$

Here, we introduced the notation:

$$\bar{q} = (\bar{q}_1, \bar{q}_2) = (q_1 + \sqrt{K}/2, q_2 + \sqrt{K}/2), \tag{3.56}$$

and the sum of quasimomenta is taken to be mod $\sqrt{K}$. Thus, the presence of an even-odd asymmetry leads to non-vanishing correlators between momenta corresponding to $q, \bar{q}$. Note that for temperatures $T > 0$ this structure is maintained, only the form of the single-site correlators is changed. The correlators in Fourier basis can then be replaced in expression (3.47), and the sum can be made more compact by noting that $w_{\bar{q}} = -w_q$. We now make the standard assumption that the transition can be found by considering time-independent auxiliary fields $\psi_q, \psi_q^*$, so that they can be taken out of the integrals. We obtain:

$$S_{\text{eff}}^{(2)} = \sum_q \psi_q^*\psi_q \left\{ t\beta - \frac{t^2 w_q}{2}\int_0^\beta d\tau \int_0^\tau d\tau_0 \left[C_e^-(\tau_0) + C_o^-(\tau_0) + C_e^+(\tau_0) + C_o^+(\tau_0)\right]\right\}$$
$$+ i\sum_q \psi_{\bar{q}}^*\psi_q \frac{t^2 w_q}{2}\int_0^\beta d\tau \int_0^\tau d\tau_0 \left[C_e^-(\tau_0) - C_o^-(\tau_0) + C_e^+(\tau_0) - C_o^+(\tau_0)\right]. \tag{3.57}$$

For the case $T \simeq 0$, after performing the time integrals one gets:

$$S^{(2)}_{\text{eff}} \simeq t\beta \sum_q \left\{ \psi^*_q \psi_q \left[ 1 - \frac{t w_q}{2} \left( \frac{n_e}{E^-_e} + \frac{n_o}{E^-_o} + \frac{n_e+1}{E^+_e} + \frac{n_o+1}{E^+_o} \right) \right] + i \psi^*_{\bar{q}} \psi_q \frac{t w_q}{2} \left( \frac{n_e}{E^-_e} - \frac{n_o}{E^-_o} + \frac{n_e+1}{E^+_e} - \frac{n_o+1}{E^+_o} \right) \right\}. \tag{3.58}$$

Thus, for each pair of modes $q, \bar{q}$, the effective action to second order has eigenvalues corresponding to a matrix of the form:

$$M_q = \mathbf{I} - \frac{t w_q}{2} (\ell_1 \sigma_z + i \ell_2 \sigma_x), \tag{3.59}$$

with $\ell_1, \ell_2$ the ($q$-independent) coefficients in Eq. (3.58). The smallest of each pair of eigenvalues reads $1 - t|w_q| \sqrt{\ell_1^2 - \ell_2^2}/2$. Hence, since the largest value of $|w_q|$ is equal to 4, the smallest eigenvalue of all pairs of modes in 2 dimensions is then $1 - 2t\sqrt{\ell_1^2 - \ell_2^2}$. The transition point is found when this eigenvalue vanishes. After replacing the coefficients $\ell_1, \ell_2$ one finds:

$$t_c^{-1} = 4 \sqrt{ \left( \frac{n_e}{E^-_e} + \frac{n_e+1}{E^+_e} \right) \left( \frac{n_o}{E^-_o} + \frac{n_o+1}{E^+_o} \right) }. \tag{3.60}$$

This result coincides with the one reported in Refs. [23–25].

### 3.3.4 *Ground-state phase diagram*

In this subsection we determine the ground-state phase diagram using the mean-field model, Eq. (3.32). By rescaling the energy with $U_0$, the ground state is fully characterized by three parameters: $\mu$, which controls the density, $U_\infty$, which scales the cavity interactions, and the tunneling $t$. The numerical analysis is performed by identifying self-consistently the ground state using a fixed-point iteration detailed in Appendix 3.7. By these means we identify four possible phases: (i) SF when $\varphi_s \neq 0$ and $\theta = 0$; (ii) lattice supersolid (SS) when $\varphi_s \neq 0$ and $\theta \neq 0$; (iii) MI when $\varphi_s = 0$ and $\theta = 0$; and finally (iv) CDW, when $\varphi_s = 0$ and $\theta \neq 0$ [26]. We further note that in the SS phase the two SF order parameters $\varphi_e$ and $\varphi_o$ take different non-vanishing values.

#### 3.3.4.1 *Ground-state phase diagram for varying density*

Figure 3.3 shows the ground-state phase diagram as a function of $U_\infty, \mu, t$, the different colors identify a different phase, the SF phase is the corresponding empty space. In the plane at $U_\infty = 0$ we recover the mean-field phase diagram of the two-dimensional Bose-Hubbard model [11, 127]. For $0 < U_\infty/U_0 < 0.5$ the MI lobes shrink along the $\mu$ axis and are sandwiched by CDW phases, which become increasingly

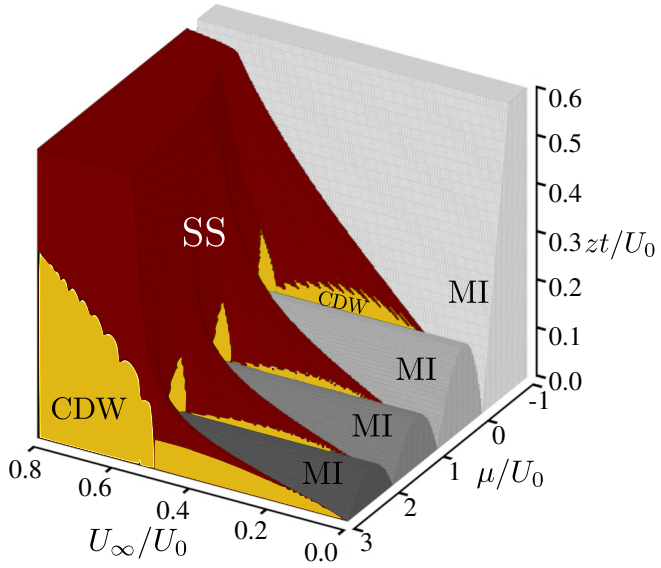


Figure 3.3: Ground-state phase diagram as a function of $U_\infty, \mu, t$ (in units of $U_0$) obtained by numerically determining the phases using the mean-field model of Eq. (3.32). The MI phase is grey, the CDW is yellow, the SS is red, the rest of the phase diagram is SF. Note that the tunneling rate is rescaled by the coordination number $z$ (here $z = 4$). In the numerical procedure the cut-off of the occupation at each site is at $n_{\max} = 31$, the precision is $\varepsilon = 10^{-8}$ and 275 initial guesses were taken (see Appendix 3.7).

visible. Here, the CDW phases are characterized by minimal population imbalance $\theta = 1$, corresponding to $n_e = n$ and $n_o = n + 1$ where $n$ is integer, or vice versa. The red regions at the tip of each CDW lobe is SS, the parameter region where the SS phase is different from zero increases with $U_\infty$.

Inspecting Fig. 3.3 we observe that the MI phases vanish at $U_\infty = 0.5U_0$ also for finite tunneling. Moreover, there is a discontinuity at $U_\infty = 0.5U_0$: the CDW phases with population $\{n, n+1\}$ completely disappear and are replaced by CDW phases with maximal population imbalance $\{0, 2n+1\}$. This result is in agreement with our analysis in the atomic limit, Subsec. 3.3.2. Moreover, at $U_\infty = 0.5U_0$ and at finite tunneling rate one observes a discontinuous transition from SF to CDW. For $U_\infty > 0.5U_0$ the CDW phases are separated from the SF phase by lattice SS phases, which almost completely surround the tip of CDW regions.

We now consider the values $U_\infty = 0.3U_0$ and $U_\infty = 0.6U_0$ and show the behaviour of SF order parameter and $\theta$, respectively, in Fig. 3.4. We first discuss the case $U_\infty = 0.3U_0$, namely, when the strength of the long-range interaction is below the threshold value $U_\infty = U_0/2$. In this case, the MI phases are stable. The transition between MI-SF and CDW-SS are characterized by a continuous change of the SF order parameter. However, there is no direct transition between the MI and SS phases. Our numerical results, moreover, predict a direct transition between CDW and MI at $t > 0$. The population imbalance changes discontinuously across the CDW-MI transition boundary. In particular, in the vicinity of the transitions between each two insulating lobes, we find a range of parameters where they are metastable: The transition line here corresponds to the parameters where the two states have the same energy. This prediction agrees with the ones of Refs. [23, 25, 128] and with the results for hard-core bosons in Ref. [129]. A direct CDW-MI transition is also predicted by a mean-field treatment in a canonical ensemble [27].

We remark that a direct CDW-MI transition, a direct CDW-SF transition, and SS phases at the tip of the CDW lobes have also been found in mean-field studies based on cluster analysis [26]. A further quantitative comparison with the phase diagram reported there is not possible. In fact, the effective strength of the long-range interaction term is not constant across the phase diagram of Ref. [26], since this depends on the overlap integral between the cavity standing wave and the Wannier functions. There, the Wannier functions are calculated by changing the depth of the confining optical lattice, after which the integrals giving $t$, $U_0$, and $U_\infty$ are determined.

We now discuss the phase diagrams in Fig. 3.4 for $U_\infty = 0.6U_0$. Comparison with the left panels show that now the CDW lobes have moved towards smaller chemical potentials, their width (with respect to the chemical potential) has decreased and the critical tunneling rate

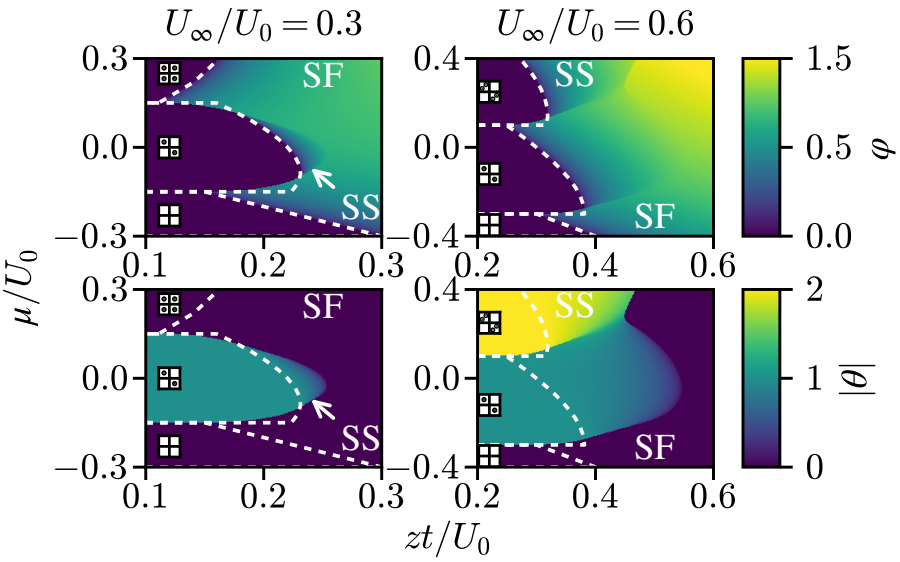


Figure 3.4: Cuts of the ground-state phase diagram of Fig. 3.3 for $U_\infty = 0.3U_0$ (left column) and $U_\infty = 0.6U_0$ (right column). Upper panels: contour plots of the SF order parameter $\varphi = \sqrt{|\varphi_e \varphi_o|}$; Lower panels: contour plots of the population imbalance $|\theta|$. The white dashed lines show the phase boundaries predicted by Eq. (3.60).

has increased. The form of this phase diagram qualitatively agrees with the one reported in [23, 25]. For both values $U_\infty = 0.3U_0$ and $U_\infty = 0.6U_0$ we observe discrepancies between the numerics and the analytical lines, which reproduce the phase boundaries predicted by Eq. (3.60). These discrepancies are visible at the direct transition CDW-SF, as well as at the transition between CDW and SS with different values of the population imbalance. At these phase boundaries the population imbalance varies discontinuously. We attribute these discrepancies to the approximations at the basis of the analytical treatment leading to Eq. (3.60). The treatment, in fact, does not include the coupling between the order parameters for superfluidity and for the population imbalance, and cannot hence appropriately describe transitions where the population imbalance undergoes a jump. We discuss in the next subsection the nature of these transitions.

Finally, we observe that at fixed chemical potential and at fixed values of $U_\infty$ above $U_0/2$ the CDW phase has constant population imbalance. This contrasts with the prediction of Ref. [24], where a transition between CDW phases with maximal population imbalance as a function of the tunneling rate was reported. Figure 3.5 shows the occupations $\rho_e$ and $\rho_o$ of the even and odd sites, respectively, as well as the corresponding SF order parameters as a function of the tunneling rate for the same parameters as in Fig. 6 of Ref. [24]. We find that in the incompressible phase the population imbalance is constant and equal to $|\theta| = 5$. We note that our self-consistent analysis at $t = 0$ gives that the CDW with occupations $\{0, 4\}$ is metastable with energy

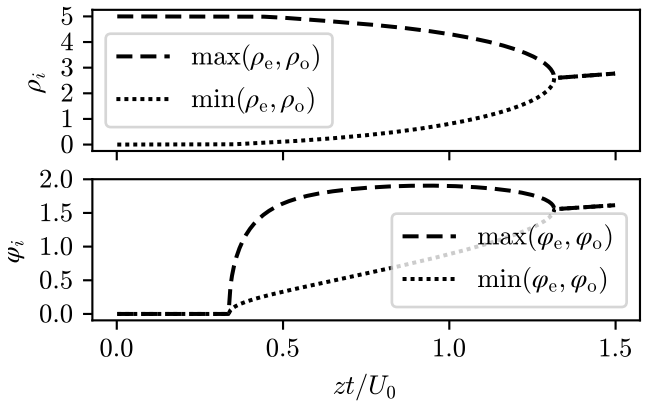


Figure 3.5: Local density $\rho_i$ and SF order parameter $\varphi_i$ as function of the tunneling $zt/U_0$ with $z = 4$. The order parameters are obtained by self-consistently diagonalizing the Hamiltonians (3.32) according to the procedure detailed in Appendix 3.7. The parameters are $\mu = U_0$ and $U_\infty = 0.7U_0$. The occupation at each site is cut off above $n_{\max} = 31$, the precision is $\varepsilon = 10^{-7}$ and 275 initial guesses were taken.

$-1.8U_0$, while the CDW with occupations $\{0, 5\}$ is the ground state with energy $-1.85U_0$. Since the mean-field energy does not depend on the tunneling rate in the incompressible phase, then the $\{0, 5\}$ CDW is the ground state for all values of $t$ where it is stable. We conclude that a transition like that reported in reference [24] is not consistent within the static mean-field assumption.

Before concluding this subsubsection, we briefly compare the phase diagrams in Fig. 3.4 for $U_\infty = 0.3U_0$ with the ones for dipolar gases, interacting repulsively in two dimensions. Here, mean-field treatments and quantum Monte Carlo calculations report the same phases as for all-to-all coupling, however the ground-state phase diagrams are qualitatively different. An important difference is that for dipolar gases there is no direct transition CDW-MI [20, 107, 110, 111, 130].

#### 3.3.4.2 *Ground state for fixed densities*

We now discuss the phase diagram as a function of $t/U_0$ and $U_\infty/U_0$ at fixed density $\rho$. Within our grand-canonical model this implies to find the values of the chemical potential $\mu$, at given $\tilde{t} = zt/U_0$ and $\tilde{U}_\infty = U_\infty/U_0$, which satisfy the equation

$$\rho(\mu/U_0, \tilde{t}, \tilde{U}_\infty) = constant. \tag{3.61}$$

Since the compressibility shall fulfill $\partial\rho/\partial\mu \geq 0$, we can use a bisection algorithm to efficiently find the chemical potential which corresponds to a fixed density. The details are reported in Appendix 3.7. This procedure did not provide a solution for all values of parameters $t/U_0$ and $U_\infty/U_0$ because the compressibility $\partial\rho/\partial\mu$ is not continuous over

the full range of $\mu$ values: we find jumps in the density as a function of the chemical potential, as we discuss in what follows.

Figure 3.6 shows the phase diagram for $\rho = 1/2, 1, 3/2$, and 2. For $\rho = 1/2$ there is no MI phase. Nevertheless, for $U_\infty > 0$, we observe parameter regions where the ground state is in the CDW phase, corresponding to the occupation $\{0, 1\}$ between neighboring sites. For $U_\infty \lesssim 0.1U_0$ CDW and SF are separated by a first order phase transition. This phase boundary is characterized by a discontinuity of the population imbalance, the transition line is at a value of the tunneling rate which scales seemingly linearly with $U_\infty/U_0$ and ends at a tricritical point. After this point the SS phase separates the CDW from the SF phase and the order parameters vary continuously at the transition lines separating SF-SS and SS-CDW. The area enclosed by the dotted lines in the diagram is the parameter region where we could not find any data point, namely, where there is no value of the chemical potential corresponding to $\rho = 1/2$. We denote this region by Phase Separation (PS), after observing that simulations for these values in a canonical ensemble using QMC reported negative compressibility [130] and have been linked to a phase separation between the SF and SS phases [28].

We first notice that this phase diagram coincides with the one reported in Ref. [23], apart from the fact that the authors seem to always find a SS phase separating the CDW and the SF phases, and thus they report neither a direct SF-CDW transition nor a PS region. In particular, all transitions they find for $\rho = 1/2$ are of second order. This difference, and especially the absence of the PS region, might be attributed to different methods for determining the ground state at a fixed density in a grand-canonical ensemble. The authors of Ref. [23] first identify the states at the target density for given $t, U_\infty$, and then search for the lowest-energy state in this set [23, 131]. We remark that the states identified by the treatment used in Ref. [23] do not minimize the energy of the grand-canonical ensemble at the given set of values. In our work, instead, we first determine the states at the lowest energy as a function of $\mu$ for given $t, U_\infty$. In this set of states we then search for the one corresponding to the target density by solving Eq. (3.61). The PS region corresponds to the parameters for which the target density cannot be found. Details of our analysis are reported in Appendix 3.7. It is difficult, though, to figure out what the PS shall describe if one considers the corresponding canonical realization. The global-range interactions, in fact, break the usual paradigm of PS for a short-range interacting (additive [132]) system, where one expects spatial coexistence of regions which are either SS at a given density or CDW at the other stable density: Due to the global range potential the interaction energy between the local phases makes them unstable.

Remarkably, the plot for $\rho = 1/2$ reproduces qualitatively the corresponding diagram obtained with QMC in Ref. [28]. In particular,

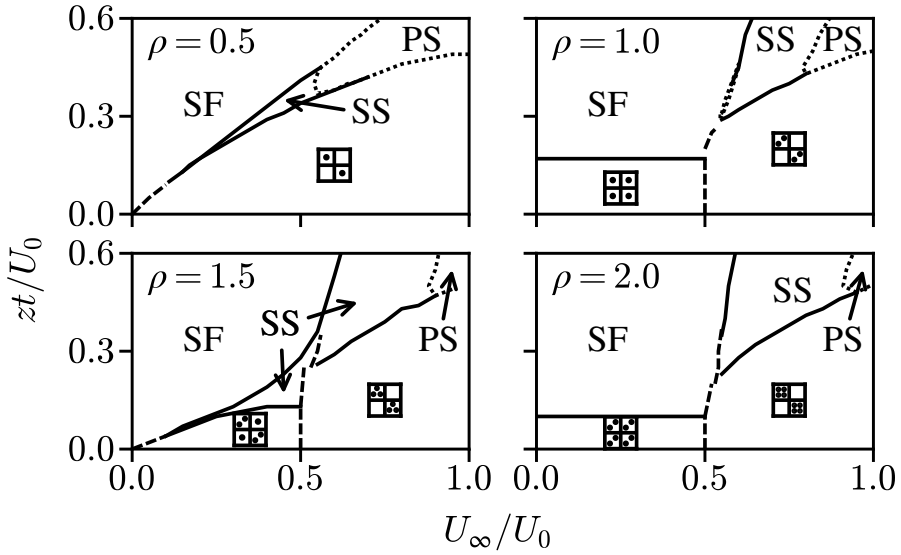


Figure 3.6: Ground state phase diagram as in Fig. 3.3 in the $U_\infty/U_0 - t/U_0$ plane and for fixed density. The subplots correspond to (from left to right) upper panel: $\rho = 1/2$, $\rho = 1$, lower panel: $\rho = 3/2$, $\rho = 2$. See text for details. Dashed (solid) lines at the phase boundaries indicate discontinuous (continuous) variation of the order parameters Dotted lines show the boundary of the PS regions. In the numerical implementation, the cutoff to the site occupation is set at $n_{\max} = 31$ and we took 175 initial guesses. The accuracy in the determination of the mean-field order parameters is $\varepsilon = 10^{-6}$, the precision in the determination of the density is $\varepsilon_\rho = 10^{-4}$. Details regarding the phase diagram at densities $\rho = 0.5$ and $\rho = 1$ are given in Appendix 3.7.

the authors claim to find a direct transition CDW-SF at smaller values of $t/U_0$ (larger values of $U_0/t$), however they cannot determine its nature due to the fact that the QMC simulations are not conclusive in this parameter regime. The salient difference with our result is that the authors do not report stable SS phases for $\rho = 1/2$. This does not exclude, in our view, that a stable SS phase could exist in a small parameter region close to the tricritical point, which might have not been included in the data sampling.

The phase diagrams for $\rho = 1$ and $\rho = 2$ have a similar structure. For both cases the phases are MI, SF, SS, and CDW with maximal population imbalance. The MI-SF and the SS-CDW transitions are continuous. The MI-CDW, instead, is a discontinuous transition. Moreover, for both densities $\rho = 1, 2$ there is a direct, discontinuous transition CDW-SF at $U_\infty \sim 0.5U_0$ which ends at a tricritical point. As $U_\infty/U_0$ is further increased, this transition line splits into two phase boundaries: the SS-CDW and the SF-SS. The SF-SS transition is continuous except for a small region close to the tricritical point. This region corresponds to the parameter regime for which we find no solution of the equation $\rho(\mu/U_0, \tilde{t}, \tilde{U}_\infty) = 1$. In the case of $\rho = 2$, instead, the SF-SS transition

is discontinuous close to the tricritical point. On the other hand, the SS-CDW is a continuous transition until a critical value $U_\infty(t,\rho)$, after which we find a PS region.

The diagram for $\rho = 1$ in Fig. 3.6 is in full agreement with the one reported in Ref. [23], within the parameter intervals considered. Moreover, it also agrees qualitatively with the phase diagram evaluated using QMC [28], apart for two salient features: The authors do not report a PS and the transition line SS-SF is continuous along the whole branch of their phase diagram. We note that the phase diagram at $\rho = 1$ in Fig. 3.6 is similar to the one of Ref. [27], obtained by minimizing the mean-field free energy of a canonical ensemble in a constrained Hilbert space. According to the free energy landscape of Ref. [27], the MI-CDW transition is characterized by a large parameter region where the two phases are metastable.

The phase diagram at $\rho = 3/2$ in Fig. 3.6 exhibits a CDW phase with $\{1,2\}$, separated by a discontinuous transition to the CDW phase with $\{3,0\}$ at $U_\infty = U_0/2$. The CDW $\{1,2\}$ emerges at infinitesimally small tunneling parameters, it has a first-order transition to a SF until a finite value $U_\infty < U_0/2$. This CDW$\{1,2\}$-SF phase boundary ends at a tricritical point, after which SF and CDW are separated by a SS phase. The transition SF-SS is continuous in the whole parameter range. On the other hand, SS-CDW$\{3,0\}$ transition, becomes discontinuous for a small interval of values about $U_\infty \sim 0.5U_0$. Within the SS phase, moreover, there is a discontinuous transition at $U_\infty = U_0/2$ where the population imbalance undergoes a jump from $|\theta| \approx 1$ to $|\theta| \approx 3$. This jump was reported also in Ref. [23]. Instead, QMC studies found it to be a crossover [28]. Moreover the direct transition between SF and CDW $\{1,2\}$ seems to not have been found by static mean-field calculations in Ref. [23]. QMC simulations [28] here reported this direct transition, however they could not determine its order. Finally, we notice a region for strong long-range interaction and large tunneling where no solution exists and which was not reported by static mean-field calculations [23].

We note that the phase diagram for $\rho = 1/2$ is similar to that of the extended Bose-Hubbard model with repulsive nearest neighbor interaction: For nearest-neighbor interactions and small tunneling rates Quantum Monte Carlo simulations report no stable SS phase but a direct transition CDW-SF [30, 109, 130], which is found to be of first order [30, 130]. Furthermore in the intermediate tunneling regime a SF-SS and SS-CDW transition is observed [110, 112]. For $\rho = 1$, in the extended Bose-Hubbard model with repulsive nearest neighbor interaction and small tunneling rates there is a MI-CDW transition [109, 112], while the author of ref. [112] finds a SF-CDW transition for an intermediate tunneling rate $zt = 0.3U_0$, and SF-SS and SS-CDW transitions for a very large tunneling rate $zt = U_0$. However, no PS at $\rho = 1$ and $\rho = 1/2$ is reported in Refs. [110, 112].

### 3.3.5 *Conclusions*

We have performed a mean-field analysis of the phase diagram of the extended Bose-Hubbard model, where the bosons have a repulsive contact interaction and experience an infinitely long-range two-body potential. The systematic comparison between the phase diagram obtained for the cavity Bose-Hubbard model and the one for repulsively interacting dipolar gases in two dimensions shows clear differences already within the mean-field treatment, such as for instance the direct first-order transition CDW-MI at a critical value of the chemical potential, that is absent for the dipolar case. The ground- state phase diagram we calculate mostly agrees with the static mean-field diagram of Ref. [23]. There are two important differences: differing from Ref. [23], for the density $\rho = 1/2$ and $\rho = 3/2$ we predict a direct transition between Superfluid (SF) and Charge-Density Wave (CDW), which is first order for the densities we considered. Moreover, in the region where the authors of Ref. [23] predict stable lattice supersolid (SS) phases, we find also regions where instead there is a Phase Separation (PS). We attribute these discrepancies to different methods for determining the ground state at fixed density from the grand-canonical ensemble calculations. We note that the PS regions correspond to a first order transition in our mean-field description: At sufficiently large strength of the all-connected potential the second-order transition SS-CDW turns into first order. This seems to be a common feature of phase transitions emerging from the competition between a short-range and a strong long-range potential [122, 133].

The stability of the SS phase has been extensively analysed by means of Quantum Monte Carlo methods for a canonical and a grand-canonical ensemble in Ref. [28]. Our diagrams and the diagrams of Ref. [23] at fixed densities, extracted from grand-canonical ensemble calculations, are in remarkable qualitative agreement with the QMC diagrams in the interval of parameters where the QMC diagram have been determined. The discrepancies regard the stability of the SS regions at fixed densities. These discrepancies could be due to the fact that the QMC collected data did not sample the regions where these differences are found (as one could conjecture by taking the parameters reported in Ref. [28] for which the stability of the SS phase was analysed and mapping them into our phase diagram). Most probably, the discrepancy arises from the fact that our static mean-field approach cannot appropriately take into account the interplay between strong long-range interactions and quantum fluctuations.

Future work shall focus on the phase separation parameter region in the presence of spatial inhomogeneities, such as when the atoms are also confined by a shallow a harmonic trap. Previous studies showed, in fact, that the interplay between the trap inhomogeneity

and cavity-mediated long-range interaction can give rise to new phases [134].

## 3.4 CAVITY-MEDIATED CORRELATED TUNNELLING: MEAN-FIELD STUDY

In the previous section we neglected the hopping terms due to the cavity-induced potential. This assumption is justified for a certain geometries, where the maxima of the cavity field intensity coincide with the minima of the optical lattice. This dynamics is different when the opposite situation is realized, namely the minima of the optical lattice are at the nodes of the cavity standing wave field. This situation is described in our model by setting the phase shift between the lattice and the cavity mode to $\phi = \pi/2$ in Eq. (3.12). The effect in the extended Bose-Hubbard model is a global correlated tunnelling term. The corresponding one-dimensional model was first studied in [36] for small chains and by exact diagonalization. Here we determine the ground state for infinite long chains using mean-field. In doing so we take the dependence of the coefficients from the setup parameters of Ref. [43, 44, 135] into account.

This section is structured as follows: We first introduce the one-dimensional extended Bose-Hubbard Hamiltonian. We then discuss the dependence of its coefficient on the phase $\phi$ between lattice and cavity mode. We apply a Gutzwiller mean-field ansatz and present the corresponding ground-state phase diagrams in the $U_1$-$t$ plane for different values of $\phi$. We then compare our results with the predictions of Ref. [36], where the phases of small chains were numerically analyzed.

### 3.4.1 *One-dimensional extended Bose-Hubbard Hamiltonian*

In the rest of this thesis we consider the system of Sec. 3.2 and assume that the atomic motion along the $y$ axis is frozen out. This can be achieved by taking the static optical lattice height along the $y$ direction sufficiently high. The corresponding one-dimensional extended Bose-Hubbard Hamiltonian is then given by [36, 37]

$$\hat{H}^{\mathrm{1D,BH}}_{\mathrm{Cavity}} = \hat{H}^{(0)}_{BH} + \hat{H}^{\mathrm{1D,BH}}_{\mathrm{LR}} \ . \tag{3.62}$$

It consists of the standard Bose-Hubbard Hamiltonian in Eq. (1.51) and the long-range part resulting from the atom-cavity coupling, which is given in 1D by [36, 37]

$$\hat{H}^{\mathrm{1D,BH}}_{\mathrm{LR}} = \frac{U_1}{N_L}\left(z^2\hat{D}^2 + zy\left(\hat{D}\hat{B} + \hat{B}\hat{D}\right) + y^2\hat{B}^2\right) \ . \tag{3.63}$$

The one-dimensional imbalance operator can now be written as

$$\hat{D} = \sum_{j=1}^{N_L} (-1)^j \hat{n}_j \quad , \tag{3.64}$$

where $j$ indicates the lattice site along the chain, while the one-dimensional tunnelling operator has the form

$$\hat{B} = \sum_{j=1}^{N_L-1} (-1)^j \left( \hat{a}_j^\dagger \hat{a}_{j+1} + h.c. \right) \quad . \tag{3.65}$$

The $z$ and $y$ coefficients in Eq. (3.63) are the one-dimensional overlap integrals along the $x$-axis of the cavity mode function $h(x) = \cos(kx + \phi)$ and the Wannier function $w_j(x)$:

$$\begin{aligned} z &= \int_0^{aN_L} dx \; w_j(x)^2 \cos(k_L x + \phi) \\ y &= \int_0^{aN_L} dx \; w_j(x) w_{j+1}(x) \cos(k_L x + \phi) \; . \end{aligned} \tag{3.66}$$

In the following we will discuss the dependence of the overlap integrals in Eq. (3.66) as a function of the parameter $\phi$, i.e. the phase shift between static optical lattice and the cavity mode standing wave.

#### 3.4.1.1 *Bose-Hubbard coefficients*

The dependence of the overlap integrals $z, y$ on $\phi$ is shown in Fig. 3.7 for different values of $\phi$. One observes that the $y$ overlap integral is larger than $z$ for the phase shift $\phi = \pi/2$, while for $\phi = 0$ the $z$ coefficient is dominating. Moreover for $\phi = \pi/4$ $y$ decreases with increasing lattice depth $V_0$, while $z$ is almost independent of the lattice depth $V_0$.

#### 3.4.1.2 *Observables*

In the following we introduce the observables we use in order to reveal the different phases of Eq. (3.62). The off-diagonal long-range order can be signaled by the Fourier transform of the single-particle correlations, i.e. the single-particle structure factor

$$M_1(k) = \frac{1}{N_L^2} \sum_{i,j} e^{ik(i-j)} \left\langle \hat{a}_i^\dagger \hat{a}_j \right\rangle \; , \tag{3.67}$$

which can be experimentally revealed by means of time-of-flight measurements [7]. For a finite value of $M_1(k)$ at $k = 0$ in the thermodynamic limit the state is superfluid (SF), whereas for $M_1(k)$ going to zero for all $k$ in the thermodynamic limit the state is in a Mott insulator (MI). As elaborated in the previous subsection the density-density

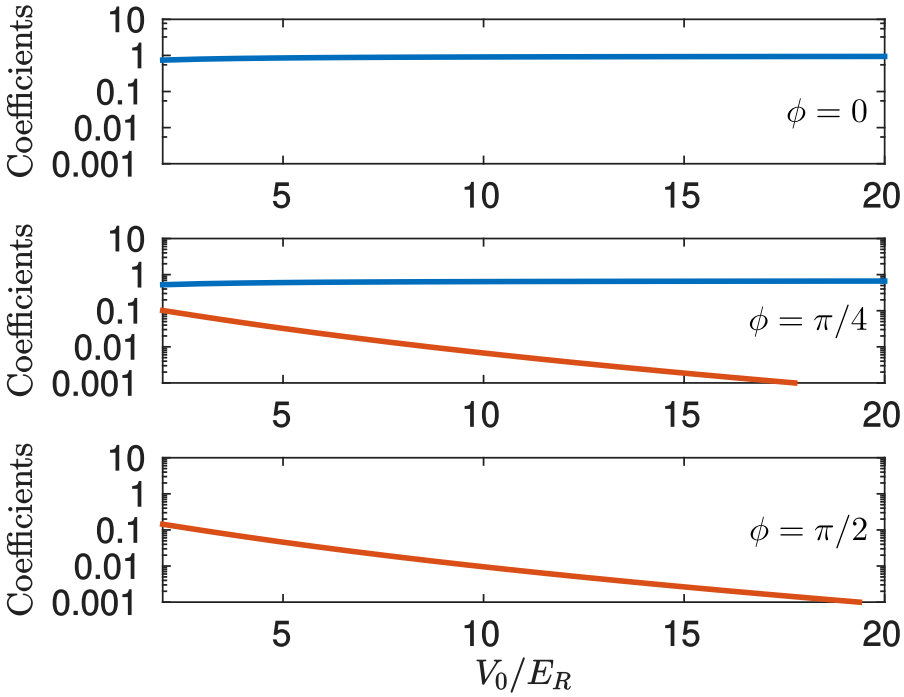


Figure 3.7: The coefficients $z$ (blue) and $y$ (orange) (see Eq. (3.11)) as a function of the lattice depth $V_0/E_R$ for $\phi = 0$, $\phi = \pi/4$, and $\phi = \pi/2$. For $\phi = 0$ and $\phi = \pi/2$ one of the overlap integrals is smaller than $10^{-3}$ and thus not visible.

interaction leads to density modulated phases. In 1D it is signaled by the order parameter

$$\mathcal{O}_D = \frac{1}{N_L} \left| \langle \hat{D} \rangle \right| \quad , \tag{3.68}$$

which is essentially the expectation value of the operator $\hat{D}$ of Eq. (3.64). A state showing a finite value of $M_1(k)$ at $k = 0$ and $\mathcal{O}_D \neq 0$ is called supersolid (SS), which has conducting character like the superfluid. For $M_1(k) = 0$ for all $k$ in the thermodynamic limit the state is in the insulating charge density wave (CDW).

The global correlated tunnelling in Eq. (3.62) leads to states consisting out of dimers along the lattice [36]. In the literature a state of this form is called dimerised or bond ordered state [36, 136, 137]. Here the bond order can be revealed by a finite expectation value of the $\hat{B}$ operator in Eq. (3.65). Thus we define the bond order parameter as

$$\mathcal{O}_B = - \langle \hat{B} \rangle / (2N_L) \, . \tag{3.69}$$

A state showing $\mathcal{O}_B \neq 0$ and $M_1(k) = 0$ for all $k$ is called bond insulator (BI). The BI shares similarities with the valence bond solid (VBS) of a spin chain [137]. Instead, a state with $\mathcal{O}_B \neq 0$ and maxima of $M_1(k)$ at $k = \pm\pi/2$ is in a bond superfluid (BSF). The BSF phase is similar to the resonating-valence-bond state (RVB), which is a gapless

| Phase | Acronyms | $\mathcal{O}_D$ | $\mathcal{O}_B$ | $M_1(k)$ |
|---|---|---|---|---|
| Mott-Insulator | MI | $= 0$ | $= 0$ | $= 0\ \forall k$ |
| Density Wave | CDW | $\neq 0$ | $= 0$ | $= 0\ \forall k$ |
| Bond Insulator | BI | $= 0$ | $\neq 0$ | $= 0\ \forall k$ |
| Superfluid | SF | $= 0$ | $= 0$ | $k_{\max} = 0$ |
| Supersolid | SS | $\neq 0$ | $= 0$ | $k_{\max} = 0$ |
| Bond Superfluid | BSF | $= 0$ | $\neq 0$ | $k_{\max} = \pm\pi/2$ |
| Bond Supersolid | BSS | $\neq 0$ | $\neq 0$ | $k_{\max} = \pm\pi/2$ |

Table 3.1: Table of the phases, of their acronyms, and of the corresponding values of the order parameters.

state with dimerised structure [138]. A superfluid showing both $\mathcal{O}_D \neq 0$ and $\mathcal{O}_B \neq 0$ is here denoted by bond supersolid (BSS).

The order parameter $\mathcal{O}_D$, Eq. (3.68), and $\mathcal{O}_B$, Eq. (3.68), can be revealed by the light at the cavity output [43, 139].

In Table 3.1 we summarize the phases and their corresponding order parameters.

### 3.4.2 *Ground-state phase diagram*

In this subsection we make use of the Gutzwiller mean-field ansatz introduced in Eq. (1.78) to find the ground state in the canonical ensemble and in 1D. Note that mean-field approaches do not capture the quantum correlations over the whole lattice, which are particularly important in 1D [6, 50]. Therefore we expect the mean-field approach to fail in certain parameter regions. Nevertheless the Gutzwiller mean-field approach can still provide insight on the impact of the interaction induced correlated tunnelling on the ground state properties. Below, we calculate the phase diagrams as a function of the single-particle tunnelling rate and the long-range interaction strength. We provide data for three different values of $\phi$ leading to different terms in the extended Bose-Hubbard Hamiltonian (3.62). We then compare our results with the ones for small system sizes reported in Ref. [36].

#### 3.4.2.1 *Extended Gutzwiller mean-field approach*

We use the Gutzwiller ansatz $|\Psi\rangle$ given in Eq. (1.78) to evaluate the energy expectation value $E_{MF} = \left\langle \Psi | \hat{H}^{1D,BH}_{Cavity} | \Psi \right\rangle$ with $\hat{H}^{1D,BH}_{Cavity}$ in Eq.

(3.62). We hereby truncate the local Hilbertspace by demanding the local states $|\psi\rangle_j$ to have the form [52]

$$|\psi\rangle_j = c(n_j-1)_j\,|n_j-1\rangle_j + c(n_j+1)_j\,|n_j+1\rangle_j + c(n)_j\,|n_j\rangle_j \ . \tag{3.70}$$

The coefficient are chosen to be [52]

$$\begin{aligned} c(n_j-1)_j &= \cos(\theta_j)\sin(\chi_j)e^{i\phi_j} \\ c(n_j)_j &= \cos(\chi_j) \\ c(n_j+1)_j &= \sin(\theta_j)\sin(\chi_j)e^{i\phi_j} \end{aligned}$$

with $\chi_j, \theta_j \in [0, \pi/2]$, $\phi_j \in [0, 2\pi]$ and $n_j \in \mathbb{N}$. This form ensures the normalization of the Gutzwiller wave function. Note that this ansatz does not capture the BI phase. Using these approximations and considerations the mean-field energy takes the form

$$E_{MF} = -t\sum_{j=1}^{N_L-1} T_j^{MF} + \frac{U}{2}\sum_{j=1}^{N_L} U_j^{MF} + \frac{U_1}{N}\left(D_{MF}^2 + 2B_{MF}D_{MF} + B_{MF}^2\right) \ .$$

The first term is the mean-field single-particle tunnelling term

$$\begin{aligned} T_j^{MF} =& 2\sin(\chi_j)\sin(\chi_{j+1})\cos(\chi_j)\cos(\chi_{j+1})\times \\ &\times\left(F\cos(\Delta_{+,j}) + G\cos(\Delta_{-,j})\right) \end{aligned}$$

with

$$\begin{aligned} F =& \cos(\theta_j)\sin(\theta_{j+1})\sqrt{n_j}\sqrt{n_{j+1}+1} \\ &+ \cos(\theta_{j+1})\sin(\theta_j)\sqrt{n_j+1}\sqrt{n_{j+1}} \end{aligned}$$

and

$$\begin{aligned} G =& \cos(\theta_j)\cos(\theta_{j+1})\sqrt{n_j n_{j+1}} \\ &+ \sin(\theta_j)\sin(\theta_{j+1})\sqrt{(n_j+1)(n_{j+1}+1)} \ . \end{aligned}$$

We will argue that the variables

$$\Delta_{+,j} = \phi_j + \phi_{j+1}$$

and

$$\Delta_{-,j} = \phi_j - \phi_{j+1}$$

are actually the mean-field order parameters for dimerised states. The onsite interaction in mean-field is given by

$$U_j^{MF} = m_j^{MF} - n_j^{MF} \ .$$

Here the expectation value of the occupation operator per site has the form

$$n_j^{\mathrm{MF}} = n_j - \sin(\chi_j)^2\cos(2\theta_j)$$

and the expectation value of the occupation operator squared is

$$m_j^{\mathrm{MF}} = n_j^2 + 2n_j(1-2\cos(\theta_j)^2)\sin(\chi_j)^2 + \sin(\chi_j)^2 \quad .$$

The cavity induced terms now read

$$B_{MF} = \sum_{j=1}^{N_L} y_j^\alpha T_j^{MF} \tag{3.71}$$

and

$$D_{MF} = \sum_{j=1}^{N_L} z_j^\alpha n_j^{\mathrm{MF}} \, . \tag{3.72}$$

Here the coefficients $y_j^\alpha$ and $z_j^\alpha$ are the overlap integrals in Eq. (3.10). By fixing the value of $\alpha$ to unity and assuming two-site translational invariance we obtain the mean-field energy per site

$$\begin{aligned} E_{\mathrm{MF}}^{\alpha=1}/N_L = &-\frac{t}{2}\left(T_e^{MF}+T_o^{MF}\right) + \frac{U}{4}\left(U_e^{MF}+U_o^{MF}\right) \\ &+ \frac{U_1}{N_L^2}\left(z^2 D_{MF}^2 + 2zyB_{MF}D_{MF} + y^2 B_{MF}^2\right) \end{aligned} \tag{3.73}$$

with $T_j^{MF} = T_e^{MF}(U_j^{MF} = U_e^{MF})$ for $j$ even and $T_j^{MF} = T_o^{MF}$ $(U_j^{MF} = U_o^{MF})$ for $j$ odd. The cavity induced mean fields transform to

$$B_{MF} = \frac{N_L}{2}\left(T_e^{MF} - T_o^{MF}\right) \tag{3.74}$$

and

$$D_{MF} = \frac{N_L}{2}\left(n_e^{MF} - n_o^{MF}\right) \, . \tag{3.75}$$

Since we consider a canonical ensemble, we fix the density over the whole phase diagram. Thus,

$$\rho = \frac{1}{2}(n_e+n_o) - \frac{1}{2}\sin(\chi_e)^2\cos(2\theta_e) - \frac{1}{2}\sin(\chi_o)^2\cos(2\theta_o) = \text{const.} \tag{3.76}$$

#### 3.4.2.2 *Mean field order parameter*

In order to find the ground state we numerically determine the values of the set $(\chi_j, n_j, \Delta_j^+, \Delta_j^-, \theta_j)$, that minimize the mean-field energy in Eq. (3.73) with the constrain of keeping the density fixed to a certain value $\rho$. The set $(\chi_j, n_j, \Delta_j^+, \Delta_j^-, \theta_j)$ defines the form of the Gutzwiller ground state and thus its properties. In the following we will discuss the mean-field order parameters used to identify the different ground state phases along the phase diagram.

For $\chi_j = 0$ the Gutzwiller wave function $|\Psi\rangle$ (1.78) reduces to the state in Eq. (1.55), where $n_j = \rho$ for the even as well as for the odd

sites. Thus for $\chi_j = 0$ and $n_j = \rho$ we associate the MI phase to the state minimizing the mean-field energy $E_{MF}$ in Eq. (3.73). If the energy is minimized for a $\chi_j \neq 0$, we consider the corresponding state to be SF. In fact the Gutzwiller mean-field state for a finite $\chi_j$ shows fluctuations in the occupation number and thus the expectation value of the annihilation operator $\hat{a}_j$, hence the SF order parameter of mean-field is finite.

Depending on the value of $\Delta_j^+$ and $\Delta_j^-$ the nearest neighbor off-diagonal correlations of the Gutzwiller state will be different. For instance, for $\Delta_j^+ = \Delta_j^- = 0$ we get $\left\langle \hat{a}_j^\dagger \hat{a}_{j+1} \right\rangle > 0$, whereas for $\Delta_j^+ = \Delta_j^- = \pi$ we get $\left\langle \hat{a}_j^\dagger \hat{a}_{j+1} \right\rangle < 0$. This state is a staggered superfluid (SSF) (see also Fig. 2.11). For $n_e \neq n_o$ the mean occupation $n_e^{MF}$ on the even sites will be different to the occupation on the odd sites $n_o^{MF}$. This is also signaled by a finite value of the density-wave order parameter defined in Eq. (3.21), which is used in the local mean-field analysis to identify the density modulated phases.

If the ground state has a finite $\chi_j$ on the even and odd sites and $n_e \neq n_o$, then the phase is SS. For $\chi_j = 0$, the state with $n_e \neq n_o$ is a CDW.

In the Gutzwiller mean-field approach the bond order parameter in Eq. (3.69) takes the form $\mathcal{O}_B^{MF} = -B_{MF}/2N_L$ with $B_{MF}$ in Eq. (3.74). It possesses a finite value for $\Delta_e^+ = \Delta_e^- = 0$ and $\Delta_o^+ = \Delta_o^- = \pi$ (or $\Delta_e^+ = \Delta_e^- = \pi$ and $\Delta_o^+ = \Delta_o^- = 0$). Thus we associate the ground states with $\Delta_e^+ = \Delta_e^- = 0$ and $\Delta_o^+ = \Delta_o^- = \pi$ (or $\Delta_e^+ = \Delta_e^- = \pi$ and $\Delta_o^+ = \Delta_o^- = 0$) to a bond ordered phase. A superfluid phase, i.e. state with $\chi_j \neq 0$, showing a finite value of the bond order parameter $\mathcal{O}_B^{MF}$ will be called BSF.

We note that within our approach we can not detect the bond insulator. This could be revealed by extending our formalism and use the CGMF, see 1.3.3.2.

The expected phases and the corresponding values of the order parameters are summarized in Table 3.2.

#### 3.4.2.3 *Phase diagrams for different densities*

We now discuss the phase diagram for two different densities $\rho = 1/2$ and $\rho = 1$. The coefficients of the long-range Bose-Hubbard Hamiltonian in Eq. (3.4) are calculated numerically by evaluating the overlap integrals using the Wannier function of the lowest band in the static optical lattice. Thereby we choose the same axial trap parameter as for the extended Bose-Hubbard model in Subsec. 2.2.1. Moreover we fix the lattice depth to $V_0 = 4E_R$, while $\phi$ will be different in the following phase diagrams. In particular we consider three different phase shifts $\phi = 0$, $\phi = \pi/4$ and $\phi = \pi/2$: For $\phi = 0$ the value of the overlap integrals are given by $z = 0.8279$ and $y \sim 10^{-17}$. Therefore due to the machine precision $y = 0$. Choosing $\phi = \pi/2$ one gets

| Phase | $\chi_j$ | $n_j$ | $\Delta_e^+$ | $\Delta_e^-$ | $\Delta_o^+$ | $\Delta_o^-$ |
|---|---|---|---|---|---|---|
| Mott-Insulator (MI) | $= 0$ | $\rho$ | $-$ | $-$ | $-$ | $-$ |
| Density Wave (CDW) | $= 0$ | $n_e \neq n_o$ | $-$ | $-$ | $-$ | $-$ |
| Superfluid (SF) | $\neq 0$ | $\rho$ | $= 0$ | $= 0$ | $= 0$ | $= 0$ |
| Supersolid (SS) | $\neq 0$ | $n_e \neq n_o$ | $= 0$ | $= 0$ | $= 0$ | $= 0$ |
| Bond Superfluid (BSF) | $\neq 0$ | $\rho$ | $= 0$ $(= \pi)$ | $= 0$ $(= \pi)$ | $= \pi$ $(= 0)$ | $= \pi$ $(= 0)$ |
| Bond Supersolid (BSS) | $\neq 0$ | $n_e \neq n_o$ | $= 0$ $(= \pi)$ | $= 0$ $(= \pi)$ | $= \pi$ $(= 0)$ | $= \pi$ $(= 0)$ |

Table 3.2: Table of the phases, of their acronyms, and of the corresponding values of the mean-field order parameters.

$z = 0$, within the precision of the machine, and $y = -0.0658$. Here we only consider the interaction induced tunnelling and discard the density-density interaction. Setting $\phi = \pi/4$ the overlap integrals are given by $z = 0.5854$ and $y = -0.0465$ and we expect to observe an interplay between density-density potential and correlated tunnelling.

Note that we fix the lattice depth and thus we tune the ratio between the single-particle tunnelling rate and the onsite interaction strength by changing the s-wave scattering length.

*Unit density*

Fig. 3.8 shows the phase diagrams as a function of long-range interaction strength and the single-particle tunnelling rate in units of $U$ for a unit density and different values of $\phi$. For $\phi = 0$ the ground-state phase diagram is depicted in Fig. 3.8(a). Here we observe insulating phases for small $t/U$. The transition between the MI and CDW phase occurs at $z^2 U_1/U = -1/2$, that agrees with the analytic result in the atomic limit (see Subsec. 3.3.3). By increasing the tunnelling rate, a direct phase transition between MI and SF will take place. For negative values of the long-range interaction strength we observe a transition from a CDW phase via a SS phase to a SF phase.

Fig. 3.8(b) shows the phase diagram for $\phi = \pi/2$, where $z \approx 0$. Here we observe a BSF phase at negative $U_1$.

In Fig. 3.8(c) the value of $\phi$ is set to $\pi/4$, and all terms in the long-range Hamiltonian in Eq. (3.62) are relevant. For negative long-range interaction strength the ground state exhibit an imbalance in the occupations of neighboring sites as well as bond order in the off-diagonal correlations. Here we observe a transition from a BSS via a SS to a SF phase. For $U_1 > 0$ the cavity field is zero and the ground state is determined by the standard Bose-Hubbard model, where the ratio $t/U$ controls the transition from MI to SF.

*Density one half*

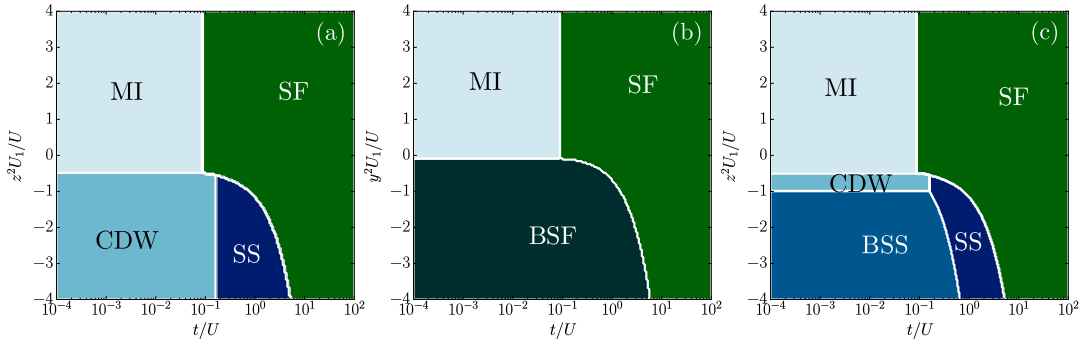


Figure 3.8: Phase diagrams of the Hamiltonian, (3.62), as a function of the cavity interaction strength $U_1$ in units of $U/z^2$ or $U/y^2$ and the tunnelling rate $t$ in units of $U$. In (a) $\phi = 0$, (b) $\phi = \pi/2$ and (c) $\phi = \pi/4$. The lattice depth is fixed to $V_0 = 4E_R$. The phases are labeled according to the Table 3.2. We consider here a canonical ensemble with density of $\rho = 1$.

For half integer density the situation is different. First of all in the absence of the cavity the phase is always SF. This is the case for $U_1 > 0$ in Fig. 3.9. The salient differences between different choices of $\phi$ became visible for $U_1 < 0$, when the cavity field terms favour the formation of patterns.

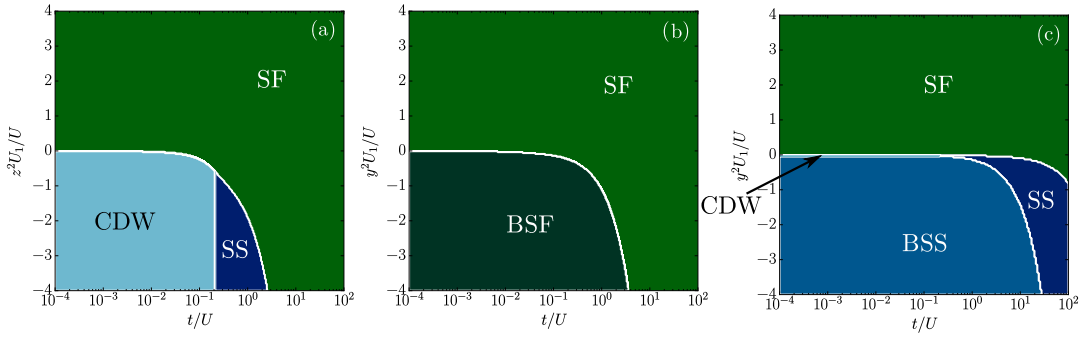


Figure 3.9: Phase diagrams of the Hamiltonian, (3.62), as a function of the cavity interaction strength $U_1$ in units of $U/z^2$ or $U/y^2$ and the tunnelling rate $t$ in units of $U$. We set the phase shift to $\phi = 0$ (a), $\phi = \pi/2$ (b) and $\phi = \pi/4$ (c). The lattice depth is fixed to $V_0 = 4E_R$. The phases are labeled according to the Table 3.2. We consider here a canonical ensemble with density of $\rho = 1/2$.

In Fig. 3.9(b) for $\phi = \pi/2$ a BSF to SF phase transition can be observed as a function of $t/U$. In Fig. 3.9(c) for $\phi = \pi/4$ we identify a small CDW region separating the MI from the BSS phase. For larger negative values of $y^2U_1/U$ a direct BSS-SS phase transition is occurs.

A comparison with the grand-canonical 2D phase diagram of Eq. (3.19) for $\phi = 0$ (see Sec. 3.3) reveals a good agreement between the canonical phase diagram, Fig. 3.8 and 3.9, and the grand-canonical 2D phase diagram, Fig. 3.6, for $\rho = 1/2$ and $\rho = 1$. Nevertheless the local mean-field predicts a phase separation region for large values

of $U_1$ and large tunnelling rates $t$. This phase separation can not be captured with our Gutzwiller mean-field analysis, since we consider a canonical ensemble and assume two site translation invariance.

For $\rho = 1$ and $\phi = 0$, Fig. 3.8(a), a similar phase diagram was reported in Ref. [36]. In contrast to our study the authors in Ref. [36] identified the phase transition at $z^2U_1/U \approx 1$ in the atomic limit. Moreover at half filling the authors in Ref. [36] reported insulating phases for positive $U_1$, while in our case these regions are solely superfluid. The authors of Ref. [36] identified a BI region with an imbalance in the occupation in a large parameter range of $y^2U_1/U$. We believe this is incorrect and due to the fact that the authors take the average of the nearest-neighbor off-diagonal correlations as SF order parameter. This property is not a sufficient signature for identifying an insulator: In fact this observable vanishes in the BSF phase. In the BSF phase, however the nearest-neighbor off-diagonal correlations do not vanish. Actually here one gets $\left\langle \hat{a}_j^\dagger \hat{a}_{j+1} \right\rangle > 0$ and $\left\langle \hat{a}_{j'}^\dagger \hat{a}_{j'+1} \right\rangle < 0$ for $j$ even (odd) and $j'$ odd (even). By means of $M_1(k)$, Eq. (3.67), we can capture these correlations and unveil that the phase is BSF.

In Ref. [36] a transition from CDW to a so-called SF dimer (SFD) phase was reported. This phase is characterized by a finite value of the average nearest-neighbor off-diagonal correlations and a finite bond order parameter. It might be that the presence of a SFD in the ground-state phase diagram is due to the small system sizes chosen in Ref. [36]. We note that the SFD is an excited state in our Gutzwiller mean-field analysis.

Note that the bond ordered phases are also present in other systems like for instance in a zig-zag optical lattice in presence of a density-dependent gauge field [140], in a spin-1/2 dipolar fermi gas in a lattice potential [141] and in a honeycomb lattice with anisotropic tunnelling [136]. In contrast to those models here the bond order is self-induced due to the cavity-atom coupling [36].

### 3.4.3 *Conclusions*

Including the cavity induced correlated tunnelling leads to phases possessing bond order analogous to valence bond solids in spin systems [137]. The bond order emerges due to the interference between the single-particle tunnelling and the cavity induced correlated hopping. We performed a Gutzwiller mean-field study and compared the results to an exact diagonalization study for small system sizes on the same model [36]. Within this comparison we identified discrepancies, which we conjecture to appear due to two main points: First the authors in Ref. [36] identified a phase in the ground-state phase diagram, which does not occur as a ground state in our Gutzwiller mean-field approach. A reason for this discrepancy might be the different system sizes considered in both approaches. Moreover, our

mean-field ansatz can not capture phases such as the bond insulator phase. In the next section we use a density matrix renormalization group (DMRG) approach in order to clarify the nature of the phases beyond mean-field.

## 3.5 SELF-ORGANISED TOPOLOGICAL INSULATOR DUE TO CAVITY-MEDIATED CORRELATED TUNNELLING

Manifestation of topology in physics [142, 143] created a revolution which is continuing for almost four decades. With the discovery of topological materials, condensed matter physics has gained a new terrain where quantum phases of matter are no longer controlled by local order parameters as in paradigmatic Landau theory of phase transitions but rather by the conservation of certain global symmetries [98]. These new phases of matter, so called symmetry-protected topological (SPT) phases, display edge and surface states depending on the dimensionality that can be robust against perturbations, making them interesting candidates for quantum computing [144].

To date, a detailed understanding of noninteracting topological materials has been obtained through a successful classification based on fundamental symmetry classes, the so-called "ten-fold way" [97, 145, 146]. On the other hand, interactions are almost unavoidable in many-body systems. It is therefore a central issue to understand whether SPT phases can survive the inter-particle interactions, or perhaps whether interactions themselves might stabilize SPT phases and even give rise to novel topological properties [147–154]. These questions are at the center of an active and growing area of research [155, 156]. Recent works have argued that the range of interactions plays a crucial role on the existence of SPT phases. Specifically, in frustrated antiferromagnetic spin-1 chain with power-law decaying $1/r^{\alpha}$ interactions, topological phases are expected to survive at any positive value of $\alpha$ [157]. This behaviour shares similarities with the topological properties of noninteracting Kitaev p-wave superconductors [158] that are robust against long-range tunnelling and pairing couplings [159–162]. It was found that for infinite-range interactions the one-dimensional Kitaev chain can exhibit edge modes for appropriate boundary conditions [163]. On the other hand, in spin chains and Hubbard models, the infinite-range interactions suppress the onset of hidden order at the basis of the Haldane topological insulator [164, 165].

In the following we study the phases of the all-connected Bose-Hubbard model of Eq. (3.62) for a phase shift $\phi = \pi/2$ using a Density Matrix Renormalization Group (DMRG) approach. We report a novel mechanism where nontrivial topology emerges from the quantum interference between infinite-range interactions and single-particle dynamics. We identify the conditions under which this coupling spontaneously breaks the discrete lattice translational symmetry and leads to the emergence of non-trivial edge states at half-filling. The topology we report shares analogies with the recent studies of symmetry breaking topological insulators [152–154, 166]. Nevertheless, differing from previous realizations, here the interference between quantum fluctua-

tions and global interactions is essential for the onset of the topological phase and can not be captured by our mean-field approach.

In this section we first review the one-dimensional extended Bose-Hubbard Hamiltonian (3.62) in the limit $\phi = \pi/2$ and discuss its corresponding mean-field Bose-Hubbard model. The mean-field model is reminiscent of the so-called Su-Schrieffer-Heeger (SSH) model [123, 167], which we will introduce in the second subsection. In the last subsection we then study the ground-state phase diagram for a density of one half using DMRG. In particular we inspect the topological non-trivial phase induced by the atom-cavity coupling.

### 3.5.1 *Mean-field considerations*

We consider a specific limit of the extended Bose-Hubbard Hamiltonian in Eq. (3.62), where we set $\phi = \pi/2$ in the overlap integrals (3.66). For this value of $\phi$ the overlap integral $z$ in Eq. (3.66) is zero (see Fig. 3.7) and the only remaining part in the long-range Hamiltonian (3.63) is the one scaling with $y^2$. Thus the extended Bose-Hubbard Hamiltonian in Eq. (3.62) reduces to

$$\hat{H}^{\text{1DBH}}_{\text{Cavity}}(\phi = \pi/2) = -t \sum_{j=1}^{N_L-1} \left(\hat{a}_j^\dagger \hat{a}_{j+1} + h.c.\right) + \frac{U}{2} \sum_{j=1}^{N_L} \hat{n}_j \left(\hat{n}_j - 1\right) + \frac{U_1}{N_L} y^2 \hat{B}^2 \,. \tag{3.77}$$

Here $t$ is the single-particle tunnelling rate, which scales the kinetic energy of the system. The positive coefficient $U$ scales the interaction energy due to the s-wave scattering among the atoms. The last part is due to the cavity-mediated interaction.

In order to study the interplay between the interaction induced and the single-particle tunnelling we combine those tunnelling terms into an effective tunnelling

$$\hat{\mathcal{T}}_{eff} = -\sum_{j=1}^{N_L-1} \left(t - \frac{U_1 y^2}{N_L}(-1)^j \hat{B}\right) \left(\hat{a}_j^\dagger \hat{a}_{j+1} + h.c.\right) \,. \tag{3.78}$$

To gain further insight we separate the operator $\hat{B}$ into its mean-field $\mathcal{B}_{MF}$ and its quantum fluctuations $\delta\hat{B}$, i.e. $\hat{B} = \mathcal{B}_{MF} + \delta\hat{B}$. Inserting the operator into the effective tunnelling and neglecting its fluctuations of second order, one gets

$$\hat{\mathcal{T}}^{MF}_{eff} \simeq -\sum_{j=1}^{N_L-1} \left(t - \frac{2U_1 y^2}{N_L}(-1)^j \mathcal{B}_{MF}\right) \left(\hat{a}_j^\dagger \hat{a}_{j+1} + h.c.\right) - \frac{U_1 y^2}{N_L} \mathcal{B}^2_{MF} \,. \tag{3.79}$$

For $\mathcal{B}_{MF} \neq 0$ the last term leads to an energy shift and we can hence neglect this term in the following discussion. This leads to

$$\hat{\mathcal{T}}_{eff}^{MF} \simeq -t_e \sum_j{}' \left(\hat{a}_j^\dagger \hat{a}_{j+1} + h.c.\right) - t_o \sum_j{}' \left(\hat{a}_j^\dagger \hat{a}_{j+1} + h.c.\right) \ , \tag{3.80}$$

where the first sum runs over all the even sites in the lattice, i.e. $j = 2i$ with $i \in \mathbb{N}$, and the second sum over all the odd sites in the lattice, i.e. $j = 2i + 1$ with $i \in \mathbb{N}$. While for the dipolar case the mean-field effective tunnelling rate is the same on every site, the staggered behaviour of the hopping term $\hat{B}$ leads to different tunnelling rates in the even and odd bonds, namely

$$t_e = t - \frac{2U_1 y^2}{N_L}\mathcal{B}_{MF} \ \text{ and } \ t_o = t + \frac{2U_1 y^2}{N_L}\mathcal{B}_{MF} \ . \tag{3.81}$$

For $\mathcal{B}_{MF} \neq 0$, hence the lattice alternates $t_e$ and $t_o$ tunnelling rates, as illustrated in Fig. 3.10. We call the bond strong if it connects two sites with the larger tunnelling rate. For instance in the case of $\mathcal{B}_{MF} > 0$ the larger tunnelling rate is given by $t_o$ and the strong bond is $o - e$. The weak bond connects two sites with the smaller tunnelling rate. For $\mathcal{B}_{MF} > 0$ the weak bonds are $e - o$.

We can identify the single-particle tunnelling rate for which either $t_e$ or $t_o$ vanishes. Setting $t_e = 0$ we find

$$t = \frac{2U_1 y^2}{N_L}\mathcal{B}_{\mathrm{MF}} \ , \tag{3.82}$$

whereas $t_o = 0$ for

$$t = -\frac{2U_1 y^2}{N_L}\mathcal{B}_{\mathrm{MF}} \ . \tag{3.83}$$

Whether $t_e$ or $t_o$ vanishes depends on the sign of $\mathcal{B}_{\mathrm{MF}}$. In the following we denote the parameter region where one of the bonds vanishes by the "destructive interference region". Note that this destructive interference condition can only be fulfilled for one kind of bond, which contrasts with the situation found for dipolar gases in Sec. 2.2.

The effective mean-field tunnelling in Eq. (3.80) is similar to the so-called Su-Schrieffer-Heeger (SSH) model [123, 167] of non-interacting fermions coupling to phonons in a chain, which we shortly review in the following.

### 3.5.2 *Connection to the SSH model*

In order to clarify analogies between our model and the SSH model, we will here introduce the SSH model following the reviews in Refs. [123, 167–169].

*SSH-Model*

The SSH model considers $N_e$ electrons hopping with a rate $t$ on a chain with periodicity $a$. The chain is generated by $N$ ions of

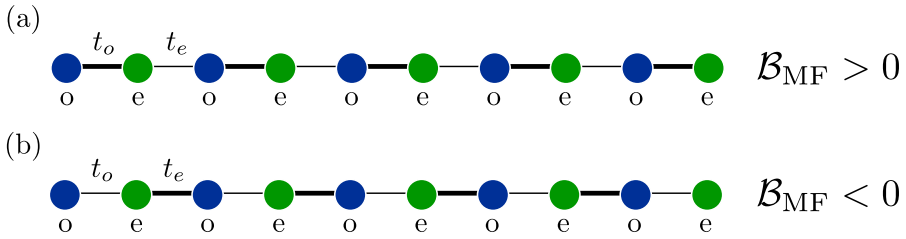


Figure 3.10: Sketch of the effective tunnelling rates connecting sites along the chain. $t_e$ labels the hopping $e - o$, $t_o$ the hopping $o - e$. Interference with cavity-mediated tunnelling leads to a breaking of the translation symmetry. Here the odd sites are indicated by blue dots, whereas the even sites are colored in green. (a) and (b) are characterized by different signs of the mean-field $\mathcal{B}_{MF}$.

mass $M$. One neglects here any interaction between the particles and the spin degrees of freedom of the electrons. In the tight-binding limit the chain's second-quantized Hamiltonian can be mapped on a Hubbard Hamiltonian with fermionic annihilation operators $\hat{c}_n$ and creation operators $\hat{c}_n^\dagger$. They obey the anti commutation relation $\{\hat{c}_{n'}, \hat{c}_n^\dagger\} = \delta_{n,n'}$ , $\{\hat{c}_{n'}^\dagger, \hat{c}_n^\dagger\} = \{\hat{c}_{n'}, \hat{c}_n\} = 0$ . If one considers also the ions vibrations about their equilibrium position, one shall include the coupling of the electrons to the phonons of the chain. The resulting effective Hubbard Hamiltonian describing the dynamics of the electrons in the chain is known as the Su-Schrieffer-Heeger (SSH) Hamiltonian [123, 167]:

$$\hat{H}_{SSH} = -\sum_{n=1}^{N} \left[t + (-1)^n 2\beta u\right] \left(\hat{c}_n^\dagger \hat{c}_{n+1} + h.c.\right) + 2NKu^2 \tag{3.84}$$

Here, $\beta$ is the phonon-electron coupling strength and $u$ the displacement of the ions from the equilibrium position, according to $x_{n+1} = a\,(1 + (-1)^n u)$, where $x_n$ is the position of the $n$-te ion. The energy cost for the deformation of the chain is proportional to $K$, the elastic constant.

The electron-phonon coupling favours a value of $u \neq 0$ , the so-called Peierls' distortion. Due to the Peierls' distortion the first Brillouin zone of the quasi-momentum $k$ is now reduced to $-\pi/2a < k \leq \pi/2a$. The SSH Hamiltonian in its diagonal form is given by [123, 167]

$$\hat{H}_{SSH} = \sum_{k \in BZ} E_k \left(\hat{n}_{k,+} - \hat{n}_{k,-}\right) \tag{3.85}$$

The zero point energy is here set to zero. The corresponding quasi-particle energy reads [123, 167]

$$E_k = \left(\epsilon_k^2 + \Delta_k^2\right)^{1/2} \tag{3.86}$$

with $\Delta_k = 4\beta u \sin(ka)$ and $\epsilon_k = 2t\cos(ka)$. The operator $\hat{n}_{k,-}$ counts the number of particles in the lowest (valence) band with a quasi-momentum $k$, while the operator $\hat{n}_{k,+}$ counts the number of particles

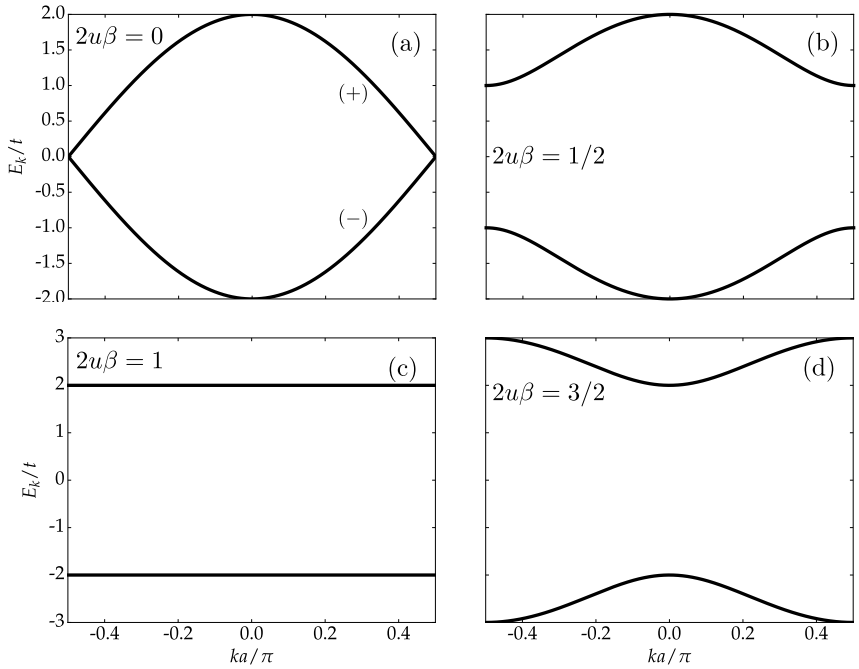


Figure 3.11: Quasiparticle energy $E_k$, Eq. (3.86), in units of the hopping rate $t$ as function of the quasi-momentum $k$ for different values of $2\beta u$. Panel (a) shows the spectrum for a displacement $u = 0$. For a finite $u$ a gap at $ka = \pm\pi/2$ opens, which can be seen for instance for $2u\beta = 1/2$ shown in panel (b). For $2u\beta = 1$ the spectrum shows a flat valence $(+)$ and conduction $(-)$ band (see panel (c)). In panel (d) the spectrum is reversed in comparison to (b) and the minimum of the valence band $(-)$ is at $ka = \pm/2$, while the minimum of of the conduction band $(+)$ is at $k = 0$.

in the upper (conduction) band. The eigenmodes are given by the set of Bloch waves $|\psi_{+,k}\rangle$ for the conduction band and $|\psi_{-,k}\rangle$ for the valence band (see Subsec. 1.2.2). The ground state of the SSH model for half-filling, i.e. $N_e/N = 1/2$, is the state, in which all eigenmodes of the valence band are occupied.

Figure 3.11 displays $E_k$ as a function of $k$ for different values of $2u\beta$. For $u = 0$ the spectrum is gapless and the ground state for any filling behaves like a conductor. For a finite $\beta u$ one observes an opening of the gap at $ka = \pm\pi/2$, as visible in Fig. 3.11(b). In this case for half-filling the ground state of this model is an insulator. For $2u\beta = 1$ we observe a flat valence $(+)$ and conduction $(-)$ band (see Fig. 3.11(c)). In Fig. 3.11(d) $2u\beta = 3/2$ and the spectrum is reversed in comparison to Fig. 3.11(b): the minimum of the valence band $(-)$ is at $ka = \pm\pi/2$, whereas the minimum of the conduction band $(+)$ is at $k = 0$. The energy gap closes at $ka = \pm\pi/2$ for $u = 0$. Note that the spectrum does not depend on the sign of $u$.

We can now write the SSH-Hamiltonian as

$$\hat{H}_{SSH} = w \sum_{n} \left( \hat{c}_n^\dagger \hat{c}_{n+1} + h.c. \right) + v \sum_{n'} \left( \hat{c}_{n'}^\dagger \hat{c}_{n'+1} + h.c. \right) \ , \tag{3.87}$$

where the first sum runs over all the ions labeled with an even number $n$ and the second sum runs over all odd numbers and

$$w = -t - 2\beta u \ \text{ and } \ v = -t + 2\beta u \ . \tag{3.88}$$

We choose the effective tunnelling rates to be positive. In the following we consider open boundaries. In the two cases $w < v$ and $w > v$ the insulating ground states will be topologically distinct. In particular for $w < v$ one gets a conventional insulator, whereas for $w > v$ the SSH model shows a so-called symmetry protected topological (SPT) phase [98, 169]. The defining property of a SPT state is that the ground state at zero-temperature can not be transformed into a conventional insulating state upon deformations of the system that do not close the excitation gap or violate the symmetry [169]. Let us now inspect the SPT phase in the case of the SSH model for half-filling. The fermionic SSH model shows two kind of symmetries: particle number conservation and chiral symmetry. The latter leads to the fact that the SSH model falls into a certain class of free fermionic theories [97, 145, 146, 170]. The band structure of this class is characterized by a $\mathbb{Z}$ topological index. This index is the so-called Zak phase [168, 171, 172]

*Zak phase*

$$\gamma = i \int_0^{2\pi} dk \, \langle u_-(k) | \partial_k | u_-(k) \rangle \ , \tag{3.89}$$

where $|u_-(k)\rangle = \exp(-ikx) \, |\psi_-(k)\rangle$ [1]. For a general band structure this Zak phase can take arbitrary values, while here it exhibits quantized values in units of $\pi$ due to the symmetry of the SSH model [172] . In particular for the case $w < v$ the Zak phase is zero, whereas $w > v$ the Zak phase gives $\gamma = -\pi$ [172]. Therefore in the case of a non-zero Zak phase the ground state for half-filling will be in a SPT phase.

*Edges states*

In this case the SSH model possesses a two-fold ground state degeneracy in a chain with open boundaries and an even number of ions. This degeneracy is due to the presence of edge states at the boundaries of the chain [169]. We can understand this by inspecting the ground state for half-filling for $v = 0$ and $w > 0$ [169]

$$|\Psi\rangle^{l,l'} = \left(\hat{c}_1^\dagger\right)^l \left(\hat{c}_N^\dagger\right)^{l'} \bigotimes_{n=2}^{N-1} \left( \frac{\hat{c}_n^\dagger + \hat{c}_{n+1}^\dagger}{\sqrt{2}} \right) |0\rangle \tag{3.90}$$

where $l, l' \in \{0, 1\}$ with $l \neq l'$ indicates the two degenerate ground states and the product runs over all $n = 2j$ with $j \in \mathbb{N}$. The operators $\hat{c}_1^\dagger$ and $\hat{c}_N^\dagger$ create an electron in the zero-energy edge modes [169]. These edge states are robust to any perturbation respecting the symmetry of the SSH model [169].

*Bosonic extension*

1 Here one considers the system in the continuum limit.

We observe a similar structure of the fermionic SSH model and the mean-field long-range Bose-Hubbard model in Eq. (3.80) by labeling $t_e = w$ and $t_o = v$. Nevertheless the situation is different for bosons, since the lack of the Pauli exclusion principle does not force the particles to fill the whole valence band for half-filling and zero temperature. The bosons would thus condense into the zero momentum state. In the hard core limit, instead, one can indeed map the bosonic analogue of the SSH model to the fermionic SSH model [172]. Nevertheless for a smaller onsite interaction the inter-particle interactions have already an effect on the edge states of the SPT phase [172]. Since inter-particle interactions are naturally present, it is thus important to better understand their role on the appearance of the SPT phase. In particular we are here interested in a global range interaction present in our model: Is the SPT phase still present in our model? What kind of role plays here the long-range interaction? For this purpose, we preformed DMRG simulations to study the ground-state phase diagram, which we will present in the following subsection.

### 3.5.3 *Topological insulator in cavity QED with bosons*

In this subsection we will consider the extended Bose-Hubbard Hamiltonian in Eq. (3.77). In particular we are here interested in the appearance of a topological non-trivial insulator in presence of the cavity mediated long-range interaction including the full quantum fluctuations. We therefore use in the following the DMRG method to determine the ground-state phase diagram for half-filling. For details on the implementation see Appendix 3.7. As discussed in the previous subsection the mean-field effective tunnelling in Eq. (3.79) of the extended Bose-Hubbard Hamiltonian in Eq. (3.77) is reminiscent of the phonon-electron coupling of the SSH model [123]. Differing from the ionic lattice of the SSH model, the bosons couple to a single oscillator – the cavity mode. Here, we expect a topological non-trivial phase in a regime, where the cavity field is finite and thus the lattice translational symmetry is spontaneously broken.

#### 3.5.3.1 *Phase diagram at half-filling*

In the following, we consider the system at half-filling, i.e. density $\rho = 1/2$. The phase diagram is determined as a function of $t/U$ and $U_1/U$. We characterize off-diagonal long-range order by the Fourier transform of the single-particle correlations, i.e. the single-particle structure factor given in Eq. (3.67). The coupling with the cavity induces off-diagonal long-range order, that is signaled by the bond-wave order parameter in Eq. (3.69). We also consider the density-wave order parameter in Eq. (3.68), which signals the onset of density-wave

| Phases | $\max M_1(k)$ | $k_{\max}$ | $\mathcal{O}_{DW}$ | $\mathcal{O}_B$ | $\mathcal{O}_S$ | $\mathcal{O}_P$ |
|---|---|---|---|---|---|---|
| Superfluid (SF) | $\neq 0$ | $= 0$ | $= 0$ | $= 0$ | $= 0$ | $= 0$ |
| Bond Superfluid (BSF) | $\neq 0$ | $\pm\pi/2$ | $= 0$ | $\neq 0$ | $= 0$ | $= 0$ |
| Density-wave (DW) | $= 0$ | – | $\neq 0$ | $= 0$ | $\neq 0$ | $\neq 0$ |
| Bond insulator (BI) | $= 0$ | – | $= 0$ | $\neq 0$ | $\neq 0$<br>$= 0$ | $= 0$<br>$\neq 0$ |

Table 3.3: Table of the phases, of their acronyms, and of the corresponding values of order parameters.

order. Moreover, we analyze the behaviour of the string and parity order parameter

$$\mathcal{O}_S(i,j) = \langle \delta\hat{n}_i e^{i\pi\sum_{k=i}^{j}\delta\hat{n}_k}\delta\hat{n}_j\rangle\,,$$
$$\mathcal{O}_P(i,j) = \langle e^{i\pi\sum_{k=i}^{j}\delta\hat{n}_k}\rangle\,. \tag{3.91}$$

These order parameters depend nonlocally on onsite fluctuations $\delta\hat{n}_j = \hat{n}_j - \rho$ from the mean density $\rho$. The phases and the corresponding observables are summarized in Table 3.3.

We first remark that, for $U_1 = 0$, hence in the absence of global interactions, the phase is Superfluid (SF). We also expect that for $U_1 > 0$ the quantum phase of Hamiltonian, Eq. (3.77), is SF, since the formation of a finite cavity field costs energy. Instead, we expect that correlated hopping becomes relevant for $U_1 < 0$. We have seen in the previous Sec. 3.4 that at a sufficient large values of $|U_1|$ the mean-field approach predicts the formation of a bond superfluid (BSF) accompanied by a finite value of bond-wave order parameter $\mathcal{O}_B$ (see Fig. 3.9). We point out that mean-field predicts that the ground state exhibits off-diagonal long-range order for any value of $U_1$ (see Fig. (3.9)(b)). In this section we want to study the quantum phases by going beyond mean-field. Thus we now discuss the quantum phase obtained from DMRG calculations. The phase diagram is reported as a function of the ratio $t/U$ and $U_1/U$. We sweep $U_1$ from positive to negative values. We note that in a cavity the sign of $U_1$ is tuned by means of the sign of the detuning $\Delta_c$. The effective strength, in particular, shall be here scaled by the parameter $y^2$, depending on the particle localization. Here, $y$ is constant across the diagram, since we keep in fact the optical lattice depth constant and tune the ratio $t/U$ by changing the onsite repulsion $U$. Figure 3.12 displays the DMRG results for (a) the maximum value of $|M_1(k)|$ (1.65), (b) the bond-wave order parameter (3.69), (c) the string order parameter (2.32)

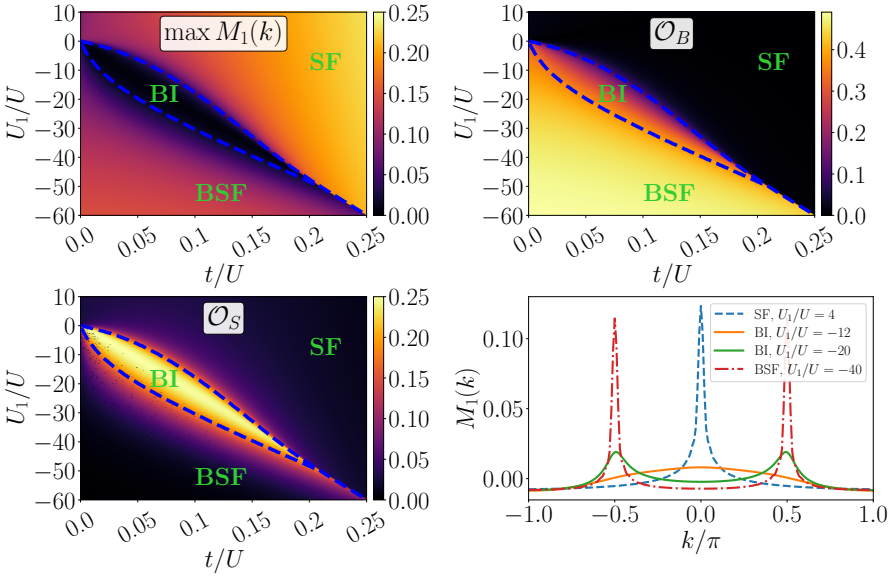


Figure 3.12: Phase diagrams of Hamiltonian in (3.77) in the $(t/U, U_1/U)$-plane determined by means of DMRG. Different panels show the behaviour of the order parameters indicated in the plots. We observe the appearance of an insulating phase for $t/U \lesssim 0.2$ between standard Superfluid (SF) and bond Superfluid (BSF) phases which disappears at larger tunnelling values. The blue dashed lines indicate the borders between the regions where the maximum of $M_1(k)$ evaluated over the ground state crosses a threshold value which we set at 0.03 to compensate finite-size effects. The bottom right panel shows the shape of $M_1(k)$ for fixed $t = 0.05U$. Sharp peaks appear at $k = 0$ for SF and $k = \pm\pi/2$ for BSF in contrast to broad peaks of lower amplitude for BI. Note that the effective strength of the correlated hopping in (3.77) scales with $y^2U_1$. Here, $N_L = 60$ and $y = -0.0658$.

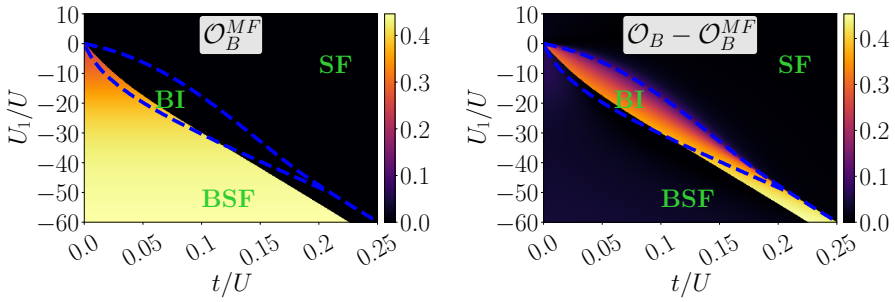


Figure 3.13: Left panel: Bond-wave order parameter predicted by mean-field Gutzwiller approach, $\mathcal{O}_B^{MF}$, in the $(t/U, U_1/U)$-plane. The right panel shows the difference $O_B - \mathcal{O}_B^{MF}$, where $O_B$ has been determined using DMRG. The blue dashed line indicates the borders between the regions same as in Fig. 3.12. The mean-field Gutzwiller approach agrees with DMRG in SF and BSF regimes, but misses the appearance of BI phase.

for $i = 10$ and $j = 49$, and (d) the dependence of $M_1(k)$ on the wave number $k$ for different values of $U_1/U$. For $U_1 < 0$ the ground state supports the creation of the cavity field, which is signaled by the finite value of the bond-wave order parameter. At sufficiently large values of $|U_1/U|$ and $t/U$ the transition is discontinuous, and it separates the SF from the BSF phase, where the effective tunnelling amplitudes $\langle \hat{a}_i^\dagger \hat{a}_{i+1} + \text{H.c.} \rangle$ attain a staggered pattern characterized by a finite value of bond-wave order parameter $\mathcal{O}_B$. The long range coherence of the BSF phase is manifested by narrow peaks of $M_1(k)$ centered at $k = \pm\pi/2$ (see Fig. 3.12). Remarkably, we observe a reentrant insulating phase separating the SF and the BSF. The insulator is signaled by vanishing off-diagonal long-range order and therefore by a value of the structure factor $M_1(k)$ close to zero for a finite lattice. It is characterized by the non-zero (zero) values of the string order parameter and by vanishing (non-vanishing) parity order parameter depending on the boundary sites of these non-local parameters (see the next subsubsection for details). We denote this phase as a Bond Insulator (BI). This phase is separated from the SF by a continuous phase transition. The transition BI-BSF seems also continuous.

We note that the bond insulator phase is entirely absent in the mean-field approach of the previous section. Figure 3.13 displays the bond-wave order $\mathcal{O}_B^{MF}$ predicted by mean-field (left panel) and the deviation of it from the DMRG result (right panel). While the exact borders between various phases quantitatively differ, the existence of both regular and bond Superfluid phases is visible in the mean-field approach. We further note that studies of the ground state of (3.77), based on exact diagonalization for small system sizes, did not report the existence of the BI phase [36]. In the following subsubsection, we characterize the topology associated with the BI phase and argue that it is stable in the thermodynamic limit.

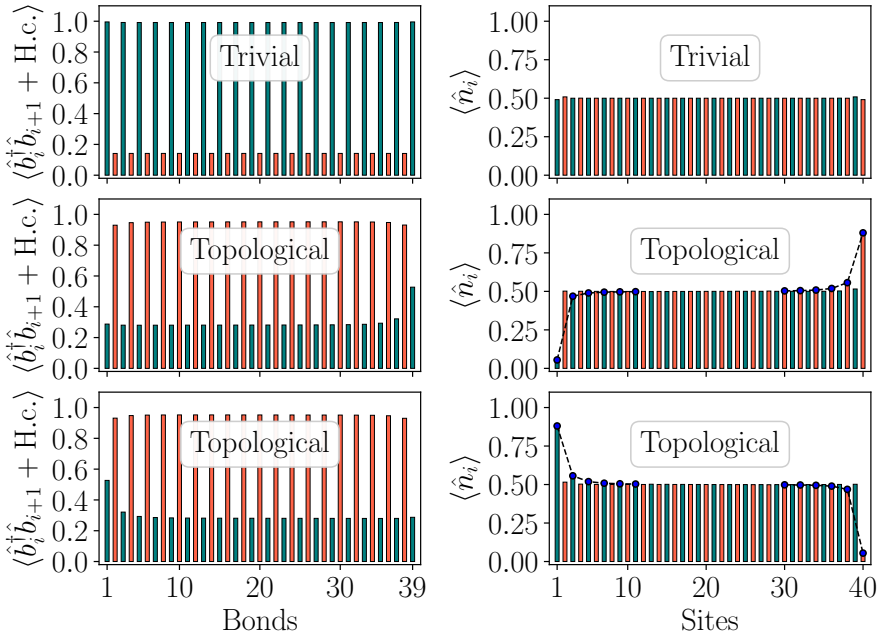


Figure 3.14: Site-dependent properties of the topological and trivial ground states of the BI phase. Left panels: Effective tunnelling amplitudes $\langle \hat{b}_i^\dagger \hat{b}_{i+1} + \text{H.c.} \rangle$ as a function of the bonds $(i, i+1)$. Orange (teal) bars denote the even (odd) bond. Right panels: Density $\langle \hat{n}_i \rangle$ as a function of the lattice site. The dashed line is a guide for the eye. Observe the characteristic alternate weak/strong pattern in the bonds with weak bonds occurring at the edges for topological states that reveal topological particle-hole edge excitations. Here, we set $U_1/U = -10$, $t/U = 0.05$, and $y = -0.0658$ (see Methods) to obtain the states using DMRG algorithm.

#### 3.5.3.2 *Emergent topology associated with the BI phase*

By means of excited-state DMRG, we reveal that the BI phase has triply degenerate ground state (quasi-degenerate for finite $N_L$) separated by a finite gap from the other excited states. The site distribution is visualized in Fig. 3.14 which shows that the absolute ground state has a uniform mean half-filling, while the other two states possess edge excitations, namely, fractional particle-hole excitations with respect to the mean half-filling (bottom two rows of Fig. 3.14). Such edge excitations are characterized by the bond-wave order parameter with opposite sign than the trivial phase. They suggest that the BI phase is a symmetry protected topological (SPT) phase. Similar topological edge states have been reported e.g., for noninteracting system [173] or in superlattice BH model [172], where the superlattice induces a tunnelling structure resembling that of the SSH model [123]. In our case, instead, the effective tunnellings are spontaneously generated by the creation of a cavity field that breaks discrete $\mathbb{Z}_2$ translational

symmetry of the system. However, bond centered inversion symmetry still remains intact – it protects this SPT phase.

On a further inspection, it is found that the string order $\mathcal{O}_S$ and parity order $\mathcal{O}_P$ can be non-zero (zero) depending on the location of the two separated sites that sit at the boundaries of the non-local operators (sites $i$ and $j$ in Eqs. (2.32) and (3.91)). We illustrate it in Fig. 3.15(a). We find that $\mathcal{O}_S \neq 0$ and $\mathcal{O}_P = 0$, as reported in Fig. 3.12, when the non-local operators start at the second site of a strong bond (i.e., the bond with larger tunnelling element) and end at the first site of a weak bond (the bond with smaller tunnelling element) further away. These are unusual properties when compared to, say, topological Haldane phases of extended BH models at unit filling [32, 165].

To check whether we are indeed dealing with topological states, we calculate the entanglement spectrum of the system. For this purpose we partition the chain into a right ($R$) and left ($L$) subsystem as $|\psi\rangle_{GS} = \sum_n \lambda_n |\psi\rangle_L \otimes |\psi\rangle_R$ where $\lambda_n$ are the corresponding Schmidt coefficients for the specific bipartition. The entanglement spectrum is then defined as the set of all the Schmidt coefficients in logarithmic scale $\varepsilon_n = -\log \lambda_n$ and is degenerate for phases with topological properties in one dimension [174]. We find that $\varepsilon_n$ are degenerate near the chain center when the bipartition is drawn across a strong bond, while it is non-degenerate at the weak bonds. In Fig. 3.15(b), we display the entanglement spectrum for trivial and topological ground states of the BI phase for $N_L = 60$, when $\varepsilon_n$ are measured across the bipartition at the chain's center. The entanglement spectrum, together with the density pattern and the behaviour of string and parity order parameters, provide convincing proof of the topological character of the BI phase. Furthermore, to show that the BI phase is stable in the thermodynamic limit, we consider the entanglement gap, $\Delta\varepsilon = \varepsilon_1 - \varepsilon_0$, for different system sizes. Fig. 3.15(c) presents the variation of $\Delta\varepsilon$ across BSF-BI-SF phases for fixed $t/U = 0.05$ – confirming the stability of SPT BI phase in the thermodynamic limit.

In order to reveal the bulk-edge correspondence, we determine the many-body Berry phase [175] and show that it is $\mathbb{Z}_2$-quantized in the BI phase. We first note that, because of the strong interactions, the winding number or the Zak phase [171, 173] is not a good topological indicator in our case. Therefore, we follow the original proposition of Hatsugai [176] and determine the *local* many-body Berry phase, which is a topological invariant playing the role of the local "order parameter" for an interacting case [176]. For this purpose, we introduce a local twist $t \to te^{i\theta_n}$ in the Hamiltonian (3.77), such that the system still remains gapped in the BI phase. Then the many-body Berry phase is defined as

$$\gamma^{(K)} = \mathrm{Arg} \prod_{n=0}^{K-1} \langle \psi_{\theta_{n+1}} | \psi_{\theta_n} \rangle \,, \tag{3.92}$$

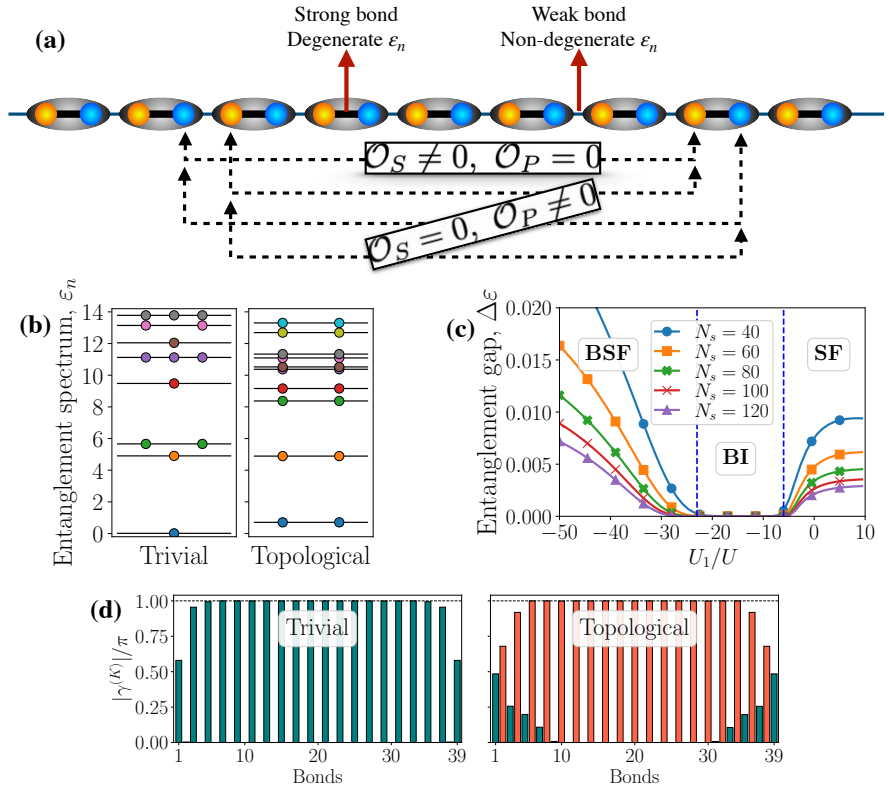


Figure 3.15: (a) Illustration of the BI ground-state properties. The ellipsoids with thick black lines indicate the dimerized strong bonds with larger effective tunnelling amplitudes, while thin lines indicate the weak alternate bonds with smaller effective tunnelling amplitudes. The string order $\mathcal{O}_S$ becomes non-zero (with $\mathcal{O}_P = 0$) only when it is measured across blue to orange sites in the figure. In all other cases it vanishes, $\mathcal{O}_S = 0$ and $\mathcal{O}_P \neq 0$. The entanglement spectrum is found to be degenerate in the bulk of the chain when it is measured across the strong bonds, while it is non-degenerate in weak bonds. (b) Entanglement spectrum $\varepsilon_n$ computed at the middle of the chain of $N_L = 60$ for the trivial and topological states. For trivial state the spectrum is non-degenerate, while it is doubly degenerate for topological states. (c) Entanglement gap ($\Delta\varepsilon = \varepsilon_1 - \varepsilon_0$) as a function of $U_1$ and for fixed $t/U = 0.05$ across BSF-BI-SF phases. Different curves refer to different system sizes. (d) Local Berry phases $\gamma^{(K)}$ (3.92), measured across every bonds for trivial (left) and topological (right) states. Here, we consider $N_L = 40$ and $K = 20$. In (b)-(d) other system parameters are the same in Fig. 3.14.

where $\psi_{\theta_n}$'s are the ground states with $\theta_0, \theta_1, ..., \theta_K = \theta_0$ on a loop in $[0, 2\pi]$. Here, we consider the local Berry phase corresponding to a bond by giving the local twist in tunnelling strength $t \to te^{i\theta_n}$ only on that particular bond, and take $K = 20$. The local Berry phases $\gamma^{(K)}$'s are displayed in Fig. 3.15(d) for the system size $N_L = 40$. Similar to the entanglement spectrum, we find $\gamma^{(K)} = \pi$ for the strong bonds, while $\gamma^{(K)} = 0$ on the weak bonds.

### 3.5.4 *Conclusions*

The BI phase of this model is a reentrant phase. It separates the SF phase from the BSF phase, where correlated tunnelling is dominant. We have provided numerical evidence that the emerging topology is essentially characterized by the interplay between quantum fluctuations and correlated tunnelling. Interactions are here, therefore, essential for the onset of topology. Their global nature is at the basis of the spontaneous symmetry breaking that accompanies the onset of this phase and which induces an asymmetry between bonds. In this respect, it is reminiscent of the Peierls' instability of fermions in resonators [166], where the topology is associated with the spontaneous breaking of $\mathbb{Z}_2$ symmetry. Differing from that case, where photon scattering gives rise to a self-organized superlattice trapping the atoms, in our model photon scattering interferes with quantum fluctuations. Like in [166], gap and edge states can be measured in the emitted light using pump-probe spectroscopy. The single-particle structure factor may be directly accessible by the time-of-flight momenta distributions [7] enabling the detection of insulator-superfluid phase transition. The two combined measurements of the cavity output and of the structure factor shall provide a clear distinction between the BI, SF and BSF phases.

We observe that the global long-range interaction of this model inhibits the formation of solitons. To conclude, in the last section we have presented a new paradigm of topological states formation via interference between single-particle dynamics and interaction induced hopping.

## 3.6 CONCLUSIONS

In this chapter we have performed an extensive analysis of the ground-state phase diagram of the Bose-Hubbard model with global interaction. This model describes the dynamics of existing experimental setups coupling photons and ultracold atoms in optical lattice [43, 44]. We have analyzed the model for different geometries, leading to different processes induced by the cavity mediated interaction. The cavity mediated processes lead to density modulated, bond ordered and topological non-trivial phases. Latter are due to a quantum interference between the tunnelling originating from the kinetic energy and the cavity induced tunnelling.

## 3.7 APPENDICES

*Supplementary material of the one-dimensional DMRG study*

In Sec. 3.5 we have focused on an immediate vicinity of $\phi = \pi/2$. This corresponds to the atoms being trapped at the nodes of the cavity mode, where $z$ vanishes. However, as $\phi$ starts to deviate from $\pi/2$ the $y$ term rapidly decreases and $z$ term becomes significant (see Fig. 3.16). Note that the quadratic form of $\hat{H}_{\mathrm{LR}}^{\mathrm{1D,BH}}$, Eq. (3.63), is responsible for

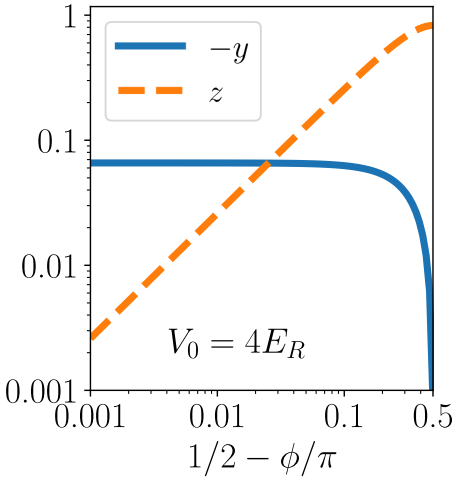


Figure 3.16: The variations of $y$ and $z$ as $\phi$ deviates from $\pi/2$. We consider $V_0 = 4E_R$.

the long-range character of the couplings. Squaring $\hat{D}$ leads then to all-to-all density-density interactions, responsible for a spontaneous formation of density wave phase for sufficient $U_1$ [23]. For the case considered in the last subsection, $z \approx 0$ and $\hat{B}^2$ term leads to the all-to-all long-range correlated tunnellings alternating in sign. In Fig. 3.17, we plot the order parameters and the phase diagram in the vicinity of $\phi = \pi/2$ for $t/U = 0.05$. As $\phi$ starts to deviate from $\pi/2$, $y$ starts to diminish and $z$ becomes increasingly larger (see right panel of Fig. 3.16). As a result, BI phase is replaced by a more standard density wave (DW) phase [23], when $\phi$ becomes sufficiently different from $\pi/2$. In the DW phase $\mathcal{O}_{DW}$ as well as $\mathcal{O}_S$ and $\mathcal{O}_P$ are both non-zero, while the structure factor vanishes.

*Details on the numerical implementation*

This appendix provides insights on the numerical implementation of extended Bose-Hubbard model. We here report details on the Density matrix renormalization group algorithm and describe the local mean-field algorithm.

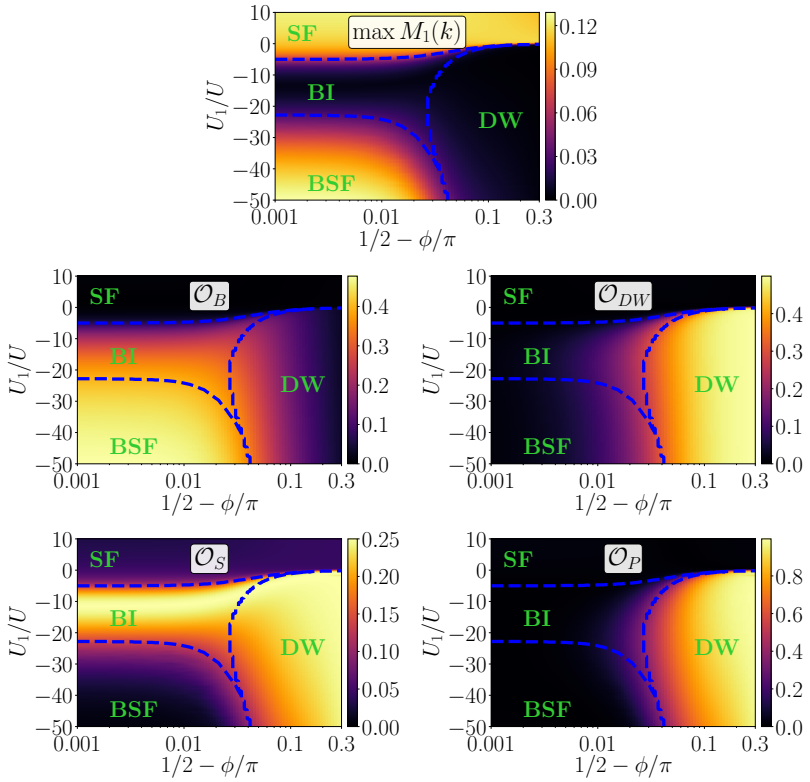


Figure 3.17: Phase diagrams in the $(\phi, U_1/U)$-plane for $t/U = 0.05$ for $N_s = 60$. The BI phase disappears when $\phi$ deviates from $\pi/2$ and density wave phase appears. Here, we choose $V_0$ to be $4E_R$ so that the values of $y$ and $z$ matches that of Fig. 3.16 (right panel). Blue dashed lines are guide to the eyes to differentiate different phases.

*Density matrix renormalization group*

We use standard matrix product states (MPS) [63] based density matrix renormalization group (DMRG) [62] method to find the ground state and low-lying excited states of the system with open boundary condition, where we employ the global $U(1)$ symmetry corresponding to the conservation of the total number of particles. For that purpose, we use ITensor C++ library (`https://itensor.org`) where the MPO for the all connected long-range Hamiltonian can be constructed exactly [177, 178] using AutoMPO class. The maximum number bosons ($n_0$) per site has been truncated to 6, which is justified as we only consider average density to be $\rho = 1/2$.

We consider random entangled states, $|\psi_{\text{ini}}\rangle = \frac{1}{\sqrt{50}} \sum_{i=0}^{49} |\psi_i^{\text{rand}}\rangle$, where $|\psi_i^{\text{rand}}\rangle$ are random product states with density $\rho = 1/2$, as our initial states for DMRG algorithm. The maximum bond dimension of MPS during standard two-site DMRG sweeps has been restricted to $\chi_{\max} = 200$. We verify the convergence of the DMRG algorithm by checking the deviations in energy in successive DMRG sweeps. When the energy deviation falls below $10^{-12}$, we conclude that the resulting MPS is the ground state of the system.

To obtain low-lying excited states, we first shift the Hamiltonian by a suitable weight factor multiplied with the projector on the previously found state. To be precise, for finding the $n^{th}$ excited state $|\psi_n\rangle$, we search for the ground state of the shifted Hamiltonian,

$$\hat{H}' = \hat{H} + W \sum_{m=0}^{n-1} |\psi_m\rangle \langle\psi_m| , \tag{3.93}$$

where $W$ should be guessed to be sufficiently larger than $E_n - E_0$.

*Local mean-field*

In this Appendix, we describe the algorithm used to find the self-consistent ground state of the local mean-field Hamiltonians (3.32). We measure all physical parameters of the Hamiltonian in units of the onsite interaction, $\tilde{\mu} = \mu/U_0$, $\tilde{U}_\infty = U_\infty/U_0$, $\tilde{t} = zt/U_0$ and obtain the Hamiltonians

$$\tilde{H}_{\text{e}} = -\tilde{t}\varphi_{\text{o}}(a + a^\dagger - \varphi_{\text{e}}) + \frac{1}{2}n(n-1) - \tilde{U}_\infty \theta n + \frac{\tilde{U}_\infty}{4}\theta^2 - \tilde{\mu} n, \tag{3.94}$$

$$\tilde{H}_{\text{o}} = -\tilde{t}\varphi_{\text{e}}(a + a^\dagger - \varphi_{\text{o}}) + \frac{1}{2}n(n-1) + \tilde{U}_\infty \theta n + \frac{\tilde{U}_\infty}{4}\theta^2 - \tilde{\mu} n, \tag{3.95}$$

with the same eigenenergies and -states as the Hamiltonians (3.32). We fix the parameters of the Hamiltonian $\tilde{t}$, $\tilde{U}_\infty$ and $\tilde{\mu}$. The mean-field order parameters $\varphi_{\text{e}}$, $\varphi_{\text{o}}$ and $\theta$ are now the free variables. The problem is formulated as follows. We first introduce the function

$$f(\varphi_{\text{e}}, \varphi_{\text{o}}, \theta) = (\langle a\rangle_{\text{e}}, \langle a\rangle_{\text{o}}, \langle n\rangle_{\text{e}} - \langle n\rangle_{\text{o}}), \tag{3.96}$$

where $\langle\cdot\rangle_s$ denotes the single-site expectation value with respect to the ground state of the Hamiltonian $H_s(\varphi_e, \varphi_o, \theta)$, for $s \in \{e, o\}$. Further, we define $F$ to be the set of fixed points of $f$,

$$F = \{(\varphi_e, \varphi_o, \theta) : f(\varphi_e, \varphi_o, \theta) = (\varphi_e, \varphi_o, \theta)\}. \tag{3.97}$$

The goal is to find the self-consistent order parameters which minimize the energy per site,

$$(\varphi_e, \varphi_o, \theta) = \underset{(\varphi_e,\varphi_o,\theta)\in F}{\operatorname{argmin}} \left\{ \frac{1}{2} \left( \langle H_e \rangle_e + \langle H_o \rangle_o \right) \right\}. \tag{3.98}$$

The basic idea of the algorithm is that of fixed point iteration: Apply $f$ repeatedly to some random $(\varphi_e, \varphi_o, \theta)$, until applying it again does not significantly change the input [26, 31].

We measure the distance between mean-field order parameters by the infinity-norm and relax the criterion for $(\varphi_e, \varphi_o, \theta)$ to be a fixed-point to

$$\left\| (\varphi_e, \varphi_o, \theta) - (\varphi'_e, \varphi'_o, \theta') \right\|_\infty = \max(|\varphi_e - \varphi'_e|, |\varphi_o - \varphi'_o|, |\theta - \theta'|) < \varepsilon, \tag{3.99}$$

where $(\varphi'_e, \varphi'_o, \theta') = f(\varphi_e, \varphi_o, \theta)$, and $\varepsilon$ is some predefined tolerance, e. g. $\varepsilon = 10^{-6}$.

This naïve algorithm has the following problems, however: First, if the algorithm converges to some point, there is no guarantee that this point minimizes the energy per site. Second, the algorithm is not guaranteed to converge. Third, the algorithm sometimes converges sublinearly, and thus extremely slowly.

We approach the first problem by taking a sufficient large number of initial guesses.We always deterministically take the following 75 initial guesses: $(\varphi_e, \varphi_o, \theta) \in \cup_{\{n\in 0,\ldots,24\}}\{(0, 0, n), (0.001, 0.002, n), (0.1, 0.2, n)\}$. Additionally, we use the Mersenne Twister and Ranlux48 algorithms to pseudorandomly sample initial guesses from the Cauchy$(0, 1)$ distribution. We find that 50 random initial values are sufficient to find the minimal energy and verify this by taking more initial guesses and verifying that the energy does not decrease significantly.

The problem that the algorithm sometimes does not converge manifests in the way of cycles of the form that $f(\varphi_e, \varphi_o, \theta) \approx (-\varphi_e, -\varphi_o, -\theta)$ and $f(-\varphi_e, -\varphi_o, -\theta) \approx (\varphi_e, \varphi_o, \theta)$. We detect this by comparing not only the mean-field order parameters, but also their absolute values. If the difference of the absolute values is smaller than $\varepsilon/10$ for 1000 consecutive iterations, we re-run the algorithm with the absolute values of the final order parameters $(\varphi'_e, \varphi'_o, \theta')$ as an initial guess. To ensure that we still find the minimal energy, we compare the energies of the result of the initial run $(\varphi'_e, \varphi'_o, \theta')$, with that of the second run, $(\varphi''_e, \varphi''_o, \theta'')$. For this comparison, we do not consider the eigenvalues of the two Hamiltonians, but the expectation value of the updated Hamiltonian with respect to the ground state of the Hamiltonian before the update. If the energy of the second run is smaller, we accept this solution, otherwise we reject it.

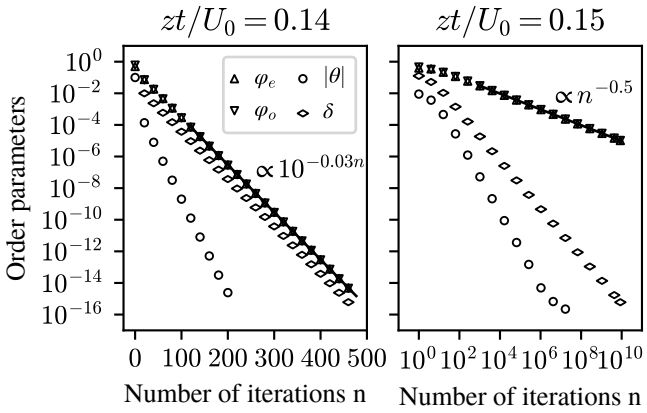


Figure 3.18: Convergence of the numerical mean-field iterative algorithm as a function of the number of iterations (or applications of $f$, as given in equation (3.96). In both cases, the occupation is cut off above $n_{\max} = 31$, $\tilde{Uz}_\infty = 0.26$, $\tilde{\mu} = 0.6$, and the initial guess is $(\varphi_e, \varphi_o, \theta) = (0.5, 0.6, 0.1)$. On the left, $\tilde{t} = 0.14$ and the convergence is linear. On the right, $\tilde{t} = 0.15$ and the convergence is sublinear. Both points are close to the MI-SF phase boundary. The markers show the order parameters and the maximum difference $\delta$ of the order parameters from one iteration to the next. The black lines are obtained by linear regression of an exponential function (left) and a power function (right) to the maximum order parameter. The calculations took around 6 CPU-days on a Intel Core i7-2600 CPU at a clock rate of $\sim 3.6$ GHz.

Finally, we note that the algorithm converges to the set tolerance within a few hundred or thousand iterations (i. e. applications of $f$) in a large region of the phase diagram. In this case, the algorithm converges linearly. However, in some cases it converges sublinearly and extremely slowly. Figure 3.18 shows a comparison of two cases, for two points in the phase diagram which are close to each other, and identical initial guesses.

The algorithm converges that slow only at relatively few points in the phase diagram. We have verified that the number of iterations does not strongly influence the value of the resulting mean-field order parameters, by comparing the results after $10^4$ and $10^6$ iterations.

For finding the ground state of the Hamiltonians (3.95), we truncate the Hilbert space of each site taking the cutoff $n_{\max} = 31$, leaving us with two tridiagonal real symmetric $32 \times 32$ matrices (in the Fock basis), which we diagonalize numerically. We identify the cutoff $n_{\max} = 31$ by performing calculations also for $n_{\max} = 23$ and $n_{\max} = 63$ and verifying that the results do not differ significantly.

*Supersolidity and phase separation for fixed densities*

In this appendix, we report details of the calculations for determining the phase diagram for constant densities of Fig. 3.6.

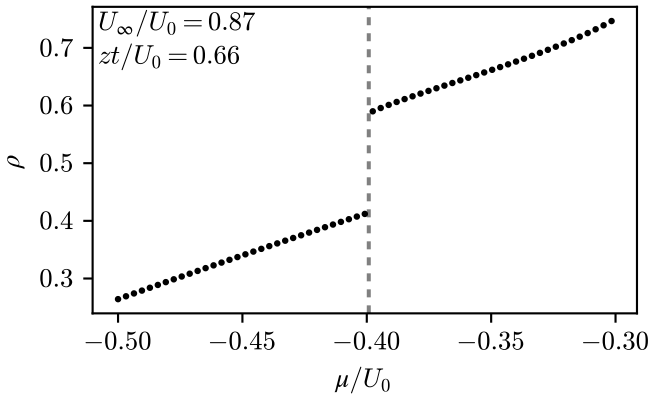


Figure 3.19: Density $\rho$ as a function of the chemical potential $\mu$ for $U_\infty/U_0 = 0.87, zt/U_0 = 0.66$. The vertical bar marks a jump in the $\rho(\mu)$ curve.

We obtain the order parameters for fixed densities by adjusting the chemical potential such that the ground state has the target density. More precisely, we perform a bisection algorithm starting at $\mu = -U_0$ which gives a density lower than the target density and $\mu = 3U_0$ which gives a density higher than the target density. In every step, the ground state for the midpoint of the $\mu$ interval is calculated following the procedure detailed in Appendix 3.7, its density is computed, and the interval is halved such that at the lower (upper) point of the interval, the density is smaller (larger) than the target density. We repeat this up to twenty times until either the target density is reached or we conclude that a solution is not possible. When the density is not attained with the required precision, which we set to $\varepsilon_\rho = 10^{-4}$, we name the corresponding point of the phase diagram phase separation, following Ref. [28]. Otherwise, we determine the phase from the values of the order parameters $\theta$ and $\varphi$.

For a density of $\rho = 0.5$, we find both a SS region and a region of phase separation, unlike Refs. [23, 28]. Fig. 3.19 shows the $\rho(\mu)$ curve for a PS point. Fig. 3.20 shows the $\rho(\mu)$ curve for a different point, where the density $\rho(\mu \approx -0.132) = 0.5$. The same figure shows the superfluid order parameter and the even-odd imbalance; for the parameters where $\rho(\mu) = 0.5$, the ground state is SS.

In Fig. 3.21, we show the $\rho(\mu)$ curve for a PS point for density $\rho = 1$, which was not reported so far [23, 28]. As shown in fig. 3.6, we also find a PS region for $\rho = 1.5$, which was not reported so far [23, 28].

In Fig. 3.22, we show the order parameters along cuts of the phase diagram in figure 3.6, specifically the density $\rho = 0.5$. We show similar plots for the density $\rho = 1$ in figure 3.23. We used plots similar to the ones shown in Figs. 3.22 and 3.23 to determine all phase boundaries of Fig. 3.6.

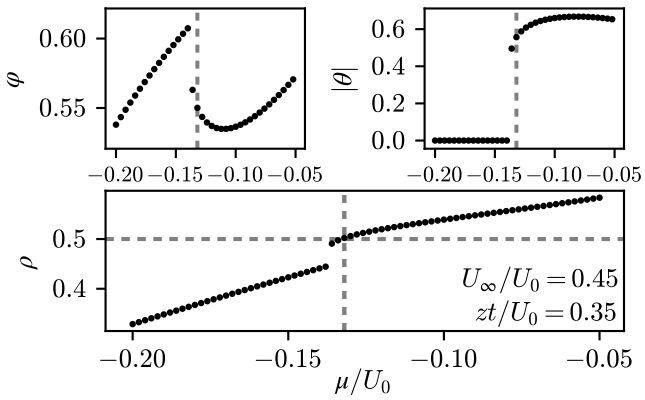


Figure 3.20: (c) Density $\rho$ as a function of the chemical potential $\mu$ for $U_\infty/U_0 = 0.45, zt/U_0 = 0.35$. The horizontal bar marks the density $\rho = 0.5$. (a) Superfluid order paramater $\varphi(\mu)$ for the same parameters. (b) Even-odd imbalance $|\theta(\mu)|$ for the same parameters. The vertical bar marks $\rho(\mu) = 0.5$.

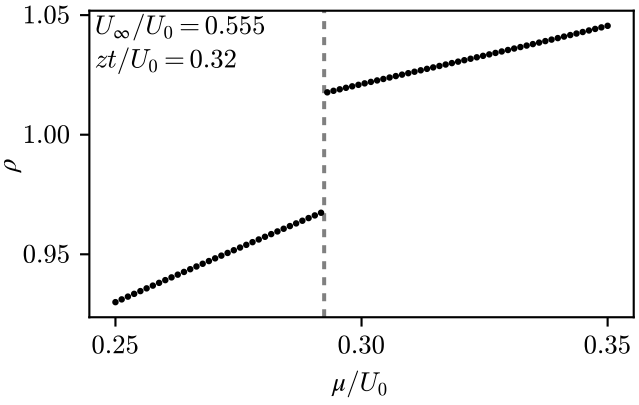


Figure 3.21: Density $\rho$ as a function of the chemical potential $\mu$ for $U_\infty/U_0 = 0.555$, $zt/U_0 = 0.320$. The vertical bar marks a jump in the $\rho(\mu)$ curve.

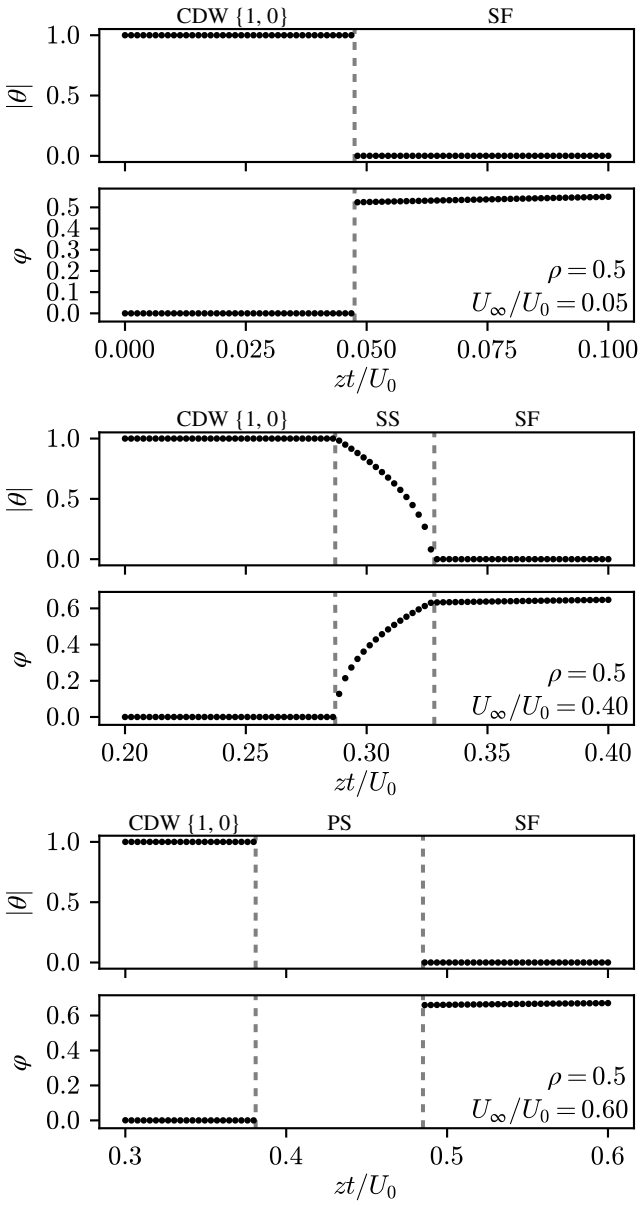


Figure 3.22: Imbalance $|\theta|$ and superfluid order parameter $\varphi$ for cuts of the phase diagram 3.6 with a constant density of $\rho = 0.5$. The vertical dashed lines show the phase transition points. The phases are indicated by the labels above the plots.

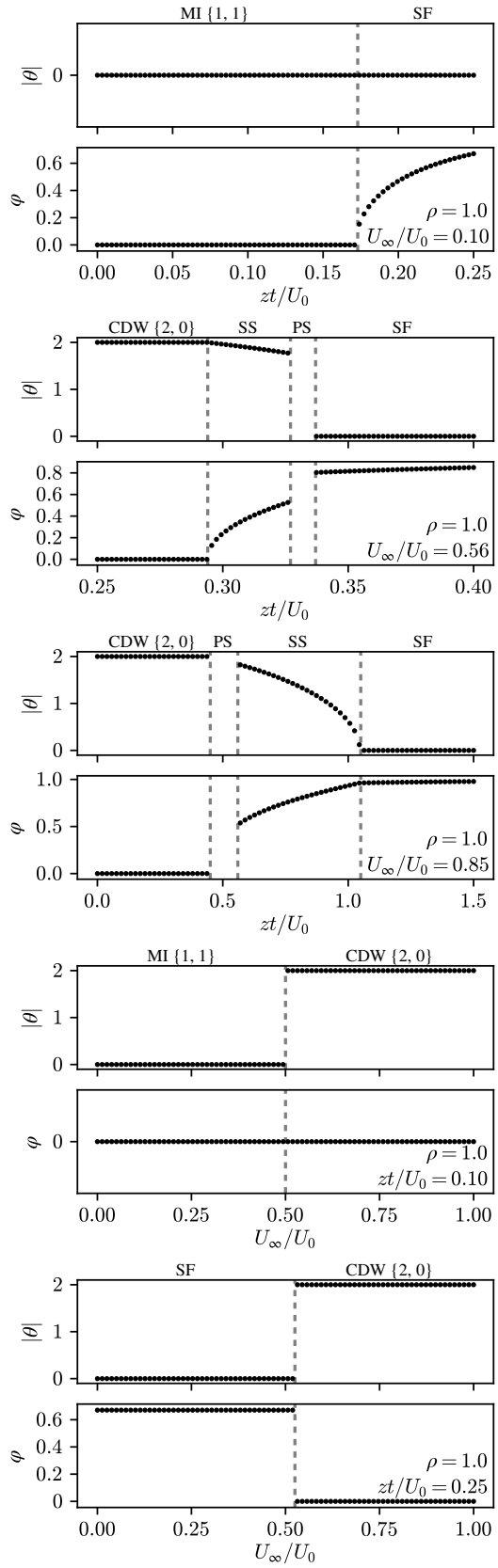


Figure 3.23: Imbalance $|\theta|$ and superfluid order parameter $\varphi$ for cuts of the phase diagram 3.6 with a constant density of $\rho = 1$. The vertical dashed lines show the phase transition points. The phases are indicated by the labels above the plots.

# OUTLOOK

In this thesis we theoretically investigated the ground-state phase diagrams of extended Bose-Hubbard models in the presence of long-range interactions. In particular we studied the influence of long-range correlated tunnelling on the quantum phase diagram. We hereby identified and examined a parameter regime, where single-particle tunnelling and correlated tunnelling interfere. In this regime we showed that this quantum interference can dramatically change the ground state properties, leading either to peculiar superfluid phases in the limit, where otherwise the phase would be incompressible, or to incompressible phases, where instead one would expect superfluidity. For global interactions, moreover, we found that this interference gives rise to non-trivial topological phases reminiscent of the ones of the celebrated SSH-model.

Our theoretical investigation on the extended Bose-Hubbard models are important for present or future experiments simulating the extended Bose-Hubbard models [43, 73].

Since the dynamics we reported do depend on interfering paths, the expected phases will depend on the geometry of the lattice. We expect different dynamics and topologies for instance in triangular geometries, such as the one considered in Ref. [40]. We also envisage novel dynamics emerging from the interplay of correlated tunnellings generated from different interactions.

# BIBLIOGRAPHY


[1] C.N. Cohen-Tannoudji. "Nobel Lecture: Manipulating atoms with photons." In: *Reviews of Modern Physics* 70.3 (1998), p. 707.

[2] W.D. Phillips. "Nobel Lecture: Laser cooling and trapping of neutral atoms." In: *Reviews of Modern Physics* 70.3 (1998), p. 721.

[3] S. Chu. "Nobel Lecture: The manipulation of neutral particles." In: *Reviews of Modern Physics* 70.3 (1998), p. 685.

[4] I. Bloch, J. Dalibard, and W. Zwerger. "Many-body physics with ultracold gases." In: *Reviews of Modern Physics* 80.3 (2008), p. 885.

[5] C. Gross and I. Bloch. "Quantum simulations with ultracold atoms in optical lattices." In: *Science* 357.6355 (2017), pp. 995–1001.

[6] M. Lewenstein, A. Sanpera, and V. Ahufinger. *Ultracold Atoms in Optical Lattices: Simulating quantum many-body systems*. Oxford University Press, 2012.

[7] M. Greiner, O. Mandel, T. Esslinger, T.W. Hänsch, and I. Bloch. "Quantum phase transition from a superfluid to a Mott insulator in a gas of ultracold atoms." In: *Nature* 415.6867 (2002), pp. 39–44.

[8] T. Stöferle, H. Moritz, Ch. Schori, M. Köhl, and T. Esslinger. "Transition from a strongly interacting 1D superfluid to a Mott insulator." In: *Physical Review Letters* 92.13 (2004), p. 130403.

[9] I.B. Spielman, W.D. Phillips, and J.V. Porto. "Condensate fraction in a 2D Bose gas measured across the Mott-insulator transition." In: *Physical Review Letters* 100.12 (2008), p. 120402.

[10] D. Jaksch, C. Bruder, J.I. Cirac, C.W. Gardiner, and P. Zoller. "Cold bosonic atoms in optical lattices." In: *Physical Review Letters* 81.15 (1998), p. 3108.

[11] M.P.A. Fisher, P.B. Weichman, G. Grinstein, and D.S. Fisher. "Boson localization and the superfluid-insulator transition." In: *Physical Review B* 40.1 (1989), p. 546.

[12] J. Hubbard. "Electron correlations in narrow energy bands." In: *Proceedings of the Royal Society of London. Series A. Mathematical and Physical Sciences* 276.1365 (1963), pp. 238–257.

[13] T. Lahaye, C. Menotti, L. Santos, M. Lewenstein, and T. Pfau. "The physics of dipolar bosonic quantum gases." In: *Reports on Progress in Physics* 72.12 (2009), p. 126401.

[14] H. Ritsch, P. Domokos, F. Brennecke, and T. Esslinger. "Cold atoms in cavity-generated dynamical optical potentials." In: *Reviews of Modern Physics* 85.2 (2013), p. 553.

[15] F. Mivehvar, F. Piazza, T. Donner, and H. Ritsch. "Cavity QED with Quantum Gases: New Paradigms in Many-Body Physics." In: *arXiv preprint arXiv:2102.04473* (2021).

[16] O. Dutta, M. Gajda, P. Hauke, M. Lewenstein, D.-S. Lühmann, B.A. Malomed, T. Sowiński, and J. Zakrzewski. "Non-standard Hubbard models in optical lattices: a review." In: *Reports on Progress in Physics* 78.6 (2015), p. 066001.

[17] L. Pollet, J.D. Picon, H.P. Büchler, and M. Troyer. "Supersolid phase with cold polar molecules on a triangular lattice." In: *Physical Review Letters* 104.12 (2010), p. 125302.

[18] M.A. Baranov, M. Dalmonte, G. Pupillo, and P. Zoller. "Condensed matter theory of dipolar quantum gases." In: *Chemical Reviews* 112.9 (2012), pp. 5012–5061.

[19] B. Capogrosso-Sansone, C. Trefzger, M. Lewenstein, P. Zoller, and G. Pupillo. "Quantum phases of cold polar molecules in 2D optical lattices." In: *Physical Review Letters* 104.12 (2010), p. 125301.

[20] C. Menotti, C. Trefzger, and M. Lewenstein. "Metastable states of a gas of dipolar bosons in a 2D optical lattice." In: *Physical Review Letters* 98.23 (2007), p. 235301.

[21] K. Góral, L. Santos, and M. Lewenstein. "Quantum phases of dipolar bosons in optical lattices." In: *Physical Review Letters* 88.17 (2002), p. 170406.

[22] S. Yi, T. Li, and C.P. Sun. "Novel quantum phases of dipolar Bose gases in optical lattices." In: *Physical Review Letters* 98.26 (2007), p. 260405.

[23] N. Dogra, F. Brennecke, S.D. Huber, and T. Donner. "Phase transitions in a Bose-Hubbard model with cavity-mediated global-range interactions." In: *Physical Review A* 94.2 (2016), p. 023632.

[24] R. Liao, H.-J. Chen, D.-C. Zheng, and Z.-G. Huang. "Theoretical exploration of competing phases of lattice Bose gases in a cavity." In: *Physical Review A* 97.1 (2018), p. 013624.

[25] B. Sundar and E.J. Mueller. "Lattice bosons with infinite-range checkerboard interactions." In: *Physical Review A* 94.3 (2016), p. 033631.

[26] A.E. Niederle, G. Morigi, and H. Rieger. "Ultracold bosons with cavity-mediated long-range interactions: A local mean-field analysis of the phase diagram." In: *Physical Review A* 94.3 (2016), p. 033607.

[27] S. Wald, A.M. Timpanaro, C. Cormick, and G.T. Landi. "Energy barriers between metastable states in first-order quantum phase transitions." In: *Physical Review A* 97.2 (2018), p. 023608.

[28] T. Flottat, L.d.F. de Parny, F. Hébert, V.G. Rousseau, and G.G. Batrouni. "Phase diagram of bosons in a two-dimensional optical lattice with infinite-range cavity-mediated interactions." In: *Physical Review B* 95.14 (2017), p. 144501.

[29] G.G. Batrouni, F. Hébert, and R.T. Scalettar. "Supersolid phases in the one-dimensional extended soft-core bosonic Hubbard model." In: *Physical Review Letters* 97.8 (2006), p. 087209.

[30] G.G. Batrouni, R.T. Scalettar, G.T. Zimanyi, and A.P. Kampf. "Supersolids in the Bose-Hubbard Hamiltonian." In: *Physical Review Letters* 74.13 (1995), p. 2527.

[31] H. Habibian, A. Winter, S. Paganelli, H. Rieger, and G. Morigi. "Quantum phases of incommensurate optical lattices due to cavity backaction." In: *Physical Review A* 88.4 (2013), p. 043618.

[32] D. Rossini and R. Fazio. "Phase diagram of the extended Bose–Hubbard model." In: *New Journal of Physics* 14.6 (2012), p. 065012.

[33] G.G. Batrouni, V.G. Rousseau, R.T. Scalettar, and B. Grémaud. "Competing phases, phase separation, and coexistence in the extended one-dimensional bosonic Hubbard model." In: *Physical Review B* 90.20 (2014), p. 205123.

[34] E. Berg, E.G. Dalla Torre, T. Giamarchi, and E. Altman. "Rise and fall of hidden string order of lattice bosons." In: *Physical Review B* 77.24 (2008), p. 245119.

[35] E.G. Dalla Torre, E. Berg, and E. Altman. "Hidden order in 1D Bose insulators." In: *Physical Review Letters* 97.26 (2006), p. 260401.

[36] S.F. Caballero-Benitez and I.B. Mekhov. "Bond order via light-induced synthetic many-body interactions of ultracold atoms in optical lattices." In: *New Journal of Physics* 18.11 (2016), p. 113010.

[37] S. Fernández-Vidal, G. De Chiara, J. Larson, and G. Morigi. "Quantum ground state of self-organized atomic crystals in optical resonators." In: *Physical Review A* 81.4 (2010), p. 043407.

[38] T. Sowiński, O. Dutta, P. Hauke, L. Tagliacozzo, and M. Lewenstein. "Dipolar molecules in optical lattices." In: *Physical Review Letters* 108.11 (2012), p. 115301.

[39] K. Biedroń, M. Łącki, and J. Zakrzewski. "Extended Bose-Hubbard model with dipolar and contact interactions." In: *Physical Review B* 97.24 (2018), p. 245102.

[40] F. Cartarius, A. Minguzzi, and G. Morigi. "Multimode Bose-Hubbard model for quantum dipolar gases in confined geometries." In: *Physical Review A* 95.6 (2017), p. 063603.

[41] M. Maik, P. Hauke, O. Dutta, M. Lewenstein, and J. Zakrzewski. "Density-dependent tunneling in the extended Bose–Hubbard model." In: *New Journal of Physics* 15.11 (2013), p. 113041.

[42] D. Johnstone, N. Westerberg, C.W. Duncan, and P. Öhberg. "Staggered ground states in an optical lattice." In: *Physical Review A* 100.4 (2019), p. 043614.

[43] R. Landig, L. Hruby, N. Dogra, M. Landini, R. Mottl, T. Donner, and T. Esslinger. "Quantum phases from competing short-and long-range interactions in an optical lattice." In: *Nature* 532.7600 (2016), pp. 476–479.

[44] L. Hruby, N. Dogra, M. Landini, T. Donner, and T. Esslinger. "Metastability and avalanche dynamics in strongly correlated gases with long-range interactions." In: *Proceedings of the National Academy of Sciences* 115.13 (2018), pp. 3279–3284.

[45] M.H. Anderson, J.R. Ensher, M.R. Matthews, C.E. Wieman, and E.A. Cornell. "Observation of Bose-Einstein condensation in a dilute atomic vapor." In: *Science* 269.5221 (1995), pp. 198–201.

[46] K.B. Davis, M.O. Mewes, M.R. Andrews, N.J. van Druten, D.S. Durfee, D.M. Kurn, and W. Ketterle. "Bose-Einstein condensation in a gas of sodium atoms." In: *Physical Review Letters* 75.22 (1995), p. 3969.

[47] C.C. Bradley, C.A. Sackett, J.J. Tollett, and R.G. Hulet. "Evidence of Bose-Einstein condensation in an atomic gas with attractive interactions." In: *Physical Review Letters* 75.9 (1995), p. 1687.

[48] L. Pitaevskii and S. Stringari. *Bose-Einstein condensation and superfluidity*. Oxford University Press, 2003.

[49] T. Giamarchi. *Quantum physics in one dimension*. Oxford University Press, 2004.

[50] M.A. Cazalilla, R. Citro, T. Giamarchi, E. Orignac, and M. Rigol. "One dimensional bosons: From condensed matter systems to ultracold gases." In: *Reviews of Modern Physics* 83.4 (2011), p. 1405.

[51] H.T.C. Stoof, K.B. Gubbels, and D.B.M. Dickerscheid. *Ultracold quantum fields*. Springer, 2009.

[52] F. Gerbier. *Quantum gases in optical lattices*. 2015. URL: http://citeseerx.ist.psu.edu/viewdoc/download?doi=10.1.1.846.9905&rep=rep1&type=pdf.

[53] W. Kohn. "Analytic properties of Bloch waves and Wannier functions." In: *Physical Review* 115.4 (1959), p. 809.

[54] H. Haken. *Quantenfeldtheorie des Festkörpers*. B.G. Teubner Stuttgart, 1993.

[55] G.H. Wannier. "The structure of electronic excitation levels in insulating crystals." In: *Physical Review* 52.3 (1937), p. 191.

[56] W.P. Schleich. *Quantum optics in phase space*. John Wiley & Sons, 2011.

[57] C. Cohen-Tannoudji, J. Dupont-Roc, and G. Grynberg. *Atom-photon interactions: basic processes and applications*. John Wiley & Sons, 1998.

[58] G.G. Batrouni, R.T. Scalettar, V.G. Rousseau, and B. Grémaud. "Competing supersolid and Haldane insulator phases in the extended one-dimensional bosonic Hubbard model." In: *Physical Review Letters* 110.26 (2013), p. 265303.

[59] F. Schwable. *Statistische Mechanik*. Springer-Verlag, 2006.

[60] T.D. Kühner and H. Monien. "Phases of the one-dimensional Bose-Hubbard model." In: *Physical Review B* 58.22 (1998), R14741.

[61] J.K. Freericks and H. Monien. "Phase diagram of the Bose-Hubbard model." In: *EPL (Europhysics Letters)* 26.7 (1994), p. 545.

[62] S.R. White. "Density matrix formulation for quantum renormalization groups." In: *Physical Review Letters* 69.19 (1992), p. 2863.

[63] U. Schollwöck. "The density-matrix renormalization group in the age of matrix product states." In: *Annals of physics* 326.1 (2011), pp. 96–192.

[64] G.G. Batrouni, R.T. Scalettar, and G.T. Zimanyi. "Quantum critical phenomena in one-dimensional Bose systems." In: *Physical Review Letters* 65.14 (1990), p. 1765.

[65] R.T. Scalettar, G.G. Batrouni, and G.T. Zimanyi. "Localization in interacting, disordered, Bose systems." In: *Physical Review Letters* 66.24 (1991), p. 3144.

[66] K. Suthar, R. Kraus, H. Sable, D. Angom, G. Morigi, and J. Zakrzewski. "Staggered superfluid phases of dipolar bosons in two-dimensional square lattices." In: *Physical Review B* 102.21 (2020), p. 214503.

[67] M. Fishman, S.R. White, and E.M. Stoudenmire. *The ITensor Software Library for Tensor Network Calculations*. 2020. arXiv: 2007.14822.

[68] S. Sachdev. *Quantum phase transitions*. Cambridge University Press, 2011.

[69] D.S. Rokhsar and B.G. Kotliar. "Gutzwiller projection for bosons." In: *Physical Review B* 44.18 (1991), p. 10328.

[70] W. Krauth, M. Caffarel, and J.-P. Bouchaud. "Gutzwiller wave function for a model of strongly interacting bosons." In: *Physical Review B* 45.6 (1992), p. 3137.

[71] K. Sheshadri, H.R. Krishnamurthy, R. Pandit, and T.V. Ramakrishnan. "Superfluid and insulating phases in an interacting-boson model: Mean-field theory and the RPA." In: *EPL (Europhysics Letters)* 22.4 (1993), p. 257.

[72] D. Yamamoto. "Correlated cluster mean-field theory for spin systems." In: *Physical Review B* 79.14 (2009), p. 144427.

[73] S. Baier, M.J. Mark, D. Petter, K. Aikawa, L. Chomaz, Z. Cai, M. Baranov, P. Zoller, and F. Ferlaino. "Extended Bose-Hubbard models with ultracold magnetic atoms." In: *Science* 352.6282 (2016), pp. 201–205.

[74] F. Böttcher, J.-N. Schmidt, M. Wenzel, J. Hertkorn, M. Guo, T. Langen, and T. Pfau. "Transient supersolid properties in an array of dipolar quantum droplets." In: *Physical Review X* 9.1 (2019), p. 011051.

[75] L. Chomaz, D. Petter, P. Ilzhöfer, G. Natale, A. Trautmann, C. Politi, G. Durastante, R.M.W. Van Bijnen, A. Patscheider, M. Sohmen, M.J. Mark, and F. Ferlaino. "Long-lived and transient supersolid behaviors in dipolar quantum gases." In: *Physical Review X* 9.2 (2019), p. 021012.

[76] L. Tanzi, E. Lucioni, F. Famà, J. Catani, A. Fioretti, C. Gabbanini, R.N. Bisset, L. Santos, and G. Modugno. "Observation of a dipolar quantum gas with metastable supersolid properties." In: *Physical Review Letters* 122.13 (2019), p. 130405.

[77] S.A. Moses, J.P. Covey, M.T. Miecnikowski, B. Yan, B. Gadway, J. Ye, and D.S. Jin. "Creation of a low-entropy quantum gas of polar molecules in an optical lattice." In: *Science* 350.6261 (2015), pp. 659–662.

[78] A. De Paz, A. Sharma, A. Chotia, E. Marechal, J.H. Huckans, P. Pedri, L. Santos, O. Gorceix, L. Vernac, and B. Laburthe-Tolra. "Nonequilibrium quantum magnetism in a dipolar lattice gas." In: *Physical Review Letters* 111.18 (2013), p. 185305.

[79] S.A. Moses, J.P. Covey, M.T. Miecnikowski, D.S. Jin, and J. Ye. "New frontiers for quantum gases of polar molecules." In: *Nature Physics* 13.1 (2017), pp. 13–20.

[80] L. Reichsöllner, A. Schindewolf, T. Takekoshi, R. Grimm, and H.-Ch. Nägerl. "Quantum engineering of a low-entropy gas of heteronuclear bosonic molecules in an optical lattice." In: *Physical Review Letters* 118.7 (2017), p. 073201.

[81] J.P. Covey, S.A. Moses, M. Gärttner, A. Safavi-Naini, M.T. Miecnikowski, Z. Fu, J. Schachenmayer, P.S. Julienne, A.M. Rey, D.S. Jin, and J. Ye. "Doublon dynamics and polar molecule production in an optical lattice." In: *Nature communications* 7.1 (2016), pp. 1–8.

[82] X. Deng and L. Santos. "Entanglement spectrum of one-dimensional extended Bose-Hubbard models." In: *Physical Review B* 84.8 (2011), p. 085138.

[83] K. Kawaki, Y. Kuno, and I. Ichinose. "Phase diagrams of the extended Bose-Hubbard model in one dimension by Monte-Carlo simulation with the help of a stochastic-series expansion." In: *Physical Review B* 95.19 (2017), p. 195101.

[84] L. Santos, G.V. Shlyapnikov, P. Zoller, and M. Lewenstein. "Bose-Einstein condensation in trapped dipolar gases." In: *Physical Review Letters* 85.9 (2000), p. 1791.

[85] K. Góral and L. Santos. "Ground state and elementary excitations of single and binary Bose-Einstein condensates of trapped dipolar gases." In: *Physical Review A* 66.2 (2002), p. 023613.

[86] K.P. Schmidt, J. Dorier, A.M. Läuchli, and F. Mila. "Supersolid phase induced by correlated hopping in spin-1/2 frustrated quantum magnets." In: *Physical Review Letters* 100.9 (2008), p. 090401.

[87] G.E. Astrakharchik, J. Boronat, I.L. Kurbakov, and Y.E. Lozovik. "Quantum phase transition in a two-dimensional system of dipoles." In: *Physical Review Letters* 98.6 (2007), p. 060405.

[88] K. Góral, L. Santos, and M. Lewenstein. "Quantum phases of dipolar bosons in optical lattices." In: *Physical Review Letters* 88.17 (2002), p. 170406.

[89] O. Jürgensen, F. Meinert, M.J. Mark, H.-Ch. Nägerl, and D.-S. Lühmann. "Observation of density-induced tunneling." In: *Physical Review Letters* 113.19 (2014), p. 193003.

[90] D.-S. Lühmann, O. Jürgensen, and K. Sengstock. "Multi-orbital and density-induced tunneling of bosons in optical lattices." In: *New Journal of Physics* 14.3 (2012), p. 033021.

[91] O. Jürgensen, K. Sengstock, and D.-S. Lühmann. "Twisted complex superfluids in optical lattices." In: *Scientific reports* 5 (2015), p. 12912.

[92] S. Wessel, F. Alet, M. Troyer, and G.G. Batrouni. "Quantum Monte Carlo simulations of confined bosonic atoms in optical lattices." In: *Physical Review A* 70.5 (2004), p. 053615.

[93] D.-S. Lühmann. "Twisted superfluid phase in the extended one-dimensional Bose-Hubbard model." In: *Physical Review A* 94.1 (2016), p. 011603.

[94] O. Dutta, A. Eckardt, P. Hauke, B. Malomed, and M. Lewenstein. "Bose–Hubbard model with occupation-dependent parameters." In: *New Journal of Physics* 13.2 (2011), p. 023019.

[95] H.-C. Jiang, L. Fu, and C. Xu. "Pair superfluid and supersolid of correlated hard-core bosons on a triangular lattice." In: *Physical Review B* 86.4 (2012), p. 045129.

[96] S. Qin, J. Lou, L. Sun, and Ch. Chen. "Nonlocal topological order in antiferromagnetic Heisenberg chains." In: *Physical Review Letters* 90.6 (2003), p. 067202.

[97] A.W.W. Ludwig. "Topological phases: classification of topological insulators and superconductors of non-interacting fermions, and beyond." In: *Physica Scripta* 2016.T168 (2015), p. 014001.

[98] X.-G. Wen. "Colloquium: Zoo of quantum-topological phases of matter." In: *Reviews of Modern Physics* 89.4 (2017), p. 041004.

[99] S. Ejima, H. Fehske, F. Gebhard, K. zu Münster, M. Knap, E. Arrigoni, and W. von der Linden. "Characterization of Mott-insulating and superfluid phases in the one-dimensional Bose-Hubbard model." In: *Physical Review A* 85.5 (2012), p. 053644.

[100] C. Trefzger, C. Menotti, and M. Lewenstein. "Ultracold dipolar gas in an optical lattice: The fate of metastable states." In: *Physical Review A* 78.4 (2008), p. 043604.

[101] B. Capogrosso-Sansone, C. Trefzger, M. Lewenstein, P. Zoller, and G. Pupillo. "Quantum phases of cold polar molecules in 2D optical lattices." In: *Physical Review Letters* 104.12 (2010), p. 125301.

[102] D. Yamamoto, I. Danshita, and C.A.R.S. de Melo. "Dipolar bosons in triangular optical lattices: Quantum phase transitions and anomalous hysteresis." In: *Physical Review A* 85.2 (2012), p. 021601.

[103] Y.-C. Chen, R.G. Melko, S. Wessel, and Y.-J. Kao. "Supersolidity from defect condensation in the extended boson Hubbard model." In: *Physical Review B* 77.1 (2008), p. 014524.

[104] K.-K. Ng. "Thermal phase transitions of supersolids in the extended Bose-Hubbard model." In: *Physical Review B* 82.18 (2010), p. 184505.

[105] R.T. Scalettar, G.G. Batrouni, A.P. Kampf, and G.T. Zimanyi. "Simultaneous diagonal and off-diagonal order in the Bose-Hubbard Hamiltonian." In: *Physical Review B* 51.13 (1995), p. 8467.

[106] T.D. Kühner, S.R. White, and H. Monien. "One-dimensional Bose-Hubbard model with nearest-neighbor interaction." In: *Physical Review B* 61.18 (2000), p. 12474.

[107] D.L. Kovrizhin, G.V. Pai, and S. Sinha. "Density wave and supersolid phases of correlated bosons in an optical lattice." In: *EPL (Europhysics Letters)* 72.2 (2005), p. 162.

[108] I. Danshita and C.A.R.S. de Melo. "Stability of superfluid and supersolid phases of dipolar bosons in optical lattices." In: *Physical Review Letters* 103.22 (2009), p. 225301.

[109] P. Sengupta, L.P. Pryadko, F. Alet, M. Troyer, and G. Schmid. "Supersolids versus phase separation in two-dimensional lattice bosons." In: *Physical Review Letters* 94.20 (2005), p. 207202.

[110] T. Ohgoe, T. Suzuki, and N. Kawashima. "Ground-state phase diagram of the two-dimensional extended bose-hubbard model." In: *Physical Review B* 86.5 (2012), p. 054520.

[111] M. Iskin. "Route to supersolidity for the extended Bose-Hubbard model." In: *Physical Review A* 83.5 (2011), p. 051606.

[112] T. Kimura. "Gutzwiller study of extended Hubbard models with fixed boson densities." In: *Physical Review A* 84.6 (2011), p. 063630.

[113] K. Suthar, H. Sable, R. Bai, S. Bandyopadhyay, S. Pal, and D. Angom. "Supersolid phase of the extended Bose-Hubbard model with an artificial gauge field." In: *Physical Review A* 102.1 (2020), p. 013320.

[114] K.-K. Ng and Y.-C. Chen. "Supersolid phases in the bosonic extended Hubbard model." In: *Physical Review B* 77.5 (2008), p. 052506.

[115] F. Heydarinasab and J. Abouie. "Inhomogeneous hard-core bosonic mixture with checkerboard supersolid phase: Quantum and thermal phase diagram." In: *Physical Review B* 96.10 (2017), p. 104406.

[116] U. Bissbort, F. Deuretzbacher, and W. Hofstetter. "Effective multibody-induced tunneling and interactions in the Bose-Hubbard model of the lowest dressed band of an optical lattice." In: *Physical Review A* 86.2 (2012), p. 023617.

[117] M. Łącki, D. Delande, and J. Zakrzewski. "Dynamics of cold bosons in optical lattices: effects of higher Bloch bands." In: *New Journal of Physics* 15.1 (2013), p. 013062.

[118] J. Major, M. Łącki, and J. Zakrzewski. "Reexamination of the variational Bose-Hubbard model." In: *Physical Review A* 89.4 (2014), p. 043626.

[119] B. Chatterjee, C. Lévêque, J. Schmiedmayer, and A.U.J. Lode. "Detecting One-Dimensional Dipolar Bosonic Crystal Orders via Full Distribution Functions." In: *Physical Review Letters* 125.9 (2020), p. 093602.

[120] T. Đurić, K. Biedroń, and J. Zakrzewski. "Fibonacci anyon excitations of one-dimensional dipolar lattice bosons." In: *Physical Review B* 95.8 (2017), p. 085102.

[121] M.L. Wall and L.D. Carr. "Dipole–dipole interactions in optical lattices do not follow an inverse cube power law." In: *New Journal of Physics* 15.12 (2013), p. 123005.

[122] J. Larson, B. Damski, G. Morigi, and M. Lewenstein. "Mott-insulator states of ultracold atoms in optical resonators." In: *Physical Review Letters* 100.5 (2008), p. 050401.

[123] A.J. Heeger, S. Kivelson, J.R. Schrieffer, and W.-P. Su. "Solitons in conducting polymers." In: *Reviews of Modern Physics* 60.3 (1988), p. 781.

[124] A.P. Kampf and G.T. Zimanyi. "Superconductor-insulator phase transition in the boson Hubbard model." In: *Physical Review B* 47.1 (1993), p. 279.

[125] B. Mühlschlegel. "Functional Integral Approach to Some Models of Solid State Physics." In: *Path Integrals*. Springer, 1978, pp. 383–418.

[126] J.W. Negele and O. Henri. *Quantum many-particle systems*. CRC Press, 2018.

[127] W. Zwerger. "Mott–Hubbard transition of cold atoms in optical lattices." In: *Journal of Optics B: quantum and semiclassical optics* 5.2 (2003), p. 9.

[128] J. Panas, A. Kauch, and K. Byczuk. "Spectral properties and phase diagram of correlated lattice bosons in an optical cavity within bosonic dynamical mean-field theory." In: *Physical Review B* 95.11 (2017), p. 115105.

[129] B. Blaß, H. Rieger, G. Roósz, and F. Iglói. "Quantum relaxation and metastability of lattice bosons with cavity-induced long-range interactions." In: *Physical Review Letters* 121.9 (2018), p. 095301.

[130] G.G. Batrouni and R.T. Scalettar. "Phase separation in supersolids." In: *Physical Review Letters* 84.7 (2000), p. 1599.

[131] N. Dogra private communication (2017).

[132] A. Campa, T. Dauxois, and S. Ruffo. "Statistical mechanics and dynamics of solvable models with long-range interactions." In: *Physics Reports* 480.3-6 (2009), pp. 57–159.

[133] T. Fogarty, C. Cormick, H. Landa, V.M. Stojanović, E. Demler, and G. Morigi. "Nanofriction in cavity quantum electrodynamics." In: *Physical Review Letters* 115.23 (2015), p. 233602.

[134] Y. Li, L. He, and W. Hofstetter. "Lattice-supersolid phase of strongly correlated bosons in an optical cavity." In: *Physical Review A* 87.5 (2013), p. 051604.

[135] P. Zupancic, D. Dreon, X. Li, A. Baumgärtner, A. Morales, W. Zheng, N.R. Cooper, T. Esslinger, and T. Donner. "P-band induced self-organization and dynamics with repulsively driven ultracold atoms in an optical cavity." In: *Physical Review Letters* 123.23 (2019), p. 233601.

[136] O. Jürgensen and D.-S. Lühmann. "Dimerized Mott insulators in hexagonal optical lattices." In: *New Journal of Physics* 16.9 (2014), p. 093023.

[137] I. Affleck, T. Kennedy, E.H. Lieb, and H. Tasaki. In: *Phys. Rev. Lett.* 59.799 (1987).

[138] P.W. Anderson. "The resonating valence bond state in La2CuO4 and superconductivity." In: *Science* 235.4793 (1987), pp. 1196–1198.

[139] K. Baumann, R. Mottl, F. Brennecke, and T. Esslinger. "Exploring symmetry breaking at the Dicke quantum phase transition." In: *Physical Review Letters* 107.14 (2011), p. 140402.

[140] T. Mishra, S. Greschner, and L. Santos. "Density-induced geometric frustration of ultra-cold bosons in optical lattices." In: *New Journal of Physics* 18.4 (2016), p. 045016.

[141] M. Di Dio, L. Barbiero, A. Recati, and M. Dalmonte. "Spontaneous Peierls dimerization and emergent bond order in one-dimensional dipolar gases." In: *Physical Review A* 90.6 (2014), p. 063608.

[142] D.J. Thouless, M. Kohmoto, M.P. Nightingale, and M. den Nijs. "Quantized Hall conductance in a two-dimensional periodic potential." In: *Physical Review Letters* 49.6 (1982), p. 405.

[143] K.v. Klitzing, G. Dorda, and M. Pepper. "New method for high-accuracy determination of the fine-structure constant based on quantized Hall resistance." In: *Physical Review Letters* 45.6 (1980), p. 494.

[144] T. Senthil. "Symmetry-protected topological phases of quantum matter." In: *Annu. Rev. Condens. Matter Phys.* 6.1 (2015), pp. 299–324.

[145] A.P. Schnyder, S. Ryu, A. Furusaki, and A.W.W. Ludwig. "Classification of topological insulators and superconductors in three spatial dimensions." In: *Physical Review B* 78.19 (2008), p. 195125.

[146] C.-K. Chiu, J.C.Y. Teo, A.P. Schnyder, and S. Ryu. "Classification of topological quantum matter with symmetries." In: *Reviews of Modern Physics* 88.3 (2016), p. 035005.

[147] S. Raghu, X.-L. Qi, C. Honerkamp, and S.-C. Zhang. "Topological mott insulators." In: *Physical Review Letters* 100.15 (2008), p. 156401.

[148] C. Weeks and M. Franz. "Interaction-driven instabilities of a Dirac semimetal." In: *Physical Review B* 81.8 (2010), p. 085105.

[149] E.V. Castro, A.G. Grushin, B. Valenzuela, M.A.H. Vozmediano, A. Cortijo, and F. de Juan. "Topological fermi liquids from coulomb interactions in the doped honeycomb lattice." In: *Physical Review Letters* 107.10 (2011), p. 106402.

[150] A.G. Grushin, E.V. Castro, A. Cortijo, F. de Juan, M.A.H. Vozmediano, and B. Valenzuela. "Charge instabilities and topological phases in the extended Hubbard model on the honeycomb lattice with enlarged unit cell." In: *Physical Review B* 87.8 (2013), p. 085136.

[151] A. Dauphin, M. Mueller, and M.-A. Martin-Delgado. "Rydberg-atom quantum simulation and Chern-number characterization of a topological Mott insulator." In: *Physical Review A* 86.5 (2012), p. 053618.

[152] D. González-Cuadra, P.R. Grzybowski, A. Dauphin, and M. Lewenstein. "Strongly correlated bosons on a dynamical lattice." In: *Physical Review Letters* 121.9 (2018), p. 090402.

[153] D. González-Cuadra, A. Dauphin, P.R. Grzybowski, P. Wójcik, M. Lewenstein, and A. Bermudez. "Symmetry-breaking topological insulators in the Z 2 Bose-Hubbard model." In: *Physical Review B* 99.4 (2019), p. 045139.

[154] D. González-Cuadra, A. Bermudez, P.R. Grzybowski, M. Lewenstein, and A. Dauphin. "Intertwined topological phases induced by emergent symmetry protection." In: *Nature communications* 10.1 (2019), pp. 1–7.

[155] M. Hohenadler and F.F. Assaad. "Correlation effects in two-dimensional topological insulators." In: *Journal of Physics: Condensed Matter* 25.14 (2013), p. 143201.

[156] S. Rachel. "Interacting topological insulators: a review." In: *Reports on Progress in Physics* 81.11 (2018), p. 116501.

[157] Z.-X. Gong, M.F. Maghrebi, A. Hu, M.L. Wall, M. Foss-Feig, and A.V. Gorshkov. "Topological phases with long-range interactions." In: *Physical Review B* 93.4 (2016), p. 041102.

[158] A.Y. Kitaev. "Unpaired Majorana fermions in quantum wires." In: *Physics-Uspekhi* 44.10S (2001), p. 131.

[159] O. Viyuela, D. Vodola, G. Pupillo, and M.A. Martin-Delgado. "Topological massive Dirac edge modes and long-range superconducting Hamiltonians." In: *Physical Review B* 94.12 (2016), p. 125121.

[160] O. Viyuela, L. Fu, and M.A. Martin-Delgado. "Chiral topological superconductors enhanced by long-range interactions." In: *Physical Review Letters* 120.1 (2018), p. 017001.

[161] A. Alecce and L. Dell'Anna. "Extended Kitaev chain with longer-range hopping and pairing." In: *Physical Review B* 95.19 (2017), p. 195160.

[162] S.B. Jäger, L. Dell'Anna, and G. Morigi. "Edge states of the long-range Kitaev chain: An analytical study." In: *Physical Review B* 102.3 (2020), p. 035152.

[163] K. Patrick, T. Neupert, and J.K. Pachos. "Topological quantum liquids with long-range couplings." In: *Physical Review Letters* 118.26 (2017), p. 267002.

[164] Z.-X. Gong, M.F. Maghrebi, A. Hu, M. Foss-Feig, P. Richerme, C. Monroe, and A.V. Gorshkov. "Kaleidoscope of quantum phases in a long-range interacting spin-1 chain." In: *Physical Review B* 93.20 (2016), p. 205115.

[165] J. Sicks and H. Rieger. "Haldane insulator in the 1D nearest-neighbor extended Bose-Hubbard model with cavity-mediated long-range interactions." In: *The European Physical Journal B* 93 (2020), pp. 1–8.

[166] F. Mivehvar, H. Ritsch, and F. Piazza. "Superradiant topological peierls insulator inside an optical cavity." In: *Physical Review Letters* 118.7 (2017), p. 073602.

[167] W.-P. Su, J.R. Schrieffer, and A.J. Heeger. "Soliton excitations in polyacetylene." In: *Physical Review B* 22.4 (1980), p. 2099.

[168] R. Shankar. "Topological Insulators–A review." In: *arXiv preprint arXiv:1804.06471* (2018).

[169] S. de Léséleuc, V. Lienhard, P. Scholl, D. Barredo, S. Weber, N. Lang, H.P. Büchler, T. Lahaye, and A. Browaeys. "Observation of a symmetry-protected topological phase of interacting bosons with Rydberg atoms." In: *Science* 365.6455 (2019), pp. 775–780.

[170] A. Kitaev. "Periodic table for topological insulators and superconductors." In: *AIP conference proceedings*. Vol. 1134. 1. American Institute of Physics. 2009, pp. 22–30.

[171] J. Zak. "Berry's phase for energy bands in solids." In: *Physical Review Letters* 62.23 (1989), p. 2747.

[172] F. Grusdt, M. Höning, and M. Fleischhauer. "Topological edge states in the one-dimensional superlattice Bose-Hubbard model." In: *Physical Review Letters* 110.26 (2013), p. 260405.

[173] M. Atala, M. Aidelsburger, J.T. Barreiro, D. Abanin, T. Kitagawa, E. Demler, and I. Bloch. "Direct measurement of the Zak phase in topological Bloch bands." In: *Nature Physics* 9.12 (2013), pp. 795–800.

[174] F. Pollmann, A.M. Turner, E. Berg, and M. Oshikawa. "Entanglement spectrum of a topological phase in one dimension." In: *Physical Review B* 81.6 (2010), p. 064439.

[175] M.V. Berry. "Quantal phase factors accompanying adiabatic changes." In: *Proceedings of the Royal Society of London. A. Mathematical and Physical Sciences* 392.1802 (1984), pp. 45–57.

[176] Y. Hatsugai. "Quantized Berry phases as a local order parameter of a quantum liquid." In: *Journal of the Physical Society of Japan* 75.12 (2006), pp. 123601–123601.

[177] G.M. Crosswhite, A.C. Doherty, and G. Vidal. "Applying matrix product operators to model systems with long-range interactions." In: *Physical Review B* 78.3 (2008), p. 035116.

[178] B. Pirvu, V. Murg, J.I. Cirac, and F. Verstraete. "Matrix product operator representations." In: *New Journal of Physics* 12.2 (2010), p. 025012.

## FIGURE CREDIT

Fig. 1.4 is taken from Ref. [60] with the permission of the American Physical Society and of their authors.

Fig. 2.5 is taken from Ref. [33] with the permission of the American Physical Society and of their authors.

# ACKNOWLEDGMENTS

Here I would like to acknowledge all the people who accompanied me during the years of my PhD.

First of all, I want to express deep thankfulness to my supervisor Prof. Giovanna Morigi. You always supported, encouraged and guided me through all these years. Thank you for inspiring me and for opening to me so many possibilities.

Moreover, I would like to give thanks to Prof. Jakub Zakrzewski for our fruitful cooperation. Thank you for hosting me in your group in Krakow. I always enjoy working with you and your group. Within this cooperation I was also happy to get to know Krzysztof Biedroń, Titas Chanda and Kuldeep Suthar. I would like to show gratitude for all the helpful discussions we had. Especially I would like to thank Krzysztof Biedroń, who patiently introduced me to Itensor.

Special gratitude goes also to my collaborates Shraddha Sharma, Lukas Himbert and Florian Cartarius for helping me through different periods of my PhD and being more then just colleagues for me. I also want to thank my collaborators Cecilia Cormick, Hrushikesh Sable and Dilip Angom.

I am grateful that during my years in the group of Prof. Giovanna Morigi I could meet so many wonderful people and even developed with some of them close friendships. I would like to thank all of them for creating such a nice atmosphere in the group, in which there was space to discuss about physics, to laugh and to help out each other in all kind of problems in life. Thank you for this Shraddha Sharma, Lukas Himbert, Florian Cartarius, Luigi Giannelli, Simon Jäger, Ralf Betzholz, Katharina Rojan, Stefan Schütz, Susanne Blum, Tim Keller, Andreas Buchheit, Tom Schmit, Francesco Rosati, Nahuel Freitas, Alexey Konovalov, Frederic Folz, Peter-Maximilian Ney, Christian Otto, Cedric Quint and Raphael Menu.

Herzlichen Dank auch an Monika Francois, Ingeborg Michel und Susanna Trampert für das souveräne Verwalten aller bürokratischen Angelegenheiten.

Außerdem möchte ich meinen Freunden, die ich während meines Studiums kennenlernte durfte, und die mich bis heute begleiten, danken. Ich danke auch meinen Freunden aus meiner WG, die für mich während dieser Zeit immer eine wichtige Stütze waren.

Zuletzt möchte ich ganz besonders meiner Familie danken: meinen Eltern Maria und Rainer, meiner kleinen Schwester Magdalena und meinem großen Bruder Raphael, die mich in jeder Lebenslage unterstützen.

## COLOPHON

This document was typeset using the typographical look-and-feel `classicthesis` developed by André Miede and Ivo Pletikosić. The style was inspired by Robert Bringhurst's seminal book on typography "*The Elements of Typographic Style*". `classicthesis` is available for both LaTeX and LyX:

https://bitbucket.org/amiede/classicthesis/

*Final Version* as of October 18, 2021 (classicthesis v4.6).